THE UNIVERSITY *of* EDINBURGH

This thesis has been submitted in fulfilment of the requirements for a postgraduate degree (e.g. PhD, MPhil, DClinPsychol) at the University of Edinburgh. Please note the following terms and conditions of use:

- This work is protected by copyright and other intellectual property rights, which are retained by the thesis author, unless otherwise stated.
- A copy can be downloaded for personal non-commercial research or study, without prior permission or charge.
- This thesis cannot be reproduced or quoted extensively from without first obtaining permission in writing from the author.
- The content must not be changed in any way or sold commercially in any format or medium without the formal permission of the author.
- When referring to this work, full bibliographic details including the author, title, awarding institution and date of the thesis must be given.

The application of laser anemometry in acoustic measurement standards.

Thomas Joseph MacGillivray

A thesis submitted in fulfilment of the requirements

for the degree of Doctor of Philosophy

to the

University of Edinburgh

2002

Abstract

The absolute measurement of acoustic particle velocity using Laser Doppler Anemometry (LDA) provides the basis for a method of microphone calibration. In this thesis, after the current standardized calibration method (called reciprocity) is explained, the application of LDA to the determination of sound pressure acting on a microphone is discussed. From a measurement of the output voltage for a given sound pressure, the sensitivity of the microphone can be calculated.

In LDA, there are two different techniques for detecting and analysing the Doppler signal generated by acoustic particle motion: continuous detection followed by frequency or time domain analysis, and photon correlation. After a brief discussion of the theory of both methods, their application to measurements within a standing-wave tube is investigated. Velocity measurements extracted from Doppler signals are used to derive values of sound pressure, which are compared with probe microphone measurements. The continuous detection and photon correlation LDA systems are used to measure particle velocity amplitude in a standing wave for frequencies between 660 Hz and 4 kHz and velocities between 1 mms^{-1} and 18 mms^{-1}.

LDA is applied to the measurement of microphone sensitivity. The frequency response of the probe microphone is characterized relative to the response of a reference microphone. From the frequency response information, the output voltage of the probe microphone, and the LDA derived sound pressure in a standing wave the sensitivity of the reference microphone is established. Using the continuous detection system, the

microphone sensitivity is measured to within ± 0.1 dB of the sensitivity obtained by reciprocity calibration for frequencies between 660 Hz and 2 kHz. Using the photon correlation system, the sensitivity is measured to within ± 0.2 dB for the same frequency range.

Initial measurements were performed in a free field environment, using the photon correlation system, to demonstrate the potential for further development of the LDA calibration technique.

Acknowledgements

I would like to thank Murray Campbell and Clive Greated, my supervisors, for their enthusiastic support and guidance during the course of this research programme. I am also very grateful to Richard Barham for his helpful comments and invaluable advice.

Financial support was provided by the National Physical Laboratory.

I would also like to thank members of the University of Edinburgh Acoustics and Fluid Dynamics research group for their help and support. In particular Alistair Shawcross and Orlando Richards for computing related matters, Frank Morris for speedy technical assistance, and John Cullen for useful suggestions. Thanks are also due to Maarten, Ted, Susan, Anthony, Dawn, Jim, Cosgrove, Dave, Sharp, Alix, Mark, Jonathon, Naz, Alan, and Scott.

Finally, I would like to express my gratitude to my parents, to my sisters (Kate and Sarah), to the rest of my family, and to my friends for their constant moral (and sometimes financial) support.

Contents

Chapter 1

Introduction

1.1 General introduction to the acoustic measurement standard

For a measurement to have any technical validity it must be founded on some physical reference quantity or standard. The provision of primary measurement standards for physical quantities is the remit of national metrology laboratories around the world. In acoustics, the fundamental measurement quantity is sound pressure measured in pascals and the primary standard for sound in air is based on the measurement of the sensitivity of laboratory standard microphones. Measuring the sensitivity of a microphone, i.e. its calibration, essentially requires the output voltage for a given sound pressure.

In the early days of modern acoustical measurement, the primary standard for sound pressure in air was based on the so-called Rayleigh disk. Acoustic particle velocity was determined from the degree of rotation of a small light weight disk suspended in an acoustic field by a fine thread along its diameter. The particle velocity was used to derive the sound pressure incident on a microphone [1].

In the 1960s, reciprocity calibration of microphones provided the potential for lower uncertainty and was adopted by the International Electrotechnical Commission (IEC) as the preferred method of realizing the primary standard and this arrangement persists today [2]. Since its adoption, the reciprocity method has been refined to the point where further efforts to develop it are producing ever diminishing returns.

The reciprocity method of calibration is indirect in that no evaluation of the acting sound pressure is required. In contrast, optical techniques provide a direct approach where the sound pressure is determined from the measurement of acoustic particle velocity using a laser Doppler system. Taylor developed such a system, based on laser Doppler anemometry (LDA) measurements inside a travelling wave tube [3]. The calibration method suffered from a prolonged measurement time and was impractical for routine implementation. Consequently it was regarded as a means of validating reciprocity rather than providing a viable alternative to it.

Recent developments in optical techniques, and particularly LDA, means that there is potential to improve calibration based on the measurement of acoustic particle velocity and return to measurement standards derived from this.

1.2 General introduction to laser Doppler anemometry

LDA is a non-intrusive point measuring technique in the field of fluid mechanics. The principle is to measure the Doppler frequency shift of laser light scattered by particles moving with the fluid. The measurement of velocity is direct and so no calibration is required. Since the pioneering work of Yeh and Cummins [4], there have been advances in both optical technologies and processing electronics resulting in the development of numerous practical LDA applications.

In a real fringe LDA system, interference fringes are formed at the intersection of two laser beams [5]. Micro-particles are suspended in the flow. As these seeding particles move across the ellipsoidal fringe volume they scatter light into a photodetector. The intensity of the scattered light fluctuates with a frequency that is proportional to the seeding particle velocity. The purpose of the seeding particles is to increase the intensity of scattered light at the detector surface. LDA has been used in the measurement of laminar and turbulent flows in both liquids and gases [6] [7]. Early work on the statistical analysis of LDA signals [8], subsequently contributed to the development of signal processing techniques.

The influence of an acoustic field causes the seeding particles to oscillate back and forth across the fringe volume. The photodetector signal takes the form of a frequency modulated wave with modulation frequency equal to the fundamental acoustic frequency. LDA has been applied to the study of sound fields using several different

methods for detecting and analysing the high pass filtered photodetector signal called the Doppler signal. Measurements of acoustic particle velocity amplitude were performed, using frequency domain analysis of the continuous Doppler signal, in air [9] [10] and in water [11]. Frequency tracking, i.e. a demodulation of the continuous Doppler signal in the time domain to yield instantaneous frequency, has been used in the measurement of instantaneous acoustic particle velocities in air [12] [13] and in water [14].

Alternatively, the photodetector signal may be interpreted as a series of discrete pulses rather than a continuous voltage signal. The signal is correlated with itself to produce the autocorrelation function which can be analysed to yield measurements of acoustic particle velocity amplitude [15] [16] and mean flow velocity [17]. Work carried out by Greated demonstrated the potential for free field measurements using photon correlation LDA [18].

1.3 Aims and contents of the thesis

The aims of the present work are to:

1. investigate techniques for processing continuous Doppler signals, produced by acoustic particle motion, in both the frequency and time domains.

2. investigate techniques for processing discrete pulse Doppler signals generated by photon correlation LDA.

3. develop photon correlation apparatus (photomultiplier and new generation of digital correlator) and software for the measurement of acoustic particle velocity.

4. verify that both the continuous signal and the photon correlation LDA systems correctly measure acoustic particle velocity amplitude by performing LDA measurements in a mono-frequency standing wave and comparing with pressure measurements made with a microphone.

5. assess the uncertainty associated with the LDA measurements.

6. develop a microphone calibration technique based on LDA measurements of acoustic particle velocity amplitude and measure the sensitivity of a microphone using both systems.

7. assess the feasibility of applying LDA to the measurement of acoustic particle velocity in a free field with the subsequent aim of developing a free field microphone calibration technique.

In chapter 2 the requirement for measurement standards is explained. The background to the acoustic pressure standard in air is discussed in relation to the history of the development of the measurement microphone. The principle of operation of the measurement microphone and the definitions of sensitivity are outlined. Reciprocity, the current standardized method for microphone calibration, is described. Finally, the application of LDA to the measurement of microphone sensitivity is considered.

Chapter 3 begins with a brief description of alternative measuring techniques before detailing the basic theory behind LDA. The form of the continuous photodetector signal is deduced for a constant mean flow and for an acoustic field. Signal processing methods are discussed along with their limitations.

Chapter 4 is concerned with photon correlation LDA and the interpretation of the photomultiplier signal as a series of discrete pulses. The theoretical form of the autocorrelation function is deduced for a mean flow superimposed onto the acoustic oscillation. The measurement of acoustic particle velocity and mean flow velocity is considered. Finally, the limitations of digital correlation are discussed.

The operational characteristics of the probe microphone are discussed in chapter 5. The relationship between particle velocity and pressure in a standing wave is established before the calculation of characteristic acoustic impedance from the environmental conditions is detailed. The two LDA systems used in the present study are introduced along with the experimental arrangement of the standing wave tube apparatus.

The measurements in chapter 6 demonstrate that the continuous signal LDA system can successfully be used to measure the mean flow velocity, the acoustic particle velocity amplitude, and the instantaneous particle velocity in a standing wave. The pressure amplitude derived from the LDA measurements is found to be in good agreement with the probe microphone measurements. Also, the uncertainty in the LDA measurements is determined. Measurements of microphone sensitivity are presented and compared

to the calibrated sensitivity, obtained by reciprocity.

The results in chapter 7 demonstrate that the theoretical form of the autocorrelation function deduced for acoustic particle motion is in agreement with the measurements obtained using the photon correlation system. The pressure amplitude in the standing wave is derived from the LDA photon correlation measurements and compared to the probe microphone measurements. The sensitivity of a microphone is measured using the system. Finally, preliminary measurements are performed in a free field to demonstrate the potential for further development of the technique.

Chapter 8 discusses the feasibility of setting up a free field calibration facility based on LDA. Signal processing techniques and seeding methods are considered. The arrangement of the LDA system and the free field chamber is discussed.

The thesis concludes with chapter 9 which summarizes the findings of the work and suggests areas for future investigation.

Chapter 2

Acoustic measurement standards

2.1 Introduction

Measurements must be founded on some physical reference quantity or standard in order to have any technical validity. The requirement for measurement standards and a measurement infrastructure in society is explained in section 2.2. The remainder of this chapter is devoted to a discussion on the background to the acoustic pressure standard. The development of the condenser microphone and the history of the acoustic pressure standard are examined in section 2.3. The principal of operation of the measurement microphone is outlined in section 2.4 along with the different definitions of sensitivity. Details of the current standardized method for microphone calibration are given in section 2.5. Finally, the application of a laser measuring technique to the realization of the acoustic pressure standard is considered in section 2.6.

2.2 The role of measurement standards

The ability to demonstrate the accuracy and consistency of measurements is essential in science, engineering, industry, and commerce. We have confidence in that, for example, a kilogram is the same quantity when measured in different parts of the country or in other countries around the world. This consistency is achieved through a defined measurement infrastructure. In the UK, the Department of Trade and Industry is responsible for this infrastructure which is called the National Measurement System (NMS). All measurements made in the UK have an ultimate reference point called the national primary standard. The NMS enables a traceable link between measurements and the applicable primary standard to be demonstrated.

The national primary standard is a measure of the relevant quantity realized to the highest possible accuracy and stability. Most of the primary standards on which the NMS is founded are developed and maintained by the National Physical Laboratory (NPL). NPL aims to guarantee the accuracy and availability of the national standards while also ensuring compatibility with those of other countries. This is achieved through ongoing research projects to continually develop and improve the primary standards and intercomparisons with overseas national laboratories.

The estimation of uncertainty is an essential part of any measurement procedure and is an indication of its quality. The evaluation of the uncertainty in a measurement allows a comparison with the relevant standard, which has an associated uncertainty.

2.3 The acoustic pressure standard

The National Measurement System is of course relevant to acoustics. The fundamental measurement quantity is sound pressure, measured in pascals and often quoted in decibels relative to a reference quantity. It may also be weighted in time or frequency or combined with other physical or subjective factors. Examples of the application of acoustical measurements include architectural acoustics, environmental noise, medical ultrasound, and musical acoustics. All of these measurements require a standard in sound pressure.

Microphones are used extensively to measure sound in air and can be very stable if kept in a controlled environment. For these reasons the primary standard for sound pressure in air is based on the measurement of the sensitivity of laboratory standard microphones. The laboratory standard microphone is a specification of condenser measurement microphone. To fully understand why the primary standard for acoustics came to be maintained in this way it is necessary to review the development of the condenser microphone and the history of acoustic standards.

2.3.1 Development of acoustic standards

The measurement of sound using the condenser microphone was first suggested by Wente [19]. The electrical output of the condenser microphone was directly proportional to sound pressure and this is the same principle employed in modern measure-

ment microphones today. The term condenser refers to a capacitor. Essentially the calibration of the microphone requires the sensitivity, that is the output voltage for a given sound pressure, to be determined. Subsequently, several methods of producing a known sound pressure were developed which were effectively early acoustic standards.

Wente used a pistonphone to generate a known sound pressure inside a sealed cavity [19]. The piston was positioned inside a wall of the cavity and the microphone diaphragm made up the opposing surface. Moving the piston in or out produces a small volume change, δV. The volume change is calculated by measuring the piston displacement and surface area. If the volume change is small compared to the cavity volume, V, and the piston is driven sinusoidally at a sufficiently high frequency for the air to be compressed adiabatically, the adiabatic gas law can be used to deduce the pressure variation within the cavity. The pressure variation is given by

$$\delta p = \frac{\gamma p_0 \, \delta V}{V} \tag{2.1}$$

where γ is the ratio of specific heats for air and p_0 is the static pressure in the cavity.

The pressure generated by the pistonphone cannot be calculated accurately because the volume of the cavity and the volume change produced by the piston are difficult to measure. Also, the cavity must have a large enough volume for the generated pressure to be insensitive to the volume of the microphone. Equation 2.1 assumes that the sound pressure is distributed uniformly in the cavity and so the dimensions of the cavity limit the acoustic wavelength and frequency that the pistonphone can be used with.

The thermophone, developed to generate a calculable sound pressure, was based on the principle that an alternating current passed through a conductor would generate heat [20]. The conductor was a thin piece of foil which had a small heat capacity and so its temperature would closely follow the alternating current. The surrounding air was heated periodically producing a sound wave. Arnold and Crandall calculated the source strength of the thermophone in a free field and for the pressure generated inside a closed cavity.

In practice the thermophone must be operated in precisely controlled environmental conditions which are difficult to establish in the space required to generate a free field. In a closed cavity the uniform distribution of sound pressure is assumed. As with the pistonphone this results in a limit to the acoustic wavelength. However, unlike the pistonphone the volume can be completely sealed off allowing it to be filled with hydrogen or helium. As the wavelength of sound is much larger in these gases than in air almost the whole audible frequency range could be used.

A third device designed to produce a standard source of sound was the electrostatic actuator. It consisted of a grid that was placed in front of the microphone diaphragm [1]. An alternating potential applied between the actuator and the diaphragm produced an electrostatic force which simulated a sound pressure. The force depends on the square of the distance between the actuator and the diaphragm. As this distance is difficult to measure with sufficient accuracy, the calibration method itself was not particularly precise.

As a highly accurate standard sound source is difficult to achieve, a number of alternative methods for the absolute calibration of microphones were developed. A method for calculating sound pressure based on measurements with a Rayleigh disk was devised. Acoustic particle velocity was determined from the degree of rotation of a small light weight disk suspended in an acoustic field by a fine thread along its diameter. For a plane progressive wave, the particle velocity was used to calculate the sound pressure incident on a microphone [1]. However, problems arose due to the delicate suspension of the disk and draughts and convection currents in the air. Also, the measurements which were intended to verify the accuracy of the thermophone, demonstrated that the sensitivity of a microphone in a free field was different to that in a closed cavity.

Greater success was achieved with the Rayleigh disk method combined with a standing wave tube. The disks were placed at the velocity antinode positions inside the tube which was terminated with a microphone. The pressure at the end of the tube can be calculated from the particle velocity and the sensitivity of the microphone can be determined by measuring the voltage output. This method was used for the absolute pressure calibration of microphones for frequencies up to 10 kHz until the early 1960's.

The reciprocal characteristics of the condenser microphone provided the basis for another calibration technique. Essentially, the sensitivity of a condenser microphone when used as a receiver can be assumed to be the same as the sensitivity when used as

a transmitter. The calibration technique involves using one microphone as a source of sound while a second microphone is exposed to the generated sound field. Provided details of the sound field and the two devices are known, the absolute calibration was possible [21] [22]. The reciprocity method is indirect in that there is no evaluation of the acting sound pressure and a standard source of sound pressure is no longer required.

In the 1960's, reciprocity calibration of microphones provided the potential for lower uncertainty and was adopted by the International Electrotechnical Commission (IEC) as the preferred method of realizing the acoustic pressure standard [2]. This arrangement persists today. Since its adoption the reciprocity method has been refined to the point where further efforts to develop it are producing ever diminishing returns.

2.4 The measurement microphone

In this next section, the operational characteristics of the modern measurement microphone will be discussed before the reciprocity technique is explained in greater detail in section 2.5. Figure 2.1 shows a selection of different types of measurement microphone. Often referred to as condenser microphones, they operate by the variation of electrical capacitance [23]. There are three definitions of sensitivity depending on the type of acoustic field in which the microphone is used. By considering the forces acting on the diaphragm and determining the mechanical and electrical behaviour of the microphone, expressions may be derived for the sensitivity.

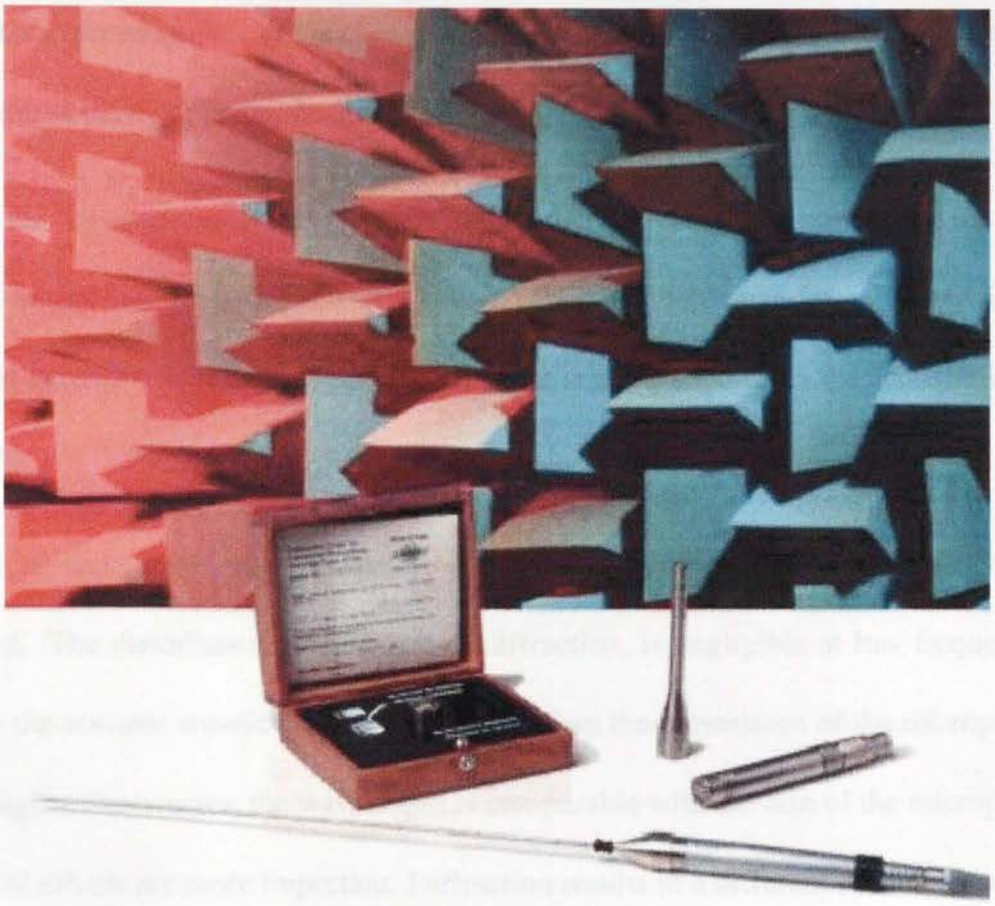

Figure 2.1: A selection of various measurement microphones.

2.4.1 Definition of sensitivity

In a pressure field, the sound pressure has the same magnitude and phase at any position. It can be assumed that the sound pressure is distributed uniformly over the diaphragm of the microphone. In this situation the pressure sensitivity (measured in volts per pascal) is defined as [23]:

"For a sinusoidal signal of given frequency and for given environmental conditions, the quotient of the open-circuit voltage of the microphone by the sound pressure acting

over the exposed surface of the diaphragm, the sound pressure being uniformly applied over the surface of the diaphragm."

Here the *"open-circuit voltage"* refers to the alternating voltage appearing at the electrical output terminals of the microphone. Pressure fields can be generated inside closed cavities which have dimensions that are small compared to the acoustic wavelength.

In an open environment the microphone will affect the sound field in which it is placed. The disturbance, mainly due to diffraction, is negligible at low frequencies when the acoustic wavelength is much greater than the dimensions of the microphone. For higher frequencies, the wavelength is comparable with the size of the microphone and the effects are more important. Diffraction results in a different sound pressure at the microphone diaphragm from that of the incident wave. The sound pressure is also no longer uniformly distributed and the effective sensitivity of the microphone is not given by the pressure sensitivity. The free-field sensitivity of the microphone should be used instead and is defined as [23]:

"For a sinusoidal plane progressive wave of given frequency, for a specified direction of sound incidence, and for given environmental conditions, the quotient of the open-circuit voltage of the microphone by the sound pressure that would exist at the position of the acoustic centre of the microphone in the absence of the microphone."

A free-field may be created inside an anechoic chamber where a small sound source

will produce a plane wave at the measurement position, provided it is placed a sufficient distance away. The free-field correction is defined as the difference between the free-field and pressure sensitivities of a microphone measured under the same environmental conditions for a given frequency and angle of incidence. The size, shape, and acoustical impedance of the microphone affect this correction value.

In a diffuse sound field, incident waves arrive with equal intensity from all directions. In such circumstances the diffuse sensitivity should be used and is defined as [23]:

"For a sinusoidal signal of given frequency in a diffuse sound field and for given environmental conditions, the quotient of the open-circuit voltage of the microphone by the sound pressure that would exist at the position of the acoustic centre of the microphone in the absence of the microphone."

A diffuse sound field may be created inside a room with hard, sound reflecting walls and which contains no sound absorbing materials. The diffuse field sensitivity may also be calculated from the free field sensitivity for particular angles of incidence.

2.4.2 Principle of operation

A measurement microphone, as shown in figure 2.2, consists of a thin metallic diaphragm positioned close to a rigid metallic backplate to form the plates of a capacitor. The housing, insulator, and diaphragm form a chamber and the equalization vent

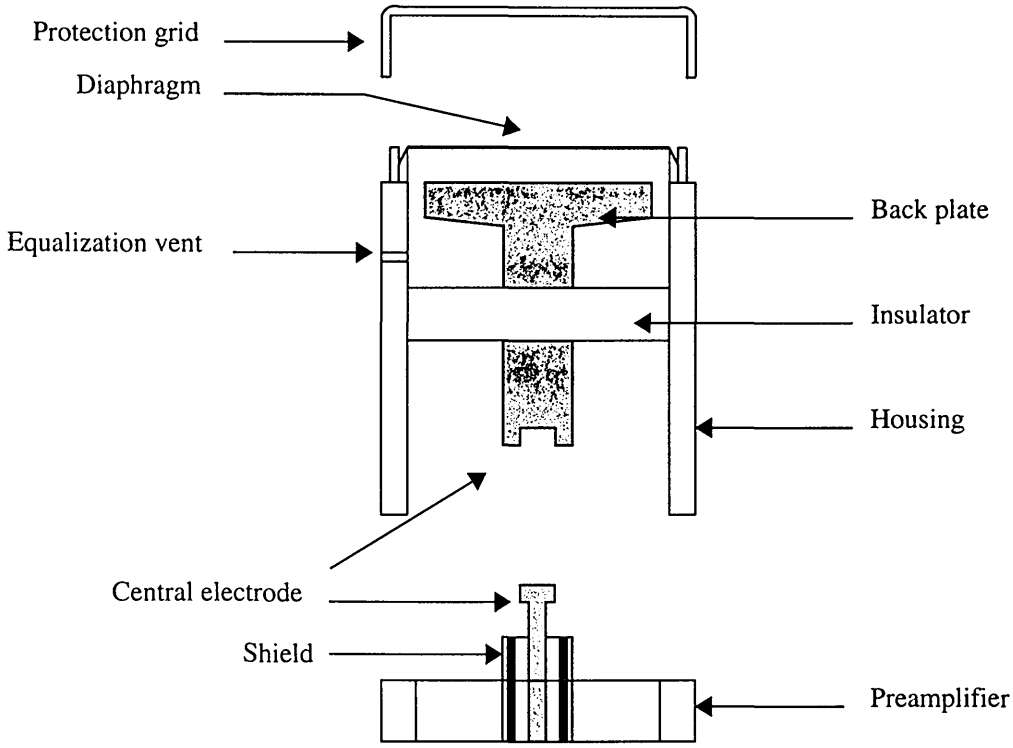

Figure 2.2: Diagram of the measurement microphone cartridge.

allows the static pressure in this chamber to equalize with external pressure, thus preventing the diaphragm from responding to changes in atmospheric pressure. The insulator isolates the backplate electrically from the cartridge housing. The microphone cartridge screws onto a preamplifier to form a complete microphone unit. The preamplifier is designed to transform the high source impedance of the transducer to the relatively low output impedance required for use with cables that connect the microphone to other instruments [24].

A fixed charge is applied to the plates by a high voltage supply. This is called the polarization voltage. When the microphone is exposed to a sound pressure, the diaphragm moves by a small amount. The variation in plate separation causes a voltage to be generated at the electrical terminals. When no current is drawn by microphone

the voltage is proportional to the sound pressure [25]. The mechanical and electrical behaviour of the microphone can be described by differential equations in terms of the diaphragm displacement and electric charge. This allows both the pressure and free field sensitivity of the microphone to be deduced [26].

The microphone is modelled by a simple mechanical system and by an electrical circuit, both of which are illustrated in figure 2.3. The mechanical description of the microphone diaphragm has an impedance given by the lumped parameters of mass M_m, resistance R_m, and compliance C_m. When the diaphragm is displaced the response of the system is assumed to be described by Hooke's law. The electrical circuit represents the microphone cartridge connected to a preamplifier where the impedance, Z, arises from the input of the preamplifier. The series resistor, located in the polarizing supply, has a very high value to maintain a constant charge on the microphone. The polarizing potential (E_0) charges the microphone, the microphone diaphragm is the low potential plate of the capacitor, and the voltage at the output terminals is $E(t)$.

The plate separation is x_1 when no polarizing voltage is applied and x_0 when polarized. The plate separation is not uniform. It depends on the distance from the centre of the diaphragm but it will be assumed that this variation is small compared to x_0 and x_1. The microphone capacitances are

$$\begin{aligned} C_1 &= \frac{\varepsilon S}{x_1} \\ C_0 &= \frac{\varepsilon S}{x_0} \end{aligned} \tag{2.2}$$

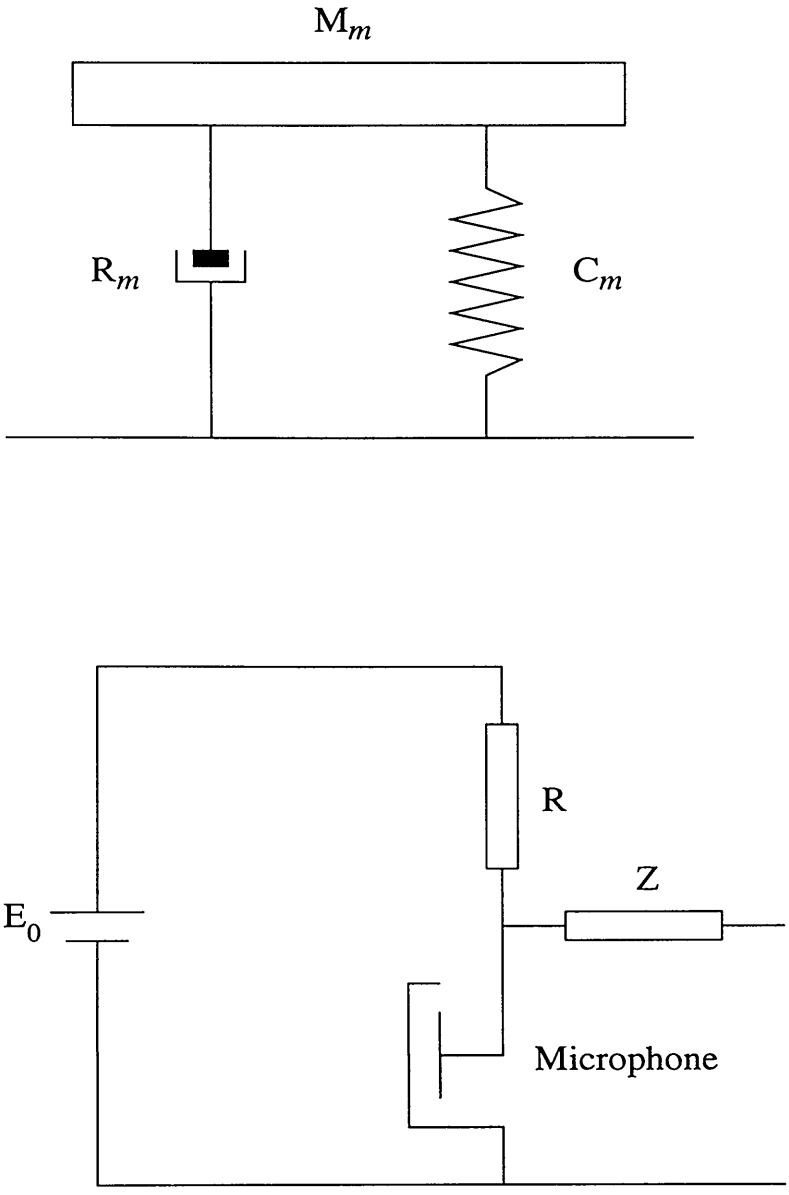

Figure 2.3: Mechanical and electrical models of the measurement microphone. Adapted from figure 2.1 of [27].

when unpolarized and polarized, respectively. ε is the permittivity of air and S is the effective plate area.

Following the derivation of Barham in [27], when the diaphragm is at its equilibrium position and the microphone is polarized the mechanical and electrostatic forces are equal giving

$$\frac{x_0 - x_1}{C_m} = \frac{q_0^2}{2C_0 x_0} \tag{2.3}$$

where q_0 is the charge on the microphone. If a force $F(t)$ acts on the diaphragm resulting in a plate separation of $x = x_0 + x(t)$ and charge $q = q_0 + q(t)$, then the corresponding microphone capacitance is

$$\begin{aligned} C &= \frac{\varepsilon S}{x_0 + x(t)} \\ &= \frac{C_0}{1 + x(t)/x_0} . \end{aligned} \tag{2.4}$$

The differential equation for the current in the electrical circuit is

$$\frac{q}{C} + Z\frac{\partial q}{\partial t} = E_0 + E(t) \tag{2.5}$$

where $E(t)$ is the variation in voltage as a result of the force. The first term on the LHS of equation 2.5 may be written as

$$\frac{q}{C} = \frac{(q_0 + q(t))(1 + x(t)/x_0)}{C_0} . \tag{2.6}$$

For a small displacement from equilibrium $q(t)x(t)$ terms can be neglected. Substituting $E_0 = q_0/C_0$ and equation 2.6 into equation 2.5 gives

$$E(t) = \frac{q(t)}{C_0} + Z\frac{\partial q}{\partial t} + \frac{q_0 x(t)}{C_0 x_0} \,. \tag{2.7}$$

Returning to the mechanical description, the total force on the diaphragm has contributions from the applied force and from the electrostatic force. The equation of motion of the diaphragm is

$$-F(t) = M_m\frac{\partial^2 x}{\partial t^2} + R_m\frac{\partial x}{\partial t} + \frac{x - x_1}{C_m} + \frac{q^2}{2Cx} \,. \tag{2.8}$$

Expanding the stiffness term and substituting equation 2.3 gives

$$\begin{aligned} \frac{x - x_1}{C_m} &= \frac{x(t) + x_0 - x_1}{C_m} \\ &= \frac{x(t)}{C_m} - \frac{q_0^2}{2C_0 x_0} \,. \end{aligned} \tag{2.9}$$

Similarly, expanding the dynamic electrostatic force term using equation 2.4 gives

$$\begin{aligned} \frac{q^2}{2Cx} &= \frac{(q_0 + q(t))^2}{2}\frac{(1 + x(t)/x_0)}{C_0(x_0 + x(t))} \\ &\simeq \frac{q_0^2(1 + 2q(t)/q_0)}{2C_0 x_0} \end{aligned} \tag{2.10}$$

where $q(t)x(t)$ terms have been neglected. Substituting equations 2.9 and 2.10 into

equation 2.8 allows the equation of motion to be expressed as

$$-F(t) = M_m \frac{\partial^2 x}{\partial t^2} + R_m \frac{\partial x}{\partial t} + \frac{x(t)}{C_m} + \frac{q_0 q(t)}{C_0 x_0} \,. \tag{2.11}$$

If the applied force $F(t) = Fe^{i\omega t}$, the diaphragm velocity is given by

$$v = \frac{\partial x}{\partial t} = i\omega x(t) \tag{2.12}$$

and the electrical current is given by

$$I = \frac{\partial q}{\partial t} = i\omega q(t) \,. \tag{2.13}$$

Using equations 2.12 and 2.13, equation 2.11 becomes

$$\begin{aligned} -F(t) &= v\left(i\omega M_m + R_m + \frac{1}{i\omega C_m}\right) + I\left(\frac{q_0}{i\omega C_0 x_0}\right) \\ &= Z_m v + I\left(\frac{q_0}{i\omega C_0 x_0}\right) \end{aligned} \tag{2.14}$$

where Z_m is the mechanical impedance of the microphone with $I = 0$. Similarly, equation 2.7 can be written as

$$\begin{aligned} E(t) &= Z\frac{\partial q}{\partial t} + \frac{1}{i\omega C_0}\frac{\partial q}{\partial t} + \frac{q_0}{i\omega C_0 x_0}\frac{\partial x}{\partial t} \\ &= IZ_e + v\left(\frac{q_0}{i\omega C_0 x_0}\right) \end{aligned} \tag{2.15}$$

where Z_e is the electrical impedance of the microphone with $v = 0$. As the charge on the capacitor remains constant, a displacement from equilibrium causes a voltage change that is directly proportional to the displacement.

The sound pressure and the volume velocity acting on the diaphragm are $p = F/S$ and $U = -vS$, respectively. The acoustic impedance is $Z_a = Z_m/S^2$. Equations 2.14 and 2.15 can be expressed as

$$p = Z_a U + TI \tag{2.16}$$

and

$$E = TU + Z_e I \tag{2.17}$$

where

$$T = \frac{-\Phi}{i\omega C_0} \tag{2.18}$$

and

$$\Phi = \frac{q_0}{x_0 S}\,. \tag{2.19}$$

T is the called the transduction coefficient as it relates an electrical quantity to an acoustical one and vice versa. Φ is real and independent of frequency and can be

considered a property of the microphone that describes the transduction process, i.e. the conversion of energy between electrical and mechanical forms. The reciprocal nature of the microphone is highlighted by the presence of T in both equation 2.16 and equation 2.17.

2.4.3 Theoretical expression for sensitivity

The pressure sensitivity of a measurement microphone is defined as the ratio of the output voltage to the incident pressure when no current flows through the microphone. From equations 2.16, 2.17, 2.18, and 2.19 and putting $I = 0$, the pressure sensitivity is

$$M_p = \frac{-\Phi}{i\omega C_0 Z_a} \,. \tag{2.20}$$

The sensitivity of the microphone as a transmitter is the ratio of the volume velocity to the driving current when the microphone is unloaded. Putting $p = 0$ in equation 2.16 and evaluating gives the same sensitivity as equation 2.20. This demonstrates the reciprocal nature of the condenser measurement microphone.

The free field sensitivity is defined as the ratio of the output voltage to the incident sound pressure that would exist at the acoustic centre of the microphone in its absence. Introducing the microphone into the field affects the pressure. For a blocked diaphragm

(i.e. $v = 0$) this is expressed as

$$p_0^{'} = \sigma(f, \varphi) p_0 \tag{2.21}$$

where $p_0^{'}$ is the average sound pressure acting on the blocked diaphragm, p_0 is the sound pressure in the absence of the microphone, and σ is the disturbance function [27]. σ depends on the frequency, f, and the angle of incidence, φ, of the sound wave on the microphone. The microphone diaphragm will experience a radiation impedance, Z_r, due to its movement. The pressure acting on the diaphragm will be less than $p_0^{'}$. This may be written as

$$\begin{aligned} p &= p_0^{'} - Z_r U \\ &= \sigma(f, \varphi) p_0 - Z_r U \end{aligned} \tag{2.22}$$

and equation 2.16 becomes

$$\sigma(f, \varphi) p_0 = (Z_a + Z_r) U + TI \, . \tag{2.23}$$

From equations 2.23, 2.17, 2.18, 2.19 and with $I = 0$, the free field sensitivity is

$$M_f = \sigma(f, \varphi) \frac{-\Phi}{i\omega C_0 (Z_a + Z_r)} \, . \tag{2.24}$$

By considering the volume velocity produced by the diaphragm, the sensitivity of the

microphone can be shown to be the same whether it is used as a receiver or a transmitter in a free field environment [27].

2.5 The reciprocity technique of calibration

The reciprocal nature of the measurement microphone has been established and the method for the absolute calibration employed by NPL will now be described. Although the reciprocity method has been standardized internationally as a means of calibration with the highest possible precision [2], no specific recommendations are given on how it should be implemented. NPL has developed and defined calibration facilities to implement the reciprocity method for the measurement of both pressure and free field sensitivity [26] [27]. This forms the basis of the UK acoustic pressure standard.

The technique involves three microphones with only one pair used at any given time. One microphone is driven electrically to act as a source of sound and the other responds to the generated pressure. A current, I_1, through the electrical terminals of the transmitter microphone produces a volume velocity, $M_1 I_1$. The resulting sound pressure, $P_2 = Z_{12} M_1 I_1$, at the receiving microphone produces an open circuit voltage, $E_2 = M_2 Z_{12} M_1 I_1$. The product of the two microphone sensitivities is

$$M_1 M_2 = \frac{E_2}{Z_{12} I_1} . \tag{2.25}$$

where Z_{12} is the acoustic transfer impedance. Repeating for the set of all three possible

sensitivity products allows the individual microphone sensitivities to be deduced [26]. For example

$$M_1 = \left[\left(\frac{R_{12} R_{31}}{R_{23}} \right) \cdot \left(\frac{Z_{23}}{Z_{12} Z_{31}} \right) \right]^{\frac{1}{2}} . \tag{2.26}$$

Similar expressions exist for the other individual sensitivities.

$R_{kl} = E_l I_k$ is the electric transfer impedance and is defined as the ratio of the open circuit voltage of the receiver microphone to the current through the electric terminals of the transmitting microphone. The electric transfer impedance is measured in the calibration procedure. The space between the two microphones is characterized by the acoustic transfer impedance, Z_{kl}. It is defined as the pressure generated at the receiver as a function of the transmitter volume velocity and is calculated from a knowledge of the acoustic field.

For the measurement of pressure sensitivity, the two microphones are placed in a small air filled coupling cavity. The dimensions of the coupling cavity are used along with the dimensions of the microphones to determine the acoustic transfer impedance. These measurements are traceable to the primary standard for length. The properties of air such as density, speed of sound, and ratio of specific heats are also required to determine Z_{kl}. The uncertainty in the reciprocity calibration is 0.03 dB.

For the measurement of free field sensitivity, it is assumed that the waves emanating from the source diverge spherically and the receiver is subject only to the direct waves. This is achieved by conducting the procedure inside a high quality free field room or

anechoic chamber. Again, the properties of the field and air are used in the calculation of the acoustical transfer impedance. The uncertainty in the free field reciprocity calibration is 0.1 dB.

2.6 Application of laser Doppler anemometry

LDA is an optical technique for the absolute measurement of particle velocity. It is based on the detection of the Doppler frequency shift of scattered laser light. This method provides a direct approach to the measurement of sound pressure which is determined from the acoustic particle velocity. Taylor developed a system involving a travelling wave tube [3]. It was similar to the Rayleigh disk method in that the sound pressure at a point in a tube where a microphone is positioned can be calculated from the velocity measurement. By measuring the output voltage of the microphone, its sensitivity is found.

Taylor's apparatus suffered from poor signal to noise ratio. Although an uncertainty of 0.03 dB was claimed, this required a large sample of measurements to be taken resulting in prolonged measurement time that was impractical for routine implementation. Consequently the method was regarded as a means of validating reciprocity rather than providing a viable alternative to it. However, recent advances in LDA mean Taylor's experimental set up can now be improved upon.

2.7 Summary

In this chapter, the importance of measurement standards was outlined. The history of the acoustic pressure standard was discussed along with the development of the condenser measurement microphone and methods for calibration. By considering mechanical and electrical systems, the operation of the measurement microphone was explained and the sensitivity defined in accordance with the IEC international standard. The reciprocity method of calibration implemented by NPL as the basis for the UK primary standard was detailed. LDA was introduced as an optical technique for the measurement of acoustic particle velocity with potential as an absolute calibration method. The basic theory for LDA measurements will be reviewed in the next chapter.

Chapter 3

Laser Doppler anemometry

3.1 Introduction

In section 2.6, a calibration method for microphones based on the absolute measurement of acoustic particle velocity LDA was introduced. However, the whole process proved impractical as a viable alternative to the standard reciprocity calibration technique. Recent advances in optical technologies and signal processing techniques mean that the method can now be improved upon. This thesis is concerned with the study of LDA for acoustical measurements and the further development of a practical system for the calibration of measurement microphones.

In this chapter the principle of LDA is explained with particular consideration given to the dual beam mode. In this type of laser Doppler system two parallel laser beams

are focused to a point to produce interference fringes and the component of fluid velocity in a single direction is measured at the point of intersection of the two beams. The fringe model of LDA is described in section 3.4 and the properties of a focused Gaussian laser beam are discussed. Two particle velocity conditions are considered, a steady mean flow velocity and an acoustic (alternating) velocity. Mathematical expressions are derived for the photodetector Doppler signal generated by both velocity conditions. The instantaneous frequency of the Doppler signal is shown to be proportional to the fluid velocity. Frequency domain analysis of the Doppler signal is explained in section 3.5 as a method for extracting information about the flow. The form of the spectral density function is considered for the two velocity cases. An alternative technique involving a demodulation of the Doppler signal is also discussed. Sources of noise in the signal are highlighted. Finally, in section 3.8 the acousto-optic effect is explained along with its effect on LDA measurements.

3.2 Alternative measuring techniques

Useful measurements of acoustic particle velocity and microphone sensitivity have been made using other techniques besides LDA. Durrani and Greated proposed an alternative two beam laser system for the measurement of flow velocities based on cross-correlation analysis [28]. The 'Microflown' is a relatively new acoustic particle velocity sensor developed by de Bree et al [29]. Behler et al recently described an optical calibration technique for microphones utilizing laser Doppler vibrometry [30].

3.2.1 Two beam cross-correlation

In the alternative laser system, two focal spots or strips of light are formed in the measuring region by focusing two laser beams with either spherical or cylindrical lenses. The optical configuration of the system is illustrated in figure 3.1 where the two spots are positioned a distance, d, apart in the mean flow direction. The light scattered by particles crossing beam 1 is collected by detector 1 and gives a voltage signal, $V_1(t)$. The light scattered by particles crossing beam 2 is collected by detector 2 and gives a voltage signal, $V_2(t)$. The theoretical form of the cross correlation of the two signals has been deduced by Durrani and Greated and used in the estimation of turbulence parameters as well as mean flow velocities [28].

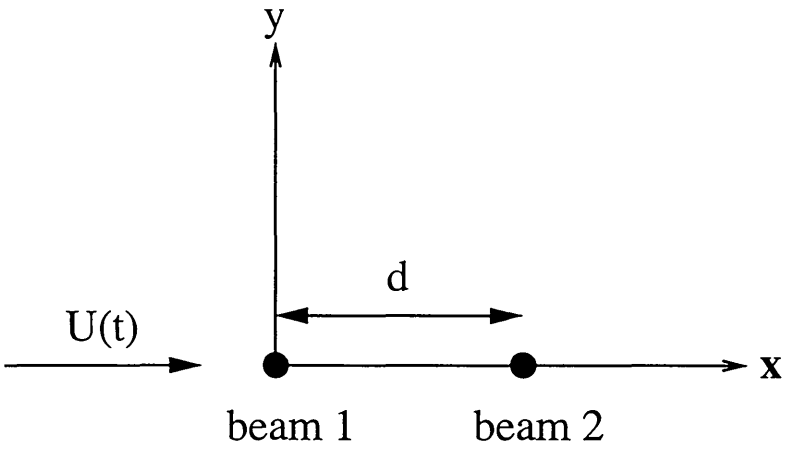

Figure 3.1: Two beam configuration for cross-correlation analysis.

The configuration of the cross-correlation system is complex due to the requirement of two sets of focusing and detector optics. The form of the cross-correlation function generated by acoustic or alternating velocities has not yet been considered.

3.2.2 The Microflown

The Microflown is a sensor designed specifically to measure acoustic particle velocity. It consists of two parallel resistive sensors of length 0.8 mm separated by a distance of 40 μm [31]. Heat is convected from the first sensor to the second as air flows past the device. This results in a difference in temperature, and hence resistance, between the two sensors. The differential resistance is proportional to the fluid velocity over a certain velocity range and can be measured using a purpose developed electronic circuit. The output voltage from the measuring circuit is proportional to the differential resistance and the flow velocity [29].

The flow direction can be resolved with the Microflown. However, unlike laser anemometry it is an intrusive measuring device. The Microflown also requires calibration as its sensitivity varies with frequency [29]. Rather than the Microflown offering a viable alternative to laser Doppler systems, it is more likely that LDA provides a practical means for Microflown calibration.

3.2.3 Laser Doppler vibrometry

An alternative optical technique for microphone calibration involves measurements made with a laser Doppler vibrometer (LDV). The laser beam is positioned on the microphone diaphragm which is orientated perpendicular to beam [32]. The transducer is driven as a source of sound to excite the diaphragm. Light scattered back from the

diaphragm surface is shifted by an amount proportional to the velocity of motion. The single point vibrometer is scanned across the diaphragm surface to collect velocity information and the microphone sensitivity is obtained by calculating the ratio between diaphragm velocity and the microphone driving current [30].

Unlike Taylor's study of LDA applied to the measurement of microphone sensitivity [3], no comparison of LDV derived sensitivity with reciprocity calibration was given. Neither was the magnitude of the uncertainty in the sensitivity measurement nor the period of time required to conduct the calibration procedure quoted. It is unclear as to whether this method could be implemented for routine calibration.

3.3 The principle of LDA

The frequency of light scattered from moving particles is shifted by an amount proportional to the velocity. By measuring this Doppler frequency shift the velocity can be determined. This forms the central principle of LDA. Consider a single particle travelling along the x axis with speed, U, as shown in figure 3.2. The particle crosses a plane wave light beam at the origin. The light beam has frequency ν, wavelength λ, and is propagating in the direction with unit vector $\hat{\mathbf{s}}$. The component of particle velocity in the direction of propagation is $U\hat{\mathbf{x}} \cdot \hat{\mathbf{s}}$, where $\hat{\mathbf{x}}$ is the unit vector in the x direction. The particle scatters light which is shifted in frequency by an amount that is proportional to the speed of the particle motion, $\nu - (U/\lambda)\hat{\mathbf{x}} \cdot \hat{\mathbf{s}}$.

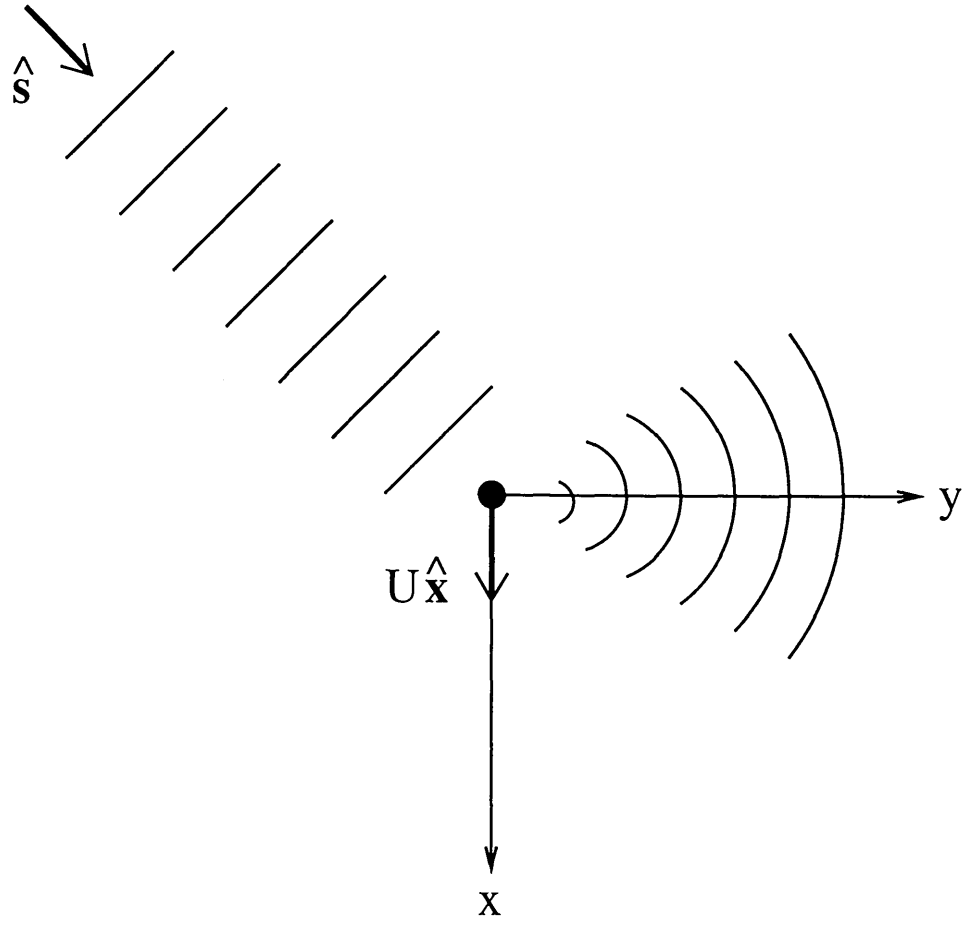

Figure 3.2: Light scattered by a moving particle.

The frequency of the scattered light is greater than the frequency of the laser beam as $\hat{\mathbf{x}} \cdot \hat{\mathbf{s}}$ is negative. The component of velocity along the y axis is zero. A particle at the origin will have no velocity component in this direction and so the scattered light will not experience any further Doppler shifts. The velocity of the particle can be determined from the Doppler shift of the frequency of the illuminating light beam. However, in practice the Doppler shift, $(U/\lambda)\hat{\mathbf{x}} \cdot \hat{\mathbf{s}}$, is very small compared to ν and is difficult to measure. In order to determine particle velocity a more complex system must be employed.

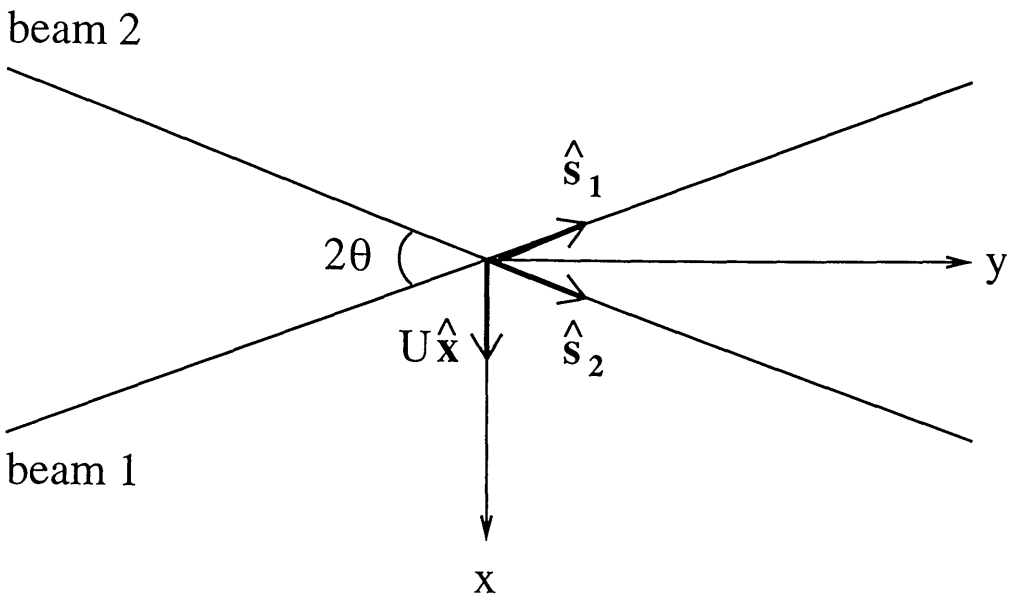

Figure 3.3: Dual beam mode.

The three main types of optical arrangements for LDA are the reference beam mode, the dual beam mode, and the differential beam mode [33] [34]. Figure 3.3 describes the dual beam mode which is the LDA system that will be considered here. A scattering particle is illuminated by two plane light waves both with frequency ν. The point of intersection of the two beams is taken to be the origin of the coordinate system. A particle with velocity $U\hat{\mathbf{x}}$ crosses the origin and scatters light with frequency $\nu_1 = \nu - (U/\lambda)\hat{\mathbf{x}} \cdot \hat{\mathbf{s}}_1$ from beam 1 and light with frequency $\nu_2 = \nu - (U/\lambda)\hat{\mathbf{x}} \cdot \hat{\mathbf{s}}_2$ from beam 2. The frequency difference between the two Doppler shifts is

$$F_D = \nu_1 - \nu_2 = \frac{U}{\lambda}\hat{\mathbf{x}} \cdot (\hat{\mathbf{s}_2} - \hat{\mathbf{s}_1}) \,. \tag{3.1}$$

This is called the Doppler frequency and can be expressed as

$$F_D = \frac{2U \sin\theta}{\lambda} \tag{3.2}$$

where θ is the angle between each beam and the y-axis.

The detected Doppler signal in equation 3.2 is independent of the detector position [34]. In dual beam LDA the two illuminating light beams, usually obtained by splitting one initial laser beam, are focused by a lens to form an interference pattern at the point of interest.

3.4 The Fringe model

As particles cross the interference fringes formed at the intersection of the two beams they scatter light which is modulated at the Doppler frequency. This forms the basis for the fringe model of LDA [5]. Rudd considered masked beams with rectangular cross section. However, the principle can also be applied to unmasked beams with a Gaussian profile.

3.4.1 Gaussian laser beam properties

The two beams of equal intensity have a diameter, $D_{e^{-2}}$, which is measured between points where the intensity is $1/e^2$ of the peak intensity at the centre. The properties of

a focused laser beam are described in figure 3.4 where s_0 is the distance from the beam waist to the lens and s_1 is the distance from the lens to the focal waist. The ideal thin lens focuses the Gaussian beam to a spot located at s_1.

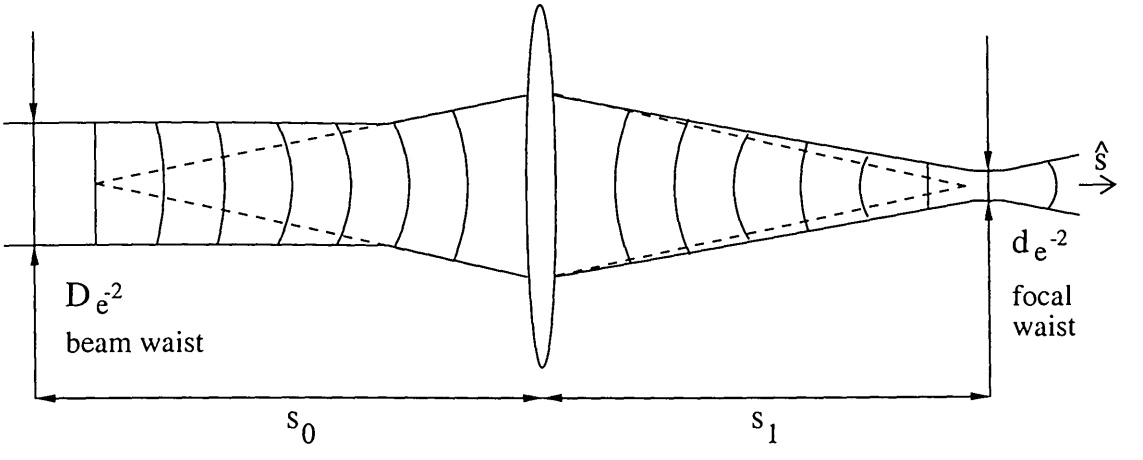

Figure 3.4: Properties of a focused Gaussian laser beam.

The position of the focal point is given in [34], such that

$$s_1 = f + \frac{s_0 - f}{(s_0/f - 1)^2 + (\pi D_{e^{-2}}^2/4f\lambda)^2} \tag{3.3}$$

where the diameter of the focal spot, $d_{e^{-2}}$, is

$$\frac{1}{d_{e^{-2}}^2} = \frac{1}{D_{e^{-2}}^2}\left(1 - \frac{s_0}{f}\right)^2 + \left(\frac{\pi D_{e^{-2}}}{4f\lambda}\right)^2 . \tag{3.4}$$

From equation 3.4, the minimum beam diameter only occurs exactly in the focal plane

of the lens if $s_0 = f$. The lens will cause parallel beams to cross at f. For $s_1 = f$,

$$d_{e^{-2}} = \frac{4f\lambda}{\pi D_{e^{-2}}} . \tag{3.5}$$

The focused beam is essentially a plane wave with a diameter that is constant and intensity distribution that is Gaussian [34].

3.4.2 Photodetector fringe current

By considering the intensity of the light scattered by a particle, the form of the photodetector signal can be deduced as a function of fluid velocity. The photodetector current is proportional to the light intensity integrated over the detector surface [33]. Consider a stationary particle located at $\mathbf{x} = (x, y, z)$. The z axis is perpendicular to both the x and y axes. In Appendix A, the photodetector fringe current due to the presence of the particle is shown to be

$$\begin{aligned} i_F(\mathbf{x}) &= 2\eta \left(\frac{1}{2} M C_{SC}\right)^2 I_0 \exp\left(-\frac{8(x^2\cos^2\theta + z^2 + y^2\sin^2\theta)}{d_{e^{-2}}^2}\right) \\ &\quad \times \left[\cosh\left(\frac{8xy}{d_{e^{-2}}^2}\sin 2\theta\right) + \cos\left(\frac{4\pi}{\lambda} x \sin\theta\right)\right] \end{aligned} \tag{3.6}$$

where η is the sensitivity of the detector, M is the magnification factor of the receiving optics, C_{SC} is the scattering cross section of the particle, and I_0 is the intensity of the two beams at the focal point.

Equation 3.6 can be written as

$$i_F(\mathrm{x}) = \kappa \mathcal{K} W(\mathrm{x}) \left[\cosh\left(\frac{8xy}{d_{e^{-2}}^2} \sin 2\theta \right) + \cos(Dx) \right] \tag{3.7}$$

where

$$W(\mathrm{x}) = I_0 \exp\left(-\frac{8(x^2 \cos^2\theta + z^2 + y^2 \sin^2\theta)}{d_{e^{-2}}^2} \right) \tag{3.8}$$

and

$$D = \frac{4\pi \sin\theta}{\lambda} . \tag{3.9}$$

κ is a constant determined from the optical geometry, the laser power, and the efficiency of the detection system. $\mathcal{K}$ depends on the size of the light scattering particles.

The fringe or probe volume is an ellipsoid described by the weighting function W. It has dimensions $\Delta x = d_{e^{-2}}/\cos\theta$, $\Delta y = d_{e^{-2}}/\sin\theta$, and $\Delta z = d_{e^{-2}}$ in the x, y, and z directions, respectively [34]. The beam crossover region within which a particle would produce an appreciable photocurrent due to collective scattering from the two beams is shown in figure 3.5. When the particle is located at the origin, the photodetector current is at a maximum. This decays to $1/e$ of the peak intensity if the particle is located on the inner ellipse and $1/e^2$ of the peak intensity on the outer ellipse.

The spacing between the interference fringes is given by

$$\Lambda = \frac{2\pi}{D} = \frac{\lambda}{2\sin\theta} \tag{3.10}$$

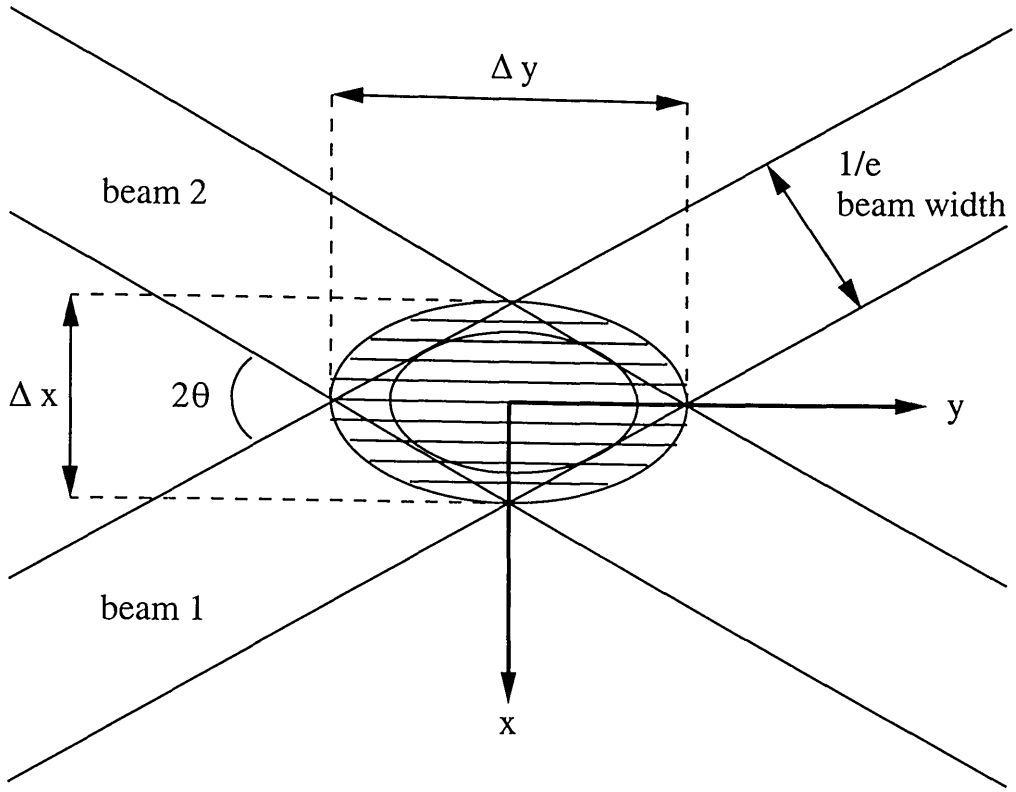

Figure 3.5: The intersection of the two beams showing the interference fringes and the elliptical probe volume. Adapted from figure 2.6.3 of [33].

and depends on the angle between the two beams and wavelength of the laser light. The total number of fringes within the probe volume is

$$N_f = \frac{\Delta x}{\Lambda} = \frac{2d_{e^{-2}}}{\lambda} \tan\theta \tag{3.11}$$

and depends on the beam angle and the wavelength of the laser light as well as the focused beam waist diameter. A particle moving in the x direction with speed U crosses the fringes with a frequency

$$F_D = \frac{U}{\Lambda} = \frac{2U \sin\theta}{\lambda} . \tag{3.12}$$

This is the Doppler frequency and is the same as the expression, derived by considering the Doppler shift of scattered light, in equation 3.2.

3.4.3 Distortion of the fringe pattern

The deviation of the focused beam waists from the focal point of the lens results in variations of the fringe spacing [35] [36]. Figure 3.6 illustrates the effect that the focal waist positions have on the fringe spacing when $s_1 \neq f$. If both of the focal waists are located on the same side of the probe volume, the fringe spacing changes in the y direction and curvature of the fringes results. If the focal waists are located on opposite sides of the probe volume the fringe spacing varies in the x direction. The percentage deviation in Doppler frequency along the probe volume is determined by the focal length of the lens [37]. The Doppler frequency gradient in the probe volume is given by the expression

$$\frac{f}{F_D}\frac{dF_D}{ds} = \frac{s_o - f}{f}. \tag{3.13}$$

In dual beam systems with focal lengths up to several hundred millimetres these errors are not considered significant [34].

3.4.4 Frequency shifting

A common experimental technique in LDA involves shifting the frequency of one of the illuminating beams to $\nu' = \nu + F_s$ [7] [33]. This causes the fringes to move through

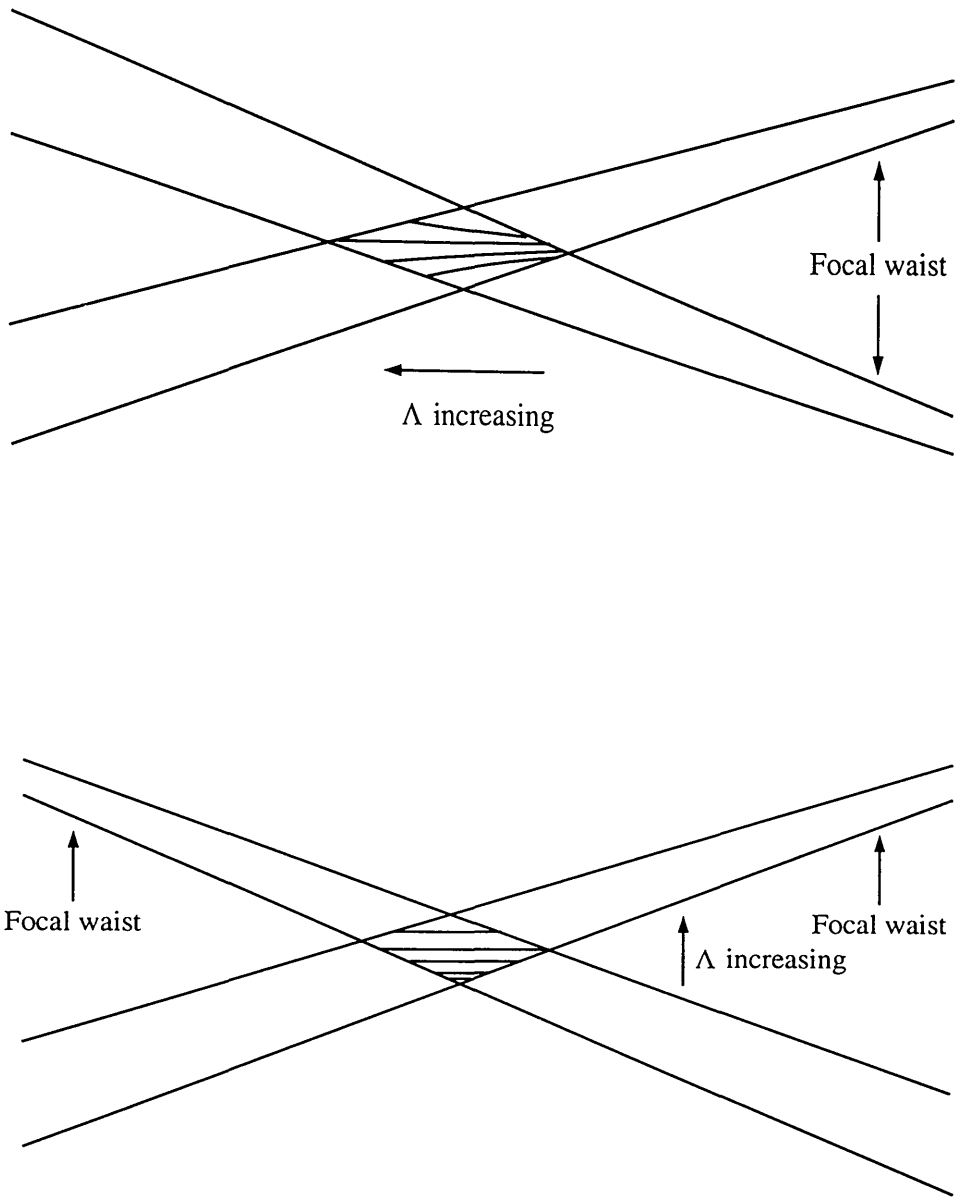

Figure 3.6: Fringe model showing variations in fringe spacing due to focal waist positions. Fringe spacing varies in y direction if both focal waists are located on same side of the probe volume and fringe spacing varies in x direction if focal waists are located on different sides.

the stationary ellipsoidal probe volume with constant velocity, $F_s\Lambda$. The resulting Doppler frequency is of the form

$$F_D = F_s + \frac{U}{\Lambda} \tag{3.14}$$

for movement in the x direction. The frequency shift acts as an artificial constant velocity and resolves directional ambiguity as well as extending the range of velocities that can be measured with the system. Equation 3.7 may be written as

$$i_F(t) = \kappa \mathcal{K} W(\mathbf{x}) \left[\cosh\left(\frac{8xy}{d_{e^{-2}}^2} \sin 2\theta \right) + \cos(2\pi F_s t + Dx) \right] \tag{3.15}$$

for a stationary particle located at $\mathbf{x}$ and a frequency shift, F_s.

The frequency shift is usually introduced to one of the illuminating beams using a Bragg cell. An alternative method for achieving the same effect is phase shifting [7] [33]. The beams are passed through two electro-optic crystals which are driven in opposite phase sense by a sawtooth electric potential. The fringes move in a cyclic fashion over the distance of one fringe spacing. The velocity of motion in the forward direction is constant while the flyback time to the initial position is made as short as possible. The overall effect of frequency shifting is to introduce an artificial constant velocity.

3.4.5 Doppler signal due to a moving particle

The photodetector fringe current, and hence the photodetector voltage, is proportional to light intensity integrated over the detector surface [33]. A particle moving in the x direction with constant speed, U, will generate a time varying photodetector voltage as it passes across the region of beam intersection. If the particle has no velocity component in the other two directions, the displacement of the particle at any time, t, is given by $x(t) = Ut + x(0)$, where $x(0)$ is the initial particle position. The photodetector voltage signal is

$$V(t) = \kappa \mathcal{K} W(\mathbf{x}) \left[\cosh\left(\frac{8x(t)y}{d_{e^{-2}}^2} \sin 2\theta \right) + \cos\left(2\pi F_s t + Dx(t) \right) \right] . \tag{3.16}$$

The constant κ now also incorporates the load resistance of the detector.

The weighting function, introduced in equation 3.8, may be expressed as the product of a time dependent term and time independent term such that

$$W(\mathbf{x}) = we^{(-8x^2(t)\beta^2)} \tag{3.17}$$

where

$$w = I_0 \exp\left(-\frac{8(z^2 + y^2 \sin^2\theta)}{d_{e^{-2}}^2} \right) \tag{3.18}$$

and

$$\beta = \frac{\cos\theta}{d_{e^{-2}}} . \tag{3.19}$$

The photodetector signal generated by the moving particle is

$$V(t) = \kappa \mathcal{K} w e^{(-8x^2(t)\beta^2)} \left[\cosh\left(\frac{8x(t)y}{d_{e^{-2}}^2} \sin 2\theta \right) + \cos\left(2\pi F_s t + Dx(t) \right) \right] . \quad (3.20)$$

The cosh term is called the pedestal term and is usually removed by high pass filtering the detector signal to give the Doppler signal,

$$V_D(t) = \kappa \mathcal{K} w e^{(-8x^2(t)\beta^2)} \cos\left(2\pi F_s t + Dx(t) \right) . \quad (3.21)$$

This is a cosine wave with a time varying amplitude and is displayed in figure 3.7 along with the form of the weighting function plotted against particle displacement. The Doppler frequency is the instantaneous frequency of the Doppler signal.

3.4.6 Multiple particle Doppler signal

The derivation of the Doppler signal may be extended to include multiple particles moving through the probe volume in the x direction with constant speed, U. The Doppler signal is the sum of individual contributions arising from light scattered by every particle. Each contribution is determined by the position and velocity of the generating particle. The Doppler signal will be

$$V_D(t) = \kappa \sum_p \mathcal{K}_p w e^{(-8x_p(t)^2\beta^2)} \cos\left(2\pi F_s t + Dx_p(t) \right) \quad (3.22)$$

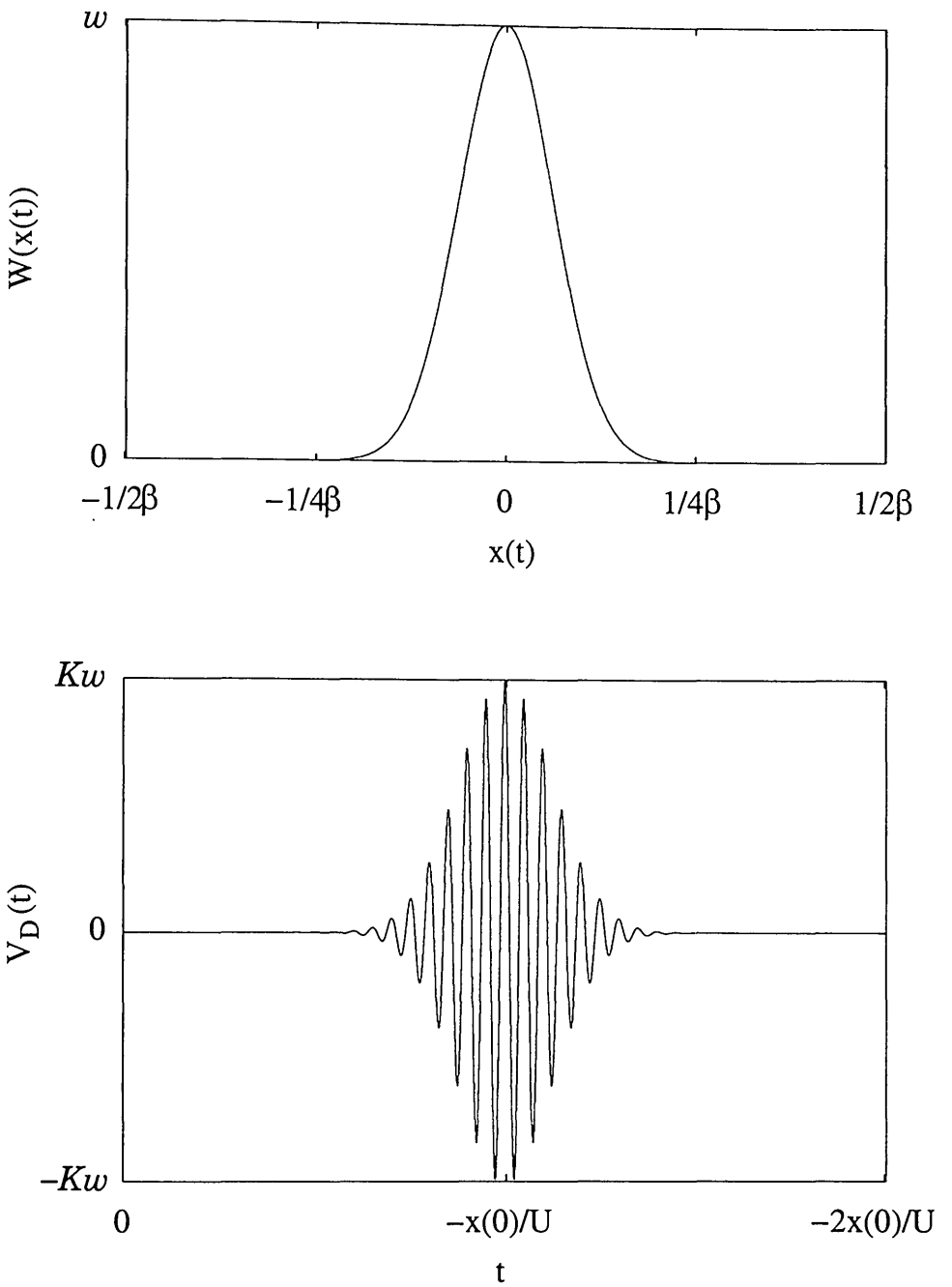

Figure 3.7: Doppler signal simulated for single particle moving with constant speed U, initial position $x(0) = -2/\beta$, and $F_s = 0$. The weighting function plotted against particle displacement is also shown.

where the summation extends over all particles in the flow. The displacement of particle p is given by $x_p(t) = Ut + x_p(0)$, where $x_p(0)$ is the position at $t = 0$.

Equation 3.22 may be expressed in the form [38]

$$V_D(t) = a(t)\cos\left(2\pi F_s t + DUt\right) - b(t)\sin\left(2\pi F_s t + DUt\right) \tag{3.23}$$

where

$$a(t) = \kappa \sum_p \mathcal{K}_p w e^{(-8x_p(t)^2\beta^2)} \cos\left(Dx_p(0)\right) \tag{3.24}$$

and

$$b(t) = \kappa \sum_p \mathcal{K}_p w e^{(-8x_p(t)^2\beta^2)} \sin\left(Dx_p(0)\right) . \tag{3.25}$$

The exponential terms in equations 3.24 and 3.25 describe the variation in amplitude due to particle motion within a Gaussian intensity distribution.

Rearranging equation 3.23 gives

$$V_D = \xi(t)\cos\left(2\pi F_s t + DUt + \phi(t)\right) \tag{3.26}$$

where

$$\xi(t) = \left(a^2(t) + b^2(t)\right)^{1/2} \tag{3.27}$$

and

$$\phi(t) = \tan^{-1}\frac{a(t)}{b(t)} . \tag{3.28}$$

Equation 3.26 may be written as

$$V_D = \xi(t) \cos \Theta(t) \tag{3.29}$$

where

$$\Theta(t) = 2\pi F_s t + DUt + \phi(t) \, . \tag{3.30}$$

The instantaneous frequency, i.e. the Doppler frequency, is the rate of change of $\Theta(t)$ divided by 2π,

$$\begin{aligned} F_D &= \frac{1}{2\pi} \frac{d\Theta}{dt} \\ &= F_s + \frac{U}{\Lambda} + \frac{d\phi}{dt} \, . \end{aligned} \tag{3.31}$$

The $d\theta/dt$ term is called ambiguity noise. It arises because the Doppler signal is composed from the superposition of multiple individual signals. The individual signals have a random phased related to the initial position of the generating particle. It can be seen from equation 3.31 that for a constant velocity and a single particle, the Doppler frequency would have a constant value. However, for multiple particles the Doppler frequency varies randomly about $F_s + U/\Lambda$ due to the ambiguity noise. A continuous Doppler signal will only be produced if there are always particles in the probe volume. As the random distribution of particles within the probe volume is constantly being replaced by a new random particle distribution, the amplitude of the signal also varies randomly.

3.4.7 Doppler signal due to an alternating velocity

A sinusoidal sound field of single frequency will cause a single particle to oscillate parallel to the x axis. The particle displacement is given by

$$x(t) = x_m \sin(2\pi f_m t + \varphi_m) + x(0) \tag{3.32}$$

where x_m is the displacement amplitude, f_m is the acoustic frequency, φ_m is the phase constant, and $x(0)$ is the initial position of the particle. Substituting equation 3.32 into equation 3.21 gives the resulting Doppler signal,

$$\begin{aligned} V_D(t) &= \kappa \mathcal{K} w \exp\Big[-8\Big(x_m \sin(2\pi f_m t + \varphi_m) + x(0)\Big)^2 \beta^2\Big] \\ &\quad \times \cos\Big(2\pi F_s t + D x_m \sin(2\pi f_m t + \varphi_m) + D x(0)\Big)\,. \end{aligned} \tag{3.33}$$

The Doppler frequency is the rate of change of the argument of the cosine term in equation 3.33 divided by 2π,

$$F_D = F_s + \Delta F_m \cos(2\pi f_m t + \varphi_m) \tag{3.34}$$

where

$$\Delta F_m = \frac{2\pi f_m x_m}{\Lambda}\,. \tag{3.35}$$

The cosine term in equation 3.33 represents a frequency modulated wave with carrier frequency F_s, modulation frequency f_m, and peak frequency deviation ΔF_m.

EX BIBL. UNIV. EDINBURGH

The acoustic particle velocity amplitude is

$$u_m = 2\pi f_m x_m \tag{3.36}$$

and equation 3.35 may be written as

$$\Delta F_m = \frac{u_m}{\Lambda} \,. \tag{3.37}$$

The peak frequency deviation is directly proportional to the acoustic particle velocity amplitude. In figure 3.8, the Doppler signal in equation 3.33 is illustrated for $F_s = 0$ and for $F_s = 2u_m/\Lambda$. Also shown, the particle displacement and the particle velocity plotted against the same time scale. The amplitude of the Doppler signal varies periodically at the acoustic frequency. The extent of this amplitude modulation depends on the particle displacement amplitude.

The frequency modulated wave, i.e. the cosine term in equation 3.33, can be expanded as a series [39], giving

$$\begin{aligned} V_D(t) \;\propto\; & J_0\left(\frac{u_m}{\Lambda f_m}\right)\sin(2\pi F_s t) \\ & + \sum_{n=0}^{\infty} J_n\left(\frac{u_m}{\Lambda f_m}\right)\sin\left(2\pi(F_s + nf_m)t\right) \\ & + (-1)^n \sum_{n=0}^{\infty} J_n\left(\frac{u_m}{\Lambda f_m}\right)\sin\left(2\pi(F_s - nf_m)t\right) \end{aligned} \tag{3.38}$$

where $J_n(\,)$ denotes a nth order Bessel function of the first kind.

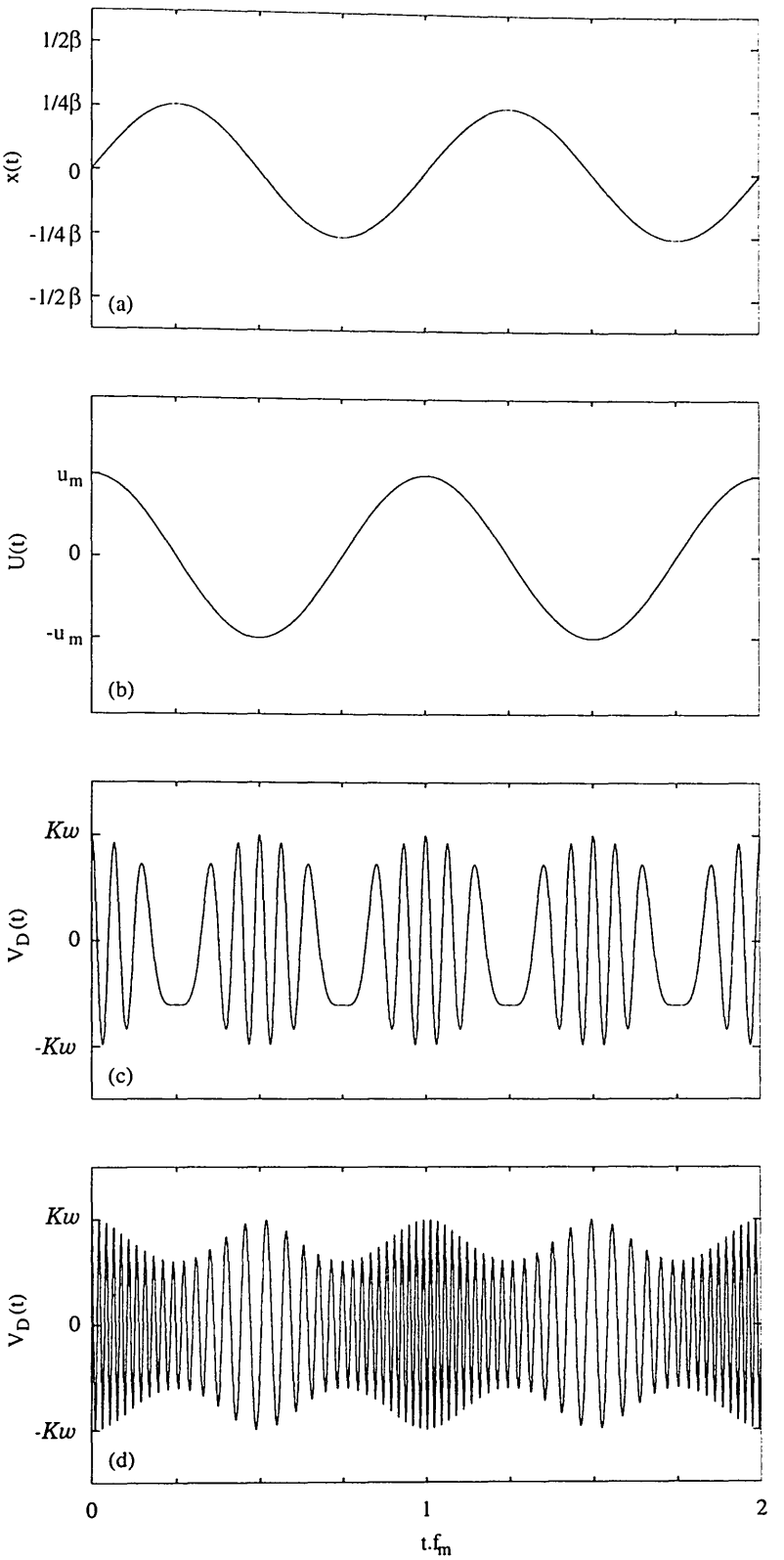

Figure 3.8: Doppler signals simulated for a single particle in a sinusoidal sound field (c) with $F_s = 0$ and (d) with $F_s = 2u_m/\Lambda$. The acoustic particle displacement amplitude $x_m = 1/4\beta$ and the initial position $x(0) = 0$. The (a) particle displacement and (b) particle velocity are also shown.

For the multiple particle case, ambiguity noise causes the Doppler frequency to vary randomly about the Doppler frequency that would be produced by a single particle. A typical measured Doppler signal is shown in figure 3.9. The amplitude of the signal varies randomly due to the random nature of the particle distribution and varies periodically at the acoustic frequency. The periodic amplitude modulation is not very pronounced for the signal in figure 3.9 because the displacement amplitude is relatively small ($x_m \simeq 1\mu m$).

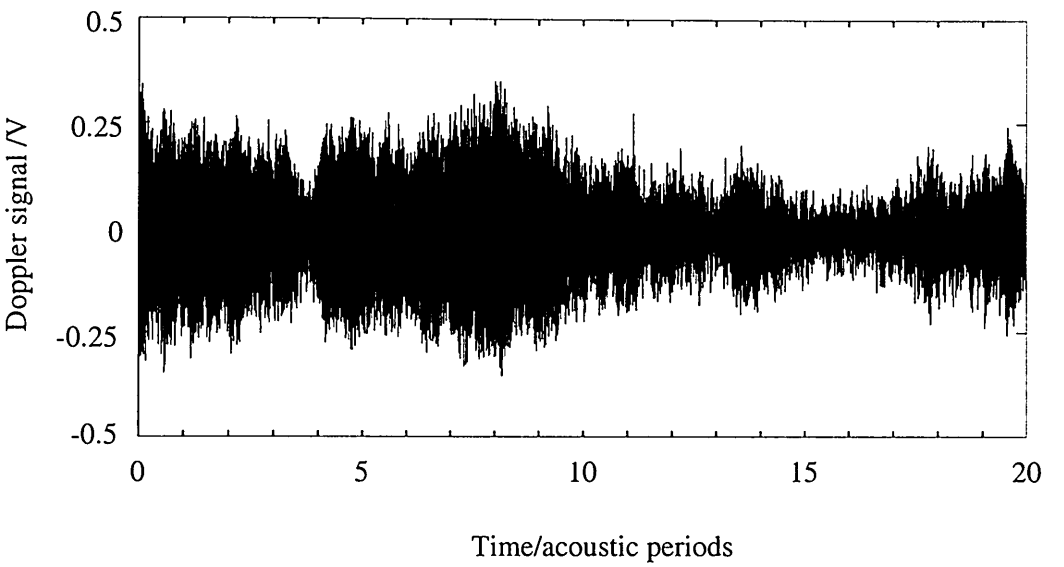

Figure 3.9: A measured Doppler signal with the acoustic frequency, $f_m = 660$ Hz.

3.5 Frequency domain analysis of Doppler signal

Having established the mathematical form of the Doppler signal, this next section is concerned with extracting velocity information. Frequency domain analysis involves

calculating the frequency spectrum of the Doppler signal to deduce the velocity. The advantage of the frequency domain analysis technique is its simplicity. The Fourier transform of the Doppler signal generates the frequency spectrum, the form of which can be determined for the constant flow and alternating velocity conditions allowing the particle velocity amplitude to be deduced.

3.5.1 Spectral density function

The Doppler signal is described in the time domain by the values of V_D as a function of time, t. The Fourier transform of the signal, denoted by $\mathcal{F}\{V_D\}$, yields amplitude as a function of frequency in the range, $-\infty < f < \infty$. In practice, the signal is sampled and windowed before the magnitude spectrum, $|\mathcal{F}\{V_D\}|$, is calculated. The spectrum is known as the voltage density spectrum or the spectral density function of $V_D(t)$ [39]. The spectral density function gives the relative weighting of each frequency component. The contribution of a given frequency band to the representation of the Doppler signal may be found by integrating to find the desired area under the spectral density function. Periodic components in the Doppler signal will produce discrete frequency components in the spectral density function .

The power spectral density function (PSD) is calculated from the magnitude spectrum and describes the distribution of power versus frequency. The form of the PSD for several velocity conditions has been investigated in detail by Cullen for determining flow characteristics [40]. However, the aim of this work is to utilize LDA in a micro-

phone calibration technique. So to minimize the amount of processing performed on the Doppler signal, the form of the magnitude spectrum for the two velocity conditions will be studied instead of the PSD.

3.5.2 Spectral density due to a moving particle

Consider the Doppler signal produced by a single particle moving parallel to the x axis with constant speed, U . The form of $\mathcal{F}\{V_D\}$ may be deduced for the resulting single Doppler burst. The particle moves through the region of the probe volume with displacement, $x(t) = Ut + x(0)$, and crosses fringes with a frequency

$$\overline{F} = \frac{U}{\Lambda} . \tag{3.39}$$

Using equation 3.39 to substitute for U in equation 3.21 gives

$$V_D(t) = \kappa \mathcal{K} w e^{-8[(Ut+x(0))^2\beta^2]} \cos\left[2\pi(F_s + \overline{F})t + Dx(0)\right] \tag{3.40}$$

for the Doppler signal. Assuming that the spectrum of the Gaussian term is narrow-band compared to the spectrum of the cosine term, cross harmonic terms can be ignored [41]. The Fourier transform of the signal is

$$\mathcal{F}\{V_D(t)\} = \kappa \mathcal{K} w \mathcal{F}\Big\{ \exp\Big[-8(Ut + x(0))^2\beta^2 \Big] \Big\} \odot \mathcal{F}\Big\{ \cos\Big[2\pi(F_s + \overline{F})t + Dx(0)\Big] \Big\} \tag{3.41}$$

where $\odot$ denotes convolution. By making use of standard mathematical identities in [42], equation 3.41 may be expressed as

$$\begin{aligned}\mathcal{F}\{V_D(t)\} &= \kappa\mathcal{K}w\left\{\frac{1}{2}\frac{\sqrt{\pi}}{2\sqrt{2}\,U\beta}\exp\left[-\left(\frac{\pi F}{2\sqrt{2}\,U\beta}\right)^2\right]\right\} \\ &\quad \odot\frac{1}{2}\left\{\delta\Big[F+(F_S+\bar{F})\Big]+\delta\Big[F-(F_S+\bar{F})\Big]\right\} \\ &= \frac{\mathcal{K}w}{8\sqrt{\pi}\sigma_F}\left\{\exp\left[-\frac{(F+F_S+\bar{F})^2}{4\sigma_F^2}\right]+\exp\left[-\frac{(F-F_S-\bar{F})^2}{4\sigma_F^2}\right]\right\}\end{aligned} \tag{3.42}$$

where

$$\sigma_F = \frac{\sqrt{2}U\beta}{\pi} \tag{3.43}$$

and δ is the Kronecker delta. The amplitude spectrum of the Doppler signal has two Gaussian peaks centred at $F = \pm(F_S + U/\Lambda)$ and with standard deviation, σ_F. The multiple particle Doppler signal has a spectrum with peaks centred at the same frequencies as the peaks of the spectrum for the single Doppler burst [34].

Evaluating the magnitude of the complex valued amplitude spectrum yields the magnitude spectrum. The magnitude spectrum is symmetric about $F = 0$ and so it is only necessary to consider the positive frequency spectral density. The positive frequency magnitude spectrum is defined as

$$\begin{aligned}|\mathcal{F}_+\{V_D(t)\}| &= 0 \qquad\qquad \text{for} \quad F<0 \\ &= |\mathcal{F}\{V_D(t)\}| \quad \text{for} \quad F\geq 0\,.\end{aligned} \tag{3.44}$$

In practice, the Doppler signal is multiplied by a window function, $h(t)$, to prevent leakage [39]. The windowed Doppler signal is $\hat{V}_D(t) = h(t)V_D(t)$. Cullen observed that this process contributes to the width of the spectral peak [40]. By considering the form of the Fourier transform of the windowed Doppler signal and approximating the Fourier transform of the Hanning window to the central lobe of a cosine squared function, the positive frequency magnitude spectrum is given by

$$|\mathcal{F}_+\{\hat{V}_D(t)\}| \simeq \Omega \exp\left[-\frac{(F - F_S - \bar{F})^2}{4\sigma^2}\right] \tag{3.45}$$

where

$$\sigma^2 = \sigma_F^2 + \sigma_W^2 \tag{3.46}$$

and

$$\sigma_W = \frac{2}{\pi T}\,. \tag{3.47}$$

Ω is a constant, σ_W is the standard deviation of the peak due to the window function, and T is the finite time interval over which the Doppler signal is recorded.

The positive frequency magnitude spectrum of the Doppler signal due to the single particle moving through the probe volume with constant speed U and $F_s = 0$ (see figure 3.7) is illustrated in figure 3.10. The Gaussian peak is centred on $F = U/\Lambda$ with standard deviation σ. Without high pass filtering the pedestal term in the photodetector signal would contribute a Gaussian peak in the frequency spectrum centred on $F = 0$.

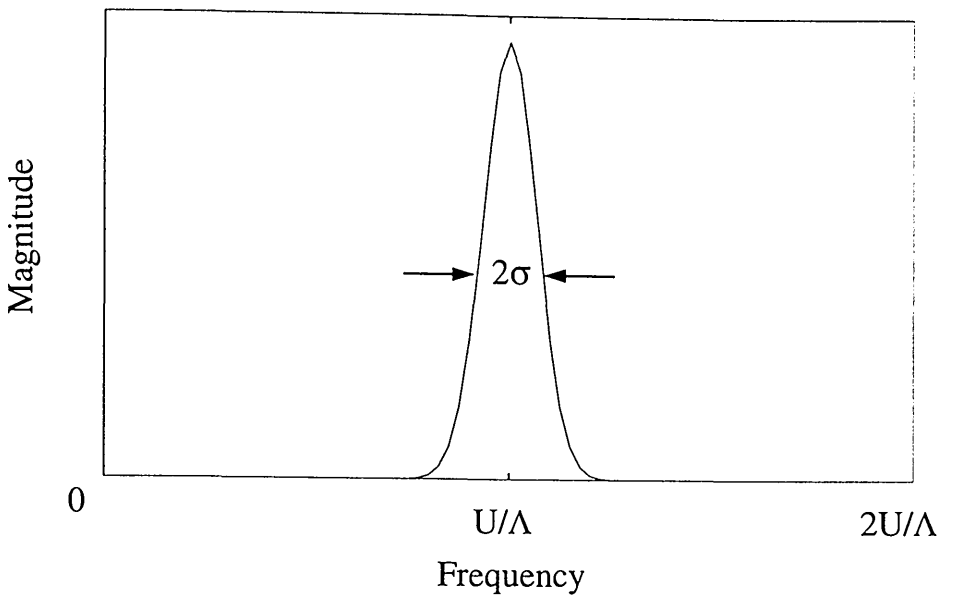

Figure 3.10: The positive frequency magnitude spectrum of the simulated Doppler burst for a single particle moving with constant speed U and $F_s = 0$.

From [39], the PSD of the windowed Doppler signal is given by

$$\hat{S}(F) = \frac{|\mathcal{F}\{\hat{V}_D(t)\}|^2}{T P_W} \tag{3.48}$$

where P_W is the average power of the window function,

$$P_W = \frac{1}{T}\int_0^T h^2(t)dt\,. \tag{3.49}$$

Multiplying the Doppler signal by a window function reduces the power of the signal. To ensure that the integral of $\hat{S}(F)$ over all frequencies is equal to the integral of the unwindowed Doppler signal, $S(F)$, over all frequencies the factor P_W is included in equation 3.48 [40]. The PSD of the Doppler signal has dimensions of voltage squared multiplied by time. From equation 3.45 and equation 3.48, the PSD of the windowed

Doppler signal generated by the constant velocity condition is

$$\hat{S}_+(F) \simeq \frac{\Omega^2}{TP_W} \exp\left[-\frac{(F - F_S - \bar{F})^2}{2\sigma^2}\right] . \tag{3.50}$$

The area under the spectral peak of the power spectrum gives an indication of the power of the Doppler signal.

3.5.3 Sources of spectral broadening

The duration of the Doppler burst is determined by the transit time, i.e. the time taken for the particle to cross the probe volume, $1/U\beta$. The duration of the burst contributes to the frequency spread of the spectral peak and this effect is called transit time broadening. The standard deviation of the Gaussian peak is inversely proportional to the transit time. Using equations 3.11, 3.19, 3.39, and 3.43 the transit time broadening relative to the mean frequency can be expressed in terms of the number of fringes in the probe volume,

$$\frac{\sigma_F}{\bar{F}} = \frac{\sqrt{2}}{\pi N_f} . \tag{3.51}$$

From equation 3.51 it can be seen that the transit time broadening is inversely proportional to N_f which depends on the angle between the illuminating beams, the wavelength of the laser light, and the focused beam waist diameter.

In the multiple particle case, the ambiguity noise is also a result of the finite transit time. The rate of change of the particle population within the probe volume, and hence

the ambiguity noise contribution to the Doppler frequency, depends on the finite transit time. The resulting contribution to the frequency spread is referred to as ambiguity broadening.

The standard deviation due to the effect of the window function, σ_W, is inversely proportional to the time interval over which the Doppler signal is recorded, T. The effect of the window function can be established by considering the ratio of the standard deviation due to transit time broadening to the standard deviation due to the effect of the window function. Using equations 3.43 and 3.47,

$$\frac{\sigma_F}{\sigma_W} = \frac{\sqrt{2}}{2} TU\beta \tag{3.52}$$

which is proportional to the ratio of the time interval to the transit time. It can be seen from equation 3.52 that for relatively low flow speeds, the broadening effect due to the window function will be significant.

Others sources of broadening include velocity gradients, velocity fluctuations, laser beam waist position, and Brownian motion. A mean velocity gradient in the flow will result in a range of particle velocities. If the variation in velocity across the probe volume is significant, a contribution to the overall spectral broadening will result. In a turbulent flow, fluctuations of volume averaged velocity and velocity fluctuations within the probe volume cause broadening. If the beam waists do not lie at the position of the focal point of the lens there will be a variation of the fringe spacing. The Doppler frequency will change as particles cross the probe volume resulting in broadening.

Under certain conditions, diffusion of the particles by Brownian motion will contribute to the spectral broadening. The motion is described using the diffusion coefficient for a sphere with Stokes drag [43], such that

$$C = \frac{k_B T}{3\pi\eta_f d_p} \tag{3.53}$$

where k_B is Boltzmann's constant, T is the thermodynamic temperature, η_f is the fluid viscosity, and d_p is the particle diameter. The characteristic diffusion time indicates the time required for a particle to move by a distance of the order of the fringe spacing due to Brownian motion. The effect of diffusion can be established by comparing the characteristic diffusion time to the transit time [7], such that

$$\left(\frac{\Lambda}{2\pi}\right)^2 \frac{1}{C} \simeq \frac{1}{U\beta}. \tag{3.54}$$

Using equation 3.54, the flow velocity at which Brownian motion is significant may be determined.

If broadening due to velocity gradients, turbulence, imprecise focusing, and Brownian motion can be neglected, the total variance of the spectral peak is due to the transit time broadening, the window function, and the ambiguity noise effect. Calculating σ_F and σ_W and substituting into equation 3.46 allows the extent of the ambiguity broadening effect to be evaluated as the total theoretical value can be compared to the standard deviation measured from the spectral density function

3.5.4 Spectral density due to an alternating velocity

The Doppler signal for a sinusoidal sound field, i.e. particles oscillate parallel to the x axis, is given by the expanded form of the frequency modulated wave in equation 3.38. The positive frequency magnitude spectrum of the signal is of the form [39]

$$|\mathcal{F}_+\{V_D(t)\}| \propto J_0\left(\frac{u_m}{\Lambda f_m}\right)\delta(F-F_s) + \sum_{n=1}^{\infty} J_n\Big(\delta[F-F_s+nf_m]+\delta[F-F_s-nf_m]\Big)\,. \quad (3.55)$$

Periodic components in the signal produce discrete frequency components in the spectral density function. The magnitude spectrum of the Doppler signal consists of a spectral component centred on the shift frequency, F_s, and side lobes spaced at discrete multiples of the acoustic frequency, f_m. In theory there are an infinite number of sidebands but only those nearest the centre of the spectrum will be of significant height. The magnitudes of the spectral components are proportional to successive orders of the Bessel functions. The ratio of magnitudes between the nth peak and the centre peak is

$$J_n\left(\frac{u_m}{\Lambda f_m}\right)/J_0\left(\frac{u_m}{\Lambda f_m}\right) \quad (3.56)$$

which can be resolved to give the acoustic particle velocity amplitude, u_m. The effective bandwidth of the signal is approximately $2(\Delta F_m + f_m)$ [39].

LDA measurements of acoustic particle velocity amplitude, determined from the frequency spectra of Doppler signals, were first reported by Taylor [9]. By determining

the magnitudes or heights of various peaks in the spectrum and finding the value for the argument of the Bessel functions at which they fit best, Taylor was able to estimate the acoustic particle velocity amplitude. The measurements could only be conducted in a steady mono-frequency sound field as the method yields the time-averaged value of velocity amplitude. Taylor's analysis also assumed that the Doppler signal had a constant amplitude when in fact a measured Doppler signal is more complex because of fluctuations in the particle concentration. Accurate results were only obtained by averaging a large sample of measurements, leading to a prolonged measurement time [3]. Davis and Hews-Taylor extended the idea for the measurement of complex acoustic impedance by determining both the magnitude and phase of the particle velocity relative to a microphone pressure signal [10]. Vignola et al developed the frequency analysis method further to include sound sources in water [11]. The effect of windowing was neglected.

Consider the form of the positive frequency magnitude spectrum of the windowed Doppler signal,

$$|\mathcal{F}_+\{\hat{V}_D(t)\}| \propto J_0\left(\frac{u_m}{\Lambda f_m}\right) H(F - F_s) + \sum_{n=1}^{\infty} J_n\Big(H[F - F_s + nf_m] + H[F - F_s - nf_m]\Big) \quad (3.57)$$

where $H(F)$ is the Fourier transform of the window function $h(t)$. Figure 3.11 shows the magnitude spectra of the two simulated Doppler signals in figure 3.8, i.e. generated for a single particle moving in a sinusoidal sound field with $F_s = 0$ and with

$F_s = 2u_m/\Lambda$, plotted against the same frequency and magnitude scales. The Hanning window function was applied. It can be seen from figure 3.11 that each spectral peak has a finite width, which is determined by the window function. If this width is significant then the magnitude of each peak is no longer given by the height but by the area under the spectral density function [39].

For the simulated Doppler signal with $F_s = 0$, the magnitude spectrum is centred on the zero frequency axis and the distance between peaks is $2f_m$. This is because in calculating the spectrum, the negative frequency section is folded back into the positive frequency range before the magnitude is evaluated. For $F < 0$ and odd n, the Bessel functions are negative and the peaks cancel out with the corresponding peaks in the positive frequency range. For $F < 0$ and even n, the Bessel functions are positive and add to the height of the corresponding peaks in the positive frequency range. For the simulated Doppler signal with $F_s = 2u_m/\Lambda$, the spectrum is centred on F_s and the spacing between peaks is f_m, as predicted using the equation for the frequency modulated wave.

For a small constant mean flow with speed u_0 in the x direction superimposed onto the alternating velocity, the particle displacement is given by

$$x(t) = x_m \sin(2\pi f_m t + \varphi_m) + x(0) + u_0 t \, . \tag{3.58}$$

The magnitude spectrum of a Doppler signal simulated for a single particle with the displacement amplitude given by equation 3.58, mean flow velocity $u_0 = u_m/10$,

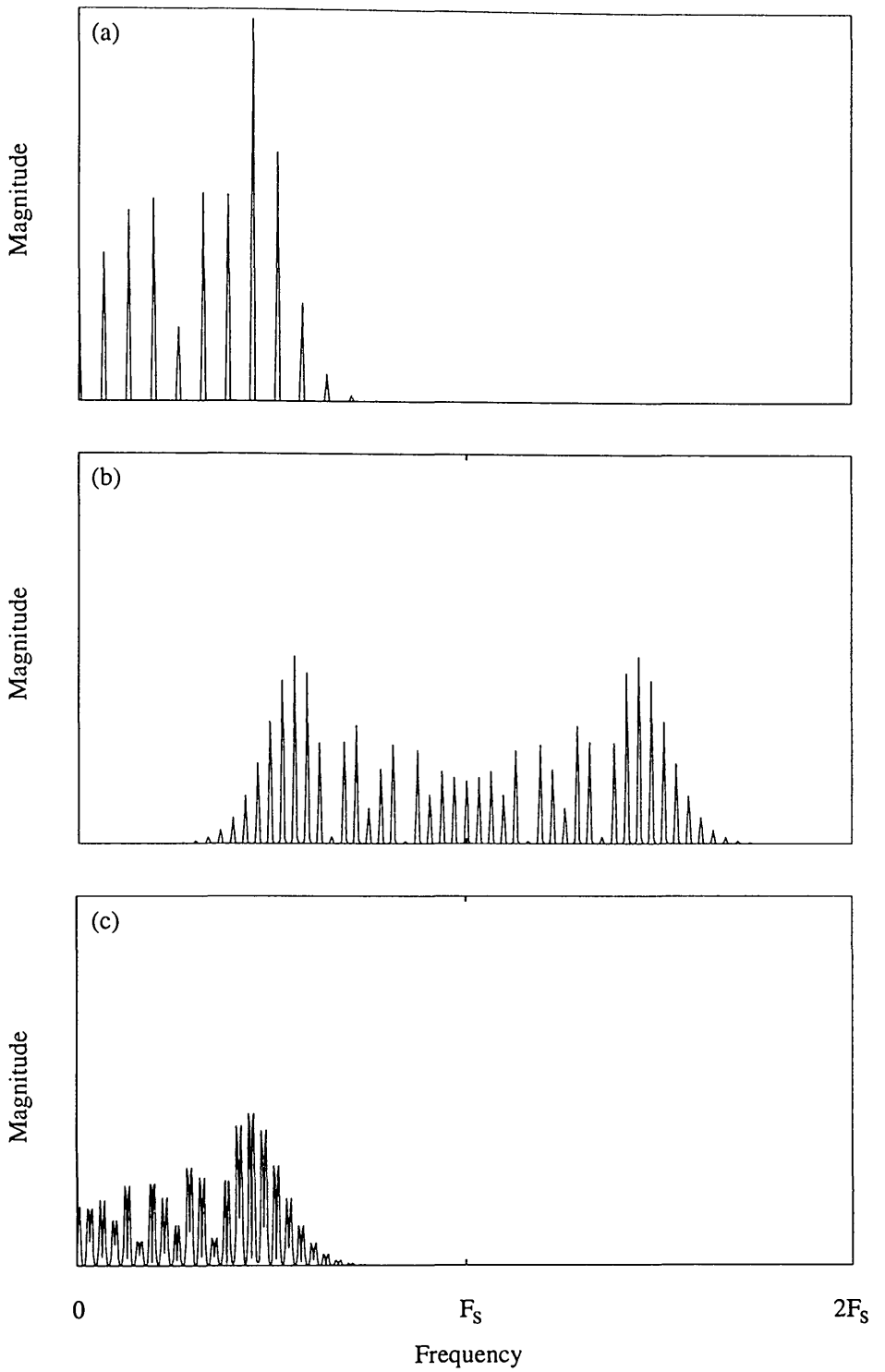

Figure 3.11: Positive frequency magnitude spectral density function due to simulated Doppler signal for a single particle moving in a sinusoidal sound (a) with $F_s = 0$, (b) with $F_s = 2u_m/\Lambda$, (c) with $F_s = 0$ and mean flow velocity $u_0 = u_m/100$. The displacement amplitude $x_m = 1/4\beta$, the initial position $x(0) = 0$, and acoustic frequency $f_m = 1$ kHz.

acoustic frequency $f_m = 1$ kHz, and $F_s = 0$ is also illustrated in figure 3.11. The variance of each spectral peak is given by $\sigma^2 = \sigma_F^2 + \sigma_W^2$. The spectrum remains centred on the zero frequency axis. However, the frequency positions of the folded peaks will not match up exactly with the frequency positions of the positive range peaks and so will not cancel out or add in height. Instead, a splitting effect is observed on calculating the magnitude spectrum, as first reported by Taylor [9]. At discrete intervals of f_m two peaks are produced, the space in between determined by the size of the mean flow velocity.

With a frequency shift, the spectrum will be centred on $F_s - u_0/\Lambda$ or $F_s + u_0/\Lambda$ depending on whether the mean flow velocity is in the same or opposite direction to the fringe motion. The mean flow velocity is estimated in [44], such that

$$u_0 = \Lambda \left(\frac{F_- + F_+}{2} - F_s \right) \tag{3.59}$$

where F_- and F_+ are the frequency positions of the highest peaks to the left and right, respectively of the frequency shift F_s.

Figure 3.12 displays the frequency spectrum of the measured multi-particle Doppler signal in figure 3.9. There is a noise floor to the spectrum. Sources of noise in the Doppler signal will be discussed in section 3.7. The spectrum is centred at a frequency position slightly to the right of F_s indicating a small mean flow in the $+x$ direction. Contributions to the spectral peak width arise from the windowing operation, the mean flow, and the ambiguity noise associated with the multi-particle signal (see section

3.4.7). The relatively narrow bandwidth of the frequency spectrum, and hence the Doppler signal, is due to the small particle displacement amplitude ($x_m \simeq 1\mu$m).

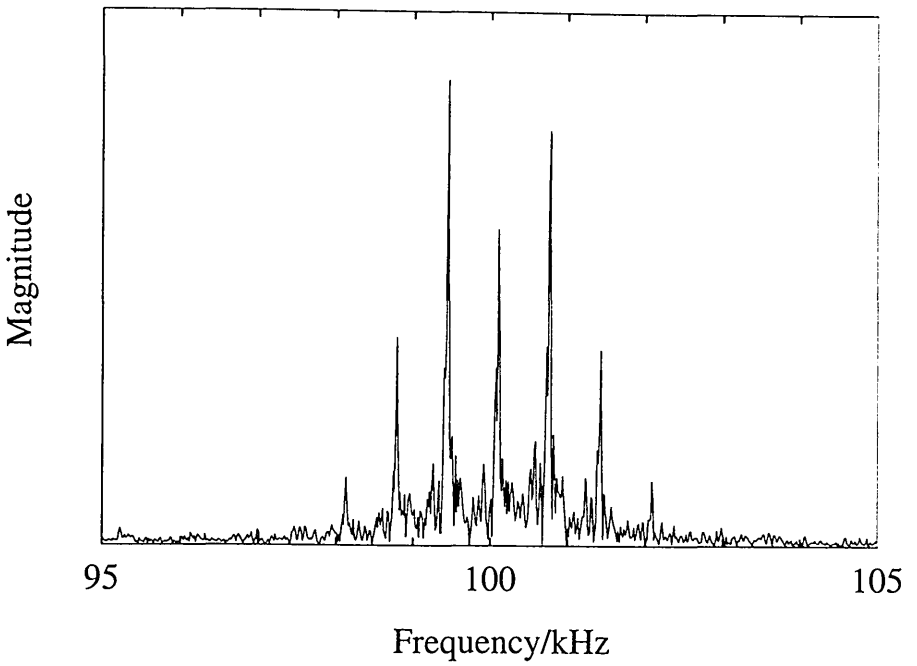

Figure 3.12: A section of the frequency spectrum for the measured Doppler signal about the shift frequency, $F_s = 100$ kHz.

3.5.5 Limitations of frequency domain analysis

In practice, the Doppler signal is sampled at discrete intervals over a finite period of time, T. If $\Delta\tau$ denotes the time interval (measured in seconds) between consecutive samples, the upper limit to the frequency that can be represented by the samples is given by the Nyquist condition,

$$F_{Ny} = \frac{1}{2\Delta\tau} . \tag{3.60}$$

Any frequency component outside of the range $-F_{Ny}$ to F_{Ny} is falsely translated back into the range [45]. This effect, called aliasing, results in a distortion of the signal but can be prevented by low pass filtering the signal. The Doppler signal is obtained by bandpass filtering the photodetector signal to remove the pedestal and prevent aliasing.

For the constant mean flow condition, the shift frequency must be selected to ensure that there is no significant overlap of the peak due to the particle motion and the pedestal peak that would exist without high pass filtering. The high pass frequency must be selected to remove the pedestal without attenuating significant low frequency components of the Doppler signal, the low pass frequency must be selected to ensure the Nyquist condition is satisfied, and the frequency shift must also be sufficiently low to prevent attenuating significant high frequency components of the Doppler signal.

For the alternating velocity condition, the bandwidth of the Doppler signal can be estimated from the frequency spectrum. With a suitable frequency shift, the maximum frequency of the Doppler signal is $2\Delta F_m$. This implies

$$\Delta F_m < \frac{1}{4\Delta\tau} \tag{3.61}$$

using the Nyquist condition and gives a theoretical upper limit to the acoustic particle velocity amplitude that can be measured of

$$u_m < \frac{\Lambda}{4\Delta\tau} \,. \tag{3.62}$$

As filters with infinitely steep cut-offs do not exist, the maximum measurable value of velocity amplitude will be lower than the theoretical value indicated by equation 3.62.

3.6 Time domain analysis of Doppler signal

An alternative to frequency domain analysis involves a demodulation of the frequency modulated Doppler signal, generated by acoustic particle motion, in the time domain to give instantaneous frequency, and hence instantaneous velocity. The particular time domain technique that will be considered here is called Hilbert transform analysis.

3.6.1 Hilbert transform

The Hilbert transform technique was first applied to Doppler signals by Grechikhin and Rinkevichius [12]. The orthogonal component of the Doppler signal is obtained through multiplication of the Fourier plane by

$$\begin{aligned} \mathcal{H}\{V_D(t)\} &= -j\mathcal{F}\{V_D(t)\} \quad F \geq 0 \\ &= +j\mathcal{F}\{V_D(t)\} \quad F < 0 \end{aligned} \tag{3.63}$$

so that the real and imaginary parts are swapped. This is then inverse Fourier transformed. The complete Hilbert transform algorithm applied to the Doppler signal is

defined as [40]

$$V_{D\perp} = \mathcal{F}^{-1}\{\mathcal{H}\{V_D(t)\}\} \tag{3.64}$$

where $\mathcal{F}^{-1}$ denotes the inverse Fourier transform operation. The instantaneous phase of the Doppler signal is given by

$$\Theta(t) = \tan^{-1}\left(\frac{V_{D\perp}(t)}{V_D(t)}\right) \tag{3.65}$$

which can be used to determine the instantaneous frequency, i.e. the Doppler frequency, of the signal and the instantaneous particle velocity.

A Hilbert transform program developed by Hann and Greated [46] was used to analyse Doppler signals in the present study. The program applies a window function to the Doppler signal before calculating the power spectral density function. A bandwidth filter is applied to the signal to maximize the signal-to-noise ratio of the Hilbert transformed signal. Through inspection of the power spectrum, the limits to the bandwidth filter are selected. Equation 3.63 and then equation 3.64 are applied to the windowed and bandpass filtered Doppler signal to produce the Hilbert transform signal. The Hilbert transform signal is divided by the window function before equation 3.65 is applied. The instantaneous frequency of the Doppler signal is then calculated by differentiating and scaling the result. Figure 3.13 shows the power spectral density of the simulated Doppler signal for a single particle moving in a sinusoidal sound field along with instantaneous velocity curve extracted using the program.

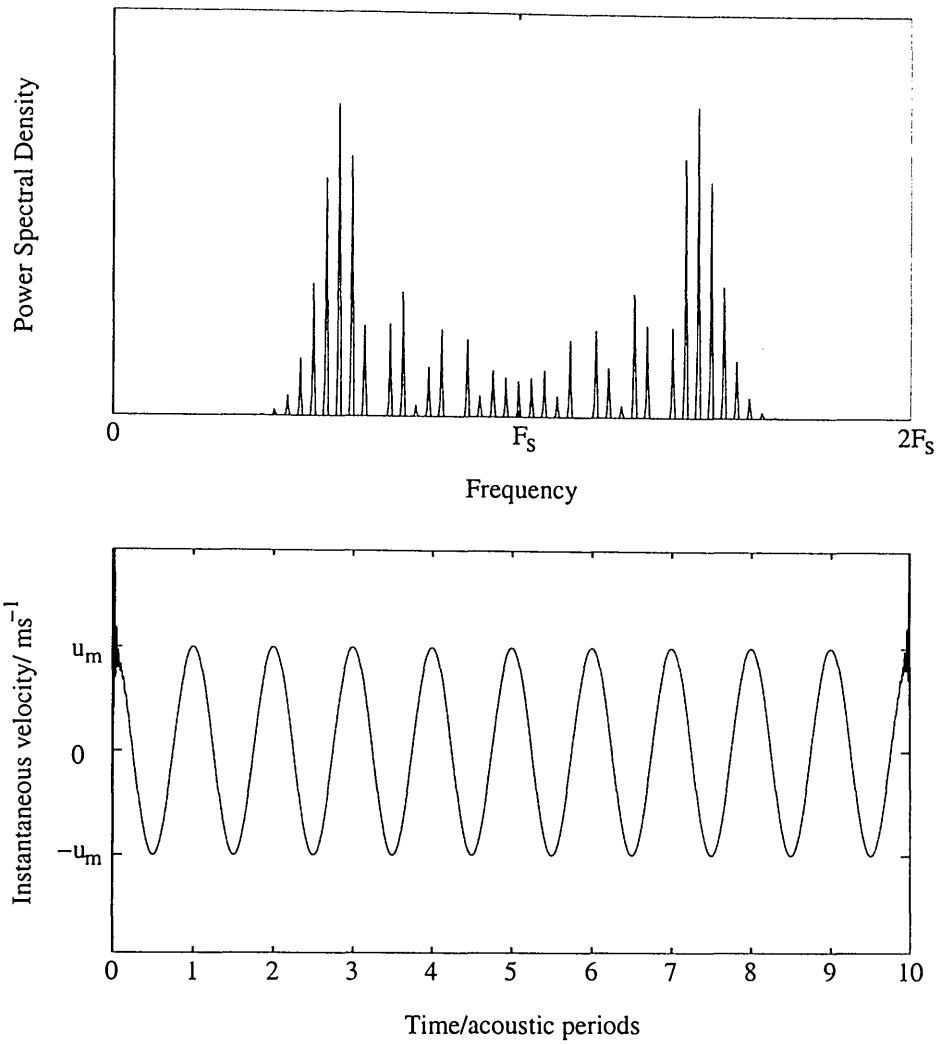

Figure 3.13: The power spectrum about the shift frequency, $F_s = 2u_m/\Lambda$. Also displayed is the instantaneous velocity extracted from the Doppler signal.

In the instantaneous frequency curve generated by the program, each point is influenced to some extent by every point in the frequency domain. These points depend on every point in the Doppler signal. If a section of the Doppler signal is degraded, it affects to some extent the entire frequency curve over the entire sample time. Also, dividing the signal by the window function can reduce the quality of the instantaneous frequency curve at the beginning and the end [46]. This effect can be observed by closer inspection of figure 3.13.

3.6.2 Limitations of time domain analysis

The Doppler signal is sampled at discrete time intervals before the Hilbert transform routine is applied. The upper limit to the frequency that can be represented by the samples is given by the Nyquist condition in equation 3.60 (see section 3.5.5). Aliasing of the signal is prevented by low pass filtering to remove the frequencies above the Nyquist limit while high pass filtering removes the unwanted pedestal signal. The Hilbert transform is not well defined unless the Doppler signal has a narrow bandwidth. This implies that the peak frequency deviation must be much smaller than the frequency shift,

$$\Delta F_m < F_s \, . \tag{3.66}$$

The shift frequency must be selected to ensure that there is no attenuation of significant high frequency components by the low pass filter. Also, the shift frequency must be selected to ensure that there is no attenuation of significant low frequency components by the high pass filter. If $F_s \simeq F_{Ny}/2$ then the same limit to the measurement of particle velocity is obtained as expressed in equation 3.62. If ΔF_m is too small compared to F_s, then frequency resolution, and hence velocity resolution, is lost.

3.7 Sources of noise

Noise is always present in the measured Doppler signal. Contributions arise from optical sources, photodetection effects, and electronic system sources [7] [47]. The com-

bined effect is to generate a noise floor in the frequency spectrum. Optical sources of noise are identified as diffractive and refractive beam perturbations, coherence degradation, light dispersion from lenses and the fluid, and laser hum. Imperfections in the optical system, e.g. angular misalignment, could also generate noise.

Conversion of the optical signal by the photodetector is the source of two noise components, thermal (Johnson) noise and shot noise [7]. The amplifier and effective load resistor of the detector causes thermal noise. Dark currents, i.e. photoemissions that occur spontaneously, also contribute to internally generated noise. The photoemission process is random and introduces shot noise into the Doppler signal. Shot noise can be reduced by minimizing the amount of background light inadvertently captured by the photodetector and maximizing the intensity of the scattered light from the probe volume.

The power spectral density of the Doppler signal is an efficient method of separating the signal component from the noise component, allowing the signal-to-noise ratio (SNR) to be estimated.

3.8 Acousto-optic effect

For Doppler signals generated by the oscillation of particles in the interference fringes, the properties of the fluid in which the sound wave is propagating can introduce complications. The signal may be dominated by the effects of refractive index change due

to the pressure variations inherent in the sound wave.

As a sound wave propagates through a medium it generates areas of tension and compression. This strain field moves with the acoustic wave through the medium creating temporal and spatial variations in the refractive index of the medium. When LDA is used to measure the sound field, the two split beams are affected by differing degrees due to the refractive index variations. A phase difference is introduced which causes the fringe pattern to move. This is called the acousto-optic effect and has been investigated by Jack et al [48] [49].

The particles suspended in the probe volume oscillate due to the sound wave and the fringes move due to the phase difference in the beams. The light collected by the photodetector as the Doppler signal will be due to a combination of both the oscillating particles and the oscillating fringes. These two sources of motion are $\pi/2$ out of phase. This gives rise to an apparent motion of the particles as seen by the detector [48],

$$y(k,x) = x_m \sin(kx) + y_m \cos(kx) \tag{3.67}$$

where k is the wavenumber, x is the distance the laser beams have travelled in the direction perpendicular to the optical axis, x_m is the amplitude of motion of the particles due to the sound wave, and y_m is the amplitude of motion of the probe volume.

For a standing wave travelling at 90° to the fringe volume (i.e. perpendicular to the

fringe orientation), the amplitude of the fringe movement has the form [49]

$$y_m = \frac{\Delta n_0 x^2 k}{n} \cos\phi \tag{3.68}$$

where Δn_0 is the amplitude of the variations in refractive index, n is the refractive index of the medium without the presence of a strain field, and ϕ is the phase. Using the refractive index of air with no strain field present in equation 3.68 gives

$$\frac{y_m}{\Delta n_0} = 0.9997 x^2 k \cos\phi \,. \tag{3.69}$$

The amplitude of the variations in refractive index is expressed in [48], such that

$$\Delta n_0 = \frac{p n^3 x_m k}{2} \tag{3.70}$$

where p is the photoelastic tensor and is calculated from the refractive index of the medium [50]. For air, equation 3.70 may be written as

$$\frac{\Delta n_0}{x_m} = 0.00029 k \,. \tag{3.71}$$

Therefore, the ratio of the fringe movement to the particle movement is

$$\frac{y_m}{x_m} = 0.00029 x^2 k^2 \cos\phi \,. \tag{3.72}$$

Increasing either the wavenumber or the distance of propagation of the laser beams

results in an increase in the ratio of the fringe movement to the particle movement.

From equation 3.67 and equation 3.72, the apparent motion of the particles observed by the detector for a standing wave is

$$\frac{y(k,x)}{x_m} = \sin(kx) + 0.00029x^2k^2\cos\phi\cos(kx)\,. \tag{3.73}$$

A signal from a vibrating particle will therefore dominate at low frequencies and short distances of propagation. As the frequency and distance of propagation increase, the signal from the oscillating fringes will begin to dominate. Analysis of the resulting Doppler will yield amplitude information that does not accurately represent the motion of the particles. The acousto-optic effect is more pronounced in liquids than in gases and for air it can generally be assumed negligible.

3.9 Summary

The basic principle of LDA was introduced. Light scattered from moving particles is frequency shifted by an amount proportional to the velocity. In practice, this Doppler shift is small compared to the frequency of the laser light. In the dual beam mode of LDA, interference fringes are formed at the intersection of two laser beams. The intensity of light scattered by particles crossing the fringes is modulated at the Doppler frequency. The photodetector fringe current due to a single particle located in the fringe volume was used to derive expressions for the Doppler signal. A single particle

steady mean flow produces a Doppler signal with constant Doppler frequency while an alternating velocity produces a frequency modulated Doppler signal. The analysis was extended to include Doppler signals produced by multiple particles.

Frequency domain analysis provides a method for extracting velocity information from the Doppler signal. The spectral density function is generated from the Fourier transform of the Doppler signal. The single particle steady mean flow spectrum consists of a central peak centred on the Doppler frequency. A set of spectral peaks is produced for the alternating velocity condition spaced at intervals of the acoustic frequency. Sources of spectral broadening were considered as were sources of noise in the photodetector signal. The Doppler signal can be demodulated, in the time domain using the Hilbert transform technique, to yield instantaneous frequency and hence instantaneous velocity.

Finally, the acousto-optic effect on LDA measurements was discussed briefly. It is most pronounced in liquids and is generally negligible in air.

Chapter 4

Photon correlation

4.1 Introduction

The photon correlation technique for laser Doppler anemometry requires the interpretation of the photomultiplier signal as a series of discrete pulses. The average number of pulses is directly related to the intensity of the scattered light, and hence the particle velocity. Counting the number of pulses in small time intervals allows the autocorrelation function (ACF) of the signal to be calculated which is then analysed to determine velocity and flow information. In section 4.2 the operation of a photomultiplier is explained along with the basic principle of photon correlation. The mathematical form of the ACF is deduced for different velocity conditions in section 4.3 and the analysis of the ACF to determine particle velocity is discussed in section 4.4. Finally, the limitations of the technique are considered in section 4.5.

4.2 The principle of photon correlation

A photomultiplier consists of a photocathode, an electron optical input system (input optics), a secondary emission system (dynode chain), and an anode. Photons striking the cathode cause electrons to be emitted from the material. The electrons are accelerated towards the dynode chain by a strong electric field. As the electrons strike the first dynode in the chain, the dynode emits more electrons than it absorbs. The electric field accelerates electrons from the emitting surface of each dynode to the absorbing surface of the next. So the number of electrons multiplies at each dynode in the chain. The electrons emitted by the final dynode are collected at the anode to produce the anode current which is then filtered and passed through a load resistor. The photodetector voltage is the voltage measured across the load resistor.

The output of the photomultiplier can be thought of as a series of discrete pulses. Each pulse corresponds to the emission of a single electron from the cathode material. If the intensity of captured scattered light is high, the series of pulses is effectively smoothed to form a continuous signal. If the intensity is low enough, individual pulses at the detector output may be counted. The signal is correlated with itself to produce the ACF in which the positions of the peaks and the turning points will be determined by the mean flow velocity and the acoustic particle velocity [7] [51]. The pulses have a finite duration due to the inherent integration times involved in the amplification process of photomultipliers. A discriminator incorporated into the photomultiplier ensures that the pulses are of the correct voltage level for use with a digital correlator.

In the dual beam mode of LDA, two parallel laser beams of equal intensity and a Gaussian profile are caused to intersect by a focusing lens. This produces the probe volume which contains a set of interference fringes and the component of fluid velocity in a single direction is measured at this point. Consider the situation in section 3.4.5 where the x axis is at right angles to the fringes, the y axis is parallel to the fringes, and the z axis is perpendicular to both the x and y axes. A particle moves parallel to the x axis with constant speed. The intensity distribution inside the fringe volume is illustrated in figure 4.1 along with the series of pulses constituting the photomultiplier signal. The probability of a pulse occurring is proportional to the integrated value of the intensity across the detector surface [51].

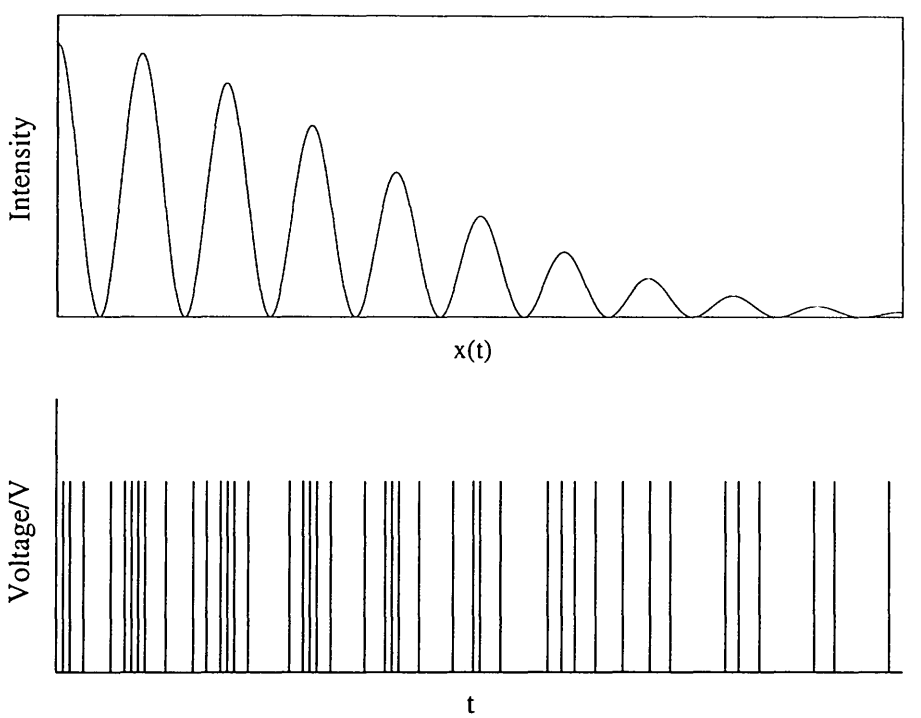

Figure 4.1: Intensity distributions inside fringe volume. Also illustrated is the series of pulses generated as the particle moves across the fringes with constant velocity.

Photon correlation is particularly suited to situations where the intensity of scattered light is low. This occurs when the laser light intensity is low, the particle diameter is small, and the particle concentration is sparse.

4.3 Mathematics of the correlation function

The correlation between the photomultiplier signal, $V(t)$, and a delayed version of the signal, $V(t-\tau)$, gives the ACF, $R(\tau)$, where τ is called the delay or lag time. The form of the ACF for a steady mean flow, an alternating velocity, and a mean flow superimposed onto an alternating velocity may be determined by deducing the form of the signal for the particle as a function of position within the probe volume [52].

4.3.1 Autocorrelation function due to a constant flow velocity

Consider particles moving parallel to the x axis with constant speed, U. From equation 3.16, the output voltage from the detector due a single particle in the probe volume may be expressed as

$$V(t) \simeq \kappa \mathcal{K} W(\beta\xi(t))\Big(1 + \cos D\xi(t)\Big) \; . \tag{4.1}$$

where the cosh term has been approximated to 1 to simplify the analysis and $F_s = 0$. κ is a constant that depends on the optical geometry and the sensitivity and load resistance of the detector. $\mathcal{K}$ characterises the particle scattering cross section, D is

the frequency to velocity conversion factor (see equation 3.9), and $\xi(t)$ is the particle displacement at time t. $W(\beta\xi(t))$ is the spatial weighting function, i.e. the weighting function defined in terms of particle position rather than time variables, and represents the envelope on the fringes due to the Gaussian cross section of the laser beams. It is expressed as

$$W(\beta\xi(t)) = we^{(-8\xi^2(t)\beta^2)} \tag{4.2}$$

where w is defined in equation 3.18 and β is defined in equation 3.19.

The total detector output signal is the sum of contributions arising from individual particles and is given by

$$V(t) \simeq \kappa \sum_p \mathcal{K}_p W(\beta\xi_p(t))\Big(1 + \cos D\xi_p(t)\Big) \tag{4.3}$$

where the summation extends over all the particles in the flow. Equation 4.3 contains a low frequency or pedestal term. In the previous chapter, high pass filtering was employed with frequency shifting to remove this term and simplify the signal processing. However, this cannot be done with photon counting and so the term is retained.

To determine the ACF for the signal $V(t)$, the initial position of the pth particle (i.e. at $t = 0$) is defined as ξ_p and the position at a time τ later along the flow axis is

$$\zeta_p = \xi_p + \int_0^\tau U dt = \xi_p + \eta_p(\tau)\,. \tag{4.4}$$

Following the derivation of Durrani and Greated in [41], it is assumed that ζ and ξ are independent random variables as the position of a particle depends only on the initial position and the instantaneous velocity. The ACF of the photomultiplier voltage signal is given by

$$\begin{aligned} R(\tau) &= E[V(t)V(t+\tau)] \\ &= \left(\kappa C_0 g_0 \int_{-\infty}^{\infty} W(\beta x)(1+\cos Dx)dx\right)^2 + \frac{\kappa^2 C_1 g_0}{2} \\ &\quad \times \int_{-\infty}^{\infty} p_\eta(x;\tau) R_W(\beta x)(1+\cos Dx)dx \end{aligned} \tag{4.5}$$

where

$$R_W(\beta x) = \frac{\sqrt{\pi}}{4\beta}\exp(-4\beta^2 x^2) \tag{4.6}$$

is the autocorrelation of the spatial weighting function. $E[\,]$ is the expectation operator, $C_0 = E[\mathcal{K}_p]$, $C_1 = E[\mathcal{K}_p^2]$, g_0 is the average number of particles per unit length of the measuring volume, and $p_\eta(x;\tau)$ is the probability density of the variable $\eta(t)$.

The first term of equation 4.5 is the square of the mean value of the Doppler signal. It can be ignored as it is time-independent if the scattering particle concentration is constant, contains no velocity information, and only contributes a constant or pedestal value to the correlation function [52]. For a constant velocity [41],

$$p_\eta(x;\tau) = \delta(x - U\tau)\,. \tag{4.7}$$

Substituting equation 4.7 into equation 4.5 and using the properties of the Dirac delta

function allows the time-dependent part of the ACF to be expressed as

$$\begin{aligned} R(\tau) &= \frac{\kappa^2 C_1 g_0}{2} \int_{-\infty}^{\infty} \delta(x - U\tau) R_W(\beta x)(1 + \cos Dx) dx \\ &= \frac{\kappa^2 C_1 g_0}{2} R_W(\beta U\tau)(1 + \cos DU\tau) \ . \end{aligned} \tag{4.8}$$

It can be seen from equation 4.8 that the ACF is periodic and decays with R_W.

Normalizing the ACF so that it has the value of unity at the origin gives

$$\tilde{R}(\tau) = \frac{1}{2} \exp(-4\beta^2 U^2 \tau^2)(1 + \cos DU\tau) \ . \tag{4.9}$$

The form of the ACF for particles moving with constant speed, U, is illustrated in figure 4.2 along with the ACF of the spatial weighting function. The number of fringes in the probe volume is reflected in the number of cycles in the ACF of the photomultiplier signal. The mean velocity determines the time between two maxima [7]. If the two illuminating laser beams are not of equal intensity, a different damping of the ACF will be observed.

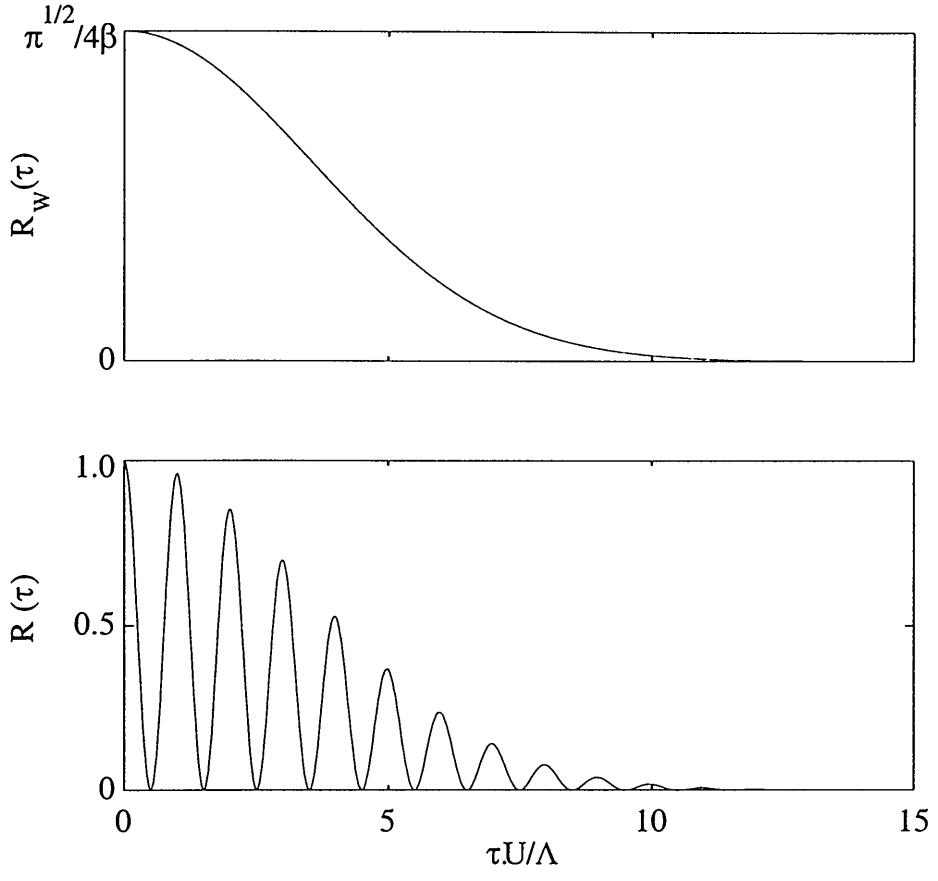

Figure 4.2: Normalized ACF for particles moving with constant speed, U. The ACF of the spatial weighting function, $R_W(\beta x)$, is also displayed.

4.3.2 Autocorrelation function due to an alternating velocity

Consider a particle oscillating parallel to the x axis in a sinusoidal sound field. The particle displacement may be written as

$$\zeta_p = \xi_p + \int_0^\tau U_p(t)dt = \xi_p + \eta_p(\tau)\,. \tag{4.10}$$

The instantaneous velocity of the particle is

$$U_p(t) = u_m \sin(2\pi f_m t + \phi_m) \tag{4.11}$$

where u_m is the acoustic particle velocity amplitude, f_m is the acoustic frequency, and ϕ_m is the phase.

Following the derivation of Sharpe and Greated in [52], $p_\eta(x;t)$ is the probability density function of the variable $\eta(\tau)$ which must be determined in order to evaluate the ACF. From equation 4.10 and equation 4.11,

$$\begin{aligned} \eta_p(\tau) &= u_m \int_0^\tau \sin(2\pi f_m t + \phi_m)dt \\ &= \frac{u_m}{\pi f_m}\Big[\sin(\pi f_m \tau)\sin(\pi f_m \tau + \phi_m)\Big] \end{aligned} \tag{4.12}$$

where ϕ_m is a random variable uniformly distributed over the interval 0 to 2π such that

$$p(\phi_m) = \frac{1}{2\pi} \qquad 0 < \phi_m < \frac{1}{2\pi}\,. \tag{4.13}$$

The relationship for a function of random variables from [53], gives

$$p_\eta(x;\tau) = \frac{2p(\phi_m)}{|d\eta(\phi_m)/d\phi_m|} \tag{4.14}$$

where the factor 2 on the RHS occurs because η is a double valued function of ϕ over the interval 0 to 2π. Equation 4.14 may be expressed as

$$\begin{aligned} p_\eta(x;\tau) &= \frac{1}{\pi\sqrt{u_m'^2 - x^2}} && -x \le u_m' \le x \\ &= 0 && |x| > u_m' \end{aligned} \tag{4.15}$$

where

$$u_m' = \frac{u_m}{\pi f_m}\Big[\sin(\pi f_m \tau)\Big] . \tag{4.16}$$

Ignoring the time-independent pedestal term, equation 4.5 becomes

$$R(\tau) = \frac{\kappa^2 C_1 g_0}{2}\frac{\sqrt{\pi}}{4\beta}\int_{-u_m'}^{u_m'} \frac{1}{\pi\sqrt{u_m'^2 - x^2}} \exp(-4\beta^2 x^2)(1 + \cos Dx)dx . \tag{4.17}$$

By substituting $x = u_m' \sin\alpha$, the integral in equation 4.17 can be written as

$$\frac{1}{\pi}\int_{-\pi/2}^{\pi/2} \exp(-4\beta^2 u_m'^2 \sin^2\alpha)[1 + \cos(Du_m' \sin\alpha)]d\alpha . \tag{4.18}$$

Substituting $p = 4\beta^2 u_m'^2$, equation 4.17 may be expressed as

$$R(\tau) = \frac{\kappa^2 C_1 g_0}{2} \frac{\sqrt{\pi}}{4\beta} (F_1 + F_2) \tag{4.19}$$

where

$$F_1 = \frac{1}{\pi} \int_{-\pi/2}^{\pi/2} \exp(-p \sin^2 \alpha) d\alpha \tag{4.20}$$

and

$$F_2 = \frac{1}{\pi} \int_{-\pi/2}^{\pi/2} \exp(-p \sin^2 \alpha) [\cos(D u_m' \sin \alpha)] d\alpha \; . \tag{4.21}$$

In order to generate the ACF, the integrals F_1 and F_2 must be evaluated and combined. From McLachlan [54], equation 4.20 can be expressed as

$$\begin{aligned} F_1 &= \frac{1}{\pi} \int_{-\pi/2}^{\pi/2} \exp\left(-\frac{p}{2}(1 - \cos 2\alpha)\right) d\alpha \\ &= \frac{1}{\pi} \exp\left(-\frac{p}{2}\right) \int_{-\pi/2}^{\pi/2} \exp\left(\frac{p}{2} \cos 2\alpha\right) d\alpha \; . \end{aligned} \tag{4.22}$$

Substituting $2\alpha = \varphi$ and using the generating function of the modified Bessel function [54], such that

$$\begin{aligned} F_1 &= \frac{1}{2\pi} \exp\left(-\frac{p}{2}\right) \int_{-\pi}^{\pi} \exp\left(\frac{p}{2} \cos \varphi\right) d\varphi \\ &= \exp\left(-\frac{p}{2}\right) I_0\left(\frac{p}{2}\right) \end{aligned} \tag{4.23}$$

where $I_0(\;)$ is a zero order modified Bessel function of the first kind.

The double angle formula and the Bessel function expansion for a cosine with a sinusoidal argument from [54] are used to express equation 4.21 as

$$\begin{aligned} F_2 &= \frac{1}{\pi}\int_{-\pi/2}^{\pi/2} \exp\left(-\frac{p}{2}(1-\cos 2\alpha)\right) \\ &\quad \times \left(J_0(Du'_m) + 2\sum_{n=1}^{\infty} J_{2n}(Du'_m)\cos(2n\alpha)\right) d\alpha \end{aligned} \tag{4.24}$$

where $J_0(\ )$ and $J_{2n}(\ )$ are Bessel functions of order zero and $2n$ respectively. Substituting $2\alpha = \varphi$ into equation 4.24 and expanding using formulae from [54], gives

$$\begin{aligned} F_2 &= \frac{1}{2\pi}\exp\left(-\frac{p}{2}\right)\int_{-\pi}^{\pi} \exp\left(\frac{p}{2}(\cos\varphi)\right) \\ &\quad \times \left(J_0(Du'_m) + 2\sum_{n=1}^{\infty} J_{2n}(Du'_m)\cos(n\varphi)\right) d\varphi \\ &= \exp\left(\frac{p}{2}\right)\left[I_0\left(\frac{p}{2}\right)J_0(Du'_m) + 2\sum_{n=1}^{\infty} I_n\left(\frac{p}{2}\right)J_{2n}(Du'_m)\right] \end{aligned} \tag{4.25}$$

where $I_n(\ )$ is the modified Bessel function of order n.

Finally, equation 4.23 and equation 4.25 are substituted into equation 4.19,

$$\begin{aligned} R(\tau) &= \frac{\kappa^2 C_1 g_0}{2}\frac{\sqrt{\pi}}{4\beta}\exp(-2u'^2_m\beta^2) \\ &\quad \times \left[I_0\left(2u'^2_m\beta^2\right)\left(1 + J_0(Du'_m)\right) + 2\sum_{n=1}^{\infty} I_n\left(2u'^2_m\beta^2\right)J_{2n}(Du'_m)\right] . \end{aligned} \tag{4.26}$$

This is the expression for the time-dependent part of the ACF for a periodic acoustic field. By considering typical magnitudes for β and u_m equation 4.26 may be simplified.

For example, for laser beams of unfocused e^{-2} width 0.5 mm focused down from 2 cm separation using a 10 cm focal length lens, β is approximately 6000. From figure 4.3 it can be seen that $e^{-p/2}I_0(p/2) \simeq 1$ and $e^{-p/2}I_n(p/2) \simeq 0$ for $n > 0$ [55]. Therefore, equation 4.26 reduces to

$$R(\tau) = \frac{\kappa^2 C_1 g_0}{2} \frac{\sqrt{\pi}}{4\beta} \left(1 + J_0\left[\frac{Du_m}{\pi f_m} \sin(\pi f_m \tau)\right]\right) . \tag{4.27}$$

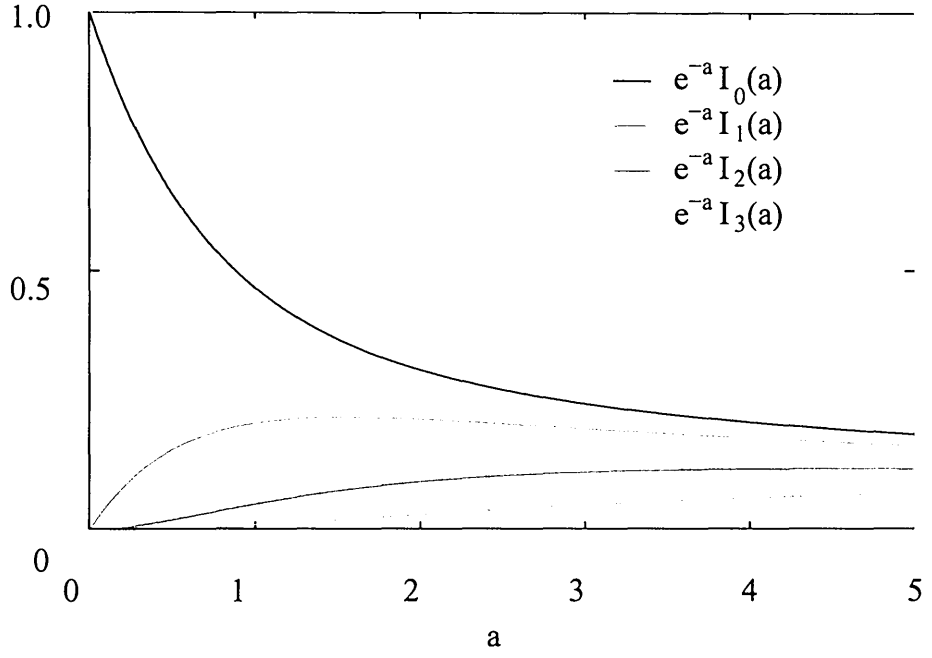

Figure 4.3: Plot of a against $e^{-a}I_n(a)$. Adapted from figure 3 of [55].

Normalizing the ACF gives

$$\tilde{R}(\tau) = \frac{1}{2}\left(1 + J_0\left[\frac{Du_m}{\pi f_m} \sin(\pi f_m \tau)\right]\right) . \tag{4.28}$$

Figure 4.4 shows the form of the ACF for an alternating velocity with particle dis-

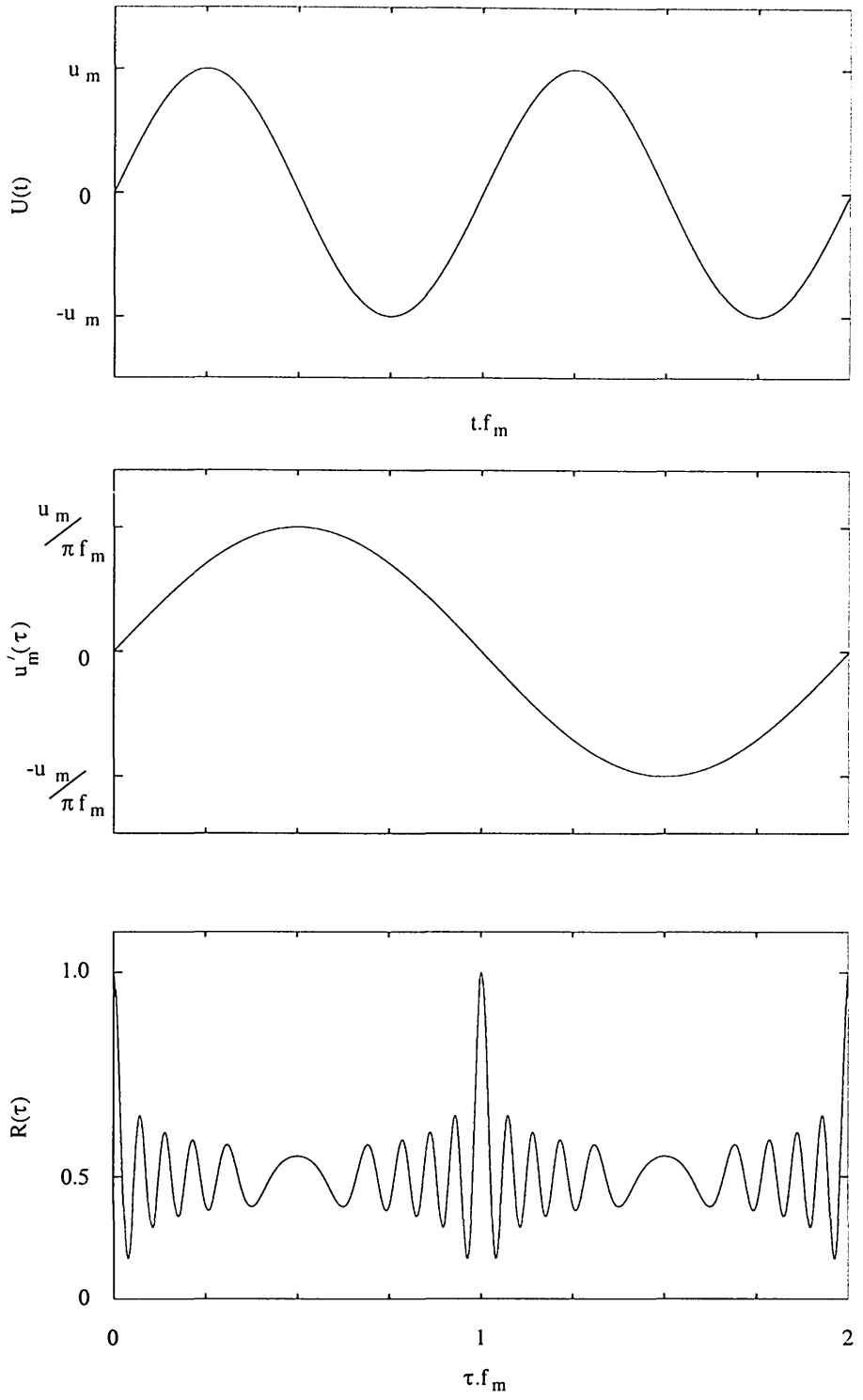

Figure 4.4: Normalized ACF simulated for an alternating velocity with particle displacement amplitude, $x_m = 1/4\beta$, and acoustic frequency, $f_m = 1$ kHz. Plots of $U(t)$ and $u'_m(\tau)$ are also displayed

placement amplitude, $x_m = 1/4\beta$, and acoustic frequency, $f_m = 1$ kHz. The acoustic particle velocity $U(t)$ and $u'_m(\tau)$ are also displayed. Equation 4.28 does not account for the Gaussian envelope on the fringe pattern. As a result there is no damping of the illustrated ACF. A more complete description of the time-dependent ACF generated by acoustic motion is therefore required.

4.3.3 Autocorrelation function due to a periodic flow

Consider the more general case of particle motion involving a mean flow in the x direction superimposed on the acoustic oscillation, also in the x direction. The instantaneous velocity of the particle is

$$U_p(t) = u_0 + u_m \sin(2\pi f_m t + \phi_m) \tag{4.29}$$

where u_0 is the mean flow velocity, u_m is the acoustic particle velocity amplitude, f_m is the acoustic frequency, and ϕ_m is a random phase.

As in the previous section, the derivation of the autocorrelation function requires the probability density function, $p_\eta(x;\tau)$, of the variable $\eta_p(\tau)$ to be determined. From equation 4.10 and equation 4.29,

$$\begin{aligned} \eta_p(\tau) &= u_0\tau + u_m \int_0^\tau \sin(2\pi f_m t + \phi_m)dt \\ &= u_0\tau + \frac{u_m}{\pi f_m}\Big[\sin(\pi f_m \tau)\sin(\pi f_m \tau + \phi_m)\Big] . \end{aligned} \tag{4.30}$$

Using the relationship for a function of random variables from [53], gives

$$\begin{aligned} p_\eta(x;\tau) &= \frac{1}{\pi\sqrt{u_m'^2-(x-u_0\tau)^2}} && -x+u_0\tau \le u_m' \le x-u_0\tau \\ &= 0 && \text{elsewhere} \end{aligned} \tag{4.31}$$

where u_m' is defined in equation 4.16. The time-independent pedestal term is ignored and following Hann and Greated [17], equation 4.5 is expressed as

$$R(\tau) = \frac{\kappa^2 C_1 g_0}{2}\frac{\sqrt{\pi}}{4\beta}\int_{u_0\tau-u_m'}^{u_0\tau+u_m'} \frac{\exp(-4\beta^2x^2)(1+\cos Dx)dx}{\pi\sqrt{u_m'^2-(x-u_0\tau)^2}}. \tag{4.32}$$

In Appendix B, the expression for the time-dependent part of the ACF is shown to be

$$\begin{aligned} R(\tau) = {} & \frac{\kappa^2 C_1 g_0}{2}\frac{\sqrt{\pi}}{4\beta}\exp(-4\beta^2u_0^2\tau^2)\exp(-2\beta^2u_m'^2) \\ & \Bigg\{\Big(1+\cos(Du_0\tau)J_0(Du_m')\Big) \\ & \times\Big[I_0(8\beta^2u_0\tau u_m')I_0(2\beta^2u_m'^2)+2\sum_{n=1}^{\infty}(-1)^nI_n(2\beta^2u_m'^2)I_{2n}(8\beta^2u_0\tau u_m')\Big] \\ & +I_0(2\beta^2u_m'^2)\cos(Du_0\tau)\Big(J_0\Big(u_m'\sqrt{D^2-\beta^4u_0^2\tau^2}\Big)-J_0(Du_m')\Big) \\ & +2\cos(Du_0\tau)\sum_{k=1}^{\infty}J_{2k}(Du_m')\sum_{m=1}^{\infty}I_m(2\beta^2u_m'^2)(-1)^{m-k}I_{2(n-k)}(8\beta^2u_0\tau u_m') \\ & +2\cos(Du_0\tau)\sum_{k=1}^{\infty}J_{2k}(Du_m')\sum_{m=1}^{\infty}I_m(2\beta^2u_m'^2)(-1)^{m+k}I_{2(n+k)}(8\beta^2u_0\tau u_m') \\ & -2\sin(Du_0\tau)\sum_{s=0}^{\infty}J_{2s+1}(Du_m')\sum_{r=1}^{\infty}J_r((2\beta^2u_m'^2)(-1)^{s+r}I_{2s+2r+1}(8\beta^2u_0\tau u_m') \\ & -2\sin(Du_0\tau)\sum_{s=0}^{\infty}J_{2s+1}(Du_m')\sum_{r=1}^{\infty}J_r((2\beta^2u_m'^2)(-1)^{s-r}I_{2s-2r+1}(8\beta^2u_0\tau u_m')\Bigg\}. \end{aligned} \tag{4.33}$$

If there is no acoustic field, i.e. $u_m = 0$, equation 4.33 reduces to equation 4.8. If there is zero mean flow, i.e. $u_0 = 0$, equation 4.33 reduces to equation 4.26.

For a combined flow, the expression may be simplified by considering a typical magnitude for β and noting the behaviour of $e^{-q}I_n(q)$ (see figure 4.3). Therefore, the normalised ACF is approximately

$$\tilde{R}(\tau) \simeq \frac{1}{2}\exp(-4\beta^2 u_0^2\tau^2) \left\{1 + \cos(Du_0\tau)J_0\left(u'_m\sqrt{D^2 - \beta^4 u_0^2\tau^2}\right)\right\}. \quad (4.34)$$

The conditions $u_0 = 0$, $u_0 = u_m/5$, and $u_0 = 5.u_m$ with $x_m = 1/4\beta$ and $f_m = 1$ kHz are illustrated in figure 4.5. With a mean flow superimposed onto the acoustic oscillation, the normalised ACF decays to zero which reflects the eventual transition of the particles across the probe volume.

4.3.4 Effect of frequency shifting

In section 3.4.4, the technique of frequency shifting was introduced as a method for resolving directional ambiguity and extending the dynamic range of the laser Doppler system. The frequency of one of the illuminating beams is shifted by F_s. This results in the movement of the interference fringes through the stationary probe volume with constant velocity, $F_s\Lambda$, in the x direction. The effect of frequency shifting on the autocorrelation function will now be examined.

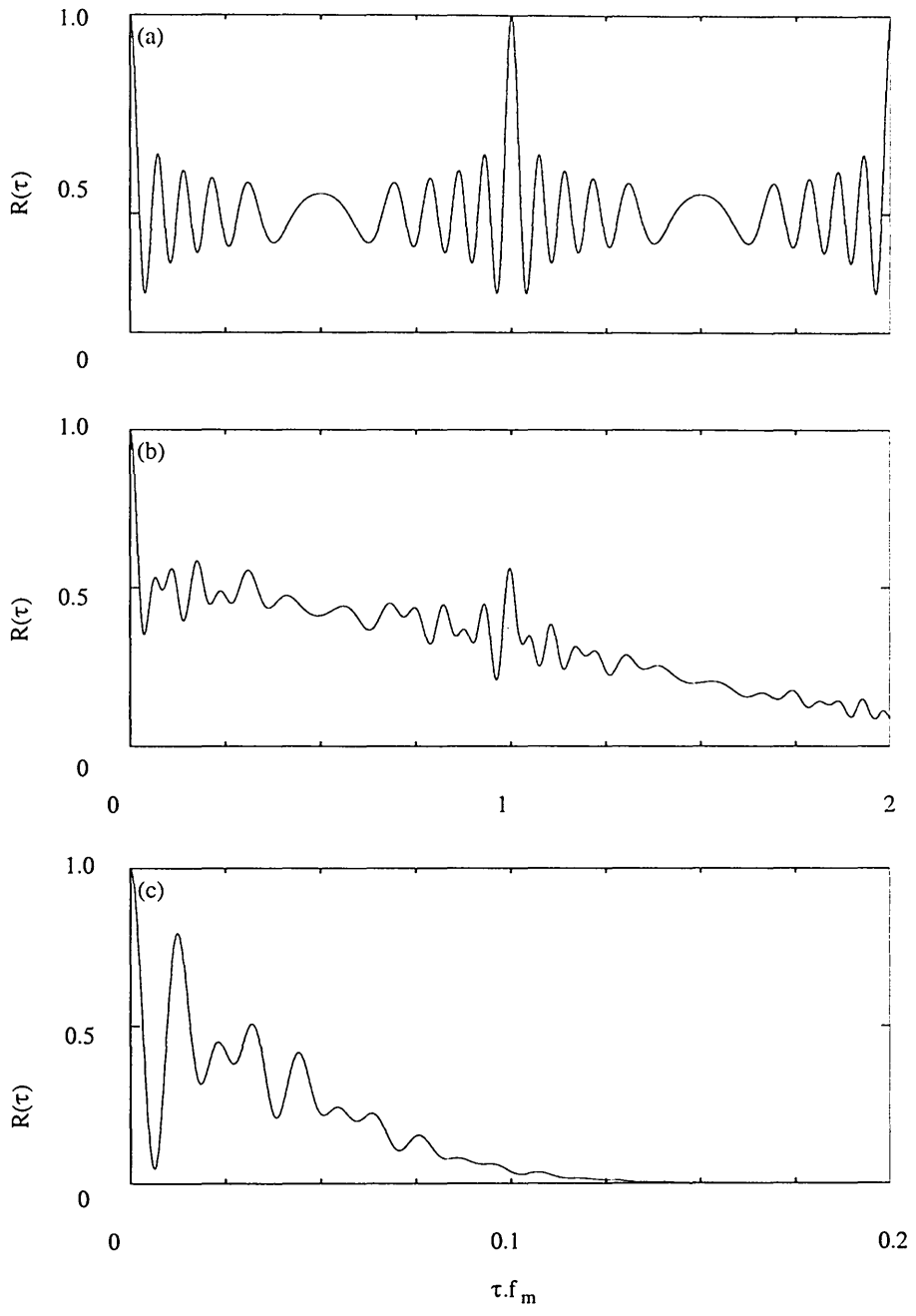

Figure 4.5: The ACF simulated for a periodic flow with displacement amplitude $x_m = 1/4\beta$ and acoustic frequency $f_m = 1$ kHz and (a) with a mean flow $u_0 = 0$, (b) $u_0 = u_m/5$, and (c) $u_0 = 5.u_m$.

Consider the mean flow situation where particles move with constant speed U parallel to the x axis. Equation 4.1 becomes

$$V(t) \simeq \kappa \mathcal{K} W(\beta \xi(t)) \Big(1 + \cos(2\pi F_s t + D\xi(t))\Big) \; . \tag{4.35}$$

The normalized ACF in equation 4.9 is rewritten as

$$\tilde{R}(\tau) = \frac{1}{2} \exp(-4\beta^2 U^2 \tau^2)(1 + \cos(2\pi F_s + DU)\tau) \; . \tag{4.36}$$

The ACF decays with R_W. The number of cycles in the ACF depends on the direction and magnitude of $F_s \Lambda$ relative to U.

Consider the general case of a mean flow in the x direction superimposed on an alternating velocity parallel to the x axis. The normalised ACF in equation 4.34 may be expressed as

$$\begin{aligned} \tilde{R}(\tau) \; &\simeq \; \frac{1}{2} \exp(-4\beta^2 u_0^2 \tau^2) \\ &\quad \left\{ 1 + \cos([2\pi F_s + D u_0]\tau) J_0\Big(u'_m \sqrt{D^2 - \beta^4 u_0^2 \tau^2}\Big) \right\} . \end{aligned} \tag{4.37}$$

The form of the ACF for $F_s = 2u_m/\Lambda$ applied to a combined periodic flow is illustrated in figure 4.6. The displacement amplitude, $x_m = 1/4\beta$, and the acoustic frequency, $f_m = 1$ kHz. The ACF was generated for the mean flow velocity conditions $u_0 = 0$, $u_0 = u_m/5$, and $u_0 = 5.u_m$. The frequency shift contributes to the position and

number of peaks in the ACF. The effect of the Gaussian envelope on the damping of the ACF and the decay time to zero remain the same as with $F_s = 0$. If u_m is small compared to $F_s\Lambda$, the contribution of the acoustic motion to the ACF becomes masked by the sinusoidal contribution due to the frequency shift.

4.4 Analysis of the correlation function

The form of the autocorrelation function of the photomultiplier signal has been established for the mean flow, the alternating velocity, and the combined velocity conditions. This section is concerned with the time domain analysis of the ACF for the extraction of velocity information. For the steady mean flow condition, the periodicity of the ACF allows the calculation of velocity. Interaction of the $J_0()$ term and the cosine term in equation 4.34 produces beats in the autocorrelation function. From a knowledge of the zeros and peaks of the zero order Bessel function, the acoustic particle velocity and the superimposed mean flow velocity may be determined.

The Fourier transform of the autocorrelation function yields the power spectral Density of the photomultiplier signal. In practice, the measured ACF is determined over a finite time interval, T. The ACF is multiplied by a window function, $h(\tau)$, before the Fourier transform operation to prevent leakage. Generating the PSD provides a method for measuring the power in the photomultiplier signal, which is useful for calculating the signal-to-noise ratio.

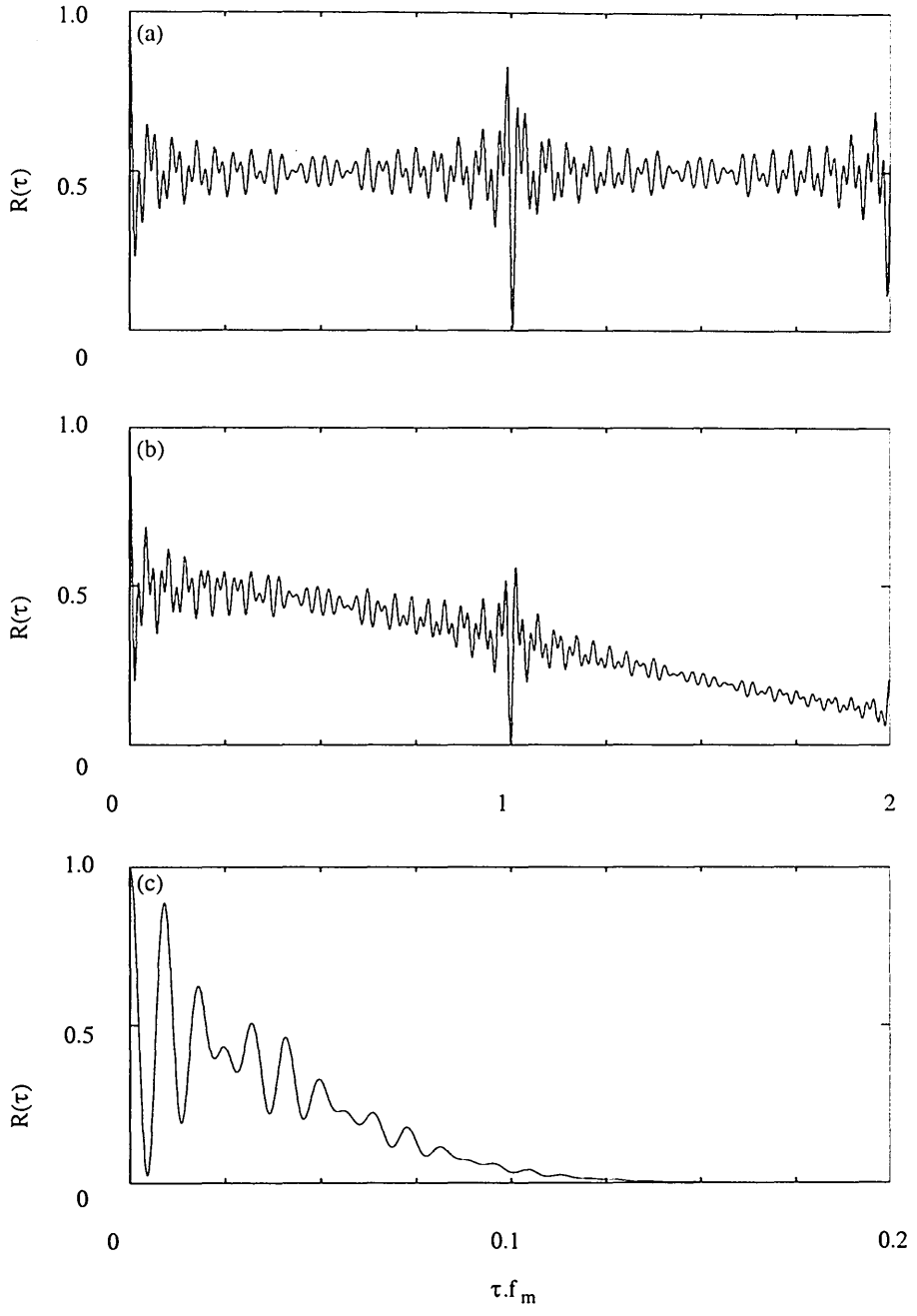

Figure 4.6: The ACF simulated for a periodic flow with displacement amplitude, $x_m = 1/4\beta$, and acoustic frequency, $f_m = 1$ kHz and (a) with a mean flow $u_0 = 0$, (b) $u_0 = u_m/5$, and (c) $u_0 = 5.u_m$. A frequency shift $F_s = 2u_m/\Lambda$ was applied.

4.4.1 Constant flow velocity

Consider the form of equation 4.34 for a mean flow with no acoustic oscillation where particles move parallel to the x axis with constant speed u_0 and $F_s = 0$. From the peaks of the ACF

$$u_0 = \frac{2m\pi}{D\tau_m} = \frac{m\Lambda}{\tau_m} \qquad m = 1, 2, 3 \ldots \tag{4.38}$$

where Λ is the fringe spacing, m is the number of the peak from zero lag time, and τ_m is the lag time to the peak. If $F_s \neq 0$, equation 4.38 becomes

$$u_0 = m\Lambda \left(\frac{1}{\tau_m} - F_s \right) \quad m = 1, 2, 3 \ldots \tag{4.39}$$

Similar equations can be constructed involving the minimum turning points of the autocorrelation function.

The PSD may also be used to determine u_0 due to the periodic nature of the ACF. In practice, the ACF is multiplied by the window function, $h(\tau)$. The Fourier transform of the ACF in figure 4.2 is shown in figure 4.7. The PSD contains a Gaussian peak centred on $F = 0$ (due to the pedestal) and a Gaussian peak centred on $F = u_0/\Lambda$.

The peaks have standard deviation $\sigma^2 = \sigma_F^2 + \sigma_W^2$ where

$$\sigma_F = \frac{\sqrt{2} u_0 \beta}{\pi} \tag{4.40}$$

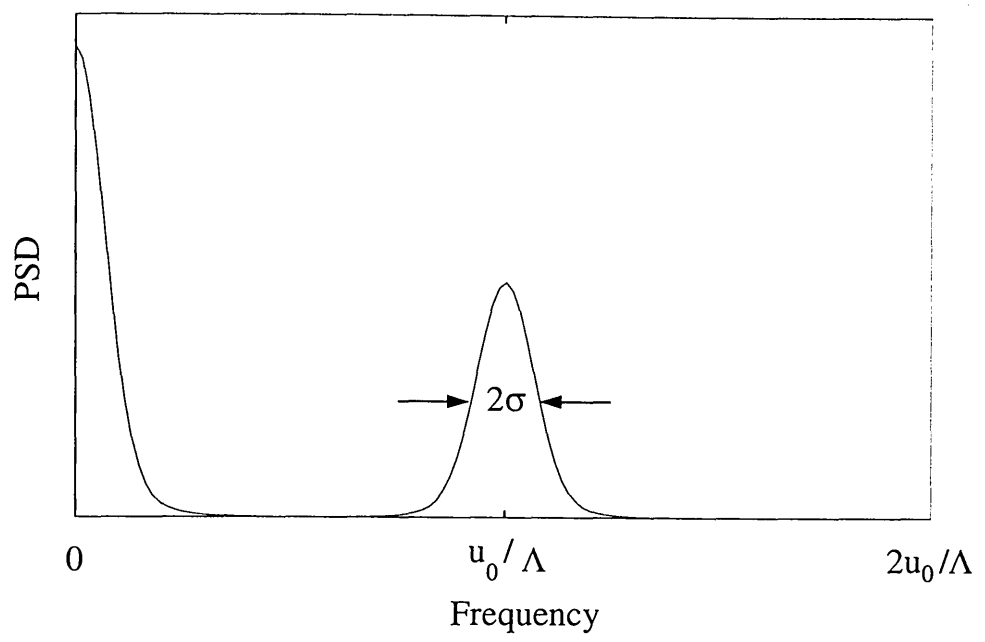

Figure 4.7: The power spectral density for particles moving with constant speed U and $F_s = 0$.

is the standard deviation due to the transit time and

$$\sigma_W = \frac{2}{\pi T} \tag{4.41}$$

is the standard deviation due to the window function. β is defined in equation 3.19 and T is the finite time interval over which the ACF is calculated.

For a more detailed discussion of deducing the form of the frequency spectrum and the PSD as well as additional sources of spectral broadening see section 3.5. Calculating particle velocity by generating the PSD is a practical method for only the constant mean flow condition as the ACF has a simple periodic form.

4.4.2 Alternating velocity

The ACF for the alternating velocity condition, with $u_0 = 0$ and $F_s = 0$, is displayed in figure 4.5 (b). The ACF repeats for $\pi f_m \tau = \pi$ as $J_0(\ )$ is an even function. The first minimum of the zero order Bessel function occurs at 3.832 and the first maximum at 7.016 [56]. Using equation 4.34,

$$u_m = \frac{3.832 \Lambda f_m}{2 \sin(\pi f_m \tau_m)} \tag{4.42}$$

where τ_m is the lag time to the first minimum of the ACF. A similar equation may be constructed involving the first peak of the ACF.

To see the first minimum, τ_m must occur before the first half period of the sinusoidal argument of the Bessel function. From equation 4.42,

$$\frac{u_m}{f_m} > \frac{3.832 \Lambda}{2} . \tag{4.43}$$

The lower limit to the acoustic particle velocity amplitude that can be measured is proportional to the fringe spacing. The fringe spacing may be decreased by increasing the beam intersection angle or decreasing the wavelength of the laser light.

Figure 4.8 shows the section of the ACF containing the first minimum for both $F_s = 0$ and $F_s = 2u_m/\Lambda$. With a frequency shift, the shape of the ACF is more complex due to the interaction of the $\cos([2\pi F_s + D u_0]\tau)$ term with the $J_0(\ )$ term in

equation 4.37. The first minimum of the Bessel function is masked by the sinusoidal contribution to the ACF arising from the frequency shift and so calculating the particle velocity amplitude is more complicated than with $F_s = 0$. Generating the PSD from the ACF is not a practical method for determining particle velocity as the form of the Fourier transform is not easily deduced.

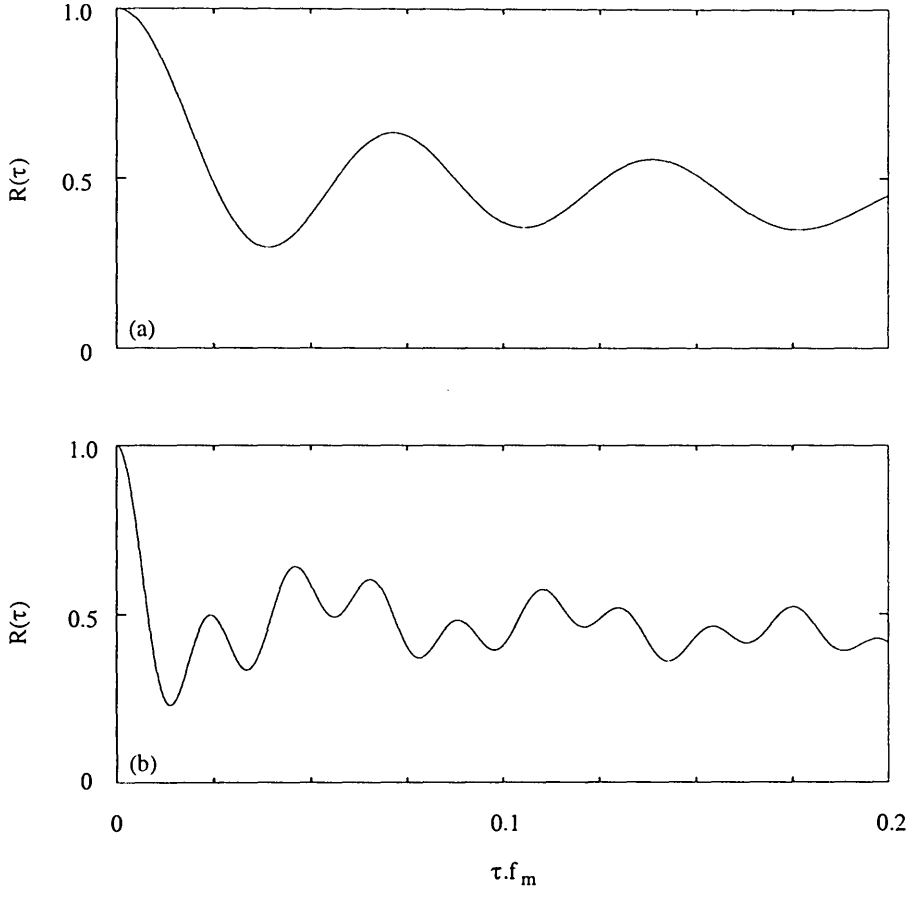

Figure 4.8: The first minimum of the ACF for an alternating velocity with $x_m = 1/4\beta$, $u_0 = 0$, and (a) with $F_s = 0$, (b) with $F_s = 2u_m/\Lambda$.

4.4.3 Periodic flow

Equation 4.34 gives the ACF for a mean flow superimposed onto an alternating velocity, with $F_s = 0$. The values of u_0 and u_m may be determined from the positions of the peaks and minima in the ACF [17]. It is necessary to know which of the two velocities is larger. If the flow velocity is larger, the decay of the ACF to zero is quick and equation 4.38 and the lag time to the first peak are used to determine u_0. If the acoustic velocity is larger, the decay to zero is long and equation 4.42 and the lag time to the first zero are used to find u_m. Having measured one of the two velocities, the theoretical expression in equation 4.34 can be calculated for different values of u_0 or u_m until the best possible match with the measured ACF is achieved.

The introduction of a frequency shift generates a more complex ACF due to the interaction of the $\cos([2\pi F_s + Du_0]\tau)$ term with the $J_0(\ )$ term in equation 4.37. The peaks and minima of the Bessel function are masked by the sinusoidal contribution to the ACF arising from the frequency shift, making the calculation of velocity less straightforward. Generating the PSD of the Doppler signal is not a practical method for deducing velocity because of the complicated nature of the ACF.

4.5 Limitations of digital correlation

In practice, a digital correlator is used to calculate the autocorrelation function of the photomultiplier signal. The number of pulses occurring in n consecutive time intervals

are observed. Each value of n corresponds to a different channel in the digital correlator and each time interval is $\Delta\tau$ seconds long. The sample time of the correlator is therefore $\Delta\tau$ and the upper limit of frequency that can be represented by the samples without aliasing is $1/2\Delta\tau$ (i.e. the Nyquist frequency). Aliasing results in a distortion of the ACF but can be prevented by only measuring velocities below a suitable limit.

The measured ACF is a discrete function of $n\Delta\tau$ instead of a continuous function of the delay time, τ. Equation 4.34 is expressed as

$$\begin{aligned}\tilde{R}(n\Delta\tau) \simeq & \frac{1}{2}\exp(-4\beta^2 u_0^2[n\Delta\tau]^2) \\ & \left\{1+\cos(Du_0 n\Delta\tau)J_0\left(u'_m\sqrt{D^2-\beta^4 u_0^2[n\Delta\tau]^2}\right)\right\} \end{aligned} \quad (4.44)$$

for the normalised autocorrelation function generated by the digital correlator.

For the constant velocity condition and zero acoustic particle velocity, the ACF was established as having a damped cosine form. The upper limit to the velocity that can be measured depends on the maximum frequency of the ACF that can be represented. This in turn depends on the sample time and implies

$$u_0 < \frac{\Lambda}{2\Delta\tau}\,. \quad (4.45)$$

For the alternating velocity condition and zero mean flow velocity, the first minimum of the Bessel function must occur after the first sample interval and within the

total sample time for any measurement to be made. This implies $\Delta\tau < \tau_m < n\Delta\tau$ where τ_m is the lag time to the minimum. By noting that

$$\sin(\pi f_m \tau_m) \simeq \pi f_m \tau_m \tag{4.46}$$

the theoretical limits to the acoustic particle velocity amplitude that can be measured are

$$\frac{3.832\Lambda}{2\pi n\Delta\tau} < u_m < \frac{3.832\Lambda}{2\pi\Delta\tau} . \tag{4.47}$$

There is also a lower limit to the measurement of velocity amplitude, expressed in equation 4.43, which depends on acoustic frequency and the fringe spacing.

4.6 Summary

The principle of the photon correlation method of LDA was introduced. The photomultiplier signal consists of a series of discrete pulses which can be correlated with itself to generate the autocorrelation function. For a constant flow velocity, the correlation function is periodic and decays with the ACF of the spatial weighting function. For an acoustic oscillation, the ACF can be generated using a zero order Bessel function. Considering a periodic flow, i.e. a mean flow superimposed onto an acoustic oscillation, enabled the effect of the Gaussian envelope of the fringe pattern on the form of the ACF to be determined. The introduction of a frequency shift was found to mask the contribution to the ACF arising from the acoustic oscillation.

The Fourier transform of the autocorrelation function generates the power spectral density of the Doppler signal but analysing the ACF in the time domain allows velocity information to be calculated. For a constant flow, the peaks and minima of the ACF are used to determine the velocity. The PSD contains a Gaussian peak centred at the Doppler frequency. For an alternating velocity, the peaks and minima of the ACF are determined by the zero order Bessel function. A measure of the appropriate lag time allows the acoustic particle velocity amplitude to be deduced. A mean flow superimposed onto an acoustic oscillation generates a more complex ACF. From inspection of the ACF, the flow and acoustic velocity may be determined.

Finally, the use of a digital correlator and the resulting limitations to velocity measurements were considered.

Chapter 5

Experimental Apparatus

5.1 Introduction

The experimental apparatus used in the present study is introduced in this chapter. In section 5.2, the operational characteristics of the probe microphone are outlined. The generation of a standing wave inside a tube is explained in section 5.3 along with the relationship between acoustic pressure and particle velocity. In section 5.4, the calculation of the characteristic acoustic impedance from measurements of the environmental conditions is established. The two LDA systems are described in section 5.6. Finally, the characteristics of the two types of seeding used here are considered in section 5.7.

Several preliminary measurements are presented including the frequency response of the probe microphone and a study of pressure amplitude in a standing wave.

5.2 Probe microphone

Pressure measurements were made using a probe attachment from the Brüel and Kjær UA0040 probe microphone kit. The probe tube has a length of 240 mm and an inside diameter of 2.5 mm. The probe attachment was fixed to a Brüel and Kjær type 4133 half inch microphone cartridge and a type 2669 preamplifier. The preamplifier was connected to a type 2690 NEXUS conditioning amplifier. A probe microphone allows measurements to be made in confined spaces that are inaccessible to standard microphones. However, the probe distorts the frequency response of the microphone and so calibration is required before the probe microphone signal can be transformed into measurements of pressure amplitude (in pascals) and pressure phase.

5.2.1 Experimental method

The effects of the probe tube may be characterized relative to the response of a similar microphone using a standard technique [57]. Figure 5.1 shows the apparatus used in this calibration process. The coupler contains an ear piece which acts as a sound source and a second half inch microphone which acts as the reference microphone. The probe microphone was connected to channel 1 of the conditioning amplifier and the reference microphone to channel 2. The frequency response of the probe microphone was measured at 5 Hz intervals from 50 Hz to 2 kHz. A sine wave signal was supplied to the sound source inside the coupling device by the PC via an amplifier and the

frequency of the signal was stepped up under the control of software developed by Cullen [40]. The two output voltage signals from the conditioning amplifier were sampled simultaneously by a Wavebook 512 A/D converter connected to the PC.

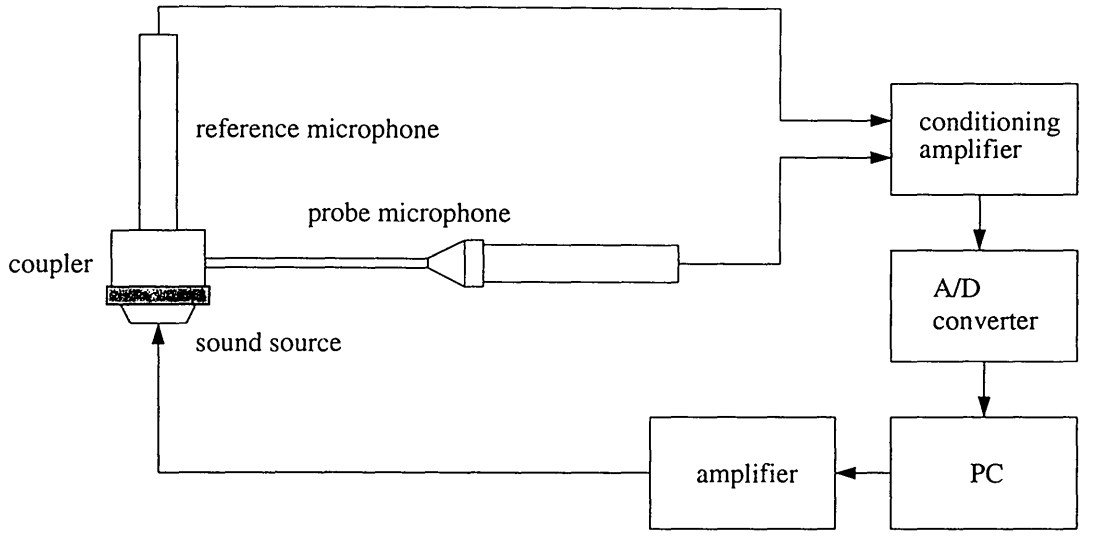

Figure 5.1: Probe microphone characterization system.

A Brüel and Kjær type 4192 half inch microphone cartridge and a type 2669 preamplifier were used to form a complete reference microphone. A second microphone system, supplied by NPL, was also used as a reference. The NPL system consisted of a Brüel and Kjær type 4133 cartridge, a G.R.A.S. type 26AG preamplifier, and a type E711 power unit (constructed at NPL). The sensitivity level of the system, obtained by reciprocity calibration at NPL, was -38.00 ± 0.03 dB referenced to 1 VPa^{-1}. This corresponds to a pressure sensitivity of $M_p = 12.59 \pm 0.04$ mVPa^{-1}. The output voltage signal was sampled directly from the power unit when the NPL system was used as the reference microphone.

The type 4133 microphone cartridge is a free field response type cartridge whereas the type 4134 and the type 4192 microphone cartridges are pressure field response types. The probe attachment is intended for use with a pressure field response type cartridge. However, over the frequency range of interest the characteristics of the type 4133 cartridge are nearly identical to that of the type 4134 (and 4192) cartridge for 0° incidence [58]. Using a free field response type cartridge for the probe microphone or the reference microphone will have no significant effects on the measurements over the frequency range considered. Above 2 kHz, the characteristics of the pressure response and free field response cartridges begin to differ slightly which will affect any measurements made.

The frequency response of the probe microphone is calculated from the two microphone signals. At each frequency interval the magnitude response of the probe microphone relative to the reference microphone is calculated as

$$R_p = 20 \log_{10} \left(\frac{V_p}{V_r} \right) . \tag{5.1}$$

V_p is the root mean square (RMS) amplitude of the output voltage signal from channel 1. V_r is the RMS amplitude of the output voltage signal from channel 2 or from the NPL system, depending on which reference microphone was used. Both channels of the conditioning amplifier were set to a scale of 1 VPa^{-1}.

The Brüel and Kjær half inch microphones are reversed biased [24]. Therefore, the phase of the pressure measured by the reference microphone is equal to π sub-

tracted from the phase of the microphone signal, α_r. The phase response of the probe microphone is $\alpha_p - \alpha_r + \pi$ where α_p is the phase of the probe microphone signal.

5.2.2 Results

Figure 5.2 shows the frequency response of the probe microphone measured relative to the reference microphone consisting of the type 4192 half inch cartridge and preamplifier. The frequency response magnitude curve contains three maxima in the range from 50 Hz to 2 kHz. If λ_m denotes the acoustic wavelength, these maxima occur when $\lambda_m/4$, $3\lambda_m/4$, and $5\lambda_m/4$ are only slightly greater than the length of the probe tube [57]. This is similar to the pressure response that would be measured at the closed end of a cylindrical tube if the opposite end was open. The frequency response information illustrated in figure 5.2 was used to convert the probe microphone voltage signal into measurements of pressure amplitude and pressure phase.

5.3 Standing wave tube

In the present study, a standing wave was generated inside an air filled glass tube sealed to a loudspeaker. The end of the tube was terminated with a piece of perspex containing a small hole through which the probe microphone could be inserted. This allowed measurements of pressure amplitude to be made at the end of the tube as well as at various positions inside. The combined system is illustrated in figure 5.3

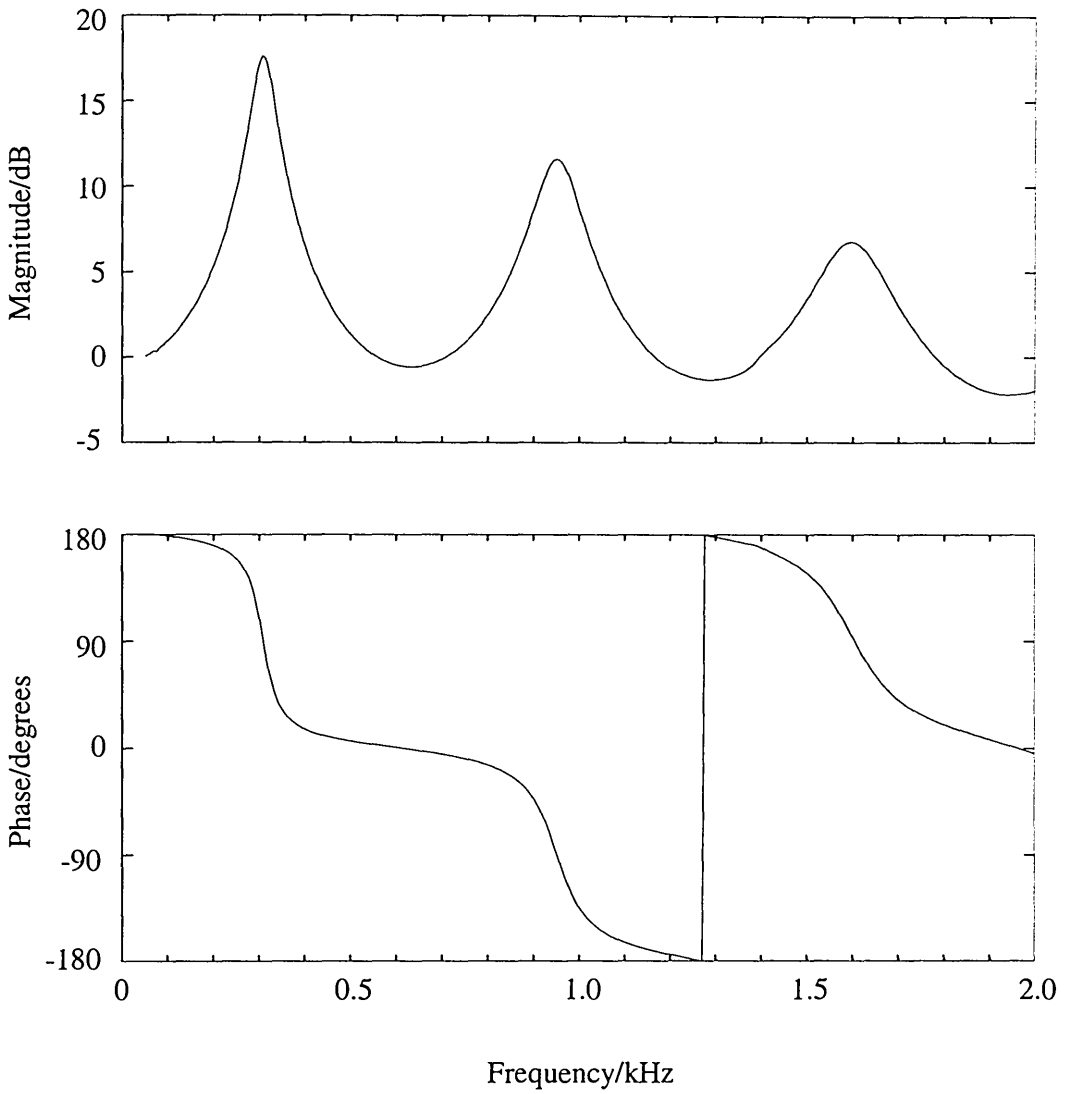

Figure 5.2: Measured frequency response of the probe microphone.

where the tube of length L is driven at $x = L$ and rigidly terminated at $x = 0$. The loudspeaker diaphragm is represented as a piston of mass m which is supported by a suspension with stiffness s and damping R_m and driven by an applied force f [59]. When a force is applied to the driver-tube system the mechanical resonances of the combined system involve the mechanical behaviour of the driver as well as that of the rigidly terminated tube [60].

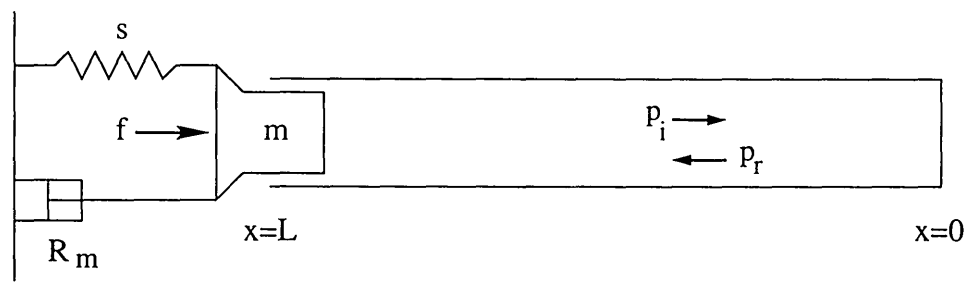

Figure 5.3: Combined driver-tube system.

The relationship between particle velocity and acoustic pressure in a standing wave may be established by considering the interaction of plane waves inside the tube. From a direct measurement of particle velocity using LDA, the acoustic pressure at a point in the tube can be determined and compared to a measurement made with the probe microphone. Calibrating a microphone requires the measurement of sensitivity, i.e. the output voltage for a given sound pressure. The output voltage from the probe microphone, the measured frequency response of the probe microphone relative to the reference microphone, and the acoustic pressure derived from LDA can be used in the calibration of the reference microphone.

5.3.1 Standing wave pattern

The phase interference between the transmitted and reflected waves in a terminated tube results in the formation of a standing wave pattern [60]. The sinusoidal vibration of the loudspeaker diaphragm produces a plane wave propagating towards the rigid termination. Neglecting propagation losses along the tube, the plane wave has the form

$$p_i = Ae^{j(\omega t + kx)} \tag{5.2}$$

with amplitude A, angular frequency ω, and wavenumber k. To simplify the analysis, the phase of the wave is chosen to be zero so that the amplitude can be represented by a real number. The wave reflected by the termination suffers a small phase change, θ, and a degradation in amplitude giving

$$p_r = Be^{j(\omega t - kx + \theta)} \tag{5.3}$$

where B is the new (real) amplitude.

Consider the effect of the interaction of the incident and reflected wave. At a point x, the total pressure will be

$$\begin{aligned} p(x,t) &= p_i + p_r \\ &= e^{j(\omega t + \theta/2)}\left[Ae^{j(kx-\theta/2)} + Be^{-j(kx-\theta/2)}\right] \\ &= e^{j(\omega t + \theta/2)}\left[(A+B)\cos(kx-\theta/2) + j(A-B)\sin(kx-\theta/2)\right] \end{aligned}$$

$$= (A+B)e^{j(\omega t+\theta/2)}\left[\cos(kx-\theta/2)+\frac{j}{SWR}\sin(kx-\theta/2)\right] \quad (5.4)$$

where the standing wave ratio (SWR) is

$$\text{SWR} = \frac{A+B}{A-B}\,. \quad (5.5)$$

From equation 5.4, the pressure amplitude is

$$|p(x)| = (A+B)\sqrt{\cos^2(kx-\theta/2)+\frac{1}{SWR^2}\sin^2(kx-\theta/2)}\,. \quad (5.6)$$

The SWR is the ratio of the amplitude at a pressure antinode to the amplitude at a pressure node. The pressure nodes are located at

$$kx_n - \theta/2 = \left(n-\frac{1}{2}\right)\pi \qquad n = 1,2,3,\ldots \quad (5.7)$$

Therefore, the phase change, θ, may be calculated from the distance of the first node from the termination, x_1. Using equation 5.7, this is expressed as

$$\theta = 2kx_1 - \pi\,. \quad (5.8)$$

The ratio of the acoustic pressure to the associated particle velocity is called the specific acoustic impedance. For the plane wave travelling towards the termination this ratio is ρc, where ρ is the density of air and c is the speed of sound in air, and is

called the characteristic acoustic impedance [60]. The corresponding acoustic particle velocity is $p_i/\rho c$. For the reflected plane wave, the ratio is $-\rho c$ and the acoustic particle velocity is $-p_r/\rho c$. The velocity at a point x in the standing wave is given by

$$\begin{aligned} u(x,t) &= \frac{1}{\rho c}(p_i - p_r) \\ &= \frac{(A+B)}{\rho c} e^{j(\omega t+\theta/2)} \left[\frac{1}{SWR} \cos(kx - \theta/2) + j \sin(kx - \theta/2) \right] . \end{aligned} \tag{5.9}$$

The rigid termination of the tube implies the position of a pressure antinode. The probe microphone was used to monitor the pressure at this point for several experiments. At $x = 0$, equation 5.4 may be expressed as

$$\begin{aligned} p(0,t) &= (A+B)e^{j(\omega t+\theta/2)} \left[\cos(\theta/2) - \frac{j}{SWR} \sin(\theta/2) \right] \\ &\simeq (A+B)e^{j(\omega t+\theta/2)} \end{aligned} \tag{5.10}$$

because the phase change, θ, is very small. The ratio of the acoustic particle velocity at x to the pressure at $x = 0$ is given by

$$\frac{u(x)}{p(0)} = \frac{1}{\rho c} \left[\frac{1}{SWR} \cos(kx - \theta/2) + j \sin(kx - \theta/2) \right] . \tag{5.11}$$

The magnitude of the ratio in equation 5.11 is

$$\left|\frac{u(x)}{p(0)}\right| = \frac{1}{\rho c}\sqrt{\frac{1}{SWR^2}\cos^2(kx-\theta/2)+\sin^2(kx-\theta/2)} \tag{5.12}$$

and the phase lead of the velocity at x relative to the pressure at $x = 0$ is

$$\angle u(x) - \angle p(0) = \tan^{-1}\left(\frac{\sin(kx-\theta/2)}{\cos(kx-\theta/2)}\right) . \tag{5.13}$$

From equation 5.12 and equation 5.13, at pressure nodes

$$\left|\frac{u(x_n)}{p(0)}\right| = \frac{1}{\rho c} \qquad n = 1,2,3\ldots \tag{5.14}$$

and

$$\begin{aligned} \angle u(x_n) - \angle p(0) &= +\pi/2 \qquad n \text{ is even} \\ &= -\pi/2 \qquad n \text{ is odd.} \end{aligned} \tag{5.15}$$

The velocity is $\pi/2$ out of phase with the pressure. The position of a pressure antinode at $x = 0$ is the position of a velocity node and the position of a pressure node at $x_1 = \lambda_m/4$ is the position of a velocity antinode, where λ_m is the acoustic wavelength. From the measurement of the particle velocity amplitude at x_1 and a knowledge of the characteristic acoustic impedance of the air inside the tube, the pressure amplitude at the end can be determined. The calculation of the characteristic acoustic impedance,

ρc, is discussed in section 5.4.

Preliminary measurements were performed with the probe microphone inside the glass tube attached to a loudspeaker. The tube has a length of 748 mm, an internal diameter of 32 mm, and a wall thickness of 2 mm. The internal diameter of the tube limits the acoustic frequencies for which plane wave propagation can be assumed [59]. For frequencies in the range 15×10^{-3} Hz $< f_m <$ 6 kHz, the expressions derived for standing wave generation may be used. Below the lower frequency limit, boundary layer effects controlled by viscosity dominate inside the tube. Above the upper frequency limit, higher modes of propagation have to be considered.

Propagation losses along the tube, resulting from absorptive processes within the fluid and at the tube walls, were neglected in the standing wave analysis. To consider these processes, k is replaced with the complex propagation constant $\mathrm{k} = k - j\alpha$ where α is called the absorption coefficient [60]. The absorption coefficient depends on the acoustic frequency, the diameter of the tube, and the properties of the fluid inside the tube. For the air-filled glass tube and $f_m <$ 6 kHz, the absorption taking place within the body of the fluid is very small and can be ignored. The wall effects dominate but the viscous and heat conducting losses at the walls are also negligible in this situation.

5.4 Characteristic acoustic impedance

To derive acoustic pressure from particle velocity measurements it is necessary to establish expressions for the density of air, ρ, and the speed of sound in air, c. For plane wave propagation, ρc is called the characteristic acoustic impedance. Both ρ and c are calculated independently as functions of the environmental conditions: air temperature t, atmospheric pressure P, and relative humidity h. The effects that variations in the environmental conditions and fluctuations in the carbon dioxide concentration have on the characteristic acoustic impedance are investigated.

5.4.1 Density of air

The density of air is calculated by Davis [61], such that

$$\rho = \frac{PM_a}{ZRT}\left[1 - X_v\left(1 - \frac{M_v}{M_a}\right)\right] \tag{5.16}$$

where P is the atmospheric pressure, T is the thermodynamic temperature, X_v is the mole fraction of water vapour, M_a is the molar mass of dry air, M_v is the molar mass of water vapour (18.015×10^{-3} kg mol^{-1}), R is the molar gas constant, and Z is the compressibility factor for moist air. The molar mass of dry air is calculated from the molar masses of its constituent gases. It is assumed constant except for local variations in the mole fraction of carbon dioxide, X_{CO_2}. The mole fraction of water vapour is

calculated by Giacomo [62], such that

$$X_v = \frac{hfp_{sv}}{P} \tag{5.17}$$

where h is the relative humidity expressed as a fraction, f is called the enhancement factor, and p_{sv} is the saturation vapour pressure of water vapour in air. The saturation vapour pressure is a function of temperature while the enhancement factor is a correction factor introduced to account for the behaviour of moist air as it does not act as a perfect gas [62]. Giacomo calculated f as a function of pressure and temperature and generated a table of values of Z for a range of environmental conditions.

The expression for the density of air in equation 5.16 is valid over the temperature range 0 °C to 30 °C and for the pressure range 60 kPa to 110 kPa. The uncertainty associated with the calculation of ρ is 0.025 % [63].

5.4.2 Speed of sound in air

The speed of sound calculation developed by Cramer [64] uses a real gas equation of state and standard thermodynamic relationships to give

$$c^2 = \gamma \frac{RT}{M}\left(1 + \frac{2PB}{RT}\right) \tag{5.18}$$

where γ is the specific heat ratio, R is the molar gas constant, T is the thermodynamic temperature, M is the molar mass of air (mixed with water vapour), P is the atmospheric pressure, and B is the second virial coefficient of state. Cramer calculates B from the mole fraction of dry air, X_a, and the mole fraction of water vapour, X_v. The mole fraction of water vapour is obtained from the relative humidity using equation 5.17. The specific heat ratio and speed of sound are determined as functions of temperature, pressure, relative humidity, and CO_2 concentration.

The expression for the speed of sound in equation 5.18 is valid over the temperature range 0 °C to 30 °C, the pressure range 75 kPa to 102 kPa, and for CO_2 concentrations up to 1%. The uncertainty associated with the calculation of c is 0.5 % [63].

5.4.3 Sensitivity analysis

A computer program based on equations 5.16, 5.17, and 5.18 was written to calculate air density and speed of sound in air as functions of temperature, atmospheric pressure, relative humidity, and CO_2 concentration. A sensitivity analysis was conducted to determine the effects that variations in the environmental conditions and fluctuations in the CO_2 concentration have on ρ and c. The results are shown in figure 5.4 for t = 0 °C, 10 °C, and 20 °C. For each case the invariant parameters have been held at P = 101.325 kPa, h = 0 %, and X_{CO_2} = 0.0004. These are called the standard conditions.

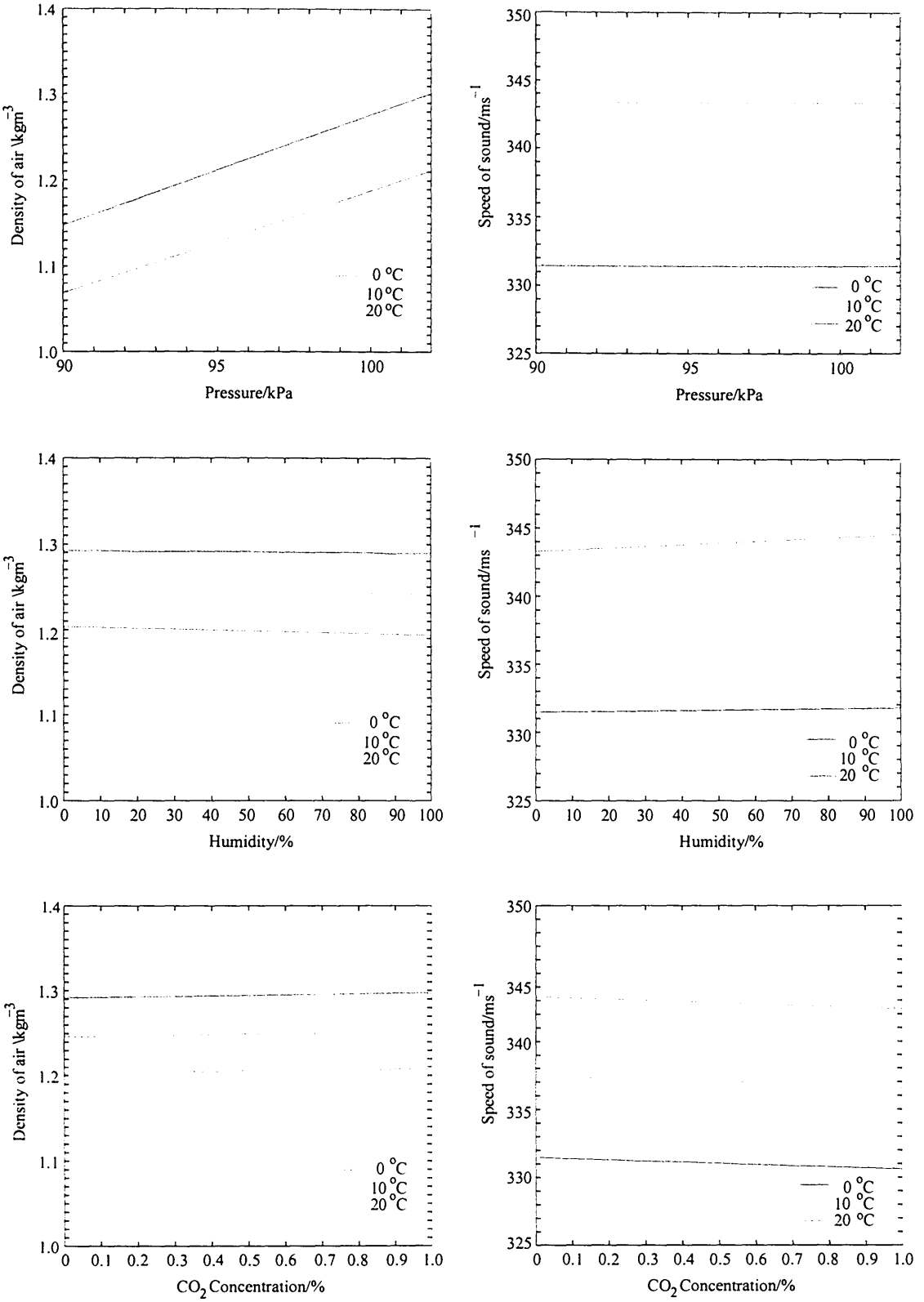

Figure 5.4: Calculation of ρ and c. For each graph the other variables have been held at $P = 101325$ Pa, $h = 0$ %, and $X_{CO_2} = 0.0004$.

The air density diminishes and the speed of sound increases with a rise in temperature. An increase in temperature of 0.1 °C decreases the characteristic impedance by approximately 0.005 dB. An increase in temperature of 1 °C decreases the characteristic impedance by approximately 0.01 dB. Changes in temperature of ± 10 °C and ± 20 °C result in changes to the characteristic impedance of approximately ± 0.15 dB and ± 0.30 dB, respectively. It appears from figure 5.4 that atmospheric pressure has no effect on the speed of sound but in fact there is a slight positive slope. Air density also increases with a rise in atmospheric pressure. An increase of 1 mb (i.e. 100 Pa) increases the characteristic impedance by approximately 0.01 dB. A change of ± 5 mb results in a change to ρc of approximately ± 0.05 dB. A rise in the relative humidity results in a decrease to the density and an increase in the speed of sound. An increase in relative humidity of 1 % has very little effect on the characteristic impedance, an increase of less than 0.001 dB. A change of ± 5 % results in a change to ρc of less than ± 0.0015 dB. The air density increases and the speed of sound diminishes with a rise in CO_2 concentration. An increase in CO_2 concentration of 0.1 % has a very small effect on the characteristic impedance, a decrease of less than 0.001 dB. A change of ± 0.5 % results in a change to ρc of approximately ± 0.0015 dB.

In the experimental study, the temperature inside the tube was measured with a probe thermometer to the nearest ± 0.1 °C. In Appendix C, the standard deviation of such a measurement is shown to be $\sigma_t = 0.1/\sqrt{3}$ °C. The atmospheric pressure and relative humidity in the laboratory were measured using an electronic barometer to the nearest ± 1 mb and ± 1 %, respectively. The standard deviations in the measurements

of P and h are therefore $\sigma_P = 1/\sqrt{3}$ mb and $\sigma_h = 1/\sqrt{3}$ %, respectively. The concentration of carbon dioxide was not recorded during the study. However, from the sensitivity analysis it was observed that fluctuations in the CO_2 concentration have very little effect on the characteristic impedance. So in the calculation of ρ and c, CO_2 concentration was kept constant and equal to the standard condition of $X_{CO_2} = 0.0004$.

5.5 Pressure measurements

Pressure measurements were performed using the probe microphone described in section 5.2 which has the measured frequency response displayed in figure 5.2. The antinodal pressure amplitude at the end of the tube as a function of acoustic frequency is examined. Also studied is the standing wave pressure amplitude as a function of displacement from the rigid end. The results of the preliminary pressure measurements are discussed in relation to the standing wave analysis in section 5.3.

5.5.1 Antinodal pressure

The rigid termination of the glass tube contained a small hole through which the probe microphone could be inserted. With the probe microphone fixed in position at the end of the tube, the frequency of the acoustic field generated by the loudspeaker was stepped up in intervals of 5 Hz from 50 Hz to 2 kHz under the control of the same software used for the probe microphone calibration. The resulting output signal from

the conditioning amplifier was sampled using the Wavebook A/D converter. The measured frequency response of the probe microphone allows the adjustment of the signal amplitude to give pressure amplitude.

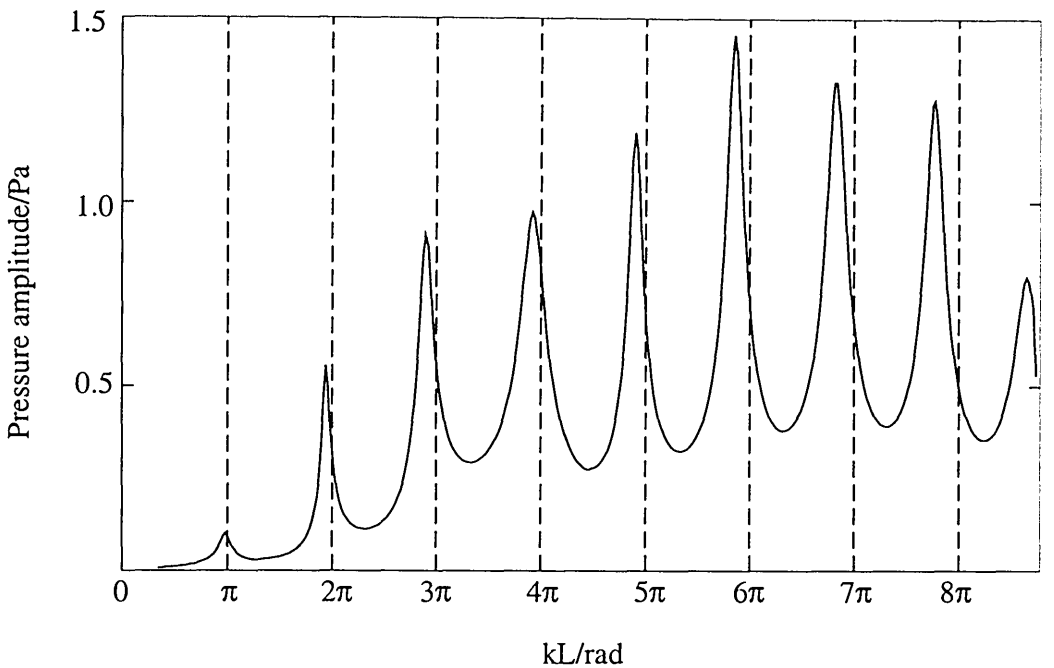

Figure 5.5: Antinodal pressure amplitude for the rigidly terminated loudspeaker-tube system. The dashed lines correspond to the theoretical resonances of a tube rigidly terminated at both ends.

The antinodal pressure amplitude measurements are displayed in figure 5.5. A plot of pressure amplitude against frequency was initially obtained but the frequency axis has been scaled in order to deduce information about the natural resonance frequencies of the combined loudspeaker-tube. It is clear from figure 5.5 that most of the resonances occur at

$$k_n L \sim n\pi \quad n = 1, 2, 3, \ldots \tag{5.19}$$

where $k_n = n\omega/c$. Equation 5.19 defines the theoretical resonances of a tube rigidly

terminated at both ends. This implies that there is nearly a pressure antinode at $x = L$ and that the driver is characterized as being heavy and stiff [60]. The combined system produces pressure amplitudes at the resonances that are much stronger for frequencies close to the resonance frequency of the driver. Driving the combined system at the natural resonance frequencies ensures the greatest possible variation in pressure amplitude between node and antinode.

5.5.2 Standing wave pressure

The loudspeaker-tube system was driven at a frequency close to one of the natural resonances. The probe microphone was inserted into the tube and measurements of the acoustic pressure amplitude were performed at 1 cm intervals from the rigid end. This process was repeated for several of the other resonance frequencies and the results are displayed in figure 5.6. The points on each graph correspond to the probe microphone measurements. The vertical scale of each standing wave plot is pressure amplitude, $|p(x)|$, divided by the antinodal pressure amplitude at $x = 0$, $|p(0)|$. The acoustic frequency, f_m, was obtained directly from the sinusoidal voltage signal used to drive the loudspeaker. The temperature inside the tube was measured by removing the probe microphone and inserting the probe thermometer. The atmospheric pressure and relative humidity were also recorded allowing the speed of sound to be calculated.

The expression in equation 5.6 was fitted to the pressure amplitude measurements using a least squares fit routine, adapted from [40] to take into account the dependence

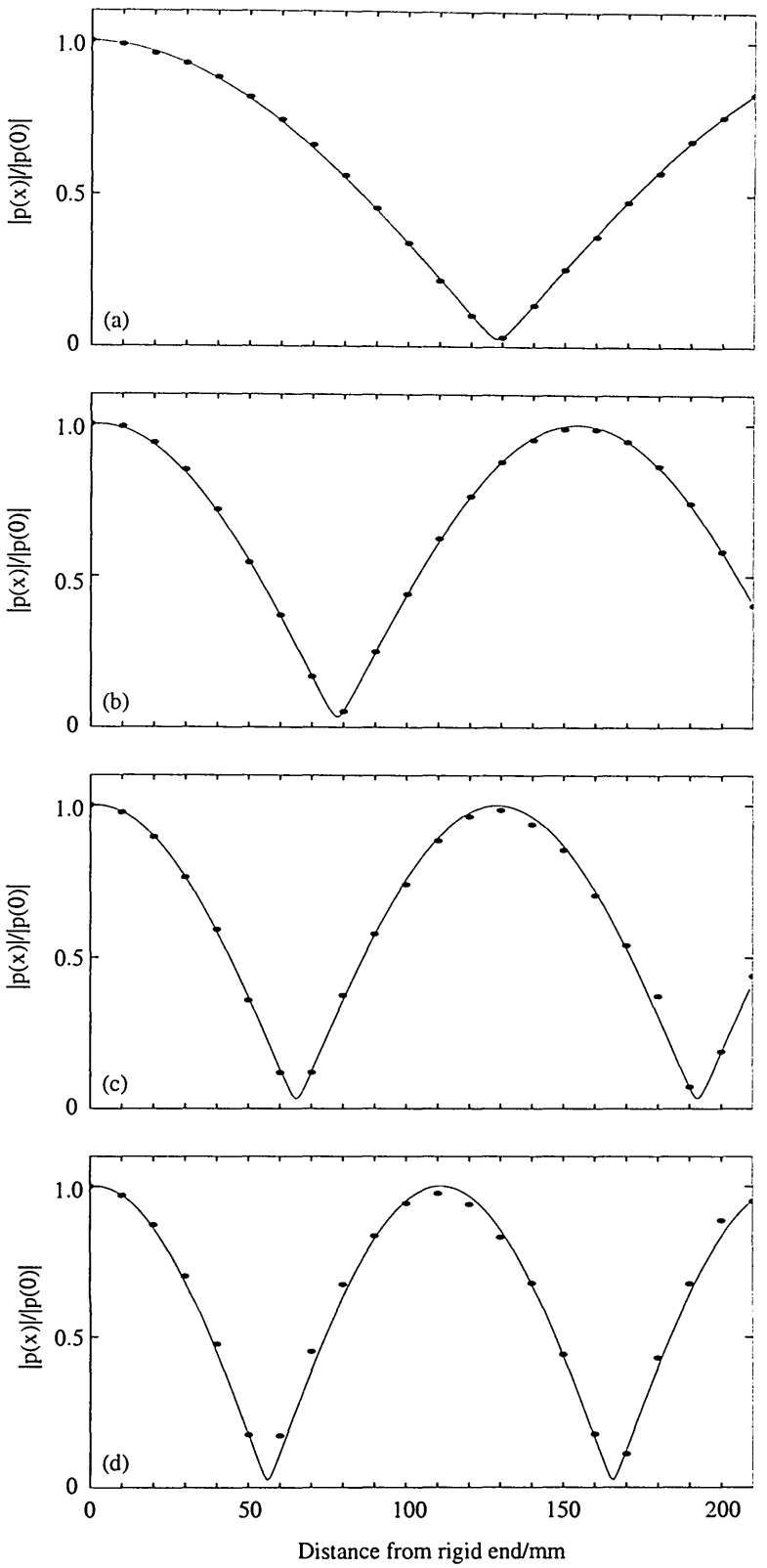

Figure 5.6: Pressure amplitude measured as a function of displacement from rigid end in a standing wave (a) with $f_m = 660$ Hz, (b) 1135 Hz, (c) 1355 Hz, and (d) 1570 Hz.

of the speed of sound on the environmental conditions. The routine obtains the optimum values of $(A + B)$, SWR, and θ which minimise the sum of the squared relative errors. The squared relative error is defined as the difference between the square of the RHS of equation 5.6 and the square of the measured pressure amplitude, all divided by the square of the measured pressure amplitude. The results are given in table 5.1 for the standing wave plots in figure 5.6, where the solid line in each graph corresponds to the best fit curve. Also displayed in table 5.1 are the acoustic frequencies and the values of $\lambda_m/4$, where λ_m is the acoustic wavelength. Closer inspection of the standing wave measurements confirms the position of the first pressure node from the end of the tube to be located at $x = \lambda_m/4$, as predicted in section 5.3. This corresponds to the position of the first velocity antinode from the end of the tube.

f_m/Hz	$(\lambda_m/4)$/mm	θ/degrees	SWR
660	130	2.5	38
1135	76	5.0	29
1355	64	4.5	30
1570	55	4.5	40

Table 5.1: Standing wave measurements and optimum values.

It can be seen from the measurements in figure 5.6 that as f_m is increased, the distance to the first velocity antinode decreases. From table 5.1, the optimum phase change, θ, obtained using the fitting routine is relatively small, supporting the assumption made in equation 5.10. If propagation losses along the tube were significant, the pressure amplitude measured at the end of the tube would be lower than the pressure amplitude measured at the first pressure antinode from the end. This is not the case for

the standing wave plots in figure 5.6. In fact for plots (c) and (d) the pressure amplitude measurements at the first pressure antinode from the end are slightly lower than $|p(0)|$. This is the result of small misalignments that occurred during the insertion of the probe microphone into the glass tube. As was concluded in section 5.3, the propagation loses are small enough to be safely neglected.

5.6 LDA apparatus

Two variations of the dual beam mode LDA system were used to capture the Doppler signals produced by acoustic particle motion, the continuous photodetector signal system and the photon correlation system. Both sets of apparatus essentially consist of three main parts; the transmitter optics which produce the interference fringes, the detector optics which detect the scattered light, and the electronic hardware system which carries out the initial signal processing.

5.6.1 Continuous signal system

The LDA apparatus based on the analysis of a continuous electronic signal from the photodetector is illustrated in figure 5.7. The optical parts consisted of DISA 55X series components. A Spectra-Physics 106-1 He-Ne 20 mW laser produced a 633 mm wavelength beam with an unfocused e^{-2} beam diameter of 0.68 mm [65]. The laser beam was passed through a beam splitter and a Bragg cell produced a 40 MHz

frequency shift in one of the beams. A 310 mm focal length achromatic lens causes the two parallel beams to intersect with $2\theta = 11.06°$ to form the probe volume [66]. The focused beam diameter $d_{e^{-2}} = 0.37$ mm (see equation 3.5), the fringe separation $\Lambda = 3.28\mu$m (see equation 3.10), and the number of fringes in the probe volume $N_f = 113$ (see equation 3.11).

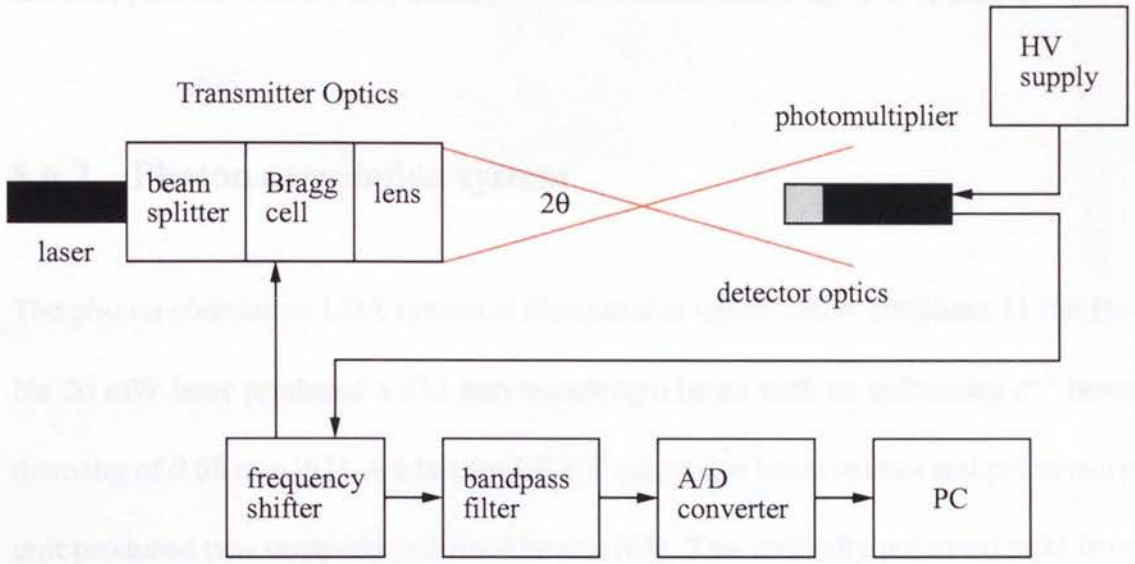

Figure 5.7: Diagram of the continuous signal laser Doppler apparatus.

The scattered light was detected using a photomultiplier and optics adapted to increase the intensity. A 150 mm focal length convex lens was positioned directly in front of the standard 150 mm focal length lens to increase the image of the measuring volume in the plane of the cathode. The pin hole was expanded from 0.1 mm to 1.0 mm to allow for the larger image size. The photomultiplier and detector optics were mounted at an angle of 15° to the horizontal beam plane to avoid detecting light from the direct beams.

A DANTEC 55N12 frequency shifter electronically downshifted the photomultiplier signal to an equivalent frequency shift of $F_s = 100$ kHz. The signal was then bandpass filtered at 2-200 kHz using a DISA 55D26 Signal Conditioner to remove the pedestal (see section 3.4.5) and to prevent aliasing (see section 3.5.5). A Wavebook 512 A/D converter connected to a PC made a 32768 point sample of the filtered signal at a frequency of 0.5 MHz. Using equation 3.62, the theoretical upper limit to the acoustic particle velocity amplitude that can be measured is $u_m < 0.41$ ms^{-1}.

5.6.2 Photon correlation system

The photon correlation LDA system is illustrated in figure 5.8. A Uniphase 1135P He-Ne 20 mW laser produced a 633 mm wavelength beam with an unfocused e^{-2} beam diameter of 0.68 mm [67]. A Malvern RF 307 adjustable beam splitter and polarisation unit produced two vertically polarised beams [68]. The vertically polarised light from the beam splitter was rotated using a half wave plate to give horizontally polarised light. The two beams were then passed through a Malvern K9023 Phase Modulator and a 100 mm focal length lens which intersected the beams with $2\theta = 11.42°$, forming the probe volume. The focused beam diameter $d_{e^{-2}} = 0.12$mm, the fringe separation $\Lambda = 3.18\mu$m, and the number of fringes in the probe volume $N_f = 37$.

The scattered light was detected using a Brookhaven BI-DS1 photomultiplier and optics adapted especially for the present study. A variable focal length and adjustable aperture size lens unit was mounted 130 mm in front of the pin hole of the photomul-

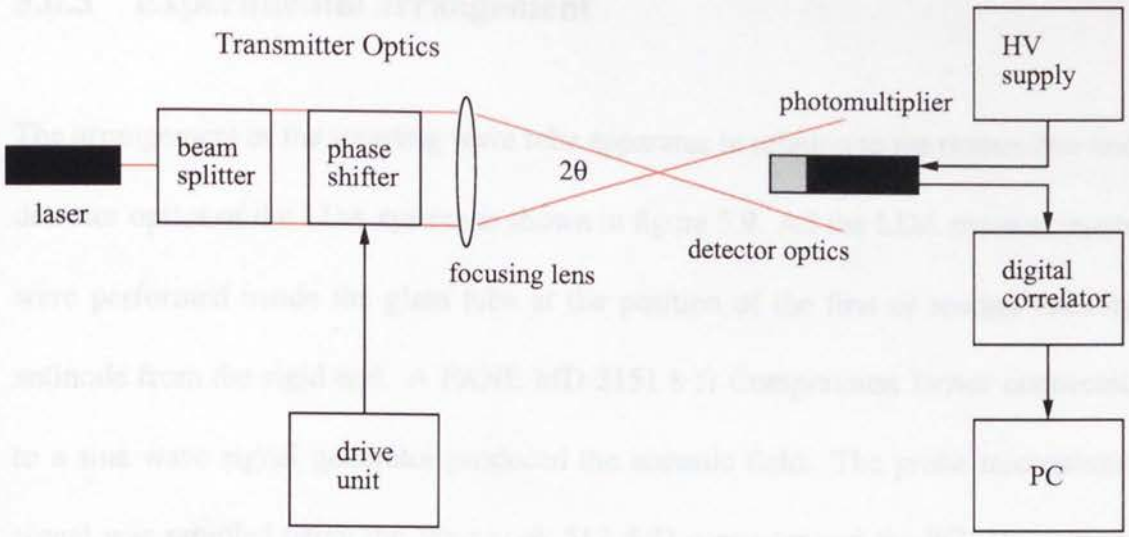

Figure 5.8: Diagram of the photon correlation laser Doppler apparatus.

tiplier to focus the scattered light. The pin hole was widened from 0.6 mm to 1.0 mm to increase the intensity of the detected light. A lens located directly behind the pin hole expands the light onto the cathode. The photomultiplier and detector optics were positioned at an angle of 15° to the horizontal beam plane to avoid detecting light from the direct beams.

A BI-9000AT Digital Correlator PCI board correlated the photomultiplier signal with itself to produced the autocorrelation function. The sample time, $\Delta\tau$, determines the number of available channels in the correlator board [69]. A sampling time of $\Delta\tau = 2\ \mu$s with 80 channels or a sampling time of $\Delta\tau = 5\ \mu$s with 200 channels was used. From equation 4.47, the theoretical limits to the acoustic particle velocity amplitude that can be measured are: $0.012\ \text{ms}^{-1} < u_m < 0.970\ \text{ms}^{-1}$ for $\Delta\tau = 2\ \mu$s, and $0.004\ \text{ms}^{-1} < u_m < 0.388\ \text{ms}^{-1}$ for $\Delta\tau = 5\ \mu$s.

5.6.3 Experimental arrangement

The arrangement of the standing wave tube apparatus in relation to the transmitter and detector optics of the LDA system is shown in figure 5.9. All the LDA measurements were performed inside the glass tube at the position of the first or second velocity antinode from the rigid end. A FANE MD 2151 8 Ω Compression Driver connected to a sine wave signal generator produced the acoustic field. The probe microphone signal was sampled using the Wavebook 512 A/D converter and the PC. The sample was 32768 points long and the sampling frequency was 0.5 MHz.

5.7 Seeding particles

Seeding particles are suspended in the fluid, which is air in the present study, to scatter sufficient light to produce the Doppler signal. It is the velocity of the suspended particles rather than the fluid velocity that is measured using LDA. Therefore, it is important to establish the relationship between the acoustic fluid velocity, u_f, and the velocity of the seeding particle, u_p. The shape, size, concentration, and relative density of the seeding particles affect their motion [7].

Consider the situation where a seeding particle is suspended in an acoustic field with acoustic velocity amplitude, $|u_f|$, and frequency, f_m. There will be a viscous drag force acting on the seeding particle. Also, the acceleration of the fluid leads to a pressure gradient in the vicinity of the seeding particle. Vignola et al [70] derived a model

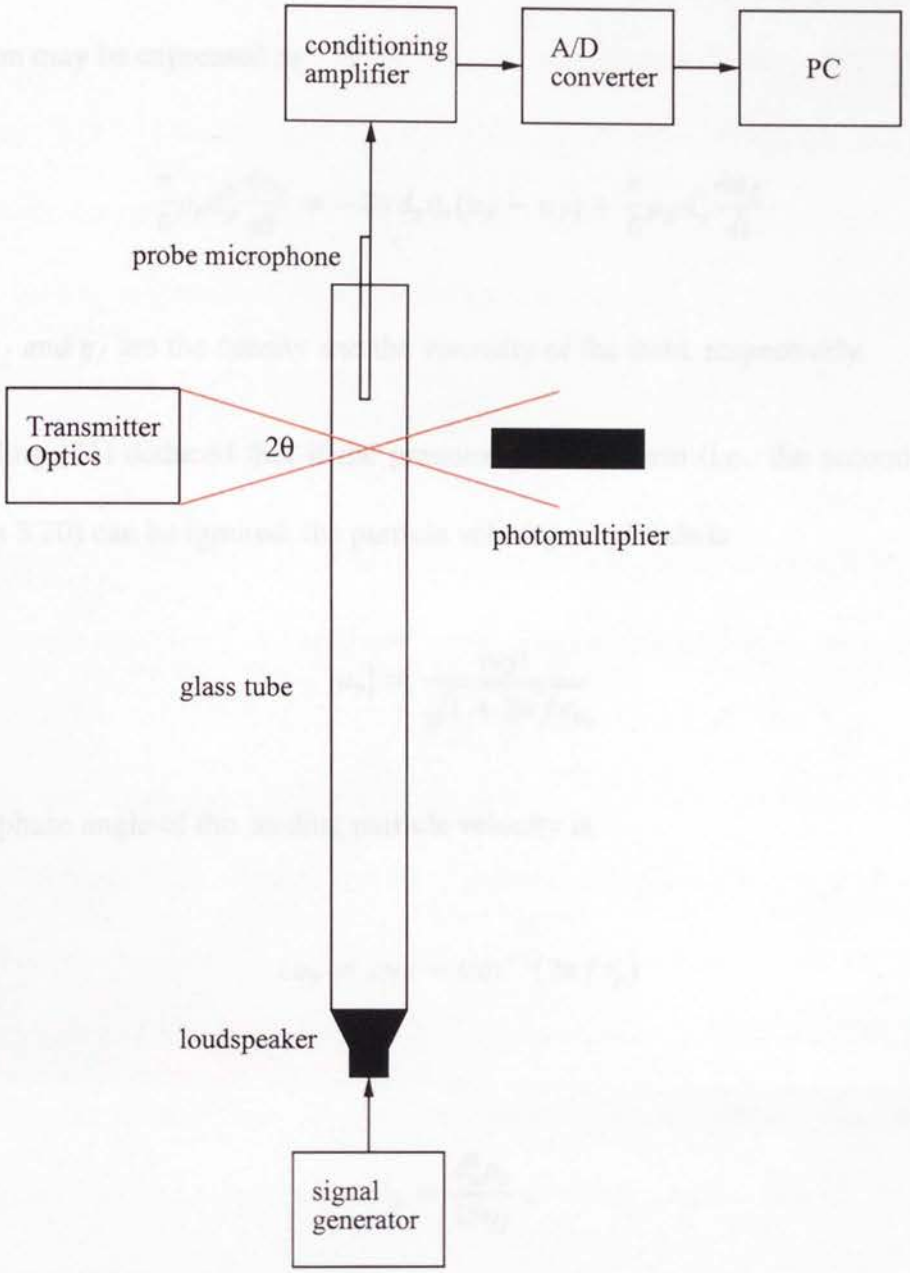

Figure 5.9: Arrangement of loudspeaker-tube apparatus for LDA measurements.

for the motion of the seeding particle in an acoustic field which takes into account both the viscous (Stokes) drag and the pressure gradient. Assuming the seeding particle is a sphere with diameter d_p and density ρ_p, the mass is $m_p = (\pi/6)\rho_p d_p^3$. The equation of motion may be expressed as

$$\frac{\pi}{6}\rho_p d_p^3 \frac{du_p}{dt} = -3\pi d_p \eta_a (u_p - u_f) + \frac{\pi}{6}\rho_f d_p^3 \frac{du_f}{dt} \tag{5.20}$$

where ρ_f and η_f are the density and the viscosity of the fluid, respectively.

Melling [71] deduced that if the pressure gradient term (i.e. the second term in equation 5.20) can be ignored, the particle velocity amplitude is

$$|u_p| = \frac{|u_f|}{\sqrt{1 + 2\pi f \tau_p}} \tag{5.21}$$

and the phase angle of the seeding particle velocity is

$$\angle u_p = \angle u_f - \tan^{-1}(2\pi f \tau_p) \tag{5.22}$$

where

$$\tau_p = \frac{d_p^2 \rho_p}{18\eta_f} \,. \tag{5.23}$$

τ_p is called the relaxation time. Vignola et al [70] found that the viscous drag force dominates at frequencies below $1/(2\pi\tau_p)$. The pressure gradient force may be neglected at frequencies well below this value.

Two types of seeding were used in the present study, incense smoke and hydrosonic haze. The smoke particles were introduced into the glass tube by removing the perspex end and inserting a burning incense stick for approximately 5 seconds. The smoke particles have diameters of less than 0.5μm and an estimated density of 1 gcm^{-3} (i.e. 1000 kgm^{-3}) [72] [73]. The value of $1/(2\pi\tau_p)$ is 212 kHz for incense smoke suspended in air. From equations 5.21 and 5.22, in a 6 kHz acoustic air flow the smoke particles oscillate with an amplitude of 98.6% of the acoustic particle velocity amplitude and lag by less than 2 °. Therefore, the viscous drag and pressure gradient forces can safely be neglected in measurements below 6 kHz.

A Hydrosonic 2000 haze generator produces seeding particles through the evaporation and condensation of a water-based liquid. The particle diameters are in the range of 1 μm to 4 μm [74]. The value of $1/(2\pi\tau_p)$ is 3 kHz to 5 kHz. This type of seeding was only used for experiments performed with $f_m \leq 2$ kHz. Assuming the relative density is approximately 1 gcm^{-3}, in a 2 kHz acoustic air flow the haze particles oscillate with an amplitude of 98.2 % to 79.0% of the acoustic particle velocity amplitude and lag by less than 2 ° to 31 °. Clearly the larger particles, i.e. $d_p > 2\ \mu$m, do not faithfully follow the acoustic flow. However, the majority of particles are thought to have $d_p \simeq 1\ \mu$m [75], which do follow the acoustic oscillation sufficiently for frequencies less than or equal to 2 kHz.

5.8 Summary

The probe microphone allows measurements to be made in confined spaces that are inaccessible to standard microphones but the probe tube attachment distorts the frequency response of the microphone that it is fixed to. The frequency response of the probe microphone was measured relative to a reference microphone. This allows the output voltage signal of the probe microphone to be interpreted in terms of pressure amplitude (measured in pascals) and pressure phase.

The combined loudspeaker-tube system provides a method for generating a standing wave. The pressure amplitude at an antinode in the standing wave is related to the particle velocity amplitude by the characteristic acoustic impedance of the air inside the tube, assuming plane wave propagation. The rigid end of the tube corresponds to the position of a pressure antinode and a velocity node. Measurements of particle velocity amplitude at a velocity antinode using LDA can be compared to measurements of pressure amplitude performed at the end of the tube.

The density of air and speed of sound in air may be calculated from measurements of temperature, atmospheric pressure, and relative humidity. Fluctuations in the concentration of carbon dioxide were found to have very little overall effect when using the theoretical expressions to calculate the characteristic acoustic impedance.

Measurements of pressure amplitude made with the probe microphone were used to establish the resonance frequencies of the combined loudspeaker-tube system and

confirm the position of the first velocity antinode from the end of the tube. Driving the combined system at the natural resonance frequencies ensures the greatest possible variation in pressure amplitude between node and antinode.

Both laser Doppler systems used in the present study consist of transmitter optics which generate the probe volume, detector optics which capture the scattered light, and an electronic hardware system which performs initial processing on the detector signal. The LDA probe volume was positioned inside the glass tube at the first or second velocity antinode from the rigid end.

Finally, the characteristics of the two types of seeding particles used in the experimental study were discussed. Seeding particles are required in LDA to scatter sufficient laser light to generate the Doppler signal. For relatively low acoustic frequencies, the viscous drag force dominates. Incense smoke particles were calculated as following the acoustic oscillation sufficiently for frequencies below 6 kHz. In comparison, the large range of particle diameters for the hydrosonic haze means that some of the particles were calculated as significantly lagging the acoustic oscillation for frequencies below 2 kHz. However, the majority of haze particles will sufficiently follow the sound field.

Chapter 6

LDA measurement of sound

6.1 Introduction

LDA provides a direct approach to the evaluation of sound pressure from the measurement of acoustic particle velocity amplitude. This chapter is concerned with measurements acquired using the continuous signal LDA system. Section 6.2 reviews the form of the Doppler signal generated by acoustic particle motion and the calculation of velocity amplitude. The experimental method is explained in section 6.3. Measurements of the mean flow velocity, the acoustic particle velocity amplitude and the instantaneous particle velocity are presented in sections 6.4, 6.5, 6.6 respectively. The calculation of pressure amplitude derived from LDA velocity measurements is evaluated in section 6.7. Finally, the application of LDA to the measurement of microphone sensitivity is presented in section 6.8.

6.2 Frequency modulation of the Doppler signal

In the dual beam LDA configuration interference fringes are formed at the intersection of two laser beams. As particles move across the ellipsoidal fringe volume they scatter light into a photodetector which is frequency shifted by an amount proportional to the velocity of motion of the particles. The spacing between fringes, Λ, depends on the angle between the two beams and on the wavelength of the laser light. A frequency shift, F_s, is introduced to one of the beams to resolve directional ambiguity and extend the dynamic range of the measuring technique. It also simplifies analysis of the Doppler signal in the frequency domain and enables the instantaneous velocity to be extracted through use of the Hilbert transform demodulation routine.

An acoustic field of single frequency f_m generates a Doppler signal of the form of a frequency modulated wave with carrier frequency F_s, modulation frequency f_m, and peak frequency deviation ΔF_m. This is illustrated in figure 3.8 and discussed in detail in section 3.4.7. The peak frequency deviation is given by $\Delta F_m = u_m/\Lambda$, where the acoustic particle velocity amplitude $u_m = 2\pi f_m x_m$ and x_m is the displacement amplitude. The peak frequency deviation is directly proportional to the acoustic particle velocity amplitude.

The positive frequency magnitude spectrum of the frequency modulated signal is illustrated in figure 3.11. It consists of a spectral component centred on the shift frequency and side lobes spaced at discrete multiples of the acoustic frequency. The mag-

nitudes or amplitudes of the peaks are proportional to successive orders of the Bessel function of the first kind with argument, $\alpha = \Delta F / f_m$. The ratio of amplitudes between the nth peak from the centre and the centre peak is given by equation 3.56. In practice, the Doppler signal is sampled and windowed before the spectrum is calculated. Each spectral peak has a finite width determined by contributions arising from the ambiguity noise, the windowing operation, and the mean flow velocity. If this width is narrow enough to be neglected, the amplitude will be indicated by the height of the peak.

The Bessel function of zero order and argument α is defined in [76] by the infinite power series

$$J_0(\alpha) = 1 - \frac{\alpha^2}{2^2} + \frac{\alpha^4}{2^2.4^2} - \frac{\alpha^6}{2^2.4^2.6^2} + \ldots \tag{6.1}$$

Similarly, the Bessel function of order one and argument α is defined by the infinite power series

$$J_1(\alpha) = \frac{\alpha}{2} - \frac{\alpha^3}{2^2.4} + \frac{\alpha^5}{2^2.4^2.6} - \frac{\alpha^7}{2^2.4^2.6^2.8} + \ldots \tag{6.2}$$

For small α, equation 3.56 reduces to

$$\frac{J_1(\alpha)}{J_0(\alpha)} \simeq \frac{4\alpha}{(8 - \alpha^2)} . \tag{6.3}$$

Solving equation 6.3 for α gives

$$\alpha = \frac{-2 \pm 2\sqrt{1 + 2[J_1(\alpha)/J_0(\alpha)]^2}}{[J_1(\alpha)/J_0(\alpha)]} . \tag{6.4}$$

The ratio, $J_1(\alpha)/J_0(\alpha)$, is evaluated by measuring the heights of the peaks in the magnitude spectrum while the acoustic frequency, f_m, is found by measuring the spacing between peaks. The substitution of $\alpha = u_m/\Lambda f_m$ into the positive solution allows equation 6.4 to be resolved to give u_m.

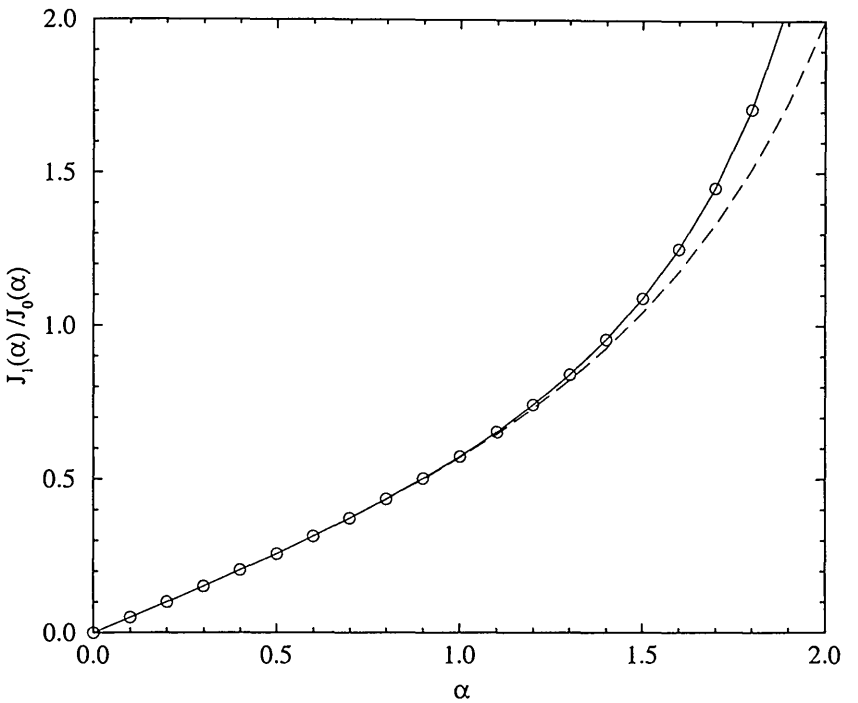

Figure 6.1: Variation of the ratio, $J_1(\alpha)/J_0(\alpha)$, with argument, α. The points on the solid line correspond to values of the ratio evaluated using tables of Bessel functions. The dashed line corresponds to the small argument approximation in equation 6.3.

Extensive tables of values for $J_0(\alpha)$ and $J_1(\alpha)$ have been calculated [56]. The graph in figure 6.1 shows how the ratio of $J_1(\alpha)$ to $J_0(\alpha)$ changes with argument in the range $0 \leq \alpha \leq 2$. It can be seen that the approximation in equation 6.3 appears valid for $\alpha \leq 1.0$. The particle velocity amplitude can also be determined by using the ratio $J_1(\alpha)/J_0(\alpha)$ to predict α and calculating $u_m = \alpha\Lambda f_m$.

6.3 Experimental method

Measurements were performed using the continuous signal LDA system described in section 5.6.1 and illustrated in figure 5.7, with the loudspeaker tube arrangement shown in figure 5.9. The loudspeaker produces an acoustic field inside the rigidly terminated glass tube. In section 5.5, measurements with the probe microphone were presented to confirm the presence of a standing wave when the loudspeaker tube system is driven at a frequency close to a natural resonance frequency of the system. Frequencies close to the natural resonances are used as there is the greatest possible variation in pressure amplitude between node and antinode. The acoustic frequency, f_m, is obtained directly from the sinusoidal voltage signal used to drive the loudspeaker.

The LDA measurements were carried out at either the position of the first or second velocity antinode from the rigid end of the glass tube. The antinodal pressure amplitude at the rigid end was monitored using the probe microphone described in section 5.2, which has the frequency response shown in figure 5.2. The downshifted photomultiplier signal was passed through a $2 - 2000$ kHz bandpass filter and simultaneously sampled at 0.5 MHz with the probe microphone signal using the Wavebook A/D converter. A 32768 point sample of each signal was made.

The magnitude response of the probe microphone for each frequency of standing wave was determined using the apparatus shown in figure 5.1 before acquiring LDA measurements. The signal generator supplies a sine wave of constant frequency and

amplitude to the sound source in the coupler. The resulting probe microphone and reference microphone RMS voltage amplitudes were measured with a digital voltmeter. Equation 5.1 is used to calculate the magnitude response, allowing the probe microphone voltage amplitude to be converted to pressure amplitude measured in pascals. The uncertainty in the magnitude response is determined by the uncertainty associated with the measurement of voltage amplitude using the digital voltmeter.

The atmospheric pressure and relative humidity were measured using an electronic barometer. The air temperature inside the tube was measured by removing the probe microphone from the rigid end and inserting a probe thermometer. The characteristic impedance, ρc, was calculated using the method described in section 5.4. Incense smoke was used to seed the air inside the tube. Whenever seeding was required the rigid end was removed and a Burning incense stick inserted into the tube for a period of approximately 5 seconds. The diameter of the smoke particles (< 0.5 μm) was less than the fringe separation (3.28 μm). The acoustic particle displacements considered in the experiments were in the range $0.1\mu\text{m} < x_m < 1.0\mu\text{m}$.

An example of the Doppler signals captured using the apparatus is shown in figure 6.2. Frequency domain analysis is performed on the positive frequency magnitude spectrum, also illustrated in figure 6.2, to deduce acoustic particle velocity amplitude. Hilbert transform analysis is performed on the time domain Doppler signal to extract instantaneous frequency, and hence instantaneous particle velocity. The probe microphone voltage signal is recorded for each Doppler signal sampled.

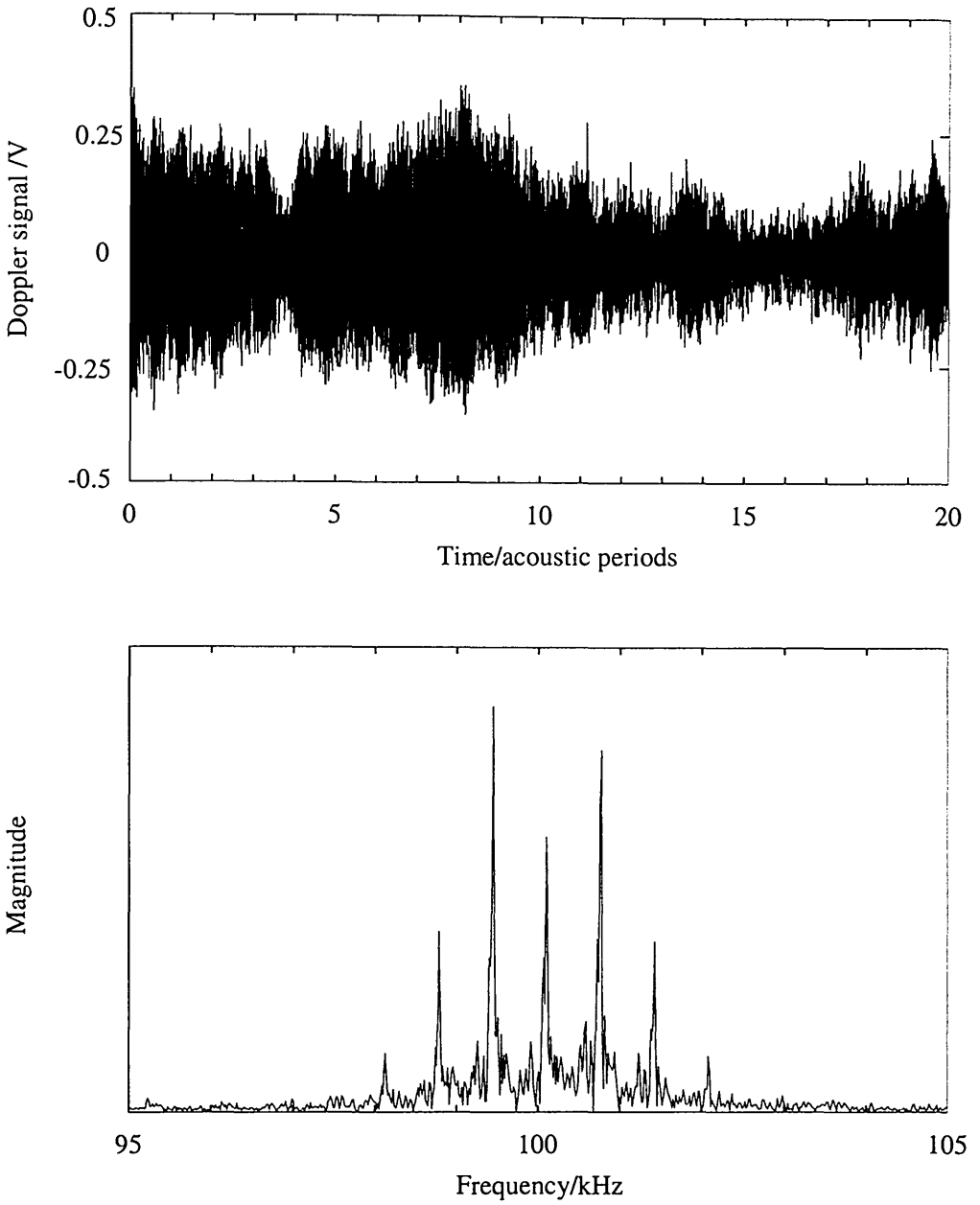

Figure 6.2: A measured Doppler signal produced by an acoustic field with frequency, $f_m = 660$ Hz. A section of the positive frequency magnitude spectrum about the shift frequency, $F_s = 100$ kHz, is also shown. The spectrum is centred at a frequency position slightly to the right of F_s indicating a small mean flow in the $-x$ direction. Contributions to the spectral peak width arise from the ambiguity noise, the mean flow, and the windowing operation performed on the sampled Doppler signal.

6.4 Measurement of mean flow velocity

A small mean flow velocity is present inside the glass tube when a standing wave is generated. Frequency domain analysis of the Doppler signal allows the magnitude of the mean flow in the x direction to be calculated. The mean flow contributes to the broadening of the peaks in the frequency spectrum by an amount that may be determined using equation 3.43. A window function is applied to the Doppler signal before the spectrum is calculated to prevent leakage, but this also results in a broadening of the spectral peaks and may be evaluated using equation 3.47. In addition, spectral broadening arises from the ambiguity noise. The theoretical spectral peak width, calculated from the combination of mean flow broadening and window broadening, is compared to the measured spectral peak width which includes the ambiguity broadening effect.

6.4.1 Signal Processing

A computer program was written to generate the positive frequency magnitude spectrum of the Doppler signals captured using the apparatus. An interpolation routine developed by Matovic [77], based on a variable width cosine squared estimator, provides an accurate means of determining the frequency positions of the peaks in the magnitude spectrum. The frequency positions of the highest peaks to the left and right of the central peak in the spectrum are found using the interpolation routine and the size of the mean flow velocity is deduced using equation 3.59.

To obtain a more accurate result, the program calculates the average value of the mean flow velocity for a set of Doppler signals generated by a standing wave with constant frequency and antinodal pressure amplitude. The standard deviation is used to obtain the uncertainty in the mean value (see Appendix C). For each Doppler signal recorded, the probe microphone output voltage is also sampled. Using the magnitude response information, the amplitude of the voltage signal is converted to RMS pressure amplitude by the program. The average value of the pressure amplitude is found for the set of probe microphone signals and the standard deviation is used along with the uncertainty in the magnitude response to determine the total uncertainty in the pressure.

6.4.2 Results and discussion

Figure 6.2 shows a Doppler signal recorded for a standing wave with acoustic frequency, $f_m = 660$ Hz, and a RMS antinodal pressure amplitude measured at the rigid end, $|p| = 1.0$ Pa. The resolution of the positive frequency magnitude spectrum of the Doppler signal is determined by the sampling frequency and the sample length; 0.5 MHz /32768 = 15.3 Hz/point. The frequency positions of the highest peaks either side of the central peak were found by the program to be $F_+ = 100763$ Hz and $F_- = 99443$ Hz giving a mean flow velocity of $u_0 = 0.5$ mms^{-1}. For a set of 20 Doppler and probe microphone signals recorded with $f_m = 660$ Hz, the average RMS pressure amplitude $|\bar{p}| = 0.995 \pm 0.001$ Pa and the average value of the mean flow velocity $\bar{u}_0 = 0.25 \pm 0.02$ mms^{-1}. The values of u_0 are always positive indicating a

flow in the $-x$ direction, i.e. towards the rigid end of the tube.

The acoustic frequency was maintained at $f_m = 660$ Hz and the RMS antinodal pressure amplitude was varied between 0.1 Pa and 1.0 Pa (i.e. a corresponding SPL range of 74 dB to 94 dB). Sets of 20 Doppler signals were recorded for 10 different antinodal pressure amplitudes and the average value was determined. In figure 6.3 the magnitude of $\bar{u}_0$ is plotted against the average RMS antinodal pressure amplitude, $|\bar{p}|$. The mean flow is no longer always in the $-x$ direction. However, it is the magnitude of the mean flow velocity that determines the size of the contribution to the spectral broadening. The uncertainty in the measurement of $\bar{u}_0$, calculated from the standard deviation using the method described in Appendix C, is between 5 % and 20 % which indicates that equation 3.59 only gives an estimation of the mean flow velocity. It can be seen from figure 6.3 that $|\bar{u}_0| \leq 0.25$ mms^{-1}. From examination of individual Doppler signals, $|u_0|$ does not exceed 0.35 mms^{-1}. Using the details of the LDA rig in section 5.6.1 and equation 3.43, the contribution to the spectral peak width resulting from the mean flow velocity is $\sigma_F < 0.5$ Hz for $f_m = 660$ Hz. For a RMS antinodal pressure amplitude $|p| < 0.3$ Pa (a SPL of less than 84 dB), the side peaks are indistinguishable from the noise level present in the frequency spectrum. The mean flow velocity was estimated from the difference between the frequency position of the central peak and the frequency shift, $F_s = 100$ kHz.

Maintaining the RMS antinodal pressure amplitude at approximately 1.0 Pa, the acoustic frequency was varied in the range of 660 Hz to 4 kHz. Sets of 20 Doppler

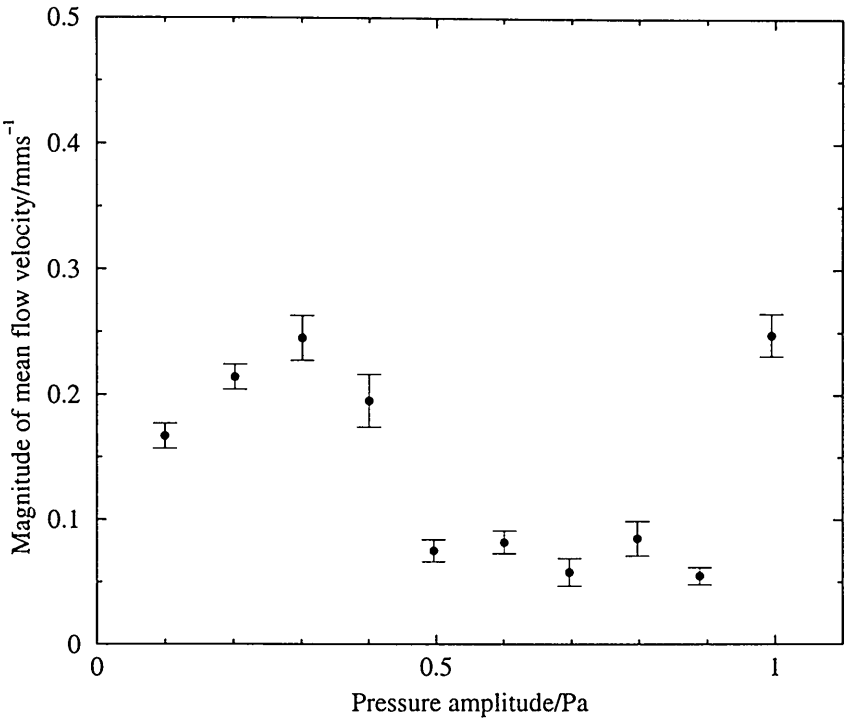

Figure 6.3: Magnitude of mean flow velocity, $|\bar{u}_0|$, measured for standing wave with $f_m = 660$ Hz versus RMS antinodal pressure amplitude, $|p|$, derived from probe microphone.

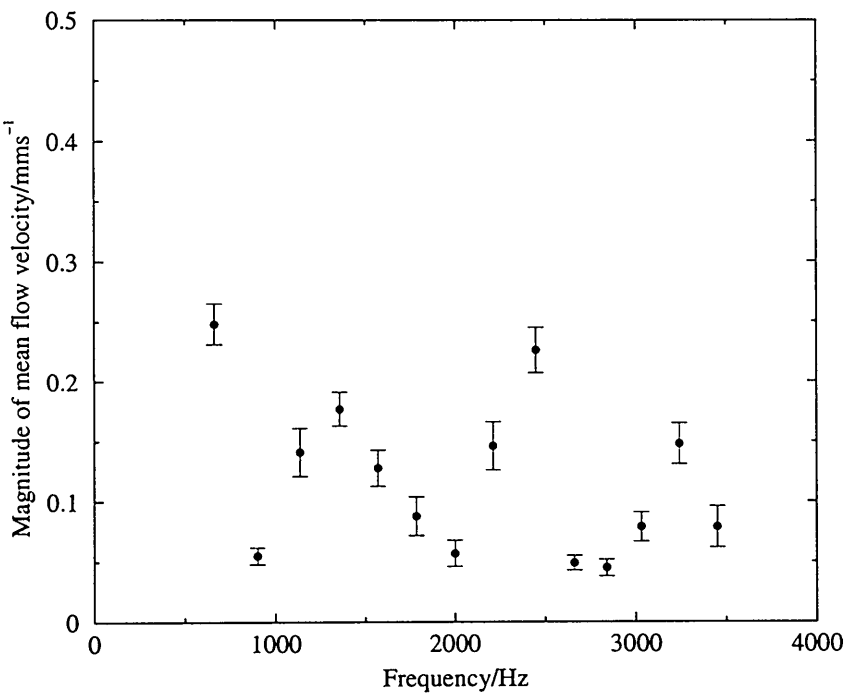

Figure 6.4: Magnitude of mean flow velocity, $|\bar{u}_0|$, measured for standing wave with RMS antinodal pressure amplitude, $|p| \simeq 1.0$ Pa, versus acoustic frequency, f_m.

signals were recorded for different acoustic frequencies that correspond to resonances of the loudspeaker-tube system and the average value of the mean flow velocity was measured. In figure 6.4, $|\bar{u}_0|$ is plotted against f_m. Again, the uncertainty in the measurement of $|\bar{u}_0|$ is between 5 % and 20 %. From the graph, $|\bar{u}_0| \leq 0.25$ mms^{-1} and from examination of individual Doppler signals, $|u_0|$ does not exceed 0.40 mms^{-1}. So the contribution to the spectral peak width resulting from the mean flow inside the tube is $\sigma_F < 0.5$ Hz for f_m in the range of 660 Hz to 4 kHz.

The period of time over which the Doppler signals are recorded, T, is determined by the number of points in the sample divided by the sampling frequency; $T = 32768/0.5$ MHz $= 0.065536$ seconds. From equation 3.47, the contribution to the width of the spectral peaks arising from the windowing operation is $\sigma_W = 9.7$ Hz. Assuming other broadening effects can be neglected (e.g. velocity gradients, velocity fluctuations, laser beam waist position, and Brownian motion), the total variance is $\sigma^2 = \sigma_F^2 + \sigma_W^2 = 94.3$ Hz^2. The broadening effect due to the windowing operation is the significant effect for low flow speeds. The theoretical spectral peak width is calculated to be $2\sigma = 19.4$ Hz. Measurements of the actual spectral peak width, $2\sigma \simeq 45$ Hz, are greater than the theoretical value. This is because the calculated peak width does not account for the broadening effect due to ambiguity noise in the spectra of the measured Doppler signals. The frequency bandwidth of a Doppler signal is approximately $2(\Delta F + f_m)$. For the Doppler signals considered here, the bandwidth ranges from 1 kHz to 10 kHz. This is several orders of magnitude greater than the spectral peak width. Shortening the sample time over which the Doppler signals are recorded

would increase the width of the peaks as σ_W is inversely proportional to T.

6.4.3 Conclusions

Using frequency domain analysis, the small mean flow in the standing wave tube can be measured. For $f_m \leq 4$ kHz and $|p| \leq 1.0$ Pa, the average mean flow velocity does not exceed 0.25 mms^{-1}. The resulting contribution to the spectral peak width will not exceed $\sigma_F = 0.5$ Hz and can therefore be safely neglected. The broadening due to the windowing operation is the significant effect as $\sigma_W = 9.7$ Hz, which leads to a theoretical peak width of 19.4 Hz. Measuring the peak width from the frequency spectra of Doppler signals yields a value greater than the theoretical value. This is due to the ambiguity broadening, which was not accounted for in the calculation. However, peak width is very narrow compared to the bandwidth of the Doppler signals, suggesting that it is negligible and that the height of a peak gives an indication of its magnitude.

6.5 Measurement of velocity using frequency domain analysis

Frequency domain analysis provides a method for extracting acoustic particle velocity information from the sampled Doppler signal. A study of the variation of the ratio of the heights of the spectral peaks is conducted to determine if the peak width can be

assumed negligible. Velocity amplitude is calculated from the magnitude spectrum of the Doppler signal using the method explained in section 6.2. The total uncertainty in the velocity measurement is evaluated by considering the individual components of the measurement procedure. The distribution of velocity amplitude in a set of Doppler signals is determined and the dynamic range of the technique is considered.

6.5.1 Signal Processing

A computer program applies the Hanning window to the sampled Doppler signal before generating the positive frequency magnitude spectrum. Using the interpolation routine based on a variable width cosine squared estimator, the amplitudes of the first side peak and the centre peak are found, thus giving the ratio of $J_1(\alpha)$ to $J_0(\alpha)$. From the values of $J_1(\alpha)/J_0(\alpha)$ shown in figure 6.1, the Bessel function argument, α, is deduced for the measured ratio using a standard interpolation routine in [45]. The acoustic particle velocity amplitude, $u_m = \alpha\Lambda f_m$, where Λ is the fringe spacing and f_m is the acoustic frequency. Λ is calculated from the angle between the two illuminating beams and the wavelength of the laser light and f_m is obtained directly from the sinusoidal voltage signal used to drive the loudspeaker. The particle velocity amplitude is also calculated using the small argument approximation method described in section 6.2, which makes use of equation 6.3.

The measured Doppler signal is more complex than the frequency modulated form envisaged because of its random amplitude which arises from the random nature of

the seeding particle distribution. In order to obtain an accurate result, a number of measurements are averaged. Twenty Doppler signals are sampled and their magnitude spectra calculated. As there is a spectral peak either side of the central peak, two values of velocity amplitude are evaluated by the program for each frequency spectrum. The mean value and standard deviation are then determined for the set of signals.

The probe microphone voltage signal is sampled simultaneously with the Doppler signal. Using the magnitude response information, the RMS voltage amplitude is converted to RMS pressure amplitude by the program. The average value and standard deviation are determined for the set of 20 probe microphone signals. The uncertainty in the average value is calculated from the standard deviation and the uncertainty in the magnitude response of the probe microphone.

6.5.2 Uncertainty analysis

The uncertainty in the measurement of acoustic particle velocity amplitude, using the LDA frequency domain analysis technique, may be evaluated by considering the individual components of the measurement process. The acoustic frequency is obtained directly from the loudspeaker driving signal, using a digital multimeter, to the nearest ± 1 Hz. Therefore, the standard deviation in the acoustic frequency is $\sigma_{f_m} = 1/\sqrt{3}$ Hz [78]. From equation 3.10, it can be seen that the uncertainty in the sine of the beam angle will provide the major contribution to the uncertainty in the fringe spacing. This

may be written as

$$\frac{\sigma_\Lambda}{\Lambda} = \frac{\sigma_{\sin\theta}}{\sin\theta} \tag{6.5}$$

where σ_Λ and $\sigma_{\sin\theta}$ are the uncertainties in Λ and $\sin\theta$, respectively. The sine of the beam angle is

$$\sin\theta = \frac{d}{\sqrt{d^2 + f^2}} \tag{6.6}$$

where $2d$ is the distance between the two parallel beams and f is the focal length of the focusing lens. As d and f are the result of independent measurements, the error in equation 6.6 is obtained from [79], such that

$$\begin{aligned} \sigma^2_{\sin\theta} &= \left(\frac{\partial \sin\theta}{\partial d}\sigma_d\right)^2 + \left(\frac{\partial \sin\theta}{\partial f}\sigma_f\right)^2 \\ &= \frac{f^2}{(d^2+f^2)^3}(f^2\sigma_d^2 + d^2\sigma_f^2)\,. \end{aligned} \tag{6.7}$$

For the transmitter optics of the continuous signal LDA system, $2d = 60$ mm and $f = 310$ mm and $\sigma_d = \sigma_f = 1.0/\sqrt{3}$ mm. This gives a fringe spacing and associated uncertainty of $\Lambda = 3.29 \pm 0.01$ μm. The mean acoustic particle velocity amplitude is calculated from a set of 20 measured Doppler signals, i.e. 40 values of u_m. The uncertainty in the mean velocity amplitude is deduced from (see Appendix C)

$$u_A = \frac{\sigma_u}{\sqrt{n}} \tag{6.8}$$

where σ_A is the standard deviation and n is the number of values. The overall uncertainty in the velocity amplitude is found by expressing σ_Λ, σ_{f_m} and u_A as percentages

of their respective values. As the individual components are independent of each other, they are combined using a root sum square to give

$$u_u = \sqrt{\sigma_\Lambda^2 + \sigma_{fm}^2 + u_A^2}\,. \tag{6.9}$$

Using equation 5.1, the magnitude response of the probe microphone at a particular acoustic frequency can be determined. The voltage amplitudes of the probe and reference microphones are measured with a digital voltmeter to the nearest ± 0.001 V, and hence the standard deviations are $\sigma_{V_p} = \sigma_{V_r} = 0.001/\sqrt{3}$ V. As V_p and V_r are the result of independent measurements, the two standard deviations are expressed as percentages of their respective values and combined as

$$u_R = 20 \log \left(1 + \frac{\sqrt{\sigma_{V_p}^2 + \sigma_{V_r}^2}}{100} \right) \tag{6.10}$$

to give the uncertainty in the magnitude response of the probe microphone. The uncertainty in the mean probe microphone measurement is calculated from the standard deviation, i.e. $u_A = \sigma_p/\sqrt{n}$, where $n = 20$. This value is expressed as a percentage of the mean value and combined with σ_{V_p} and σ_{V_r} to give

$$u_p = \sqrt{\sigma_{V_p}^2 + \sigma_{V_r}^2 + u_A^2}\,. \tag{6.11}$$

This is the overall uncertainty in the mean pressure amplitude derived from the probe microphone.

Section 3.4.3 describes how the deviation of the focused beam waists from the focal point of the lens results in variations of the fringe spacing, which effects the Doppler frequency. However, as the transmitter optics are combined in a fixed unit (DISA 55X series components) and the focal length of the focusing lens is several hundred millimetres, these errors can be considered negligible. The beam distances inside the standing wave tube are approximately 0.05 m, the LDA measurements were conducted in air, and the highest frequency of standing wave was 4 kHz. From equation 3.72, for $f_m \leq 4$ kHz the amplitude of the fringe movement, y_m, is less than 0.4 % of the particle displacement amplitude, x_m, and so the acousto-optic effect can be ignored.

6.5.3 Results and discussion

Measurements were performed for a standing wave with $f_m = 660$ Hz. The antinodal pressure amplitude was varied between 0.1 Pa and 1.0 Pa (a corresponding SPL range of 74 dB to 94 dB) and sets of 20 Doppler signals were recorded. Magnitude spectra calculated from individual Doppler signals sampled at different pressure amplitudes are illustrated in figure 6.5. The spacing between peaks remains constant as f_m is kept constant. As the antinodal pressure amplitude is decreased, the side peaks drop in height. A decrease in pressure amplitude results in a decrease of particle velocity amplitude and particle displacement amplitude. The effective bandwidth of the Doppler signal diminishes from 4 kHz down to 2 kHz for the spectra displayed in figure 6.5. From examination of the magnitude spectra, the spectral peak width remains constant.

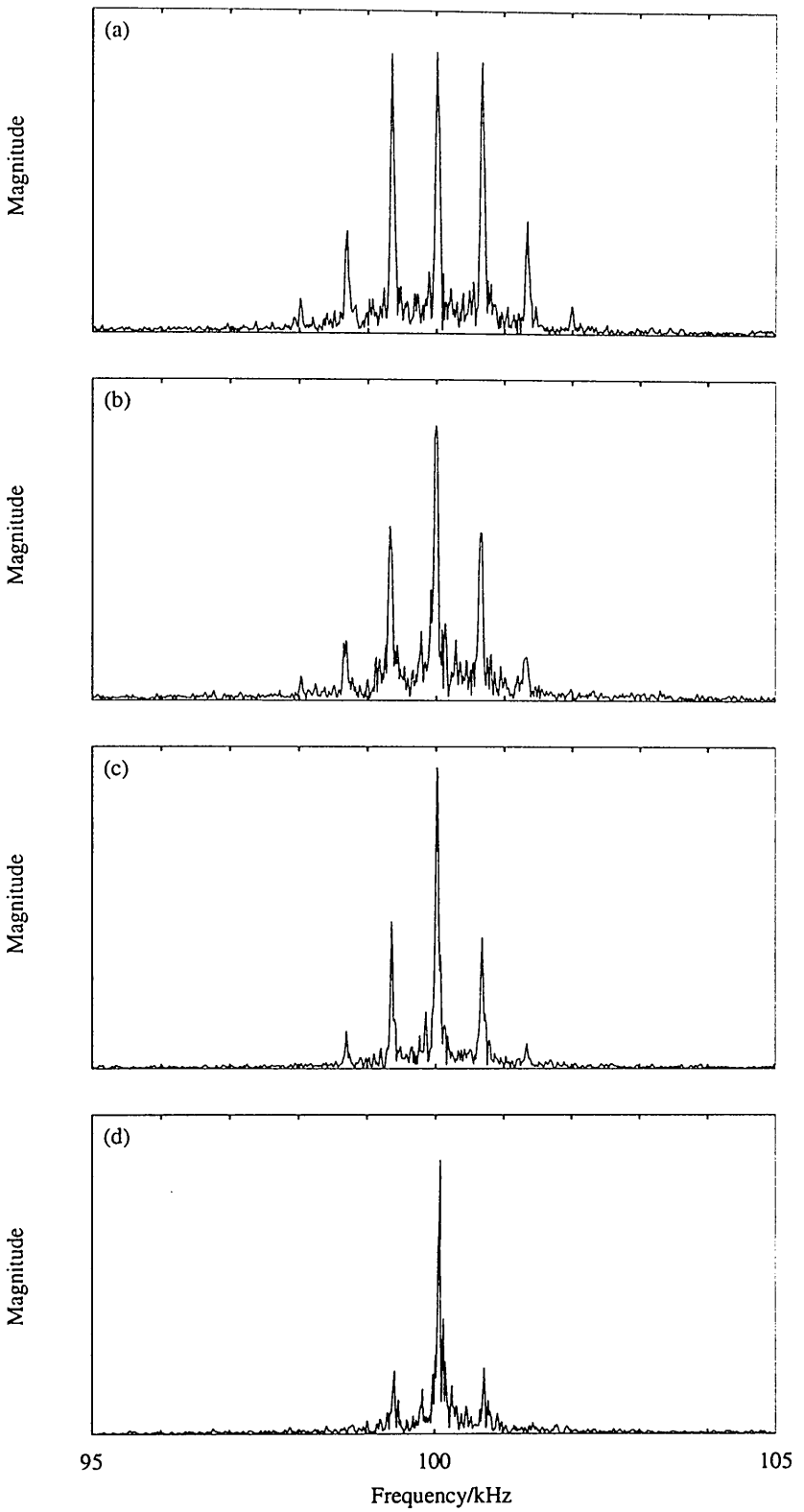

Figure 6.5: Magnitude spectra calculated from Doppler signals produced by an acoustic field with $f_m = 660$ Hz and (a) with RMS antinodal pressure amplitude at rigid end $|p| \simeq 0.9$ Pa, (b) 0.7 Pa, (c) 0.5 Pa, and (d) 0.3 Pa.

The average ratio of the first side peak amplitude to the central peak amplitude was calculated for each set of 20 Doppler signals. The results are displayed in figure 6.6 where the points are the measured ratio values derived by frequency domain analysis, the solid line corresponds to the theoretical behaviour of the ratio using the calculated values in figure 6.1, and the dashed line corresponds to the behaviour of the ratio using the approximation for small α in equation 6.3. The uncertainties in the measured ratio values are less than 0.5 % and too small to be displayed on the graph. The x axis in figure 6.1 was rescaled by multiplying α by $\rho c \Lambda f_m / \sqrt{2}$ to give RMS pressure amplitude, with air density $\rho = 1.2$ kgm^{-3} and speed of sound $c = 343.5$ ms^{-1}.

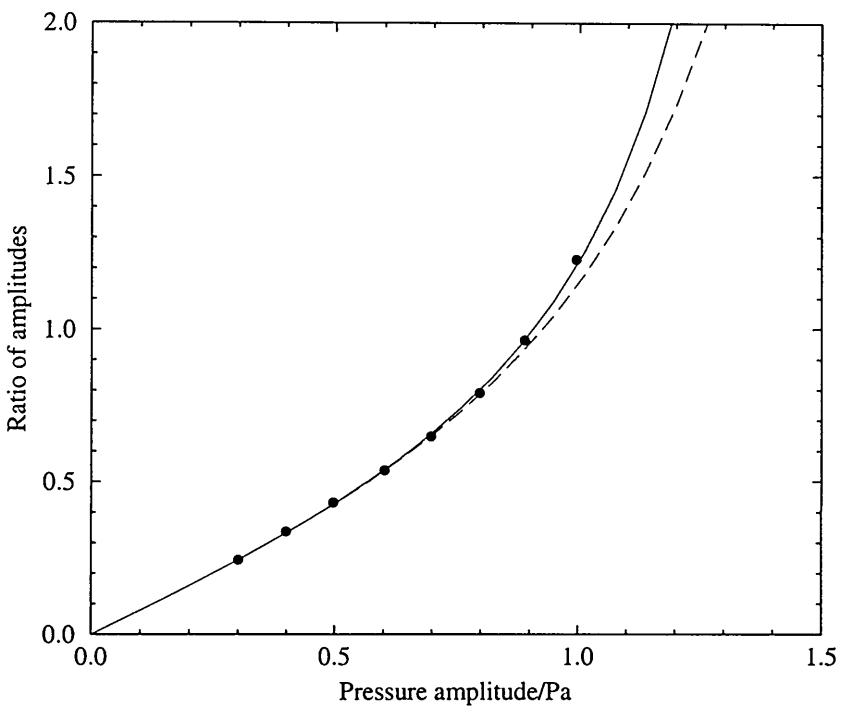

Figure 6.6: Variation of the ratio of amplitudes with antinodal pressure amplitude for acoustic frequency, f_m = 660 Hz. The points are the measured values derived by frequency domain analysis. The solid line indicates the expected theoretical behaviour of the ratio from the tabulated values in figure 6.1 and the dashed lined indicates the behaviour from the small α approximation (with $\rho = 1.2$ kgm^{-3} and $c = 343.5$ms^{-1}).

It can be seen from figure 6.6 that a decrease in the pressure amplitude at the rigid end results in a decrease to the ratio of amplitudes. The side peaks gradually die away until they are indistinguishable from the noise level in the spectrum. At this point the particle displacement amplitude is small compared to the fringe spacing and the central peak in the spectrum results from the moving fringes passing across the near stationary particles. The lowest measurable ratio is determined by the smallest side peak amplitude that can be measured above the noise level. For the Doppler signals considered here, the smallest ratio was 0.252 ± 0.004 which corresponds to a particle velocity amplitude $u_m = 1.06 \pm 0.02$ mms^{-1}, measured for $|p| \simeq 0.30$ Pa. The measured ratio values agree very well with the expected behaviour. The small argument approximation agrees with the measured values for $|p| \leq 0.6$ Pa (i.e. $\alpha \leq 1.0$). Above this value, the approximation no longer holds resulting in an underestimation of the ratio compared with the measured values. The uncertainty in the average ratio of amplitudes is less than 3 % for a set of 20 Doppler signals.

A constant pressure amplitude was maintained at the end of the tube while sets of 20 Doppler signals were recorded for several different acoustic frequencies in the range of 660 Hz to 4 kHz. The chosen frequencies were approximately resonances of the loudspeaker-tube system. Magnitude spectra calculated from individual Doppler signals produced by different acoustic frequencies are illustrated in figure 6.7. The spacing between peaks reflects the acoustic frequency, f_m. As the acoustic frequency is increased, the spacing between side peaks increases and the heights of the side peaks decrease. Both the particle displacement amplitude and particle velocity amplitude

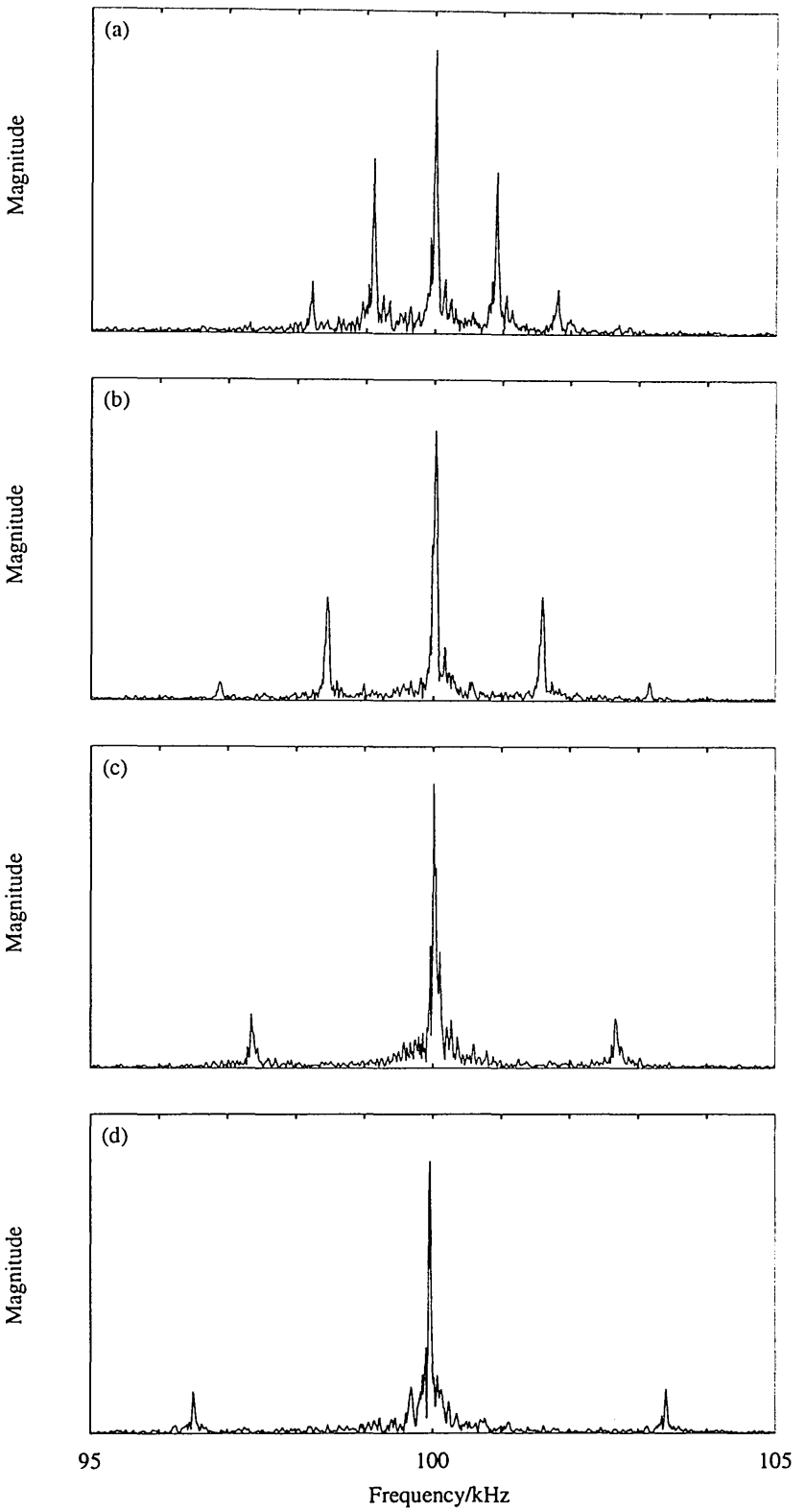

Figure 6.7: Magnitude spectra calculated from Doppler signals produced by an acoustic field with antinodal pressure amplitude $|p| \simeq 1.0$ Pa and (a) with $f_m = 900$ Hz,(b) 1570 Hz, (c) 2660 Hz, and (d) 3450 Hz.

diminish with an increase in f_m while maintaining a constant pressure amplitude.

The average value of the ratio of the first side peak amplitude to the central peak amplitude was calculated for each set of Doppler signals and the results are displayed in figure 6.8. The points are the measured ratio values derived by frequency domain analysis, the solid line corresponds to the theoretical behaviour of the ratio using the calculated values in figure 6.1, and the dashed line corresponds to the behaviour of the ratio using the approximation for small α in equation 6.3. The uncertainties in the measured ratio values are too small to be displayed on the graph. The x axis in figure 6.1 was rescaled using $f_m = \sqrt{2}/(\rho c \alpha \Lambda)$, and $\rho = 1.2$ kgm^{-3} and $c = 343.5$ ms^{-1}.

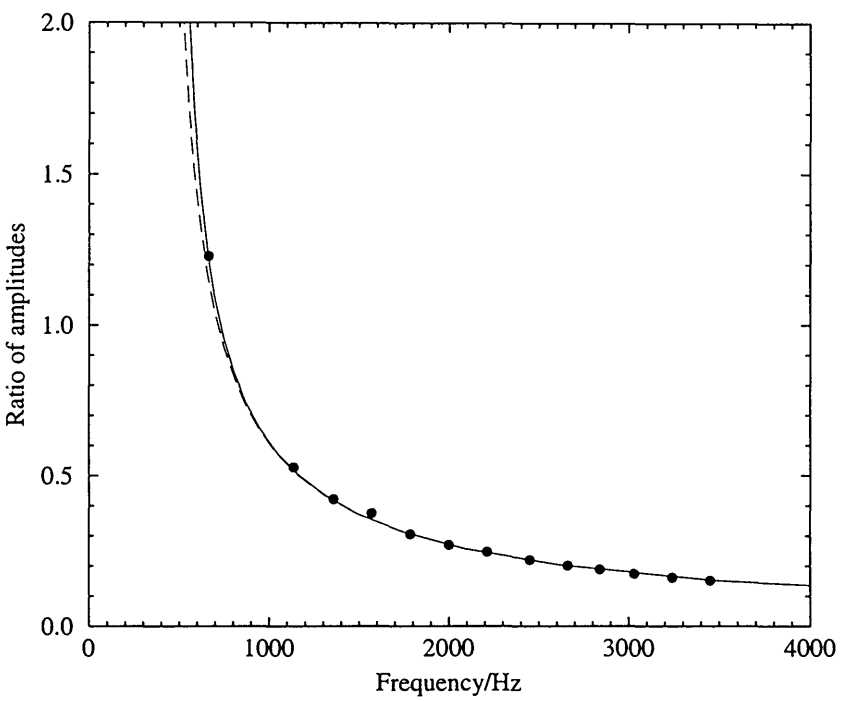

Figure 6.8: Variation of the ratio with acoustic frequency for RMS antinodal pressure amplitude $|p| \simeq 1.0$ Pa. The points are the measured values derived by frequency domain analysis, the solid line indicates the expected theoretical behaviour of the ratio from the tabulated values in figure 6.1, and the dashed lined indicates the behaviour from the small α approximation (with $\rho = 1.2$ kgm^{-3} and $c = 343.5$ms^{-1}).

From figure 6.8 it can be seen that the ratio of amplitudes decreases with an increase in the acoustic frequency while maintaining a constant antinodal pressure amplitude. The side peaks gradually die away until they are indistinguishable from the noise level, leaving only the central peak in the frequency spectrum. As the acoustic frequency increases the particle displacement decreases. The displacement will be small compared to the fringe spacing and the scattered light results from the fringes moving over the near stationary particles. Only the central peak is produced in the frequency spectrum. The lowest measurable ratio is determined by the smallest side peak amplitude that can be measured above the noise level. The measured values correspond very well with the expected behaviour of the ratio and the small argument approximation is valid for $f_m > 1$ kHz (i.e. $\alpha \leq 1.0$). For frequencies below 1 kHz, the ratio is underestimated by equation 6.3.

Mean particle velocity amplitude

Figure 6.9 (a) shows the distribution of particle velocity amplitude, measured using the interpolation method and the calculated values in figure 6.1, for a set of 20 Doppler signals generated by an acoustic field with $f_m = 660$ Hz. The mean particle velocity amplitude and standard uncertainty were calculated to be $\bar{u}_m = 3.43 \pm 0.01$ mms^{-1}. The distribution of particle velocity amplitude determined using the small argument approximation for the same set of signals is illustrated in figure 6.9 (b). The mean particle velocity amplitude and standard uncertainty were found to be $\bar{u}_m = 3.55 \pm 0.02$

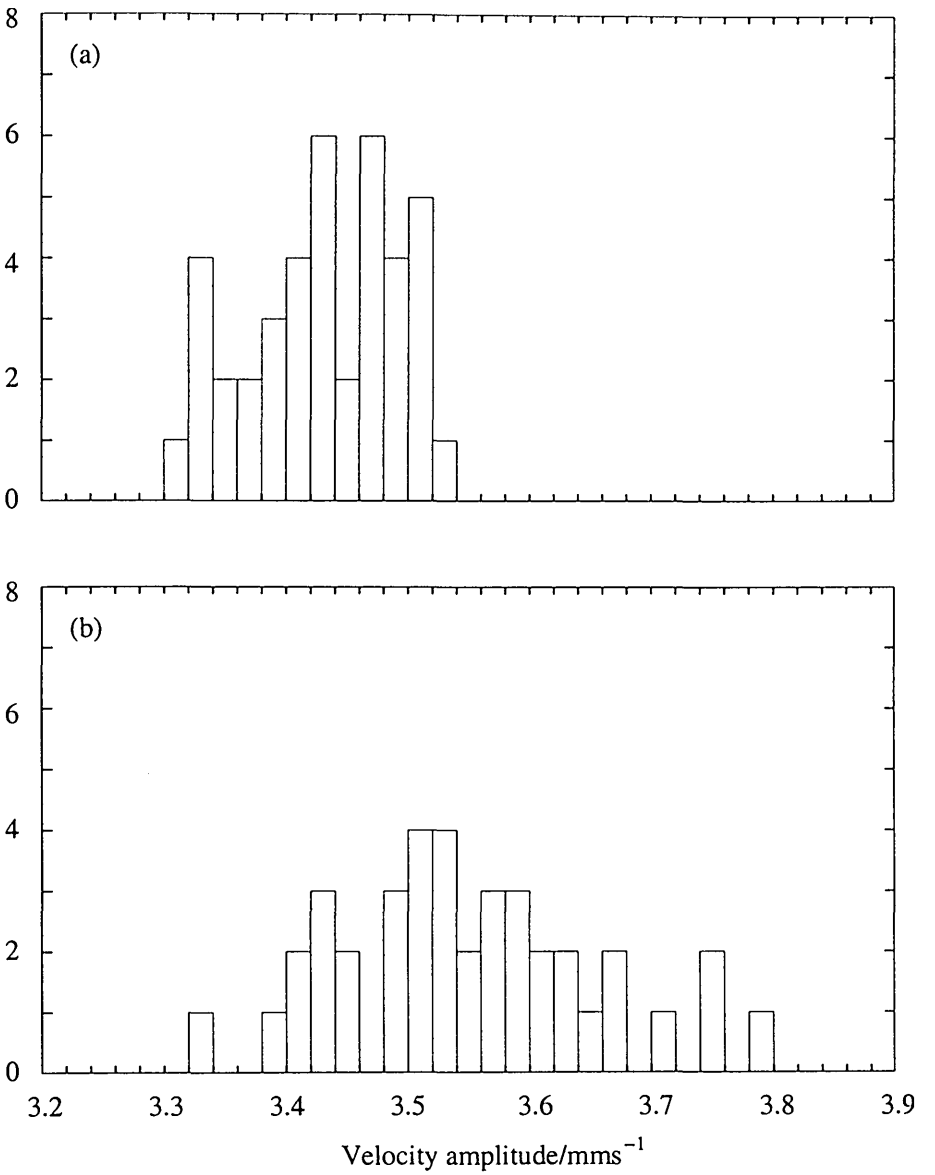

Figure 6.9: (a) Distribution of particle velocity amplitude measured using frequency domain analysis on a set of 20 Doppler signals subjected to an acoustic field with $f_m = 660$ Hz. The mean value of particle velocity amplitude $\bar{u}_m = 3.43 \pm 0.01$ mms^{-1}. (b) Distribution of particle velocity amplitude calculated using the small argument approximation in equation 6.3 for the same set of signals. The corresponding mean value is $\bar{u}_m = 3.55 \pm 0.02$ mms^{-1}.

mms^{-1} which is larger than the velocity obtained using the interpolation method. For the LDA measurements, $\alpha \sim 1.6$. It can be seen from figure 6.1 that using equation 6.3 to determine α from $J_1(\alpha)/J_0(\alpha)$ over estimates the argument compared to the method that uses values calculated from the tables of Bessel functions. Subsequently, a greater value of mean particle velocity amplitude is obtained. The greater spread of velocity values in the second graph is also a direct result of the inaccuracy of the small argument approximation for $\alpha \sim 1.6$.

There is no appreciable difference between particle velocity amplitude calculated from the interpolation method and particle velocity amplitude calculated from the small argument approximation method when $\alpha \leq 0.6$. For the results in figure 6.6 (i.e. $f_m = 660$ Hz), the small argument approximation gives exactly the same particle velocity amplitude as the interpolation method when the RMS antinodal pressure amplitude, $|p| \leq 0.4$ Pa. For the results in figure 6.8 (i.e. $|p| \simeq 1.0$ Pa), the same particle velocity amplitude is obtained when the acoustic frequency, $f_m \geq 2$ kHz.

Dynamic range

The measurements displayed in figure 6.10 were performed with an acoustic frequency $f_m = 660$ Hz. The RMS antinodal pressure amplitude was varied between 0.1 Pa and 1.0 Pa (a corresponding SPL range of 74 dB to 94 dB). The gradient of the best fit straight line to the measured points corresponds to a characteristic impedance of 412 $Pasm^{-1}$. The characteristic impedance calculated from a record of the environmental

conditions was between 410 Pasm^{-1} and 414 Pasm^{-1} for the LDA measurements. The lowest measurable acoustic particle velocity amplitude was $\bar{u}_m \simeq 1$ mms^{-1}, which corresponded to $|\bar{p}| \simeq 0.3$ Pa derived from the probe microphone. For a velocity amplitude lower than this value, the side peaks in the magnitude spectrum are indistinguishable from the noise level. From a study of the sets of Doppler signals recorded for different acoustic frequencies in the range of 660 Hz to 2 kHz, the lowest measurable acoustic particle velocity amplitude was determined to be $\bar{u}_m \simeq 1$ mms^{-1}. Equation 3.62 defines the theoretical upper limit to the measurement of particle velocity amplitude and for the continuous signal LDA system this is $u_m < 0.4$ ms^{-1}.

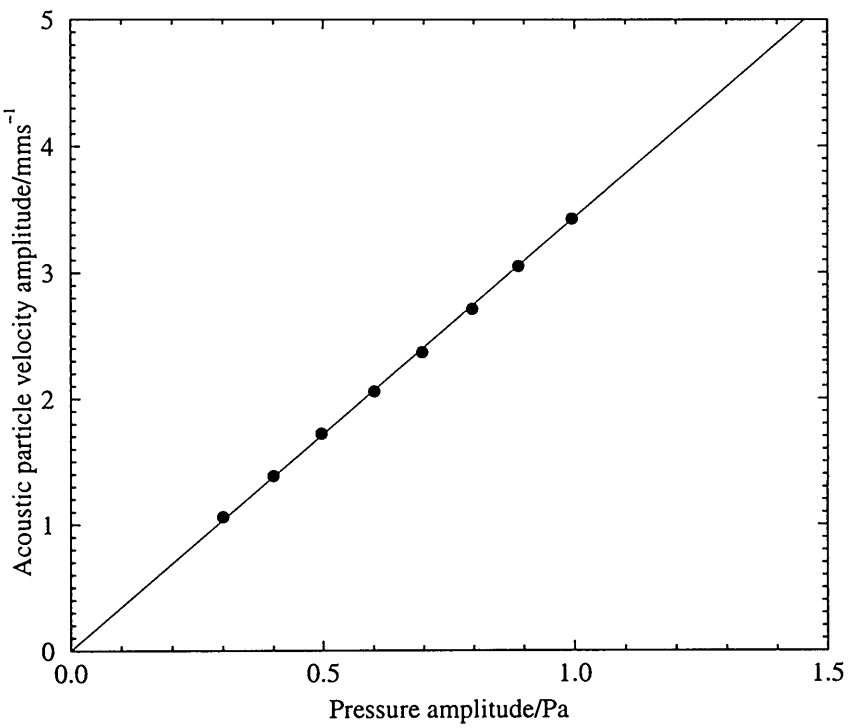

Figure 6.10: LDA measurements of acoustic particle velocity amplitude at a velocity antinode, using frequency domain analysis, against probe microphone measurement of antinodal pressure amplitude. The acoustic field had a frequency of $f_m = 660$ Hz.

Uncertainty in velocity amplitude

For RMS pressure amplitudes in the range of 0.3 Pa to 1.0 Pa and acoustic frequencies in the range of 660 Hz to 4 kHz, the total uncertainty in the measurement of the acoustic particle velocity amplitude was found to be between 0.010 mms^{-1} and 0.045 mms^{-1} (i.e $u_u < 2$ % of $\bar{u}_m$). This involves frequency domain analysis performed on 20 Doppler signals, i.e. 40 values of u_m. The uncertainty in the LDA velocity amplitude measurement is an order of magnitude smaller than the size of mean flow velocity measured in section 6.4.

6.5.4 Conclusions

The acoustic particle velocity amplitude in a standing wave has been measured using frequency domain analysis. The uncertainty in the measurement was evaluated by considering the calculation of the fringe spacing, the measurement of acoustic frequency, and the standard deviation of the mean value of velocity amplitude. The heights of the peaks in the magnitude spectra generated from the captured Doppler signals follow the behaviour defined by the equations relating particle velocity amplitude and Bessel functions. The small argument approximation in equation 6.3 is valid for $\alpha \leq 0.6$. The smallest velocity amplitude that can be measured in the frequency range of 660 Hz to 2 kHz was $\bar{u}_m \simeq 1$ mms^{-1}. Measurements have been performed in the frequency range of 660 Hz to 4 kHz for $\bar{u}_m \simeq 3.5$ mms^{-1} and with a total uncertainty of less than 2%.

6.6 Measurement of velocity using Hilbert transform analysis

Hilbert transform analysis is used to extract instantaneous velocity from the captured Doppler signals, thus allowing the velocity amplitude to be determined. The inherent problems associated with this signal processing technique are highlighted, the distribution of the velocity amplitude in a set of measured Doppler signals is examined, and the associated uncertainty is evaluated. The dynamic range of the Hilbert transform technique is also considered.

6.6.1 Signal Processing

The instantaneous particle velocity is extracted from the Doppler signal using the Hilbert transform demodulation technique described in section 3.6.1 and the program developed by Hann and Greated [46]. Figure 6.11 illustrates the velocity curve obtained from the Doppler signal shown in figure 6.2. The instantaneous pressure curve, obtained from the probe microphone voltage signal and the phase response of the probe microphone (see figure 5.2), is plotted against the same time scale. It can be seen that the pressure is $\pi/2$ out of phase with velocity as predicted in section 5.3. The positive frequency magnitude spectrum of the instantaneous velocity curve, also shown in figure 6.11, is used to determine the particle velocity amplitude.

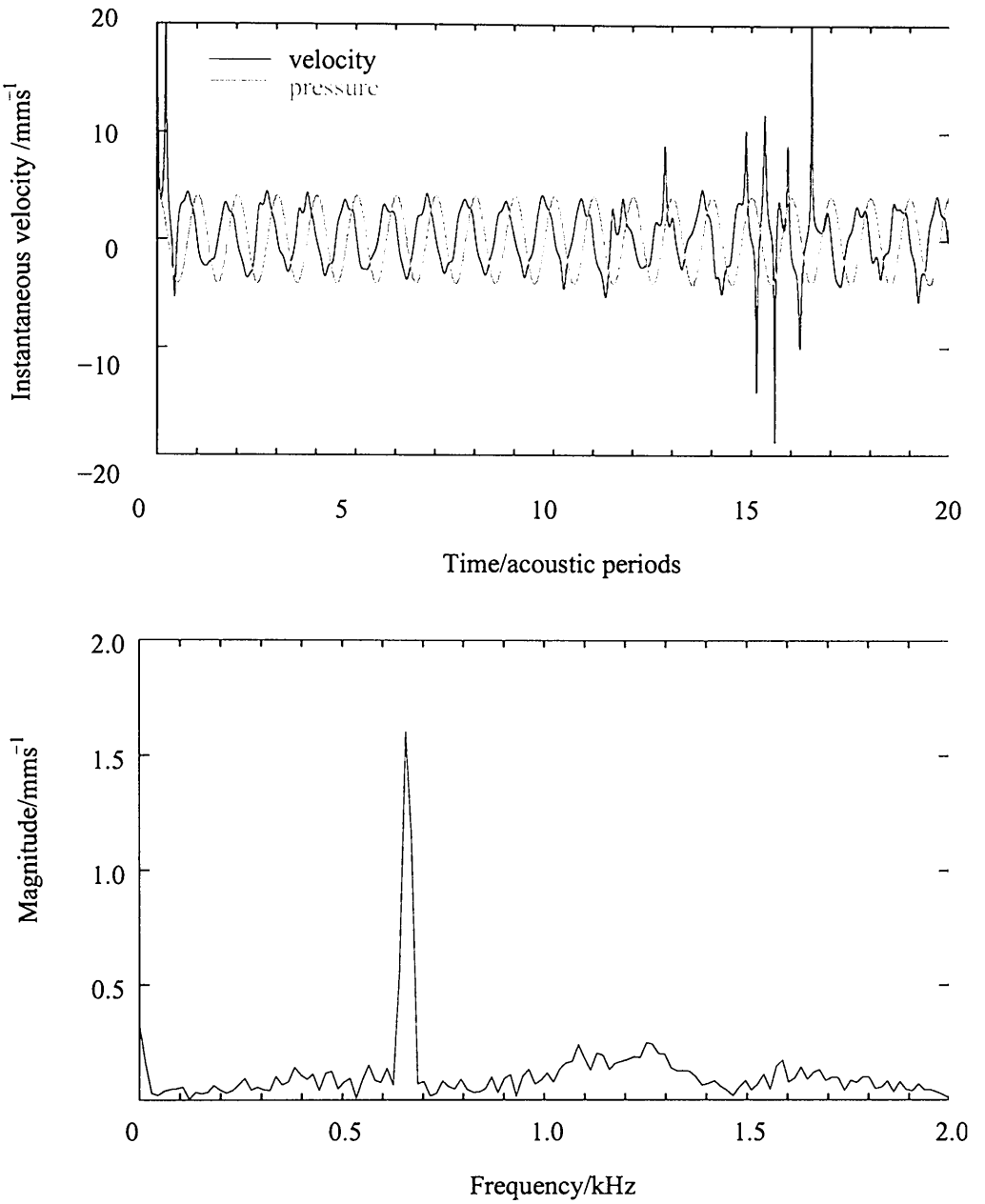

Figure 6.11: The instantaneous velocity extracted from the Doppler signal displayed in figure 6.2. The instantaneous pressure obtained from the probe microphone voltage signal is plotted against the same time scale (but with differing amplitude scale). Also shown is the magnitude spectrum of the instantaneous velocity curve. The degradation of the velocity curve affects the magnitude spectrum and hence the measurement of particle velocity amplitude.

The velocity curve in figure 6.11 highlights the inherent problems associated with the Hilbert transform technique. The velocity curve is obtained from the windowed and bandpass filtered Doppler signal. Dividing the signal by the window function reduces the quality of the curve at the beginning and end. From figure 6.2, it can be seen that the amplitude of the Doppler signal is degraded over the first 15 to 17 acoustic periods. This degradation or signal dropout is due to a small seeding particle concentration in the probe volume, which scatters an insufficient amount of light into the detector. The degraded section of the Doppler signal not only affects the instantaneous velocity curve over the same region but also affects, to some extent, the entire curve over the whole sample time. The quality of the instantaneous velocity curve affects the subsequent measurement of particle velocity amplitude.

6.6.2 Results and discussion

The LDA measurements were performed with acoustic frequencies in range of 660 Hz to 2 kHz and RMS antinodal pressure amplitudes in the range of 0.1 Pa to 1.0 Pa (a corresponding SPL range of 74 dB to 94 dB).

Mean particle velocity amplitude

The distribution of particle velocity amplitude, determined using the Hilbert transform routine for a set of 20 Doppler signals recorded with $f_m = 660$ Hz, is displayed in figure 6.12. The mean value of particle velocity amplitude was measured to be

$\bar{u}_m = 3.40 \pm 0.02$ mms^{-1}. This is less than the value obtained by frequency domain analysis of the same set of signals (see figure 6.9). The individual amplitude measurements are spread over a wider range of velocities than with frequency domain analysis. Therefore, the standard deviation and associated uncertainty is larger with the Hilbert transform method than with frequency domain analysis. As was highlighted in the previous section, any degradation of the Doppler signal affects the instantaneous velocity curve and results in an inferior measurement of the particle velocity amplitude.

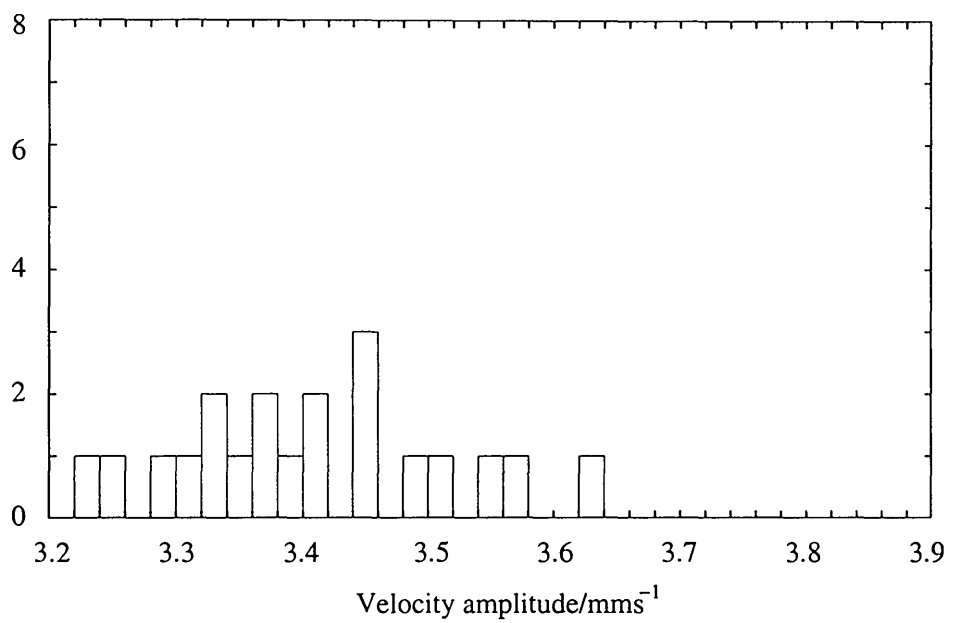

Figure 6.12: Distribution of particle velocity amplitude, measured using Hilbert transform analysis to extract instantaneous particle velocity, for a set of 20 Doppler signals subjected to an acoustic field with frequency, $f_m = 660$ Hz. The mean particle velocity amplitude, calculated from the magnitude spectra of the velocity curves, is $\bar{u}_m = 3.40 \pm 0.02$ mms^{-1}.

Dynamic range

The measurements displayed in figure 6.13 were performed with an acoustic frequency of $f_m = 660$ Hz. The RMS antinodal pressure amplitude was varied in the range of 0.1 Pa to 1.0 Pa (a corresponding SPL range of 74 dB to 94 dB). The lowest measurable acoustic particle velocity amplitude was determined to be $\bar{u}_m \simeq 1$ mms^{-1}, recorded for a pressure amplitude of $|\bar{p}| \simeq 0.3$ Pa derived from the probe microphone signal. Below this RMS pressure amplitude, the instantaneous velocity can no longer be extracted using the Hilbert transform technique as the velocity curve is very degraded, due to the small particle displacement amplitude. In figure 6.13, the gradient of the best fit straight line to the measured points corresponds to a characteristic impedance of 424 Pasm^{-1}. This value is greater than the characteristic impedance calculated from the environmental conditions (i.e. $410 - 414$ Pasm^{-1}) because the LDA measurements underestimate the particle velocity amplitude (by up to 0.75 dB) when compared to the probe microphone measurements. From the sets of Doppler signals recorded for acoustic frequencies in the range of 660 Hz to 2 kHz, the lowest measurable acoustic particle velocity amplitude was found to be $\bar{u}_m \simeq 1$ mms^{-1}.

In section 3.6.2 it was explained that the Hilbert transform is not well defined unless the Doppler signal has a narrow bandwidth. If the bandwidth is too narrow frequency resolution, and hence velocity information, is lost. From equation 3.66, the theoretical upper limit to the measurement of particle velocity amplitude, using the Hilbert transform demodulation routine, is $u_m < 0.33$ ms^{-1}.

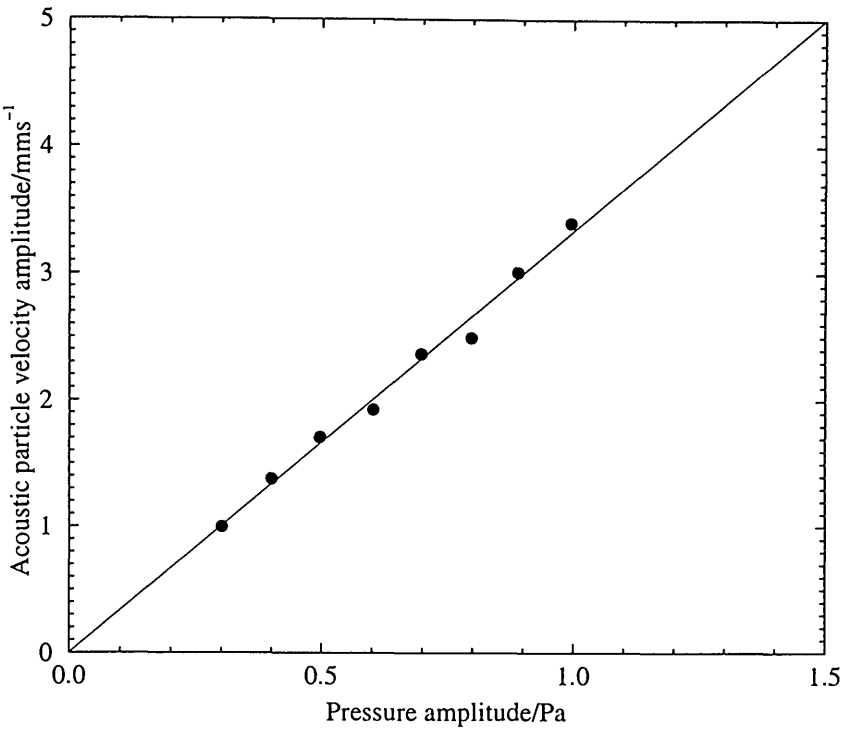

Figure 6.13: LDA measurements of acoustic particle velocity amplitude at a velocity antinode, using Hilbert transform analysis, against probe microphone measurement of antinodal pressure amplitude. Performed with $f_m = 660$ Hz.

Uncertainty in velocity amplitude

The uncertainty in the measurement of acoustic particle velocity amplitude using Hilbert transform analysis is evaluated in a similar way to the method described in section 6.5.2. In this case, 20 measurements of velocity amplitude are derived and the contribution to the uncertainty in the mean value is determined by the standard deviation, $u_A = \sigma_A/\sqrt{n}$. The program used to extract the instantaneous velocity requires the value of the fringe spacing. So the uncertainty in the fringe spacing, σ_Λ, contributes to the overall uncertainty in the measurement of particle velocity amplitude. The total uncertainty is found by combining the two individual components using a root sum

square to give $u_u = \sqrt{\sigma_\Lambda^2 + u_A^2}$. For the Hilbert transform derived measurements, the uncertainty is between 0.025 mms^{-1} and 0.040 mms^{-1} (i.e. less than 2.5% of $\bar{u}_m$) for $f_m < 4$ kHz and RMS antinodal pressure amplitude in the range 0.3 Pa to 1.0 Pa. This is slightly larger than the uncertainty associated with frequency domain analysis but it is still an order of magnitude smaller than the measured mean flow velocity.

6.6.3 Conclusions

The Hilbert transform analysis method has been used to extract instantaneous particle velocity from Doppler signals recorded with RMS antinodal pressure amplitude in the range 0.3 Pa to 1.0 Pa and acoustic frequency in the range 660 Hz to 4 kHz. The mean value of velocity amplitude is generally less than the value obtained by frequency domain analysis of the same set of signals. Degradation or dropout of the Doppler signal affects the quality of the instantaneous velocity curve and the magnitude spectrum, from which the velocity amplitude is deduced. The lowest measurable acoustic particle velocity amplitude was determined to be $\bar{u}_m \simeq 1$ mms^{-1}, recorded for an RMS $|\bar{p}_m| \simeq 0.3$ Pa derived from the probe microphone. The Hilbert transform results underestimate the velocity amplitude by up to 0.75 dB compared to the probe microphone measurements. The uncertainty associated with the Hilbert transform measurement is slightly larger than the uncertainty associated with the frequency domain analysis measurement.

6.7 Measurement of pressure amplitude

The pressure amplitude derived from LDA measurements of acoustic particle velocity amplitude is compared to the pressure amplitude derived from the probe microphone measurements. The uncertainty associated with the LDA measurement of pressure amplitude is evaluated along with the uncertainty in the discrepancy between LDA and probe microphone measurements. The frequency domain and Hilbert transform methods of analysing Doppler signals are assessed and results are presented for several frequencies of standing wave.

6.7.1 Signal Processing

The computer program described in section 6.5 uses frequency domain analysis to obtain the mean value of acoustic particle velocity amplitude, $\bar{u}_m$, for the sets of measured Doppler signals. The mean value of the RMS pressure amplitude, $|\bar{p}|$, is obtained by the program from the corresponding sets of probe microphone signals and a measurement of the magnitude response. The computer program described in section 6.6 uses Hilbert transform analysis to extract the instantaneous velocity from the measured Doppler signals. Particle velocity amplitude is determined from the magnitude spectrum of the velocity curve allowing the mean value of velocity amplitude to be calculated for the sets of measured Doppler signals. The computer program described in section 5.4 calculates the characteristic impedance from measurements of the air

temperature, the atmospheric pressure, and the relative humidity.

The discrepancy between the pressure amplitude derived from LDA measurements and the pressure amplitude derived from the probe microphone measurements is determined using the equation

$$D = 20 \log \left(\frac{\bar{p}_m}{|\bar{p}|} \right) \tag{6.12}$$

where

$$\bar{p}_m = \frac{\rho c \bar{u}_m}{\sqrt{2}} \,. \tag{6.13}$$

$\sqrt{2}$ is required in equation 6.13 to give the RMS pressure amplitude from the LDA measurement of peak particle velocity amplitude.

6.7.2 Uncertainty analysis

The characteristic acoustic impedance is required to calculate the pressure amplitude at the end of the tube from the acoustic particle velocity amplitude (see section 5.3). The uncertainties in the calculation of ρ and of c are estimated to be $u_\rho = 0.025\%$ and $u_c = 0.05\%$, respectively. These values are combined with the total uncertainty in the particle velocity amplitude (see section 6.5.2) to give the overall uncertainty in the acoustic pressure amplitude derived from the LDA measurements. The individual contributions are expressed as percentages of their respective values and combined

using a root sum square to give

$$u = \sqrt{u_\rho^2 + u_c^2 + \sigma_\Lambda^2 + \sigma_{fm}^2 + u_A^2}\,. \tag{6.14}$$

In equation 6.14 it has been assumed that the individual components are statistically independent of each other. The number of values used to establish the mean velocity amplitude is 40 or 20 depending on whether frequency domain analysis or Hilbert transform analysis was used. The uncertainty in the discrepancy between LDA derived pressure amplitude and the probe microphone derived pressure amplitude is given by

$$u_D = 20 \log \left(1 + \frac{\sqrt{u^2 + u_p^2}}{100} \right) \tag{6.15}$$

where u_p is defined in equation 6.11.

The probe tube forms part of the rigid termination of the standing wave tube. As the probe diameter is very small compared to the tube diameter it is assumed that the effect on the impedance when it forms part of the termination is negligible.

6.7.3 Results and discussion

For the measurements of acoustic velocity amplitude displayed in figure 6.9, the mean RMS pressure amplitude derived from the probe microphone readings was found to be $|\bar{p}| = 0.995 \pm 0.001$ Pa. Using frequency domain analysis and the interpolation

method of deducing the Bessel function argument, the mean particle velocity amplitude and associated uncertainty were determined to be $\bar{u}_m = 3.426 \pm 0.012$ mms^{-1}. From the calculated values of ρ and c and using equation 6.13, the RMS pressure amplitude at the end of the tube is $p_m = 0.992 \pm 0.005$ Pa. Thus, the probe microphone and the LDA measurements agree to within the calculated uncertainties. From equation 6.12 and equation 6.15, the discrepancy between pressure amplitude derived from the LDA measurements and pressure amplitude derived from the probe microphone measurements is $D = -0.03 \pm 0.04$ dB. Using frequency domain analysis and the small argument approximation (see equation 6.3), $\bar{u}_m = 3.548 \pm 0.017$ mms^{-1} giving $p_m = 1.027 \pm 0.005$ and the discrepancy, $D = 0.27 \pm 0.04$ dB. The pressure amplitude derived from LDA measurements is greater than the probe microphone readings because the small argument approximation overestimates the size of α.

Applying Hilbert transform analysis to the same set of Doppler signals (see figure 6.12), $\bar{u}_m = 3.398 \pm 0.024$ mms^{-1} giving $p_m = 0.984 \pm 0.007$ Pa. The uncertainty in the pressure amplitude derived from the LDA measurements is greater for Hilbert transform analysis than frequency domain analysis because the uncertainty in the mean particle velocity amplitude is larger. The discrepancy, $D = -0.10 \pm 0.06$ dB, indicates that the pressure amplitude is lower than the probe microphone measurements. Signal dropout can influence the quality of the instantaneous velocity curve, and hence affects the subsequent measurement of particle velocity amplitude, yielding a pressure amplitude lower than the probe microphone derived value.

Figure 6.14 shows the discrepancy between the pressure amplitude derived from the LDA measurements in figure 6.10 and the mean pressure amplitude derived from the probe microphone, versus $|\bar{p}|$. It can be seen from the graph that the LDA and probe microphone measurements are in good agreement for the range of pressure amplitudes considered as the discrepancy is within ± 0.1 dB. For mean pressure amplitude $|\bar{p}| > 0.5$ Pa, the uncertainty in the discrepancy, $u_D < 0.1$ dB. For mean pressure amplitude 0.3 Pa $\leq |\bar{p}| \leq 0.5$ Pa, the uncertainty in the discrepancy, $u_D < 0.15$ dB. Below 0.3 Pa, the side peaks are indistinguishable from the noise level present in the frequency spectrum and no value for particle velocity can be evaluated. The size of the uncertainty in the discrepancy increases with decreasing pressure amplitude. This is because the magnitude of the uncertainty in the $\bar{u}_m$ is approximately 0.02 mms^{-1} and as the velocity amplitude decreases the resulting contribution to the uncertainty in LDA derived pressure amplitude, and hence the uncertainty in the discrepancy, increases.

The discrepancy between the pressure amplitude derived from the LDA measurements in figure 6.13 and the mean pressure amplitude derived from the probe microphone versus $|\bar{p}|$ is displayed in figure 6.15. The Hilbert transform method of analysis is clearly less accurate than the frequency domain analysis technique as the discrepancy is as much as -0.75 dB. The pressure amplitude is underestimated compared to the probe microphone measurements. For $|\bar{p}| \geq 0.4$ Pa, the uncertainty in the discrepancy, $u_D < 0.13$ dB. For $|\bar{p}| < 0.4$ Pa, the uncertainty in the discrepancy, $u_D < 0.20$ dB.

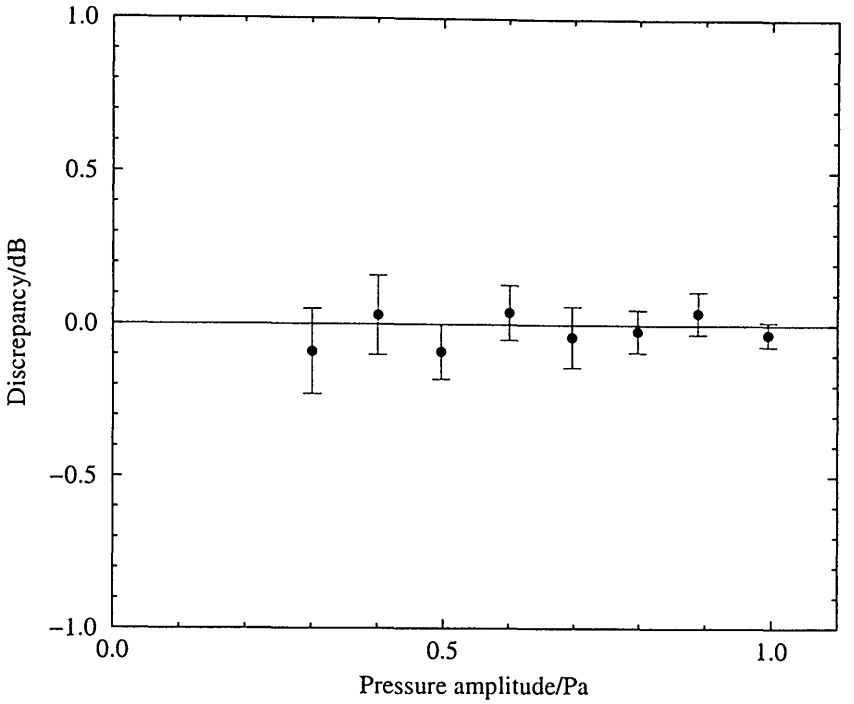

Figure 6.14: Discrepancy between pressure amplitude derived from LDA by frequency domain analysis and pressure amplitude derived from probe microphone, $f_m = 660$ Hz.

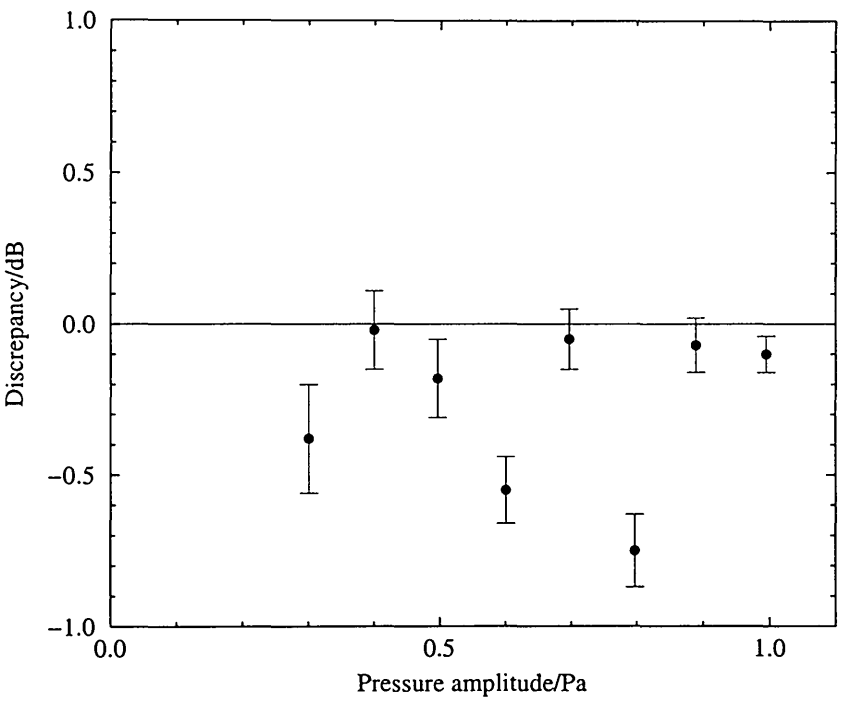

Figure 6.15: Discrepancy between pressure amplitude from LDA by Hilbert transform analysis and pressure amplitude derived from probe microphone, $f_m = 660$ Hz.

The discrepancy between the pressure amplitude derived from LDA measurements and the pressure amplitude derived from the probe microphone measurements versus $|\bar{p}|$ for standing waves with $f_m = 1135$ Hz, 1570 Hz and 2000 Hz are displayed in figures 6.16, 6.17, and 6.18 respectively. The peak particle velocity amplitude is in the range 1.0 mms^{-1} to 3.5 mms^{-1}. For mean pressure amplitude $|\bar{p}| \geq 0.5$ Pa, the discrepancy is within ± 0.10 dB. For 0.4 Pa $< |\bar{p}| < 0.5$ Pa, the discrepancy is within ± 0.17 dB. For $|\bar{p}| \leq 0.4$ Pa, the heights of the first two side peaks approach the magnitude of the noise level in the spectrum and the particle velocity amplitude is overestimated by approximately $+0.1$ dB for all three standing wave frequencies. Below 0.3 Pa, the side peaks become indistinguishable from the noise level present in the magnitude spectra and no value for particle velocity can be evaluated. The uncertainty in the discrepancy: $u_D \leq 0.1$ dB for $|\bar{p}| > 0.5$ Pa and $u_D \leq 0.17$ dB for $|\bar{p}| \leq 0.5$ Pa. This uncertainty increases with decreasing pressure amplitude. The uncertainty associated with the frequency domain analysis method is approximately 0.02 mms^{-1} and so as the particle velocity amplitude decreases, the contribution to the uncertainty in LDA derived pressure amplitude increases.

A constant pressure amplitude ($|\bar{p}| \simeq 1.0$ Pa) was maintained at the end of the tube while measurements were performed for acoustic frequencies corresponding to different resonances of the loudspeaker-tube system, in the range 660 Hz to 4kHz. The discrepancy between pressure amplitude derived from LDA measurements and pressure amplitude derived from probe microphone measurements versus $|\bar{p}|$ are displayed in figure 6.19. The discrepancy, D, is within ± 0.08 dB for $f_m < 2.4$ kHz and within

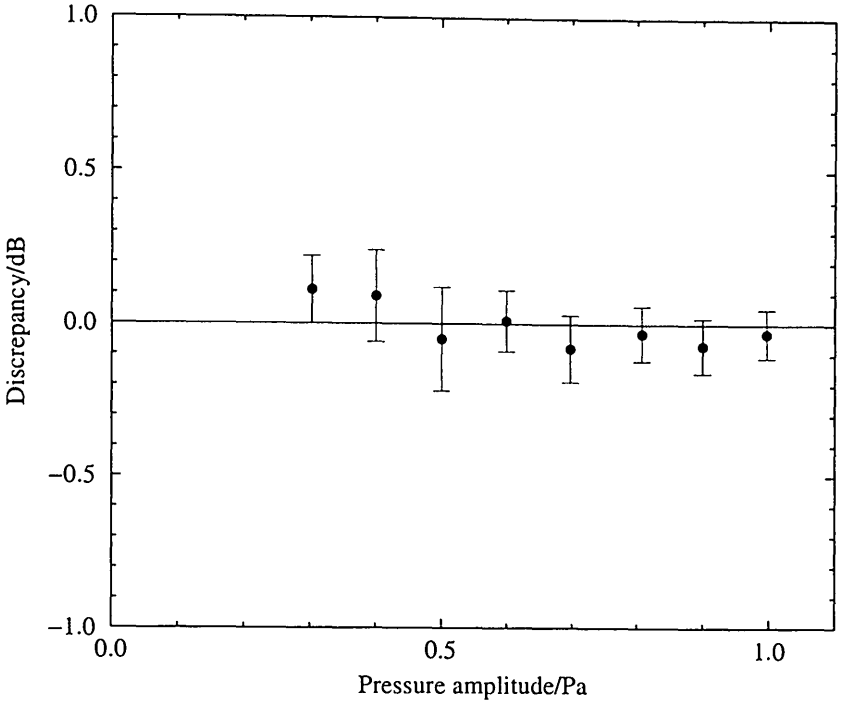

Figure 6.16: Discrepancy between pressure amplitude derived from LDA measurements and pressure amplitude derived from probe microphone, $f_m = 1135$ Hz.

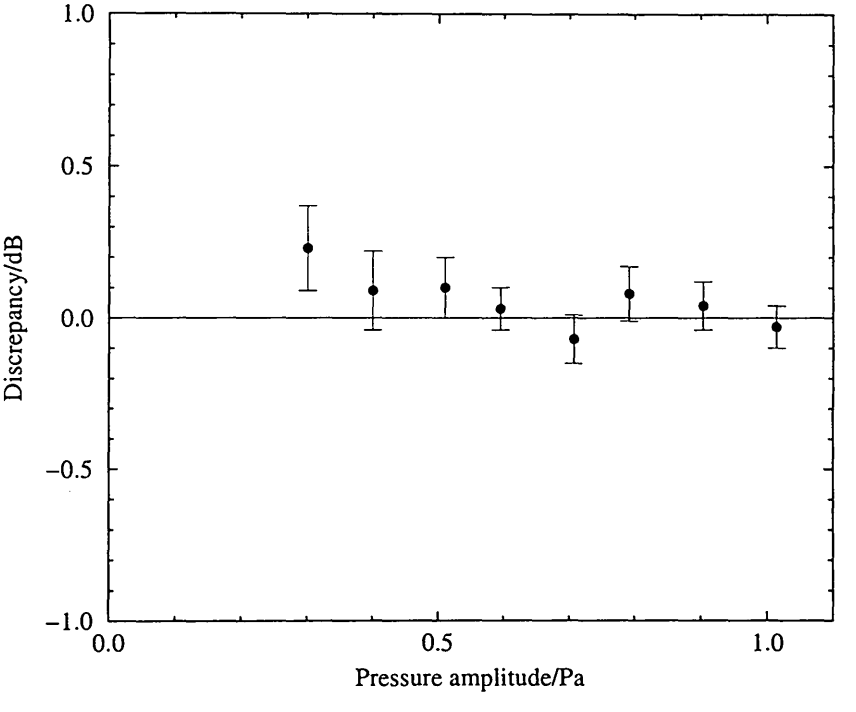

Figure 6.17: Discrepancy between pressure amplitude derived from LDA measurements and pressure amplitude derived from probe microphone, $f_m = 1570$ Hz.

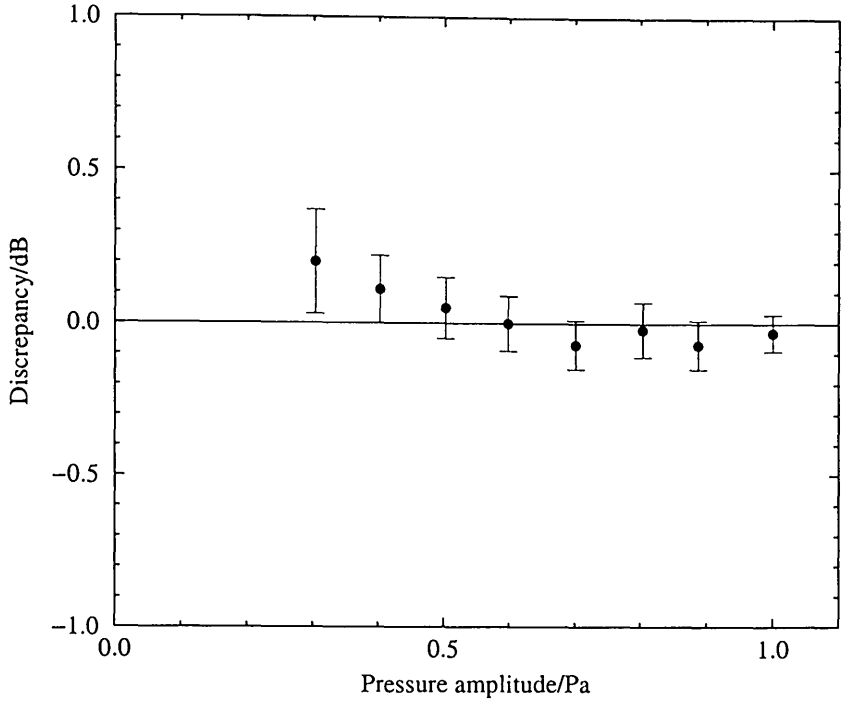

Figure 6.18: Discrepancy between pressure amplitude derived from LDA measurements and probe microphone derived from probe microphone, $f_m = 2000$ Hz.

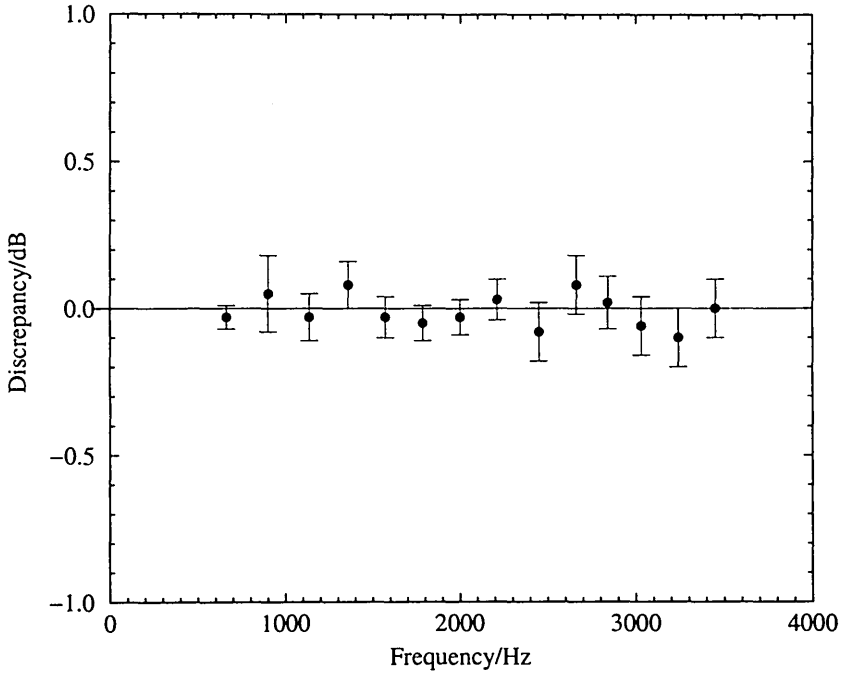

Figure 6.19: Discrepancy between pressure amplitude derived from LDA measurements and pressure amplitude derived from probe microphone. RMS pressure amplitude at end of-tube, $|\bar{p}| \simeq 1.0$ Pa.

± 0.1 dB for $f_m < 4$ kHz. The uncertainty in the discrepancy: $u_D \leq 0.08$ dB for $f_m < 2.4$ kHz and $u_D \leq 0.1$ dB for $f_m < 4$ kHz. The velocity amplitude decreases with increasing frequency and constant pressure amplitude. The size of the uncertainty in the mean velocity amplitude does not change significantly with an increase in frequency (i.e. $u_u = 0.02$ mms^{-1} for $f_m < 4$ kHz). This results in a larger contribution to the uncertainty in the pressure amplitude, and hence to the uncertainty in the discrepancy.

6.7.4 Conclusions

The pressure amplitude at the end of the standing wave tube has been derived from LDA measurements using both frequency domain analysis and Hilbert transform analysis. From a comparison with the probe microphone measurements, frequency domain analysis was found to provide the more accurate results and with a lower associated uncertainty than Hilbert transform analysis. Using frequency domain analysis, pressure amplitude derived from LDA measurements and pressure amplitude derived from probe microphone measurements agree to within ± 0.1 dB for acoustic frequencies in the range of 660 Hz to 2 kHz and peak particle velocity amplitudes in the range of 1.4 mms^{-1} to 3.5 mms^{-1}. For a peak particle velocity amplitude of $|\bar{u}| \simeq 3.5$ mms^{-1} and acoustic frequencies in the range of 660 Hz to 4 kHz, the discrepancy between LDA and probe microphone measurements is within ± 0.1 dB.

6.8 Measurement of microphone sensitivity

The pressure amplitude in a standing wave can be derived from the LDA measurement of acoustic particle velocity amplitude and a knowledge of the characteristic acoustic impedance of air. LDA measurements are now applied to the determination of microphone sensitivity. The sensitivity of the microphone system supplied by the National Physical Laboratory is measured using the standing wave tube apparatus and the results are compared to the sensitivity level obtained by reciprocity calibration.

6.8.1 Experimental method

Measurements were performed using the continuous signal LDA system and the standing wave tube apparatus. The magnitude response of the probe microphone was measured using the apparatus illustrated in figure 5.1, with the NPL microphone system acting as the reference microphone. For this procedure, the magnitude response is simply calculated as V_p/V_N where V_p and V_N are the RMS voltage amplitudes from the probe microphone and NPL microphone system, respectively. Characterizing the probe microphone relative to the NPL microphone system allows the sensitivity of the NPL microphone system to be determined.

The calibration of a microphone, i.e. the measurement of its sensitivity, requires the output voltage for a known sound pressure. The probe microphone is fixed into the rigid end of the standing wave tube and the output voltage is recorded while the LDA

measurement is performed. The measurement of velocity amplitude is used to derive the pressure amplitude at the end of the tube (see equation 6.13). The probe microphone voltage amplitude is divided by the magnitude response to give the equivalent voltage amplitude for the NPL system. The sensitivity of the NPL microphone system is given by

$$M = \left(\frac{V_N}{V_p}\right) \times \left(\frac{V}{\bar{p}_m}\right) \tag{6.16}$$

where V is the RMS voltage amplitude from the probe microphone recorded during the LDA measurement and $\bar{p}_m$ is the pressure amplitude derived from the LDA measurement (see equation 6.13).

The sensitivity level is the microphone sensitivity quoted in terms of decibels relative to a reference level. For a reference sensitivity of 1 VPa^{-1} this is expressed as

$$SL = 20\log(M)\,. \tag{6.17}$$

The NPL microphone system had a sensitivity level, measured by reciprocity calibration at NPL, of -38.00 ± 0.03 dB which is equivalent to a pressure sensitivity of $M_p = 12.59 \pm 0.04$ mVPa^{-1} [80].

6.8.2 Signal processing

Frequency domain analysis is used to extract velocity information from the captured Doppler signals. In previous sections it was observed that this method produced the

most accurate results with the lowest associated uncertainties out of all the signal processing techniques considered. The computer program described in section 6.5 is used to obtain the mean value and standard deviation of the acoustic particle velocity amplitude for a set of Doppler signals. The mean value and standard deviation of the voltage amplitude are also determined for the corresponding set of probe microphone signals. The mean probe microphone voltage amplitude is converted to the equivalent voltage amplitude for the NPL system by the program using the measured magnitude response of the probe microphone. The program described in section 5.4 calculates the characteristic impedance from a record of the environmental conditions.

6.8.3 Uncertainty analysis

The uncertainty in the magnitude response of the probe microphone, relative to the NPL microphone system, is determined by the accuracy with which the voltage amplitudes are measured using the digital voltmeter. The reading is to the nearest 0.001 V giving standard deviations of $\sigma_{V_p} = \sigma_{V_N} = 0.001/\sqrt{3}$ in the probe and NPL microphone voltage amplitudes, respectively. From the set of probe microphone signals, the uncertainty in the mean voltage amplitude is $u_V = \sigma_V/\sqrt{n}$ where σ_V is the standard deviation of the mean value and n is the total number of values (i.e. $n = 20$). The uncertainties in the LDA velocity amplitude measurement and the pressure calculation have been discussed in section 6.5.2 and section 6.7.2, respectively.

As the individual components of the microphone sensitivity calculation are the re-

sult of independent measurements, they are expressed as percentages of their respective values and combined as a root sum square to give the total uncertainty in the sensitivity. This may be expressed as

$$u_M = \sqrt{\sigma_{V_p}^2 + \sigma_{V_N}^2 + u_V^2 + u^2} \tag{6.18}$$

where u is defined in equation 6.14.

The uncertainty in the measured sensitivity level is therefore given by

$$u_{SL} = 20 \log\left(1 + \left[\frac{u_M}{100}\right]\right) \tag{6.19}$$

where the reference sensitivity is 1 VPa^{-1}. Microphone sensitivity is a function of frequency. The NPL microphone system was calibrated using the reciprocity technique for a range of frequencies and at a particular sound pressure level. It is assumed that for the range of acoustic frequencies (i.e. 660 Hz to 2 kHz) and for the RMS pressure amplitude (i.e. $|p| \simeq 1.0$ Pa or an equivalent SPL of 84 dB) considered in this study, the sensitivity of the NPL microphone system remains constant.

6.8.4 Results and discussion

Measurements were performed for frequencies of standing wave, which correspond to resonances of the loudspeaker tube system, in the range of 660 Hz to 2 kHz. The

measurements of the sensitivity level of the NPL microphone system are displayed in figure 6.20, where the horizontal line corresponds to the calibrated level of -38.00 ± 0.03 dB obtained by reciprocity. For the sensitivity experiment, the mean acoustic particle velocity amplitudes were measured to be between 3.4 mms^{-1} and 4.0 mms^{-1}. It can be seen from the graph that the measured sensitivities agree with the calibrated value to within $\pm$ 0.1dB and that the uncertainty in the measured sensitivity level, $u_{SL} \leq 0.1$ dB. For the measurement of sensitivity performed at an acoustic frequency of $f_m = 1785$ Hz, $SL = -37.92 \pm 0.05$. Although this lies above the horizontal, it is still consistent with the calibrated level which has an associated uncertainty of ± 0.03 dB.

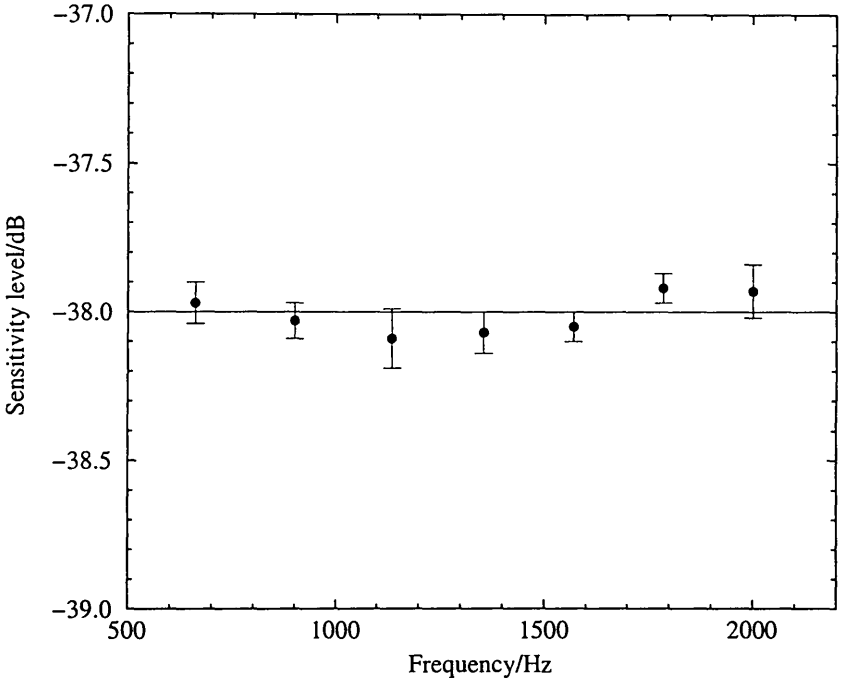

Figure 6.20: Sensitivity level derived from LDA measurements and probe microphone voltage readings. The horizontal line corresponds to the calibrated sensitivity level of -38.00 ± 0.03 dB, obtained by reciprocity.

The calibration measurements presented here do not yield standardized sensitivity in accordance with the International Electrotechnical Commission [23] (as described in section 2.5), because the acoustic field generated inside the glass tube is neither a true pressure field nor a free field. However, the results do suggest that there is potential for the further development of the LDA calibration technique for use in such environments.

6.8.5 Conclusions

The sensitivity of a microphone has been measured using the continuous signal LDA system, the standing wave tube apparatus, and the frequency domain analysis method. Pressure amplitude derived from LDA measurements of particle velocity amplitude and the probe microphone output voltage signal are used to calculate the sensitivity level of the reference microphone, provided the frequency response of the probe can be determined. The uncertainty in both the sensitivity and sensitivity level has been evaluated. The measured sensitivity levels agree to within ± 0.1 dB of the calibrated level and the uncertainty associated with the measurement is ≤ 0.1 dB.

6.9 Summary

The principle of calculating acoustic particle velocity amplitude from a ratio quantity that relates acoustic displacements to the wavelength of laser light was introduced. An

acoustic field of single frequency generates a Doppler signal of the form of a frequency modulated wave. The amplitudes of the peaks in the frequency spectrum are related to Bessel functions of the first kind. The behaviour of the zero order and first order Bessel functions can be used to determine the particle velocity amplitude.

The experimental method employed with the continuous signal LDA system and the standing wave tube apparatus was explained. Measurements of the small mean flow velocity in the standing wave tube were performed using frequency domain analysis on the captured Doppler signals produced by the particle motion. The magnitude of the mean flow velocity and the windowing operation applied to the sampled Doppler signal both contribute to the peak width in the magnitude spectrum. In theory, the broadening effect due to windowing operation is the dominant effect for the flow speeds measured in the tube. However, the theoretical analysis does not account for the broadening effect due to ambiguity noise in the multi-particle Doppler signal, which also contributes to the spectral peak width. From the LDA measurements, it was observed that the width of the spectral peaks is very narrow compared to the bandwidth of the Doppler signals.

Frequency domain analysis was used to study the behaviour of the heights of the spectral peaks. It was found that the width of the peaks could be ignored and the heights used to deduce velocity amplitude. Hilbert transform analysis allows the instantaneous velocity to be extracted from the measured Doppler signals. However, it was determined to be a less accurate method of calculating particle velocity amplitude

compared to frequency domain analysis because of the problems caused by degradation or signal dropout.

Pressure amplitude at the end of the tube was calculated from the LDA measurements and compared to pressure amplitude derived from probe microphone measurements. The total uncertainty in the pressure calculation was evaluated by considering the individual components of the measurement process. Finally, LDA was used successfully to measure the sensitivity of a microphone. The measurements were in good agreement with the calibrated level, obtained by reciprocity.

Chapter 7

Photon correlation measurement of sound

7.1 Introduction

In the previous chapter, measurements acquired using the continuous signal LDA system were used to evaluate the sound pressure in a standing wave and determine the sensitivity of a microphone. This chapter is concerned with measurements acquired using the photon correlation LDA system. Section 7.2 reviews the form of the ACF of the photomultiplier signal generated by acoustic particle motion. The experimental method employed with the apparatus is explained in section 7.3. Measurements of particle velocity amplitude and pressure amplitude in a standing wave are presented in sections 7.4 and 7.5, respectively. The application of the photon correlation system

to the measurement of microphone sensitivity is detailed in section 7.6. Finally, preliminary measurements performed in a semi-free field environment are presented in section 7.7.

7.2 Autocorrelation function

Interference fringes are formed at the intersection of two laser beams in the dual beam mode LDA configuration. Light scattered onto the surface of a photomultiplier tube by particles transversing the fringe volume is frequency shifted by an amount proportional to the velocity of motion. The detector current is proportional to the light intensity integrated over the detector surface. As was explained in chapter 4, the basis for the photon correlation technique is the interpretation of the photomultiplier signal as a series of discrete pulses. The correlation between the photomultiplier signal, $V(t)$, and a delayed version of the signal, $V(t-\tau)$ gives the autocorrelation function, $R(\tau)$, where τ is called the delay time.

The envelope on the fringe volume due to the Gaussian cross section of the laser beams is described by a weighting function defined in terms of particle position rather than time variables (see equation 4.2). The ACF of this spatial weighting function is given in equation 4.6. In section 4.3, the form of the ACF for acoustic particle motion was deduced by integrating the velocity probability density over the time dependent form of the fringe pattern intensity ACF. The complete description of the time depen-

dent ACF is given in equation 4.33. It involves the interaction of a cosine term with the zero order Bessel function, which has a sinusoidal argument. For an acoustic oscillation in the x direction, the ACF takes the form of a frequency modulated wave with zero carrier. A mean flow in the x direction superimposed onto the acoustic oscillation results in a decay of the ACF.

In practice a digital correlator is used to calculate the ACF from the photomultiplier signal. The number of pulses occurring in consecutive time intervals are observed. A digital correlator contains a finite number of channels (e.g. $n = 200$ channels) spaced at time intervals of $\Delta\tau$ seconds. The measured ACF is a discrete function of $n\Delta\tau$ instead of a continuous function of τ. The complete description of the time dependent discrete ACF is given in equation 4.44.

The acoustic particle velocity amplitude, u_m, and the mean flow velocity, u_0, are deduced from the measured ACF using the peaks and minimums of the zero order Bessel function. For the standing wave experiments considered here, the acoustic particle velocity amplitude will be greater than the mean flow velocity (i.e. $u_m >> u_0$). The first minimum of the Bessel function must occur before the first half period of the sinusoidal argument (see equation 4.43). Digital correlation also imposes limits. The first minimum of the Bessel function must occur after the first sample interval and within the total sample time. The theoretical limits are expressed in equation 4.47.

The measured ACF is more complicated than equation 4.44 suggests. In deriving the form of the ACF for acoustic particle motion it was assumed that the two beam

intensities are equal. However, this is difficult to achieve in practice and was not the case for the apparatus used to acquire the LDA measurements. Differences in the beam intensities are unavoidable and are introduced by the beam splitter. Slight misalignments of the transmitter and detector optics will also affect the measured ACF. The overall result is observed as a damping of the measured ACF. Shot noise and thermal noise, inherent to the conversion of the optical signal by the photomultiplier, may also complicate the measured ACF.

7.3 Experimental method

Measurements were acquired using the photon correlation LDA system described in section 5.6.2 and illustrated in figure 5.8, with the loudspeaker-tube arrangement shown in figure 5.9. The loudspeaker was driven at frequencies close to the resonances of the tube system to generate standing waves inside the rigidly terminated tube. LDA measurements were performed at either the position of the first or second velocity antinode from the rigid end. The photomultiplier signal was passed to the BI-9000AT PCI board which correlates the signal with itself to produce the ACF. A sampling time of $\Delta\tau = 2\mu$s with $n = 80$ channels or a sampling time of $\Delta\tau = 5\mu$s with $n = 160$ channels was used.

The antinodal pressure amplitude at the rigid end was monitored using the probe microphone described in section 5.2. The magnitude response of the probe microphone

was determined using the apparatus shown in figure 5.1 before the acquisition of LDA measurements. A signal generator supplies a sine wave of constant frequency and amplitude to the sound source in the coupler and the resulting probe microphone and reference microphone RMS voltage amplitudes were measured with a digital voltmeter. Equation 5.1 is used to calculate the magnitude response, allowing the probe microphone voltage amplitude to be converted to pressure amplitude (measured in pascals). The uncertainty in the magnitude response is determined by the uncertainty associated with the measurement of voltage amplitudes using the digital voltmeter. The probe microphone voltage amplitude was recorded for each measured ACF.

The air temperature inside the tube was measured using a probe thermometer that could be inserted through the small hole in the rigid end. The atmospheric pressure and relative humidity were recorded using an electronic barometer and the characteristic impedance, ρc, was calculated using the method described in section 5.4. Incense smoke was used to seed the air inside the tube. Whenever seeding was required, the rigid end was removed and a burning incense stick inserted into the tube for a period of approximately 2 seconds. The diameter of the smoke particles ($< 0.5\mu$m) was less than the fringe separation (3.18 μm). The acoustic particle displacements considered in the experiments were in the range $0.1\mu\text{m} < x_m < 6.0\mu\text{m}$.

Without the glass tube attached to the loudspeaker, a set of preliminary measurements were performed in a semi-free field environment. LDA has previously been used in a free field to measure the acoustic particle velocity in front of a loudspeaker.

Greated placed absorbing foam pads on the wall opposite the loudspeaker to prevent the formation of standing waves [18]. Poggi conducted measurements above an absorbing surface to enhance the quality of the free field [81]. No such apparatus was employed here as the purpose of the experiment was simply to demonstrate the potential of the photon correlation LDA system for free field measurements rather than to obtain a detailed set of results.

The loudspeaker was driven at a frequency of 1 kHz or 2 kHz while the LDA measurements were carried out at 20 mm intervals from the loudspeaker. The loudspeaker was moved rather than the transmitter and detector optics. The sound waves are assumed to be plane at the point of measurement and the particle motion caused by only the direct waves. A phase shifter was used to produce a moving fringe pattern within the probe volume. This imposes a frequency shift of $F_s = 50$ kHz on the output signal so that when there is no motion the ACF takes the form of a cosine wave. The haze generator was used to seed the air in the vicinity of the probe volume and the particles have diameters in the range of 1 μm to 4 μm (see section 5.7).

The pressure amplitude at the LDA measurement position was monitored using the NPL microphone system, described in section 5.2, with the microphone diaphragm located underneath the probe volume and kept parallel to the direction of the sound. This corresponds to a 90 ° angle of incidence and the type 4133 cartridge has zero free field correction for frequencies below 2 kHz [58]. The voltage amplitude of the output signal from the NPL system was measured using a digital voltmeter.

7.4 Measurement of velocity

The acoustic particle velocity amplitude and the mean flow velocity amplitude are calculated by analysing the measured autocorrelation function in the time domain. The uncertainty in the velocity amplitude measurement is evaluated by considering the individual contributions to the calculation. The distribution of particle velocity amplitude from a set of measured ACF's is examined and the dynamic range of the photon correlation technique is considered.

7.4.1 Signal processing

The acoustic particle velocity amplitude, u_m, is larger than the mean flow velocity, u_0, for the standing wave tube experiments. From the position of the first minimum in the measured ACF, u_m is calculated. The measured ACF of the photomultiplier signal is generated by the control software supplied with the digital correlator. A computer program was written to extract the information from the raw data files produced by the correlator program. The program normalises the measured ACF and fits the theoretical expression in equation 4.44 to the points around the first minimum. This requires a measurement of the acoustic frequency, f_m, which is obtained directly from the sinusoidal voltage signal used to drive the loudspeaker. The Bessel function of first kind with zero order is calculated, with the sinusoidal argument, using a standard routine in [45]. The program finds the values of u_m and u_0 which minimise the sum of the

squared relative errors, where the squared relative error is defined as the difference between the square of the RHS of equation 4.44 and the squared of the measured ACF, all divided by the square of the measured ACF. A plot of the ACF for the optimum values of u_m and u_0 is generated by the program.

7.4.2 Uncertainty analysis

A detailed uncertainty analysis of the LDA measurement of acoustic particle velocity amplitude for the continuous signal system is presented in section 6.5.1. The uncertainty in the measurement is evaluated by considering the individual components of the calculation. This is relevant to the photon correlation system as several of the components are the same, i.e. the fringe spacing and the acoustic frequency. The analysis is expanded to include aspects of the photon correlation measurement.

The acoustic frequency is obtained directly from the loudspeaker driving signal, using a digital multimeter, to the nearest 1 Hz. Therefore, the standard deviation in the acoustic frequency is $\sigma_{f_m} = 1/\sqrt{3}$ Hz [78]. Assuming the two incoming beams are initially parallel, the sine of the beam angle depends on the distance between the two illuminating beams, $2d$, and the focal length of the focusing lens, f. The uncertainty in the sine of the beam angle will provide the major contribution to the uncertainty in the fringe spacing and is obtained from the expression in equation 6.7. For the transmitter optics of the photon correlation system, $2d = 20$ mm and $f = 100$ mm and $\sigma_d = \sigma_f = 1.0/\sqrt{3}$ mm. This gives the fringe spacing and associated uncertainty to be

$\Lambda = 3.18 \pm 0.02$ μm.

The computer program described in the previous section finds the optimum value of u_m to the nearest 0.01 mms^{-1}, so $\sigma_u = 0.01$ mms^{-1}. The individual components σ_Λ, σ_f, and σ_u are expressed as percentages of their respective values and combined as a root sum square to give

$$u_u = \sqrt{\sigma_\Lambda^2 + \sigma_f^2 + \sigma_u^2} \tag{7.1}$$

the total uncertainty in the measurement of acoustic particle velocity amplitude. In equation 7.1, individual components are the result of independent measurements.

The magnitude response of the probe microphone at a particular acoustic frequency is calculated using equation 5.1. The voltage amplitudes of the probe and reference microphones were measured with a digital voltmeter to the nearest 0.001 V, which gives standard deviations of $\sigma_{V_p} = \sigma_{V_r} = 0.001/\sqrt{3}$ V. These two standard deviations are expressed as percentages and combined as in equation 6.10. The uncertainty in the pressure amplitude derived from the probe microphone is calculated from the uncertainty in the magnitude response and the standard deviation of the probe microphone voltage amplitude reading, σ_V. This is may be written as

$$u_p = \sqrt{\sigma_{V_p}^2 + \sigma_{V_r} + \sigma_V^2} \tag{7.2}$$

provided the individual components are statistically independent. In equation 7.2, the standard deviations are expressed as percentages of their respective values before being

combined.

In section 3.3.3, the variation in the fringe spacing due to the deviation of the focused beam waists from the focal point of the focusing lens was explained. However, the focal length of the focusing lens is $f = 100$ mm and this is large enough for errors arising from the deviation to be considered negligible. The beam distances involved are relatively small (~ 0.05 m) and the measurements are conducted in air. From equation 3.72, for $f_m < 2$ kHz the amplitude of the fringe movement, y_m, is less than 0.5% of the particle displacement amplitude, x_m. Therefore, the acousto-optic effect can also be considered negligible.

7.4.3 Results and discussion

Measurements were performed for a standing wave with $f_m = 660$ Hz. The antinodal pressure amplitude at the end of the tube was varied in the range of 1.0Pa to 10.0 Pa (a corresponding SPL range of 94 dB to 114 dB). A selection of the measured ACF's are illustrated in figure 7.1. A sample time of $\Delta\tau = 5\mu$s with $n = 200$ channels was used. As the RMS antinodal pressure amplitude at rigid end was increased the delay time to the first minimum of the ACF, τ_m, decreases. From equation 4.42, this indicates particle velocity amplitude, u_m, increases with an increase in pressure amplitude, $|p|$. It can be seen that $R(n\Delta\tau)$ decays with $n\Delta\tau$. This indicates the presence of a small mean flow velocity but contributions to the damping may also arise from a mismatch in beam intensities and slight misalignments of the optics.

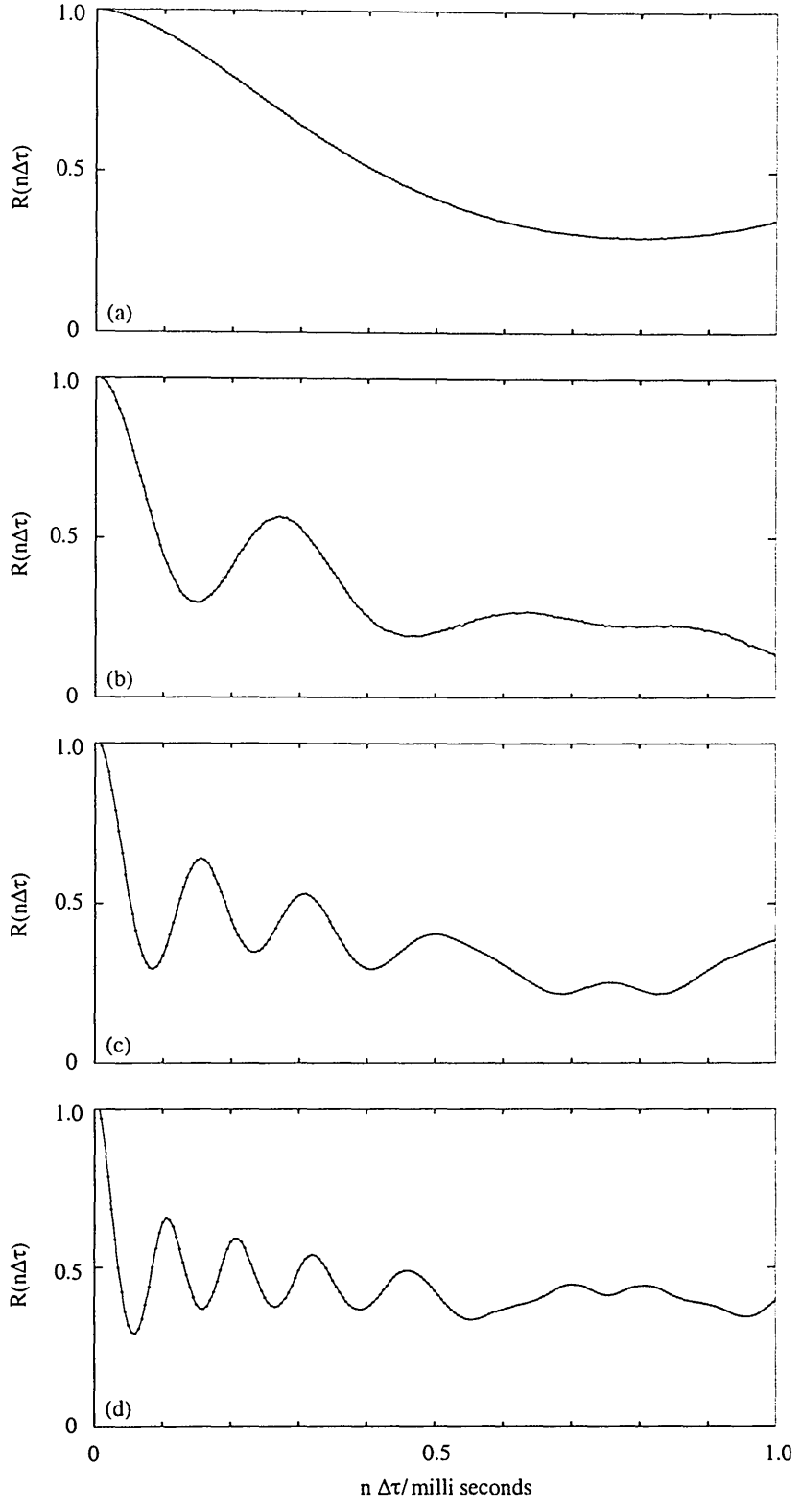

Figure 7.1: Measured ACF for the photomultiplier signal generated by an acoustic field with frequency, $f_m = 660$ Hz. The sample time was $\Delta\tau = 5\mu$s with $n = 200$ channels. RMS pressure amplitude measured at rigid end (a) $|p| \simeq 1.0$ Pa, (b) 4.0 Pa, (c) 7.0 Pa, and (d) 10.0 Pa.

A constant level of pressure amplitude was maintained at the end of the tube while the ACF of the photomultiplier signal was generated for several different acoustic frequencies in the range 660 Hz to 2 kHz. The frequencies corresponded approximately to resonances of the loudspeaker-tube system. A selection of the measured ACF's are illustrated in figure 7.2. Maintaining a constant antinodal pressure amplitude gives the same delay time to the first minimum of each ACF indicating that the particle velocity amplitude remains constant. $R(n\Delta\tau)$ decays with $n\Delta\tau$ indicating the presence of a small mean flow velocity as well as other possible sources of damping.

Figure 7.3 shows the measured ACF from figure 7.2 (d), calculated from the photomultiplier signal generated by a standing wave with antinodal pressure amplitude, $|p| \simeq 5.0$ Pa, and frequency, $f_m = 2$ kHz. The particle velocity amplitude is calculated by fitting the theoretical expression in equation 4.44 to the points leading up to and including the first minimum (i.e channels 10 through to 30) of the ACF. The value of $|u_0|$ was varied between $0 - 1.0$ mms^{-1} in the theoretical expression and the results are displayed in figure 7.3. It can be seen that $\hat{R}(n\Delta\tau)$ follows the form predicted by equation 4.44, i.e. the interaction of the cosine term with the zero order Bessel function, which has a sinusoidal argument. However, the shape of the measured ACF cannot be completely accounted for by a mean flow velocity superimposed onto the acoustic motion as the theoretical expression never completely fits the points. The acoustic particle velocity amplitude was measured by the program to be $u_m = 17.1 \pm 0.1$ mms^{-1}, where the uncertainty in u_m was calculated using equation 7.1. The mean flow velocity was

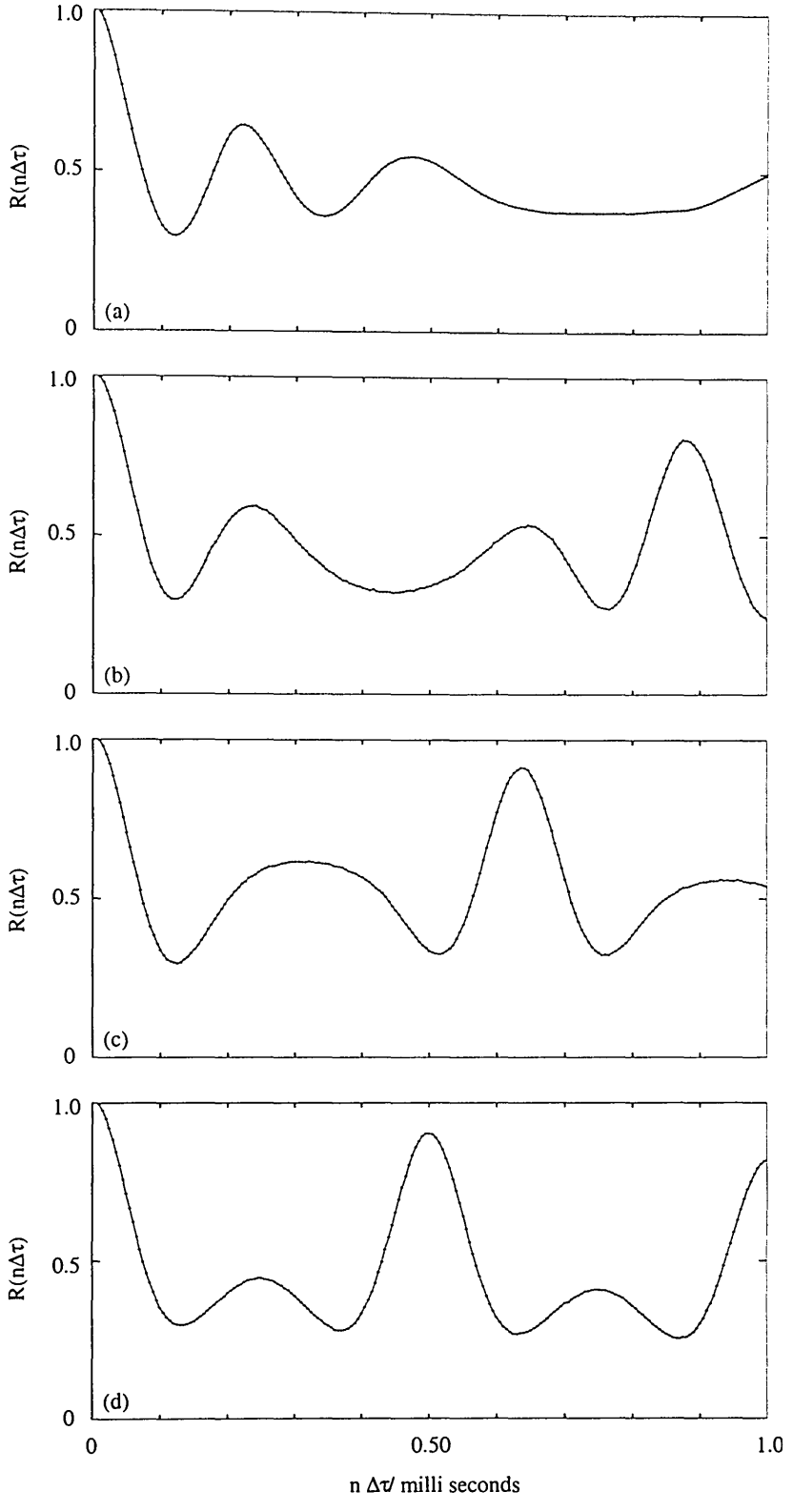

Figure 7.2: Measured ACF for the photomultiplier signal generated by an acoustic field with RMS pressure amplitude measured at rigid end $|p| \simeq 5.0$ Pa and (a) with acoustic frequency $f_m = 660$ Hz, (b) 1135 Hz, (c) 1570 Hz, and (d) 2000 Hz. The sample time was $\Delta\tau = 5\mu$s with $n = 200$ channels.

estimated by the program to be $|u_0| \sim 0.6$ mms^{-1}.

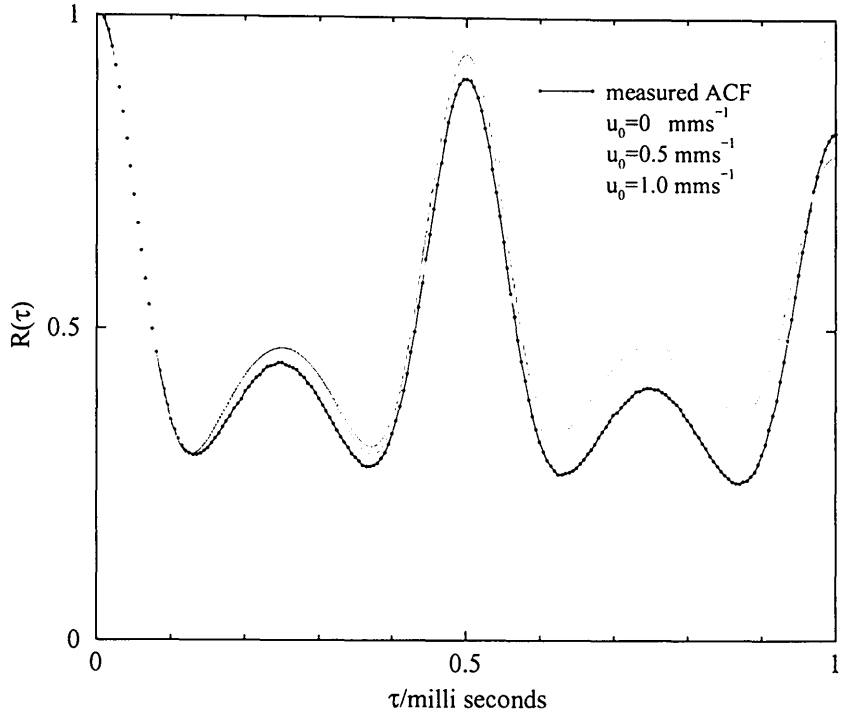

Figure 7.3: A measured ACF for the photomultiplier signal generated by an acoustic field with frequency, $f_m = 2$ kHz. The sample time was $\Delta\tau = 5\mu$s and $n = 200$ channels. Also shown, the ACF calculated by fitting equation 4.44 to channels 10 through to 30 and with $|u_0| = 0$ mms^{-1}, 0.5 mms^{-1}, 1.0 mms^{-1}. The acoustic particle velocity amplitude was determined to be $u_m = 17.1 \pm 0.1$ mms^{-1}.

For the standing wave experiments, the acoustic particle velocity amplitude is calculated from the first minimum of the zero order Bessel function. To see the first minimum the delay time to the first minimum, τ_m, must occur before the first half period of the sinusoidal argument of the Bessel function. This limit is expressed in equation 4.43. Digital correlation also limits the range of velocity amplitudes that can be measured. The first minimum must occur after the first sample interval and within the total sample time. From equation 4.47, the theoretical limits to the measurement of

velocity amplitude are 12 $\text{mms}^{-1} < u_m < 970$ mms^{-1} for $\Delta\tau = 2.0\mu$s with $n = 80$ channels, and 2 $\text{mms}^{-1} < u_m < 390$ mms^{-1} for $\Delta\tau = 5.0\mu$s with $n = 200$ channels. In theory the sample time of $\Delta\tau = 5.0\mu$s allows a smaller value of particle velocity amplitude to be measured than the sample time of $\Delta\tau = 2.0\mu$s. However, using equation 4.43 a more realistic lower limit to the velocity amplitude is $u_m > 4$ mms^{-1} for $f_m \geq 660$ Hz.

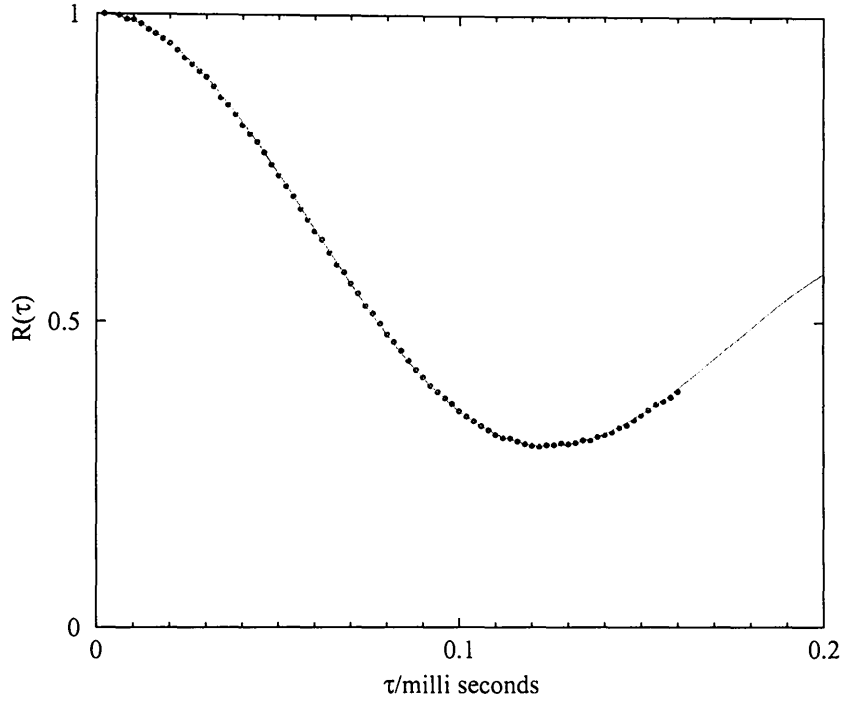

Figure 7.4: A measured ACF for the photomultiplier signal generated by an acoustic field with frequency $f_m = 660$ Hz. The sample time $\Delta\tau = 2\mu$s and $n = 80$ channels. Also shown, the ACF calculated by fitting equation 4.44 to 30 channels before the minimum and 10 after. The acoustic particle velocity amplitude was measured to be $u_m = 15.9 \pm 0.1$ mms^{-1} and the mean flow velocity estimated to be $|u_0| \sim 0.2$ mms^{-1}.

The points in figure 7.4 correspond to the measured ACF ($\Delta\tau = 2\mu$s and $n = 80$ channels) for the photomultiplier signal generated by a standing wave with acoustic

frequency, $f_m = 660$ Hz. The solid line corresponds to the ACF calculated by fitting equation 4.44 to 30 channels before the minimum value and 10 channels after. The acoustic particle velocity amplitude and the mean flow velocity amplitude are measured by the program which finds the values of u_m and u_0 that minimise the sum of the squared relative errors. For the example in figure 7.4, $u_m = 15.9 \pm 0.1$ mms^{-1} and $|u_0| \sim 0.2$ mms^{-1}. The velocity amplitude is within the measurement limits determined by the sample time and the total number of channels. Using a sample time of $\Delta\tau = 2.0\mu$s instead of $\Delta\tau = 5.0\mu$s allows for a more accurate measurement of the particle velocity amplitude, provided u_m is within the measurement limits. This is because the measured ACF contains only the first minimum, which enables a more precise fit of the theoretical expression to the points to be made.

Mean particle velocity amplitude

Figure 7.5 shows the distribution of particle velocity amplitude measured using the least squares fitting procedure for a set of 20 ACF's generated by an acoustic field with frequency, $f_m = 660$ Hz. The sample time of the digital correlator $\Delta\tau = 2\mu$ with $n = 80$ channels. The acoustic particle velocity amplitude was calculated by fitting equation 4.44 to the data points corresponding to 30 channels before minimum point and 10 channels after. For the measurements displayed in figure 7.5, the average value of particle velocity amplitude and standard uncertainty were determined to be $\bar{u}_m = 15.58$ mms^{-1} and $u_A = 0.05$ mms^{-1}, where the standard uncertainty is

calculated using the method described in Appendix C. The total uncertainty in the velocity measurement, found by evaluating the individual components of the calculation, is ± 0.1 mms^{-1}. The average value of the mean flow velocity amplitude was measured to be $|\bar{u}_0| = 0.5 \pm 0.5$ mms^{-1}. It can be seen that the size of the uncertainty in the average value of the mean flow velocity is of the same order of magnitude as the actual value. Therefore, only an estimate of $|u_0|$ may be obtained using the least squares fitting technique.

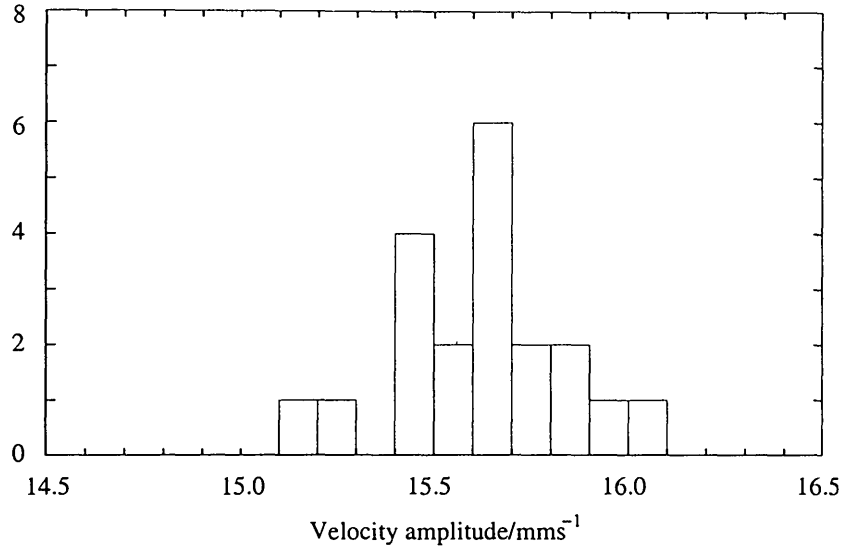

Figure 7.5: Distribution of acoustic particle velocity amplitude for 20 photon correlation measurements conducted with frequency, $f_m = 660$ Hz. The sample time $\Delta\tau = 2\mu$ and $n = 80$ channels. The average value of particle velocity amplitude, $\bar{u}_m = 15.58 \pm 0.05$ mms^{-1}, and the average value of mean flow velocity amplitude, $|\bar{u}_0| = 0.5 \pm 0.5$ mms^{-1}.

Dynamic range

The measurements displayed in figure 7.6 were performed with an acoustic frequency $f_m = 660$ Hz. The RMS antinodal pressure amplitude, measured at the rigid end of the tube, was varied between $4.0 - 5.0$ Pa (a corresponding SPL range of 106 to 108 dB). The sample time $\Delta\tau = 2\mu$s and $n = 80$ channels. The gradient of the best fit straight line to the measured points corresponds to a characteristic impedance of 412 Pasm^{-1} while the characteristic impedance calculated from a record of the environmental conditions was found to be 409 Pasm^{-1}. The uncertainty in the pressure amplitude derived from the probe microphone measurement is ± 0.03 Pa.

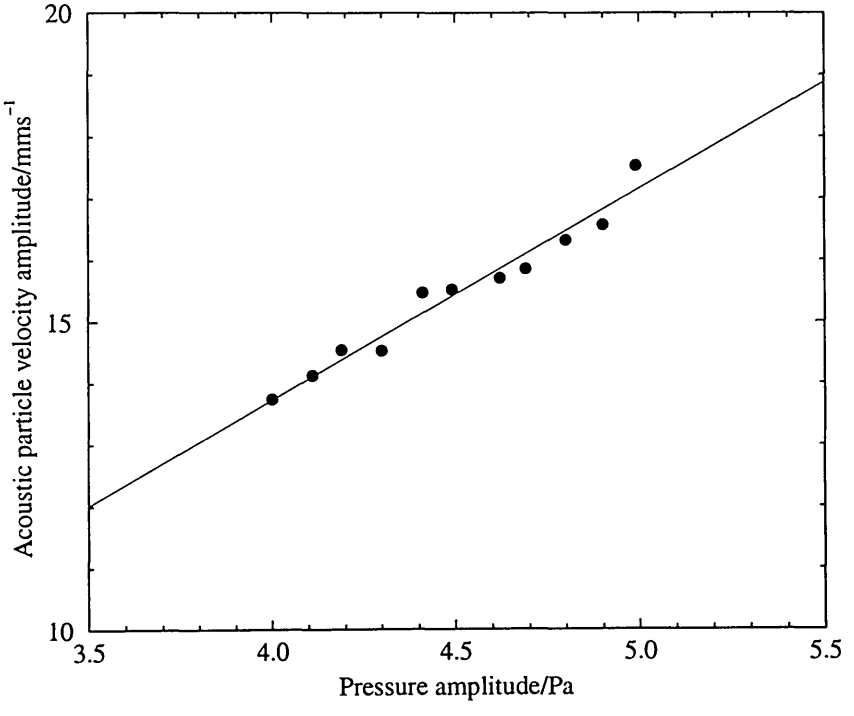

Figure 7.6: Photon correlation measurements of acoustic particle velocity amplitude at a velocity antinode against probe microphone measurement of antinodal pressure amplitude for an acoustic field with frequency, $f_m = 660$ Hz.

The position of the first minimum of the ACF affects the accuracy of the velocity amplitude measurement as a sufficient number of points around the minimum are required to carry out the least squares fitting procedure. If the delay time to the minimum, τ_m, is close to the total sample time, $n\Delta\tau$, the least squares fitting procedure determines the velocity amplitude incorrectly. For a sample time of $\Delta\tau = 2\mu$s, a realistic limit to the delay time to the minimum is $\tau_m < 0.15$ ms which corresponds to the minimum point of the measured ACF located in the first 75 channels. Using equation 4.43, this gives a lower limit to the measurement of velocity amplitude of $u_m > 13$ mms^{-1} for $f_m = 660$ Hz. For the measurements displayed in figure 7.6, u_m was in the range of 13 mms^{-1} to 16 mms^{-1}.

The measurements displayed in figure 7.7 were performed with an acoustic frequency, $f_m = 2$ kHz and with RMS antinodal pressure amplitude varied between $4.0 - 5.5$ Pa (a corresponding SPL range of 106 dB to 109 dB). The sample time $\Delta\tau = 2\mu$s and $n = 80$ channels. The gradient of the best fit straight line to the measured points corresponds to a characteristic impedance of 407 Pasm^{-1} while the characteristic impedance calculated from a record of the environmental conditions was found to be 409 Pasm^{-1}. The uncertainty in the pressure amplitude derived from the probe microphone measurement is ± 0.03 Pa.

The condition that the minimum of the measured ACF must be located within the first 75 channels results in a limit to the measurement of velocity amplitude of $u_m > 15$ mms^{-1} for $\Delta\tau = 2\mu$s and $f_m = 2$ kHz. For the measurements shown in figure 7.7, u_m

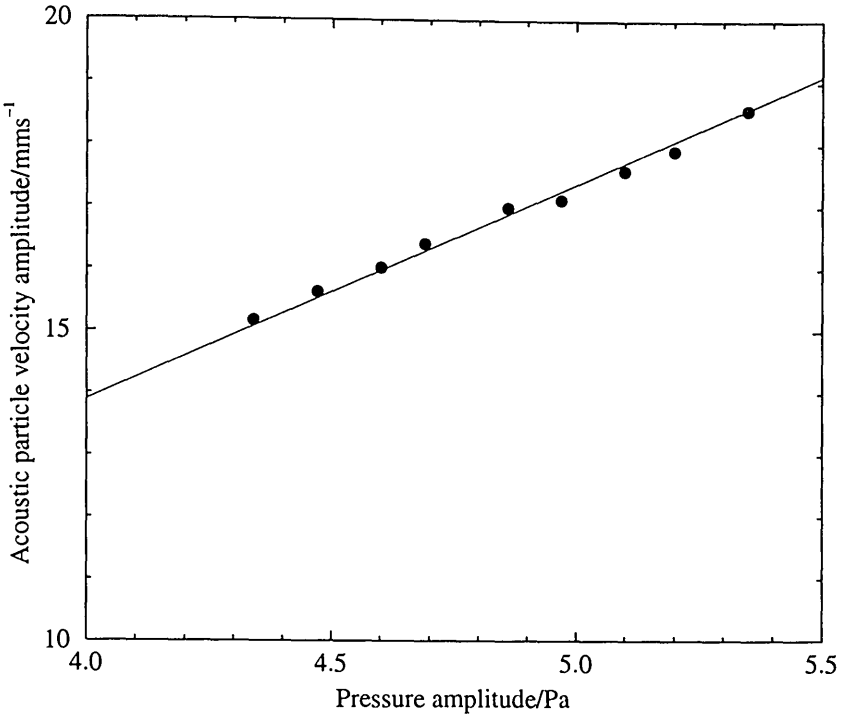

Figure 7.7: Photon correlation measurements of acoustic particle velocity amplitude at a velocity antinode against probe microphone measurement of antinodal pressure amplitude for acoustic field with $f_m = 2$ kHz.

was in the range of 15.2 mms^{-1} to 18.6 mms^{-1}. No measurement of velocity amplitude is possible using the least squares fitting procedure below 15 mms^{-1}, a corresponding RMS antinodal pressure amplitude of approximately $|p| \simeq 4.3$ Pa.

Uncertainty in velocity

For RMS antinodal pressure amplitudes in the range of 4.0 Pa to 5.4 Pa and acoustic frequencies in the range of 660 Hz to 2 kHz, the total uncertainty in the measurement of the acoustic particle velocity amplitude was found to be ± 0.1 mms^{-1} (i.e. $u_u < 1$ % of u_m). This involves the least squares fitting procedure applied to a single photon correlation measurement. Increasing the number of LDA measurements reduces the

standard uncertainty in the mean value of velocity amplitude. For 20 measurements, the standard uncertainty is less than or equal to 0.05 mms^{-1} (i.e. $u_u < 0.4$ % of $\bar{u}_m$). However, the total uncertainty in the acoustic particle velocity amplitude was ± 0.1 mms^{-1}. So averaging 20 measurements does not significantly reduce the total uncertainty in the photon correlation LDA measurement. For 20 measurements, the uncertainty in the average value of mean flow velocity amplitude is of a similar order of magnitude to the average value indicating that only an estimate of $|u_0|$ can be obtained using this technique.

7.4.4 Conclusions

The acoustic particle velocity amplitude in a standing wave has been measured using photon correlation LDA by fitting the theoretical expression for the time dependent ACF to the measured ACF of the photomultiplier signal. The uncertainty in the measurement was evaluated by considering the calculation of the fringe spacing, the measurement of acoustic frequency, and the standard deviation of velocity amplitude. The smallest velocity amplitude that can be measured was 13 mms^{-1} for $f_m \leq 660$ Hz and 15 mms^{-1} for $f_m \leq 2$ kHz. LDA measurements were performed in the frequency range of 660 Hz to 2 kHz for particle velocity amplitudes in the range of 13 mms^{-1} to 18 mms^{-1} and with a total uncertainty of less than 1 %. Averaging 20 measurements was found not to significantly reduce the total uncertainty in the photon correlation LDA measurement.

7.5 Measurement of pressure amplitude

Pressure amplitude derived from photon correlation measurements of acoustic particle velocity amplitude is compared to pressure amplitude derived from probe microphone measurements. The uncertainty associated with the LDA measurement of pressure amplitude is evaluated along with the discrepancy between LDA and probe microphone measurements. Results are presented for several different acoustic frequencies.

7.5.1 Signal processing

The computer program described in section 7.4.1 uses the position of the first minimum in the measured ACF to calculate u_m. By fitting the theoretical expression for the ACF in equation 4.44 to the measured values around the first minimum using a least squares procedure, the program finds the optimum values of u_m and u_0. The computer program described in section 5.4 calculates the characteristic impedance, ρc, from the air temperature, atmospheric pressure and relative humidity.

The discrepancy between the pressure amplitude derived from the LDA photon correlation measurement and the pressure amplitude derived from the probe microphone measurement is determined from

$$D = 20 \log \left(\frac{p_m}{|p|} \right) \tag{7.3}$$

where

$$p_m = \frac{\rho c u_m}{\sqrt{2}} \tag{7.4}$$

and $|p|$ is the RMS pressure amplitude obtained from the probe microphone. The RHS of equation 7.4 is divided by $\sqrt{2}$ to give the RMS pressure amplitude from the LDA measurement of velocity amplitude.

7.5.2 Uncertainty analysis

The characteristic acoustic impedance of the air inside the tube is required to calculate the pressure amplitude at the end of the tube from the measurement of acoustic particle velocity amplitude. The uncertainties in the calculations of ρ and c are $u_\rho = 0.025\%$ and $u_c = 0.05\%$, respectively. These values are combined with the total uncertainty in particle velocity amplitude, which was evaluated in section 7.4.2 and expressed in equation 7.1, to give the overall uncertainty in acoustic pressure amplitude derived from the LDA measurement. Provided the individual contributions are statistically independent, they can be expressed as percentages or their respective values and combined as a root sum square to give

$$u = \sqrt{u_\rho^2 + u_c^2 + \sigma_\Lambda^2 + \sigma_{fm}^2 + \sigma_u^2}\,. \tag{7.5}$$

The uncertainty in the discrepancy between LDA derived pressure amplitude and the probe microphone derived pressure amplitude is given by equation 6.15 where u_p is

defined in equation 7.2.

The probe tube forms part of the rigid termination of the standing wave tube. As the probe diameter is very small compared to the tube diameter it is assumed that the effect on the impedance when it forms part of the termination is negligible.

7.5.3 Results and discussion

For the 20 measurements of acoustic particle velocity amplitude shown in figure 7.5, the average RMS pressure amplitude derived from the 20 probe microphone readings was found to be $|\bar{p}| = 4.54 \pm 0.03$ Pa. From analysis of the measured ACF's in the time domain, using the least squares fitting procedure, the mean particle velocity amplitude and total uncertainty was measured to be $\bar{u}_m = 15.6 \pm 0.1$ mms^{-1}. From the values of ρ and c and using equation 7.4, the RMS antinodal pressure amplitude derived from LDA is calculated to be $p_m = 4.51 \pm 0.03$ Pa. The photon correlation LDA and probe microphone measurements agree to within the calculated uncertainties. From equation 7.3, the discrepancy between the LDA derived pressure amplitude and the probe microphone derived pressure amplitude, $D = -0.06 \pm 0.08$ dB.

Figure 7.8 shows the discrepancy between the pressure amplitude derived from the photon correlation LDA measurements in figure 7.6 and the pressure amplitude derived from the probe microphone versus $|p|$. The measured particle velocity amplitudes were between $13.7 - 17.6$ mms^{-1}. It can be seen from the graph that the discrepancies

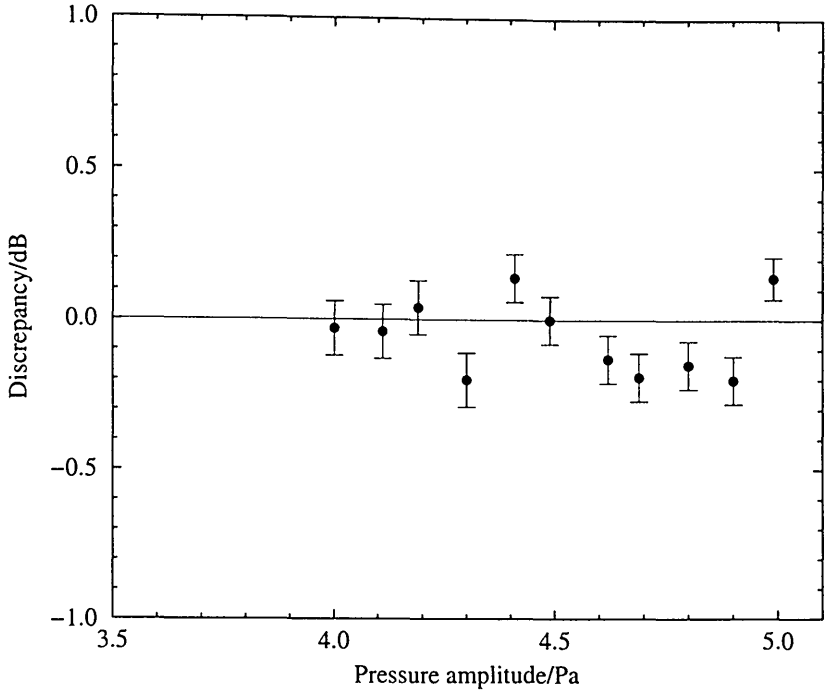

Figure 7.8: Discrepancy between pressure amplitude derived from LDA photon correlation measurement and probe microphone measurement for acoustic field with $f_m = 660$ Hz.

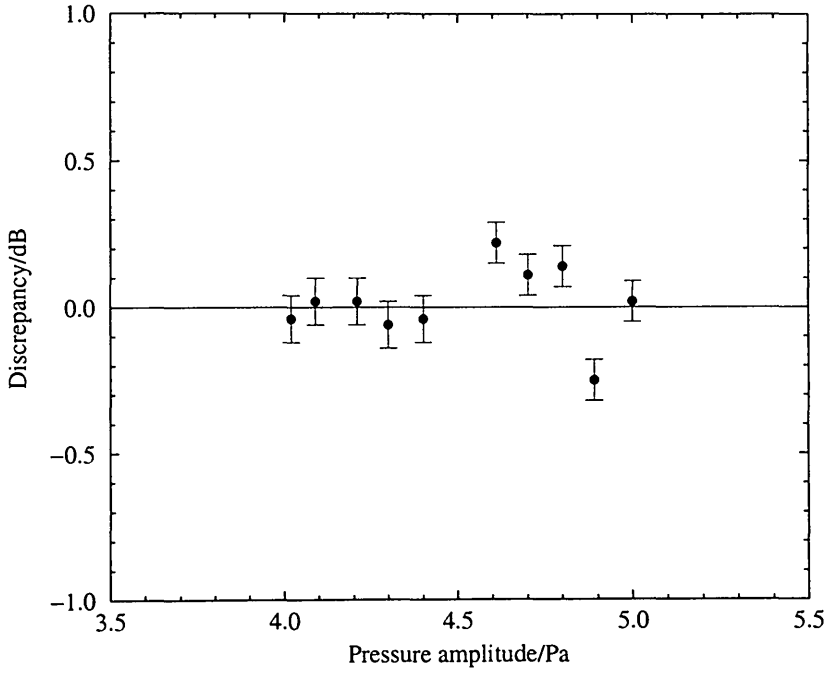

Figure 7.9: Discrepancy between pressure amplitude derived from LDA photon correlation measurement and probe microphone measurement for acoustic field with $f_m = 1135$ Hz.

are within ± 0.2 dB for RMS pressure amplitudes in the range of 4.0 Pa to 5.0 Pa. Below 4.0 Pa, the delay time to the minimum of the measured ACF approaches the maximum delay time, $n\Delta\tau$, and the least squares fitting procedure cannot be used. The uncertainty in the discrepancy is less than 0.1 dB for the range of pressure amplitudes considered. The size of the uncertainty in the discrepancy increases with decreasing pressure amplitude. This is because the uncertainty in the velocity amplitude obtained by the least squares fitting procedure is ± 0.01 mms^{-1}. As particle velocity decreases this results in a larger percentage contribution to the uncertainty in both p_m and D. The uncertainty in the pressure amplitude derived from the probe microphone is less than 1 %.

The discrepancy between the pressure amplitude derived from LDA measurements and the pressure amplitude derived from the probe microphone measurements versus $|\bar{p}|$ for standing waves with $f_m = 1135$ Hz, 1570 Hz and 2000 Hz are displayed in figures 7.9, 7.10, and 7.11 respectively. The measured peak particle velocity amplitudes were between $13 - 18$ mms^{-1} and the RMS antinodal pressure amplitude measured at the end of the tube with the probe microphone was in the range of 4.0 Pa to 5.0 Pa. For $f_m = 1135$ Hz, the discrepancy is within ± 0.25 dB. For $f_m = 1570$ Hz, the discrepancy is within ± 0.15 dB, ignoring the two spurious results at $|p| = 4.5$ Pa and 4.6 Pa. Figure 7.11 shows the discrepancy for the photon correlation LDA measurements in figure 7.7. For $f_m = 2$ kHz, the discrepancy is within ± 0.11 dB. The discrepancy improves with increasing acoustic frequency because at higher acoustic frequencies, i.e. $f_m > 1.5$ kHz, the interaction of the cosine term with the zero order Bessel function in

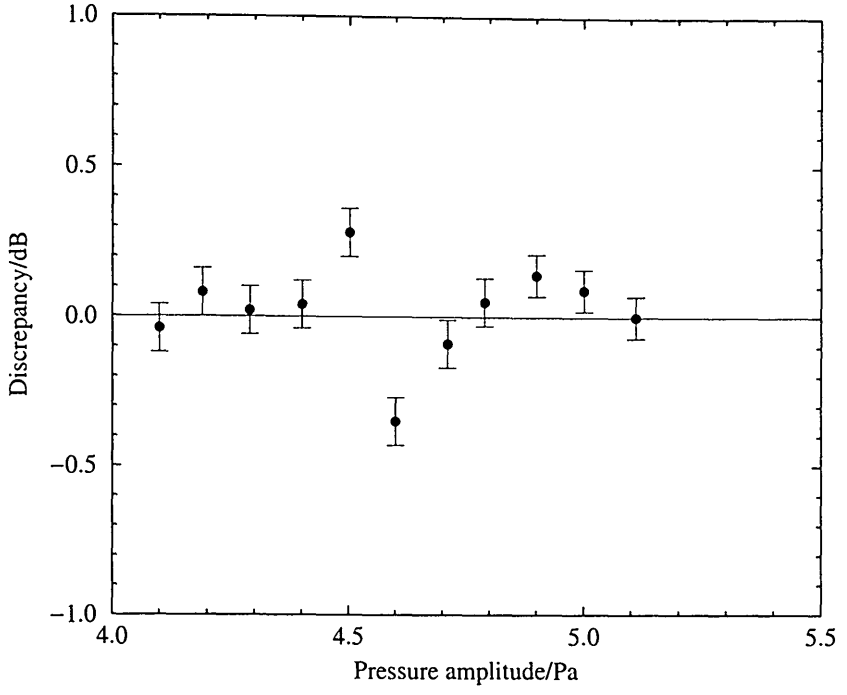

Figure 7.10: Discrepancy between pressure amplitude derived from LDA photon correlation measurement and probe microphone measurement for acoustic field with $f_m = 1570$ Hz.

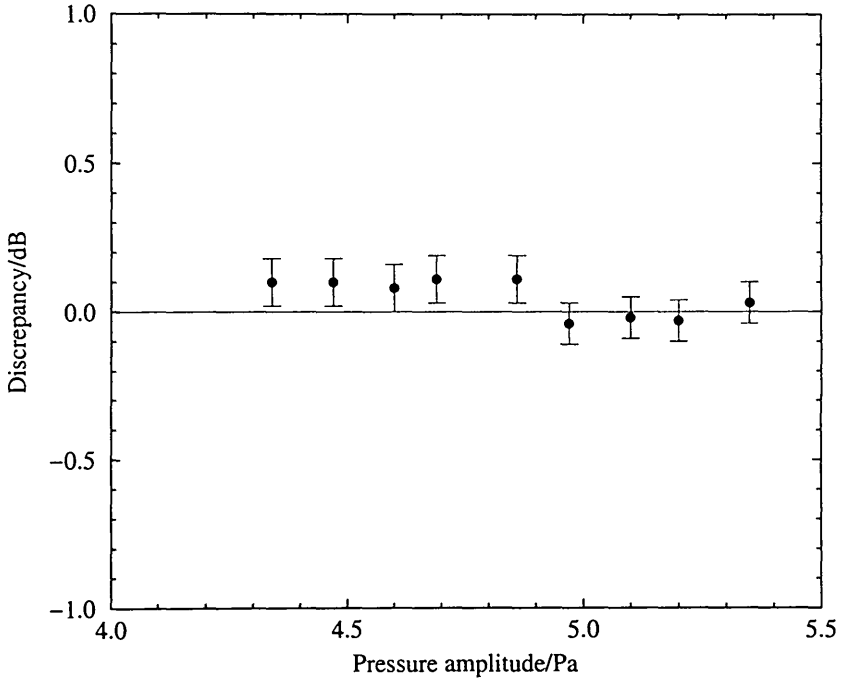

Figure 7.11: Discrepancy between pressure amplitude derived from LDA photon correlation measurement and probe microphone measurement for acoustic field with $f_m = 2000$ Hz.

equation 4.44 is more pronounced. The first minimum of the ACF clearly corresponds to the first minimum of the zero order Bessel function. This allows a more accurate measurement of u_m than with lower acoustic frequencies where the first minimum of the Bessel function can be masked by the cosine term in equation 4.44.

The uncertainty in the calculated discrepancy for $f_m \leq 2$ kHz is approximately ± 0.08 dB for $|p| \geq 4.5$ Pa. However, this uncertainty increases with decreasing pressure amplitude. This is because the uncertainty in the velocity amplitude obtained by the least squares fitting procedure is ± 0.01 mms^{-1} and as particle velocity decreases a larger percentage contribution to the uncertainty in both p_m and D results. The uncertainty in the pressure amplitude derived from the probe microphone is less than 1 %. Below $|p| = 4$ Pa for $f_m < 2000$ Hz and below $|p| = 4.4$Pa for $f_m = 2000$ Hz, the delay time to the minimum of the measured ACF approaches the maximum delay time and the least squares fitting procedure cannot be used.

The results in figure 7.5 suggest that the discrepancy between LDA derived pressure amplitude and probe microphone derived pressure amplitude cannot be improved significantly by averaging a number of measurements. The total uncertainty in u_m is of a similar magnitude to the total uncertainty in $\bar{u}_m$. There is no sizeable change to the uncertainty in the probe microphone derived pressure amplitude when a number of measurements are averaged. Thus, the uncertainty in the discrepancy will not be significantly reduced by averaging several measurements. However, the averaging procedure would improve the quality of the results by removing spurious measurements

such as those observed in figure 7.10 at $|p| = 4.5$ Pa and 4.6 Pa.

The measured ACF cannot be completely accounted for by the theoretical expression in equation 4.44, which describes the form of the ACF for a mean flow velocity superimposed onto an acoustic oscillation. Other sources of damping such as mismatches in beam intensities and the misalignment of transmitter and detector optics contribute to the shape of the measured ACF. These factors introduce uncertainties which are not accounted for in the calculation of the uncertainty in particle velocity amplitude.

7.5.4 Conclusions

Time domain analysis of the autocorrelation function of the photomultiplier signal has been used to calculate the pressure amplitude at the end of the standing wave tube. Pressure amplitude derived from the LDA measurements and pressure amplitude derived from the probe microphone measurements agree to within ± 0.25 dB for acoustic frequencies in the range of 660 Hz to 2 kHz and peak particle velocity amplitudes in the range 13 mms^{-1} to 18 mms^{-1}. Although, a more realistic evaluation obtained by ignoring the small number of inferior measurements is ± 0.20 dB for $f_m \geq 660$ Hz and ± 0.1 dB for $f_m \geq 1570$ Hz. Averaging several measurements is not expected to significantly reduce the total uncertainty in the value of pressure amplitude derived from LDA but it would remove the spurious results observed in some of the photon correlation experiments.

7.6 Microphone sensitivity

The pressure amplitude in a standing wave can be derived from the photon correlation LDA measurement of acoustic particle velocity amplitude and a knowledge of the characteristic acoustic impedance of air. Photon correlation velocity measurements, obtained using the least squares fitting procedure, are now applied to the evaluation of microphone sensitivity. The sensitivity of the microphone system supplied by the National Physical Laboratory is determined from measurements performed with the standing wave tube apparatus. The results for several acoustic frequencies are compared to the sensitivity level obtained by reciprocity calibration.

7.6.1 Experimental method

Measurements of microphone sensitivity were performed using the photon correlation LDA system and the standing wave tube apparatus. All the LDA measurements were carried out at the position of the first or second velocity antinode in the standing wave. The loudspeaker-tube system was driven at frequencies corresponding to the resonances of the system. The magnitude response of the probe microphone was measured using the apparatus illustrated in figure 5.1, with the NPL microphone system acting as the reference microphone. The magnitude response is calculated as V_p/V_N where V_p and V_N are the RMS voltage amplitudes from the probe microphone and NPL microphone system, respectively.

Characterizing the probe microphone relative to the NPL microphone system allows the sensitivity of the NPL microphone system to be determined. The LDA results are used to derive the pressure amplitude at the end of the tube using equation 7.4. With the probe fixed into the rigid end, the voltage amplitude is divided by the magnitude response to give the equivalent voltage amplitude for the NPL system. The sensitivity of the NPL microphone system is calculated using equation 6.16 where V is the RMS voltage amplitude from the probe microphone recorded while the LDA measurements were performed. Equation 6.17 is used to determine the sensitivity level, i.e. the microphone sensitivity quoted in terms of decibels relative to a reference level. The sensitivity level of the NPL system obtained by reciprocity calibration is -38.00 ± 0.03 dB *re* 1 VPa^{-1} which is equivalent to a sensitivity of $M = 12.59 \pm 0.04$ mVPa^{-1}.

7.6.2 Signal processing

Analysis of the measured ACF in the time domain allows the velocity information to be extracted from the photomultiplier signal. A sample time of $\Delta\tau = 2\mu$s was used giving $n = 80$ channels in the digital correlator. The computer program described in section 7.4 obtains the acoustic particle velocity amplitude using the least squares fitting procedure, the theoretical expression for the ACF (see equation 4.44), and the measured ACF. The voltage amplitude of the probe microphone, measured with a digital voltmeter, is converted to the equivalent voltage amplitude for NPL microphone system by the program using the magnitude response information. The characteristic

impedance is calculated by the program described in section 5.4 from a record of the environmental conditions.

7.6.3 Uncertainty analysis

The uncertainty in the magnitude response of the probe microphone is determined by the accuracy with which the voltage amplitudes are measured using the digital voltmeter. The voltage reading is to the nearest 0.001 V giving a standard deviation of $0.001/\sqrt{3}$ V in all the voltage amplitudes. Sections 7.4.2 and 7.5.2 discuss the uncertainties in the photon correlation LDA velocity amplitude and pressure amplitude measurements, respectively. Assuming the individual components are results of independent measurements, the uncertainty in the measured sensitivity is given by

$$u_M = \sqrt{\sigma_{V_p}^2 + \sigma_{V_N}^2 + \sigma_V^2 + u^2} \tag{7.6}$$

where σ_{V_p} and σ_{V_N} are the standard deviations of V_p and V_N, respectively. σ_V is the standard deviation of V, i.e the probe microphone voltage amplitude recorded during the LDA measurement. Equation 7.5 defines u. The uncertainty in the measured sensitivity level is

$$u_{SL} = 20 \log \left(1 + \frac{u_M}{100}\right) \tag{7.7}$$

where the reference sensitivity is 1 VPa^{-1}.

Microphone sensitivity is a function of frequency. The NPL microphone system

was calibrated using the reciprocity technique for a range of frequencies and at a particular sound pressure level. It is assumed that for the range of acoustic frequencies (i.e. 660 Hz to 2 kHz) and for the range of RMS pressure amplitude (i.e. 5.1 Pa to 5.5 Pa)considered in this study, the sensitivity of the system remains approximately constant.

7.6.4 Results and discussion

Measurements of the sensitivity of the NPL microphone system were performed for acoustic frequencies in the range of 660 Hz to 2 kHz. The results are displayed in figure 7.12 where the horizontal line corresponds to the calibrated level of -38.00 ± 0.03 dB. The acoustic particle velocity amplitudes were measured to be between $17.5 - 19.0$ mms^{-1}. The measured sensitivities agree with the calibrated value to within $\pm$ 0.2 dB. Using equation 7.7, the uncertainties in the measured sensitivity levels were determined to be ± 0.08 dB. Other factors such as beam intensity mismatches and optical misalignments have not been accounted for in the calculation of uncertainty. For $f_m = 660$ Hz, 1355 Hz, 1785, and 2000 Hz the measured sensitivity levels lie above the horizontal line and out with the calculated uncertainties. This indicates that the technique is slightly underestimating the particle velocity amplitude. However, the measurements are still consistent with the calibrated level which has an associated uncertainty of ± 0.03 dB.

The calibration measurements presented here do not yield standardized sensitiv-

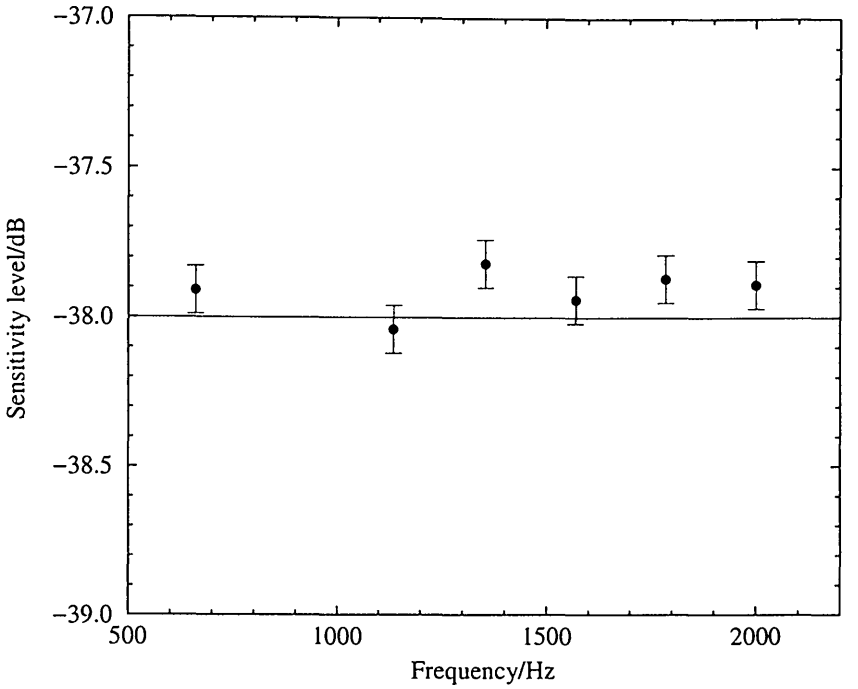

Figure 7.12: Sensitivity level derived from photon correlation LDA measurements and probe microphone voltage readings. The horizontal line corresponds to the calibrated sensitivity level of -38.00 ± 0.03 dB

ity as described in section 2.5 as the acoustic field inside the glass tube is neither a true pressure field nor a true free field. Although, the results do suggest that there is potential for the further development of the calibration technique for use in such environments.

7.6.5 Conclusions

The sensitivity of a microphone has been measured using the photon correlation LDA system, the standing wave tube apparatus, and the least squares fitting procedure. Pressure amplitude derived from LDA measurements of particle velocity amplitude and readings of probe microphone voltage amplitude were used to calculate the sensitiv-

ity level of the NPL microphone system. The uncertainty in both the sensitivity and sensitivity level has been evaluated by considering the individual components of the calculation. The measured sensitivity levels agree to within ± 0.2 dB of the calibrated level for acoustic frequencies in the range 660 Hz to 2 kHz. The total uncertainty in the microphone sensitivity measurement is ± 0.08 dB.

7.7 Free field measurements

The photon correlation LDA system has been used to measure acoustic particle velocity amplitude and pressure amplitude in a standing wave. The LDA apparatus is now applied to the measurement of acoustic particle velocity in front of the loud speaker in the absence of the glass tube. The aim of these preliminary measurements is to demonstrate the potential of the photon correlation LDA system for use in a free field environment. Results are presented for measurements performed at two acoustic frequencies, 1 kHz and 2 kHz.

7.7.1 Signal processing

Velocity information is obtained from analysis of the ACF of the photomultiplier signal in the time domain. A phase shifter is used to impose an artificial velocity by causing the fringes to move within the probe volume (see section 3.4.4). The result is to

introduce a frequency shift, F_s, which leads to an effective mean velocity of

$$\begin{aligned} \bar{U} &= \Lambda \times F_s \\ &= 3.18 \times 10^{-6} \times 50 \times 10^3 \\ &= 0.159 \text{ ms}^{-1} . \end{aligned} \tag{7.8}$$

where for the purposes of this experiment $F_s = 50$ kHz. The particle velocity amplitude is estimated by observing the number of cycles in the cosine wave between zero delay and the minimum of the Bessel function [18] [51]. The minimum value of the Bessel function occurs when the argument, $\alpha = 2.405$ [56]. To simplify the analysis it is assumed that $\sin(\pi f_m \tau) = \pi f_m \tau$ and $\bar{U} >> u_0$ such that u_0 is small enough to be ignored. In equation 4.37, the argument of the cosine term is $D\bar{U}\tau$ and the argument of the Bessel function is $u_m D\tau$. If there are d complete cycles in the cosine wave between zero delay and the first minimum, $D\bar{U}\tau = 2d\pi$ and $u_m D\tau = 2.405$. The particle velocity amplitude is given by

$$u_m = \frac{2.405\bar{U}}{2d\pi} . \tag{7.9}$$

Equation 7.9 enables an estimation of velocity amplitude to be made from inspection of the ACF of the photomultiplier signal generated by acoustic particle motion in a free field.

The pressure amplitude at the position of the probe volume was monitored using the

NPL microphone system. The acoustic particle velocity amplitude is calculated from the voltage amplitude of the output signal, the sensitivity of the microphone system, and the characteristic impedance of the air. This may be expressed as

$$|u| = \frac{\sqrt{2}V}{M\rho c} \tag{7.10}$$

where V is the voltage amplitude, M is the sensitivity, ρ is the air density, and c is the speed of sound in air. The NPL microphone system has a pressure sensitivity $M_p = 12.59$ mVPa^{-1}. Its position in relation to the direct sound waves emanating from the loudspeaker corresponds to a 90 ° angle of incidence, for which the type 4133 cartridge has zero free field correction at frequencies below 2 kHz. The computer program described in section 5.4 calculates the characteristic impedance of the air from a record of the environmental conditions. The factor of $\sqrt{2}$ is included in equation 7.10 to give the peak value of particle velocity amplitude from the RMS voltage amplitude measurement.

7.7.2 Uncertainty analysis

The uncertainties in the photon correlation LDA and microphone free field measurements are evaluated by considering the individual components of the respective velocity amplitude calculations. The uncertainty in the value of the fringe spacing was determined in section 7.4.2 to be $\sigma_\Lambda = 0.02\mu$m. The standard deviation in d will be

$\sigma_d = 1/\sqrt{3}$. The value of the frequency shift, $F_s = 50$ kHz, is obtained from the drive unit of the phase shifter and can be checked using the digital correlator [82]. With no signal supplied to the loudspeaker, the measured ACF takes the form of a damped cosine wave. The ACF is normalised, windowed, and FFT'ed to generate the frequency spectrum. This frequency spectrum has a resolution of $1/n\Delta\tau = 6250$ Hz/point where $\Delta\tau = 2\mu$s and $n = 80$ channels. The spectral peak was found to be located at 50500 kHz with a width measured to be approximately 4 kHz. A suitable estimation of the error in the frequency shift is taken to be $\sigma_{F_s} = 2000$ Hz (i.e. 4 % of F_s). Assuming the individual components are statistically independent, they are expressed as percentages of their respective values and combined as

$$u_{PC} = \sqrt{\sigma_\Lambda^2 + \sigma_d^2 + \sigma_{F_s}^2} \tag{7.11}$$

to give the total uncertainty in particle velocity amplitude derived from the photon correlation measurement.

The RMS voltage amplitude of the microphone signal, V, is measured using a digital voltmeter. V was in the range of 9 mV to 80 mV for the results considered here. The voltage amplitude is low because of the sensitivity of the NPL microphone system and the sound pressure level range (i.e. $90-110$ dB) of the measurements. The voltage reading is to the nearest 5 mV which reflects the fluctuations in the microphone signal observed while the LDA measurements were performed. This gives an associated uncertainty of $u_V = 5/\sqrt{3}$ mV. The sensitivity of the microphone system was measured

by reciprocity calibration at NPL with an associated uncertainty of$\pm$0.03 dB giving an uncertainty in the microphone sensitivity of $u_M = 0.04$ mVPa^{-1}. The uncertainties in the air density and speed of sound are $u_\rho = 0.025$ % and $u_c = 0.5$ %, respectively. Provided the individual components are statistically independent, they are expressed as percentages of their respective values and combined as

$$u_{mic} = \sqrt{u_V^2 + u_M^2 + u_\rho^2 + u_c^2} \tag{7.12}$$

to give the total uncertainty in the particle velocity amplitude derived from the microphone measurement.

7.7.3 Results and discussion

The results of the free field measurements performed for an acoustic field generated by the loudspeaker with $f_m = 1$ kHz are illustrated in figure 7.13. A sample time of $\Delta\tau = 5\mu$s with $n = 200$ channels in the digital correlator was used. The measurements were obtained with the probe volume positioned at intervals of 20 mm from the loudspeaker. The number of completes cycles between zero delay and the minimum of the Bessel function are given in table 7.1 for the ACF's in figure 7.13 along with the estimation of particle velocity calculated using equation 7.9 and equation 7.10.

From table 7.1 it may be observed that as the distance between the probe volume and the loudspeaker is increased, the measured particle velocity amplitude decreases.

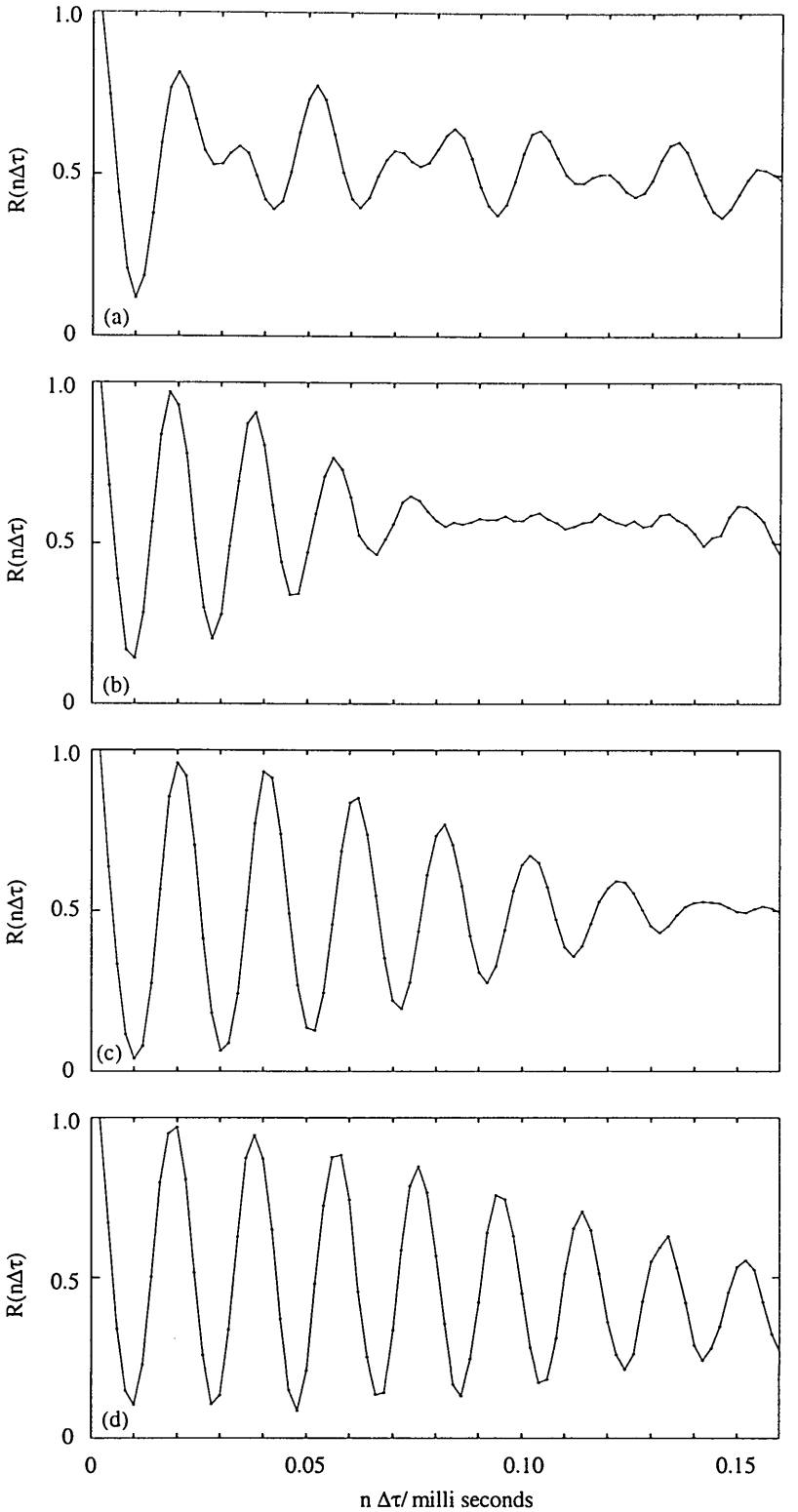

Figure 7.13: Measured ACF for the photomultiplier signal generated by an acoustic field with $f_m = 1$ kHz and (a) with distance from the loudspeaker $r = 20$ mm, (b) 40 mm, (c) 60 mm, and (d) 80 mm. The sample time $\Delta\tau = 5\mu$s, $n = 200$ channels, and $F_s = 50$ kHz.

r/mm	n/cycles	u_m/ms^{-1}	$\|u\|$/ms^{-1}
20	2	0.030 ± 0.009	0.0139 ± 0.0008
40	5	0.012 ± 0.001	0.0073 ± 0.0008
60	8	0.008 ± 0.001	0.0055 ± 0.0008
80	N/A	N/A	0.0048 ± 0.0008
100	N/A	N/A	0.0046 ± 0.0008
102	N/A	N/A	0.0042 ± 0.0008

Table 7.1: Results for free field measurements performed with $f_m = 1$ kHz

For a distance of $r \geq 80$ mm, the measured ACF takes the form of a damped cosine wave within the total sample time and no value of velocity amplitude can be resolved. At this position, the signal from the photomultiplier results from the fringes moving across the near stationary particles. In general, the LDA measurement overestimates the velocity amplitude compared to microphone measurement. The discrepancy between the two measurements ranges from $3 - 6$ dB and is out-with the calculated uncertainties. Reflections caused by the hard surface on which the apparatus is mounted and the walls of the laboratory mean that the nature of the acoustic field generated by the loudspeaker is not a complete free field. Thus, the particle motion in the region of probe volume cannot be assumed to be simply the result of plane waves generated by the loudspeaker.

It can be see from figure 7.13 that the delay time to the first minimum of the cosine wave, τ_m, does not appear to change as the distance between the probe volume and the loudspeaker is increased. This is because the effective velocity imposed by the frequency shift is much larger than the acoustic oscillations. $R(n\Delta\tau)$ follows the form predicted by equation 4.37, i.e. the interaction of the cosine term containing $\bar{U}$ with the zero order Bessel function. The measured ACF cannot be completely ac-

counted for by the equation due to the complex nature of the acoustic field as well as complications arising from particle dispersion, beam intensity mismatches, and optical misalignments.

Free field measurements were also performed for an acoustic field generated by the loudspeaker with $f_m = 2$ kHz. The results are illustrated in figure 7.14 which shows the measurements obtained when the probe volume was positioned at intervals of 20 mm from the loudspeaker. Table 7.2 gives the number of completes cycles between zero delay and the minimum of the Bessel function for the ACF's in figure 7.14 along with the estimation of particle velocity calculated using equation 7.9 and equation 7.10.

r/mm	n/cycles	u_m/ms^{-1}	$\|u\|$/ms^{-1}
20	2	0.030 ± 0.009	0.0200 ± 0.0008
40	4	0.015 ± 0.002	0.0097 ± 0.0008
60	5	0.012 ± 0.001	0.0064 ± 0.0008
80	7	0.009 ± 0.001	0.0044 ± 0.0008
100	N/A	N/A	0.0029 ± 0.0008
102	N/A	N/A	0.0025 ± 0.0008

Table 7.2: Results for free field measurements performed with $f_m = 2$ kHz

The results in table 7.2 show that as the distance between the probe volume and the loudspeaker is increased, the particle velocity amplitude decreases. For a distance of $r \geq 100$ mm, the measured ACF takes the form of a damped cosine wave within the total sample time and no value of velocity amplitude can be resolved. Again, the LDA measurement overestimates the velocity amplitude compared to microphone measurement by $3 - 6$ dB and is out-with the calculated uncertainties. The major contribution to the inaccuracy of the results is the complex nature of the acoustic field

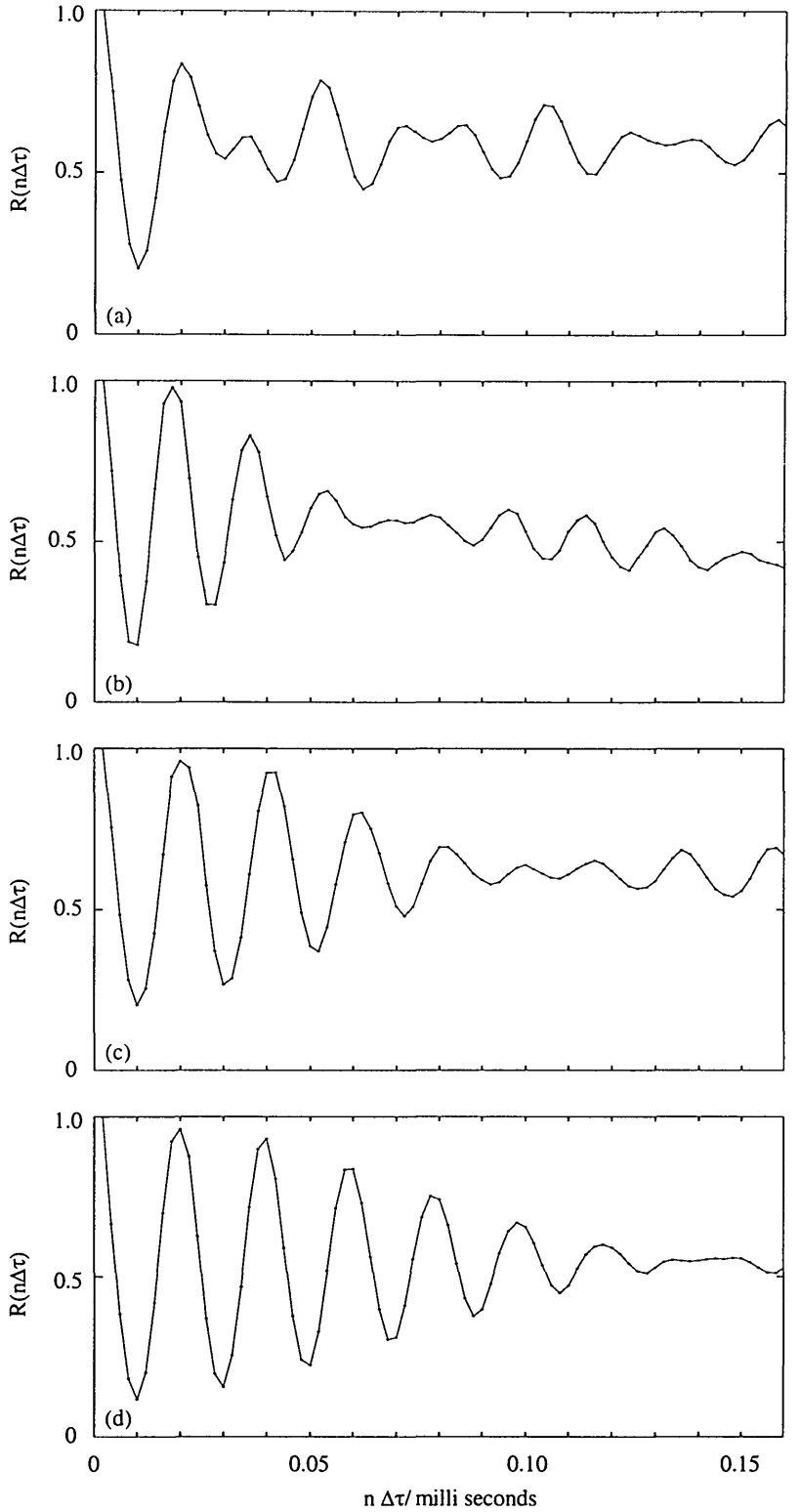

Figure 7.14: Measured ACF for the photomultiplier signal generated by an acoustic field with $f_m = 2$ kHz and (a) with distance from the loudspeaker $r = 20$ mm, (b) 40 mm, (c) 60mm, and (d) 80mm. The sample time $\Delta\tau = 5\mu$s, $n = 200$ channels, and $F_s = 50$ kHz.

generated by the loudspeaker. This not a complete free field due to reflections caused by the hard surface on which the apparatus is mounted and the walls of the laboratory.

It can be seen from figure 7.14 that the delay time to the first minimum does not appear to change as r is increased. This is due to the size of the effective mean velocity imposed by the frequency shift compared to the smaller acoustic oscillations. $R(n\Delta\tau)$ does follows the form predicted by equation 4.37 but the measured ACF cannot be completely accounted for by the equation due to the complex nature of the acoustic field, particle dispersion, beam intensity mismatches, and optical misalignments.

The photon correlation LDA measurement overestimates the particle velocity amplitude and acoustic pressure amplitude by several decibels compared to the microphone measurement. As this discrepancy is so large no accurate value of the free field microphone sensitivity may be deduced. Instead, the behaviour of both the particle velocity amplitude and the microphone voltage amplitude with increasing distance from the loudspeaker is considered. The RMS voltage amplitude, V, obtained from the NPL microphone system is plotted against r in figure 7.15. The graph suggests that the voltage amplitude is indirectly proportional to r^2 indicating that $|p| \propto 1/r^2$, where $|p|$ is acoustic pressure amplitude derived from the microphone signal. This demonstrates that the free field microphone measurements follow the expected behaviour of the acoustic pressure amplitude in front of a loudspeaker [83].

The velocity amplitude, u_m, obtained from the photon correlation measurement is plotted against the distance from loudspeaker, r, in figure 7.16. Inspection of the

graph suggests that the velocity amplitude is indirectly proportional to r^2 indicating that $p_m \propto 1/r^2$, where p_m is the acoustic pressure amplitude derived from LDA. This shows that the free field LDA photon correlation measurements follow the behaviour of the microphone pressure measurements and so observes the behaviour of the acoustic pressure amplitude in front of a loudspeaker.

The aim of the experiment was to demonstrate the potential of photon correlation for performing free field measurements. The results are not as accurate when compared to the standing wave tube results. However, the measured ACF's follow the expected form predicted by the theoretical equation. The measurements of velocity amplitude and hence pressure amplitude follow the expected trend in front of a loudspeaker. The results could be improved upon in several ways. Mounting the apparatus on a sound absorbing surface would improve the quality of the free field by preventing some of the reflections. Alternatively, the entire experimental system could be placed in a free field chamber to ensure a superior quality of free field environment to that of the existing experimental arrangement. A more rigorous signal processing technique could also be developed involving a similar curve fitting procedure to that employed in the previous sections. Adjustments to the alignment of the optics may help to eliminate damping of the measured autocorrelation function.

7.7.4 Conclusions

Measurements of acoustic particle velocity amplitude have been performed in a semi-free-field environment by analysing the measured ACF of the photomultiplier signal. The photon correlation LDA measurements overestimate the acoustic pressure amplitude by as much as 6 dB when compared to the microphone measurement. The main cause of this inaccuracy is that the acoustic field is more complex than the assumed free field environment. The acoustic pressure amplitude derived from both the microphone measurement and the LDA measurement is found to be indirectly proportional to r^2, where r is the distance from the loudspeaker. Although the current experimental method is not very accurate, the potential for the application of photon correlation to free field measurements has been demonstrated.

7.8 Summary

The form of the autocorrelation function for the photomultiplier signal generated by a mean flow superimposed onto an acoustic oscillation was reviewed. The principle of extracting velocity information from the measured ACF was discussed in conjunction with digital correlation. Sources of damping in the measured ACF were also highlighted.

The experimental method employed with the photon correlation LDA system, the standing wave tube apparatus, and the probe microphone was explained. Measure-

ments of the acoustic particle velocity amplitude and mean flow velocity amplitude in the standing wave tube were performed using time domain analysis of the measured ACF. A least squares fitting procedure is used in conjunction with the theoretical expression derived for the time dependent form of the ACF to determine the velocity amplitudes.

The pressure amplitude at the end of the tube was calculated from the photon correlation LDA measurements and compared to the pressure amplitude derived from the probe microphone measurements. The total uncertainty in the pressure calculation was evaluated by considering all of the individual components. The photon correlation LDA system and standing wave tube apparatus were used successfully to measure the sensitivity of a microphone. The measurements were in good agreement with the calibrated level obtained by the reciprocity method but not as accurate as the measurements obtained using the continuous signal LDA system.

Finally, photon correlation was applied to the measurement of acoustic particle velocity in a semi-free-field environment. The results demonstrate the potential of the technique and justify further development.

Chapter 8

Free field calibration facility

8.1 Introduction

The measurements presented in chapter 6 and chapter 7 demonstrate that LDA can be used in conjunction with the standing wave tube apparatus to measure the sensitivity of a microphone. In section 7.7, preliminary measurements performed in a free field environment using the photon correlation system were also presented.

In this chapter the application of LDA to the free field calibration of microphones will be discussed. The first section contains a review of alternative laser Doppler systems applied to acoustical measurements in air. Additional seeding methods are assessed in section 8.3. Details of the free field reciprocity calibration facility at NPL are given in section 8.4 and the design and arrangement of a LDA system is considered.

8.2 Comparison of LDA systems

Useful LDA measurements of acoustic particle velocities in air have been made by several researchers in recent studies [13] [40] [81]. In this section the different optical and experimental arrangements of the LDA apparatus are examined. The various signal processing techniques are also considered. The dynamic range of each systems is assessed and the suitability for free field application is briefly discussed.

8.2.1 Random sampling system

Loizeau and Gervais performed LDA measurements of particle velocity amplitude and acoustic frequency in a standing wave tube [13]. The experimental apparatus consisted of a glass tube 1 m in length with an internal diameter of 50 mm and a wall thickness of 9 mm. This was positioned vertically above a loudspeaker and left open at both ends. A half inch microphone fixed into the wall at the middle of the tube was used to monitor the sound pressure. The two illuminating beams were generated from a 15 mW He-Ne laser ($\lambda = 633$ nm). The transmitter optics of the laser Doppler system incorporated a Bragg cell and a focusing lens with $f = 300$ mm. The resulting fringe spacing was $\Lambda = 3.3\mu$m and the probe volume contained 70 fringes.

The entire experimental system was encased in a sealed volume allowing the air to be seeded with microparticles of oil. Loizeau and Gervais superimposed a small mean flow onto the acoustic oscillation to maintain an even distribution of seeding

particles. Non-uniform time interval sampling of the detector signal was employed to extract instantaneous particle velocity information and a relative error of less than 5 % in the measurements was quoted. No dynamic range of the measuring technique is given but the results are presented for acoustic and mean flow velocities of several hundred millimetres per second. The signal processing technique requires a high level of seeding that would be difficult to achieve in a free field environment, especially using oil droplets.

8.2.2 Backscattering system

More information is available for a backscatter LDA system, employing commercially available hardware and software as well as custom designed signal processing algorithms, at the Laboratoire d' Acoustque de l'Université du Maine (LAUM) [75] [81] [84]. The backscatter mode leads to a lower intensity of light at the detector than forward scatter but it is useful for measurements conducted close to surfaces. Initial LDA measurements were performed with a travelling wave tube which consisted of a loudspeaker attached to a glass tube with a length of 1.8 m and an internal diameter of 45 mm. Two microphones were fixed into the wall of the tube at 600 mm intervals from the loudspeaker to monitor the acoustic pressure.

The argon ion laser used in the system emits three colours; green at $\lambda = 514.5$ nm, blue at $\lambda = 488$ nm, and purple at $\lambda = 476.5$ nm. This allows the simultaneous measurement of several velocity components. A fibre optic delivery system employed

for the illuminating beams allows greater control over the beam angle. Increasing the beam angle reduces the fringe spacing so that a smaller range of velocities can be measured. The power at the end of each fibre is approximately 20 mW and the focusing length of the transmitter optics is 60 cm. Experiments were conducted with $2\theta = 30\ ^\circ$ and fringe spacing, $\Lambda = 1.0\mu$m. The preferred seeding method was a fog generator based on water condensation with an aerosol. For high acoustic levels, the fog condenses quickly and so measurements were performed with smoke particle seeding generated from oil droplets.

Valière et al used a DANTEC Burst Spectrum Analyzer, based on FFT analysis, to extract instantaneous velocity information from the detector signal [75]. Poggi established the lower limit to the dynamic range of the system to be 1 mms^{-1} [81]. The system does not require a particularly high level of seeding and Poggi conducted preliminary measurements in a free field environment.

8.2.3 Frequency tracking system

A DANTEC frequency tracking LDA system has been used in the measurement of both instantaneous acoustic particle velocity and acoustic particle velocity amplitude [40] [44]. Measurements were performed inside a glass tube with a length of 0.5 m, an internal diameter of 24 mm, and a wall thickness of 2 mm. One end of the tube was terminated with a baffle and loudspeaker box while measurements were made with the opposite end both open and closed.

The DANTEC 55X series transmitter optics described in section 5.6.1 were used to create the interference fringes. The scattered light was detected using the detector optics also described in section 5.6.1. The beam angle, $2\theta = 11.06°$ and the fringe separation, $\Lambda = 3.28\mu$m. The photodetector signal was either passed to a DISA 55N21 frequency tracker or bandpass filtered and sampled by an A/D converter attached to a PC. Seeding methods included two different atomizers and incense smoke. The sampled signal was analysed using the Hilbert transform demodulation routine described in section 3.6. The frequency tracker also demodulates the photodetector signal giving instantaneous frequency, thus allowing instantaneous particle velocity to be calculated.

Cullen successfully measured sinusoidal sound fields in air with acoustic particle velocity amplitudes in the range of 1 mms^{-1} to 700 mms^{-1} with an accuracy of ± 0.3 dB [40]. The results in chapter 6 suggest that a greater accuracy can be achieved for lower velocity amplitudes using spectral analysis techniques. Analogue and digital frequency tracking methods require extensive seeding which would create problems for free field measurements.

8.2.4 Conclusions

Only the backscatter LDA system has previously been applied to free field measurements. Both the random sampling system and frequency tracking system require a high level of seeding that would be impractical to achieve inside a free field chamber. The dynamic range of the backscatter system is similar to that of the continuous signal

system used in the present study. Increasing the beam angle of the photon correlation system used in the present study or reducing the wavelength of the laser light will lower the limit to the particle velocity amplitude that can be measured.

8.3 Seeding methods

Air flows can be seeded with either solid particles or with liquid droplets. In the previous section several seeding methods were mentioned in conjunction with studies conducted using different types of LDA systems. This included oil droplets, water droplets, and incense smoke. In section 5.7, the characteristics of incense smoke seeding used in the present study are discussed. Liquid droplet seeding tends to offer a steadier production rate than is feasible with solid particles as well as particles that are inherently spherical [71]. The generation of scattering particles by condensation and atomization is now considered.

8.3.1 Generation of droplets by condensation

Seeding particles can be generated by the evaporation and condensation of a suitable liquid. For example, oil is evaporated by a heater and the vapour condenses to form fine droplets in the air flow. This type of seeding tends to be difficult to regulate and so the delivery rate tends to be unsteady. The range of particle diameters is quite large (1 μm to 4 μm). Alternatively, the fog generator produces particles from a water based

liquid but with a similar range of particle diameters [44]. For high acoustic levels the fog condenses quickly [81]. Due to the large particle sizes of both types of seeding, the droplets will significantly lag the acoustic oscillation at high frequencies (see section 5.7). Deposition of the liquid on surfaces will also occur.

8.3.2 Generation of droplets by atomization

In a nebulizer, liquid is drawn into a thin film which disintegrates into a large number of droplets through the action of a shear force working against the surface tension [7]. Particle concentrations in the range of 10^9 m^{-3} to 10^{10} m^{-3} can be achieved in this way [71]. Cullen investigated the use of two types nebulizers, one which produced water droplets with diameters between 0.5 μm and 5 μm and one which produced water droplets with approximately 4 μm diameters [44]. On comparing with incense smoke seeding, Cullen found that periodic amplitude modulation is more pronounced with water droplet seeding than it is with smoke particle seeding. This can lead to signal processing problems due to signal dropout.

8.3.3 Conclusions

The seeding particles created by both condensation and atomization have a large range of particle diameters. For high acoustic frequencies, the particles will significantly lag the acoustic oscillation. Incense smoke contains smaller particles but the seeding of a

free field environment is impractical to achieve. The neutrally buoyant fog particles are more suited to this application but problems have been experienced with condensation at high acoustic levels. The use of a photon correlation system would require the minimum amount of seeding.

8.4 Free field apparatus

In order to measure the free field sensitivity of a microphone, the environment in which the measurement takes place must act as a free field, i.e. waves emanating from the sound source diverge spherically and the receiver is subject only to these direct waves. This is achieved through the use of a high quality free field room. Problems arising from LDA applied to free field measurements are discussed and the arrangement of the LDA system with the free field room is proposed.

8.4.1 Reciprocity calibration facility

The facility to support free field microphone calibration at NPL is described by Barham in [27]. The chamber is constructed from double skinned steel panels filled with damping material and is mounted on anti-vibrational supports. The interior of the chamber is lined with polyurethane foam wedges, illustrated in figure 8.1, to prevent the reflection of sound waves. The total height of each wedge is 400 mm. The free field performance of the room has been rated by Barham using a procedure proposed by Delaney [85].

Essentially, the root mean square deviation of the variation of the measured pressure with distance from a sound source, from ideal behaviour was determined.

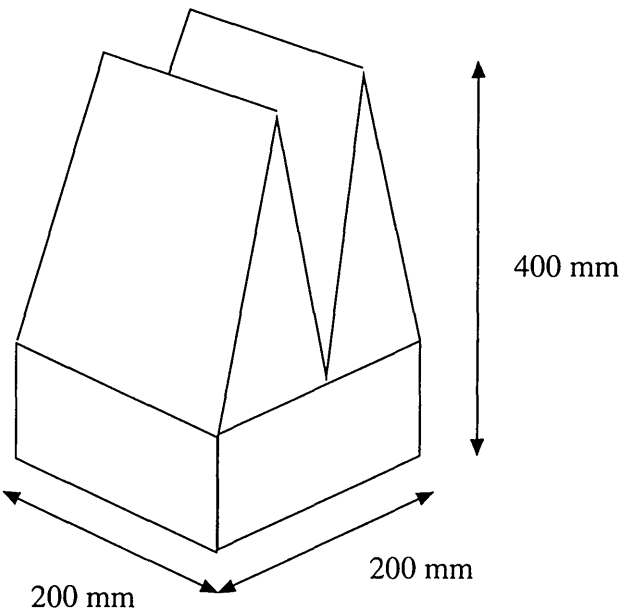

Figure 8.1: Foam wedge design used at NPL free field chamber.

The cross section of the lined chamber is illustrated in figure 8.2. The chamber has internal dimensions of 2.4 m $\times$ 2.4 m $\times$ 2.6 m. For reciprocity calibration, the microphones are mounted on rods with diameters equal to the diameter or the microphone. The mounts are aligned vertically with the upper one holding the transmitter microphone and the lower one the receiver microphone. The separation between the microphones may be varied from between 5 cm to 60 cm.

The reciprocity calibration method is described in section 2.5. A more detailed description of the free field technique employed at NPL can be found in [27]. The overall aim of research conducted in the present study has been to demonstrate the

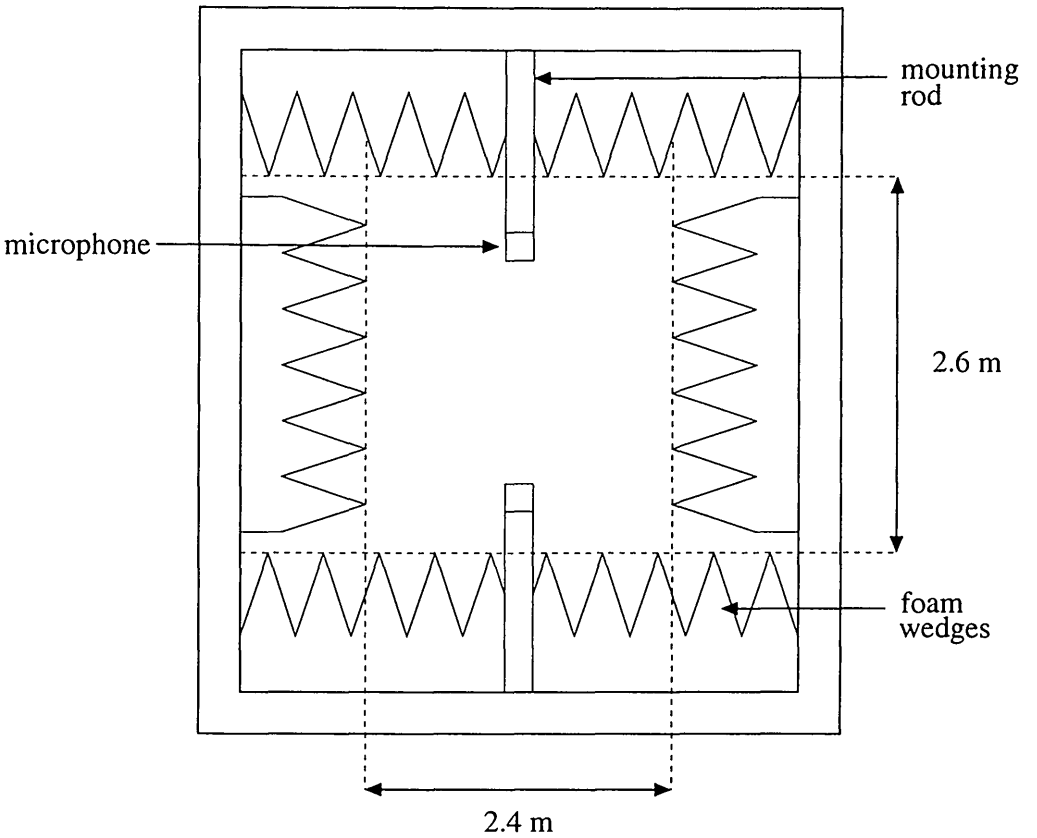

Figure 8.2: Side on diagram of the NPL free field chamber.

potential for point measuring optical techniques such as LDA to be used in microphone calibration. The measurements of microphone sensitivity presented in this thesis were performed in a closed tube. The LDA technique needs to be applicable in free field situations if it is to replace reciprocity as the standardized method of calibration. This is discussed in the following section.

8.4.2 LDA calibration facility

The application of LDA to free field situations raises a number of important issues that must be addressed before the technique can be implemented for routine microphone

calibration. These issues are separated into 3 sections; the experimental arrangement of the LDA apparatus in relation to the free field chamber, seeding considerations, and signal processing techniques.

Experimental arrangement

The transmitter and detector optics of the LDA system will be mounted outside the free field room as placing any equipment inside the chamber could significantly alter the properties of the free field environment. Introducing two windows, located on opposite sides of the chamber, will allow light transmission and collection. This is illustrated in figure 8.3 where the x axis is vertical, the y axis is horizontal, and the z is perpendicular to the other two. To keep the size of the transmission window as small as possible, the beam angle must be kept relatively small. In order to prevent this increasing the fringe spacing, the wavelength of the illuminating laser light can be reduced. For example, a green laser with $\lambda = 514.5$ nm could be used instead of the red laser with $\lambda = 633$ nm in the present study. The forward scatter mode is selected instead of the backscatter mode as this gives a higher intensity of scattered light.

Assuming the probe volume is located in the middle of the free field room, the distance of the focal length of the focusing lens, f, in the transmitter optics needs to be slightly greater than half the length of the chamber. Therefore, $f > (2.4 + 0.4)/2$ m. Consider $f = 1.5$ m and the separation between the two parallel illuminating beams to be $2d = 0.38$ m. The window for the illuminating laser light is taken to be as wide as

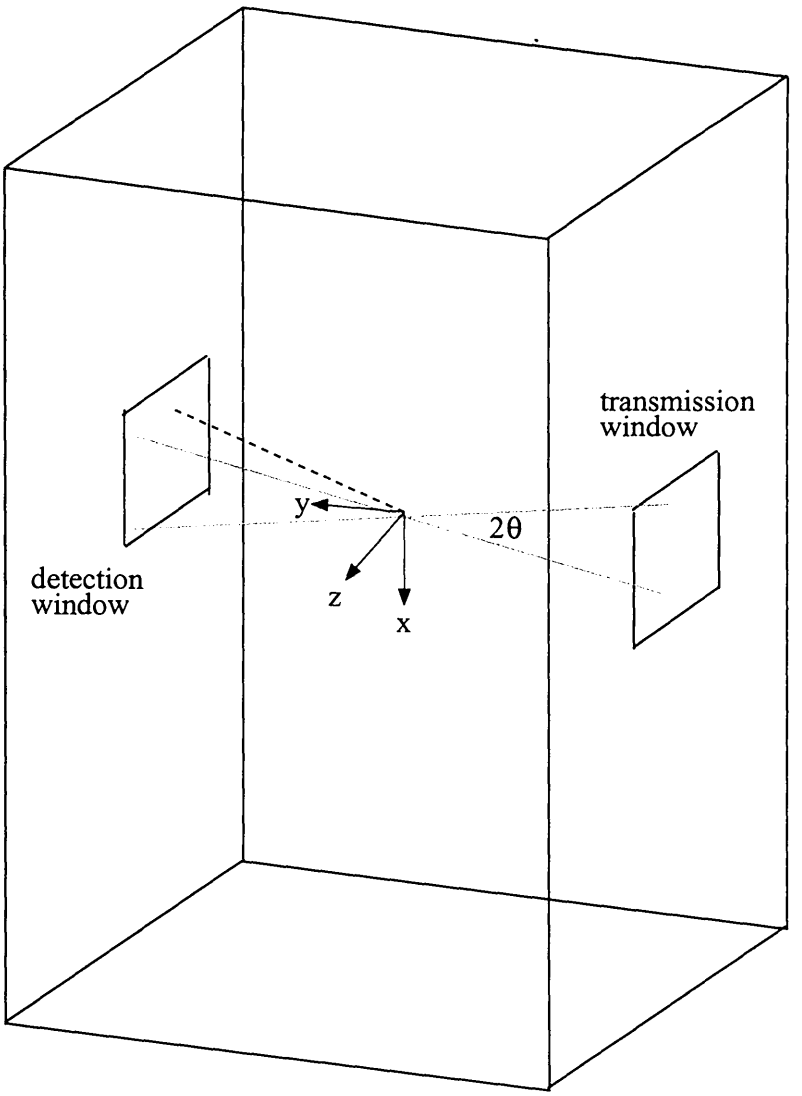

Figure 8.3: Diagram of the free field chamber and LDA apparatus.

the width of the base of one foam wedge section (see figure 8.1). Using equation 6.6 this gives the beam angle, $\theta = 7.2°$. With a green laser the fringe spacing, $\Lambda = 2.05\mu$m (see equation 3.10). If the unfocused e^{-2} beam diameter is approximately 0.7 mm then from equation 3.5, the focused beam diameter will be $d_{e^{-1}} = 1.4$ mm. The dimensions of the probe volume are $\Delta x = 1.4$ mm, $\Delta y = 11.1$ mm, and $\Delta z = 1.4$ in the x, y, and z directions respectively (see section 3.4.2). Using equation 3.11, the total number of fringes in the probe volume, $N_f = 689$.

The scattered light is detected using a photomultiplier and optics. The photomultiplier is positioned at an angle of 15 ° to the optical axis (i.e. the y axis) to avoid detecting light from the direct beams. The distance from the centre of the probe volume to the detector optics will be approximately 1.55 m. In figure 8.3, the detector is mounted outside of the chamber behind a glass plate.

The long focal length of the focusing lens results in a large length of the probe volume along the optical axis. This may present problems with the spatial resolution. Distortions in the fringe spacing may also arise, due to the deviation of the focused beam waists from the focal plane of the lens, as the Doppler frequency gradient in probe volume depends on the focal length (see section 3.4.3). Increasing the beam separation further through the use of a fibre optic delivery system would reduce the size of the probe volume in the direction of the optical axis and decrease the fringe spacing. The fibre optics, which could be mounted inside the chamber, would remove the need for a glass plate in the wall, provide greater control over the beam angle allowing smaller particle velocity amplitudes to be measured, and eliminate fringe spacing distortion problem. Increasing the angle at which the photomultiplier is positioned with respect to the optical axis will help to improve the spatial resolution.

Seeding

It is not practical to use high levels of seeding inside the free field chamber as the optical paths for beam transmission and detection will be obscured. In addition, the

speed of sound may be altered significantly. Low seeding densities or small particle sizes result in low signal levels and a low signal to noise ratio. Large seeding particles, such as those produced by condensation and atomization, do not faithfully follow the acoustic motion at high frequencies. Smoke or oil droplet seeding particles are not suited for use in a confined space such as the free field chamber due to deposition. Introducing any type of seeding into the chamber may have a detrimental effect on the sound absorbing lining material.

Using a photon correlation system would enable seeding levels to be kept to a minimum. In fact, dust particles naturally occurring inside the chamber may be sufficient to scatter the laser light. If additional seeding were required, the haze generator could be used to generate low levels of seeding. However, the haze particles would introduce complications at high frequencies due to a lag with the acoustic oscillation as well as problems with condensation.

Signal processing

Microphone calibration measurements are carried out with mono-frequency sound signals in the range 500 Hz to 20 kHz and with a SPL of 70 dB [27]. Digital correlation or frequency domain analysis would be the most effective method of Doppler signal processing. Frequency shifting is required for both digital correlation and frequency domain analysis in the free field application. The results in section 7.7 indicate that further development of the photon correlation technique is required before an accurate

measurement of particle velocity amplitude can be extracted from the autocorrelation function of the photomultiplier signal.

The theoretical limits to the particle velocity amplitude that can be measured with the photon correlation technique are given in equation 4.47 and depend on the sample time of the digital correlator, $\Delta\tau$, and the fringe spacing, Λ. The sample time determines the number of available channels in the digital correlator. The free field measurements in section 7.7 where performed with $\Delta\tau = 2\mu$s and $n = 80$ channels. Decreasing the fringe spacing would bring the range of measurable particle velocity amplitudes closer to the particle velocity amplitude corresponding to a SPL of 70 dB. The sample time can be reduced to $\Delta\tau = 1\mu$s or $\Delta\tau = 0.5\mu$s. Although this limits the number of available channels to $n = 40$ or $n = 20$ respectively, the digital correlator can be upgraded with extra channels [69]. For high acoustic frequencies, a fast sample time is required to accurately represent the autocorrelation function. For small particle velocity amplitudes, a large number of channels is needed to see the minimum of the Bessel function (see section 7.7).

The theoretical upper limit to the particle velocity amplitude that can be measured with the continuous detection system and frequency domain analysis is given in equation 3.62, and depends on the fringe spacing and the sample time of the A/D converter. From the results in chapter 6, the lower limit depends on the smallest side peak amplitude that can be measured above the noise level in the frequency spectrum of the Doppler signal. Decreasing the fringe spacing would allow the measurement of parti-

cle velocity amplitude corresponding to a SPL of 70 dB for frequencies in calibration range. In theory, the range of Doppler frequencies will be within the Nyquist condition. However, for high acoustic frequencies, the amplitude displacement will be much smaller than the fringe spacing. Further investigation of the dynamic range of frequency domain analysis technique is required along with its application to free field measurements.

The size of the free field chamber means that the light transmission and collection lengths are long compared to a typical dual beam arrangement. Taking this into account and the frequency range of the calibration, the acousto-optic effect may have to be considered. In section 3.8 it was explained that at high frequencies the signal from the oscillating fringes will begin to dominate over the signal from the oscillating particles. Analysis of the Doppler signal will give information that does not accurately represent the particle motion. Further investigation of the acousto-optic effect is required to establish at what frequency it can longer be ignored.

8.5 Summary

Alternative LDA systems to the two used in the present study were introduced and discussed. The different optical arrangements and signal processing techniques were briefly touched upon as well as the application to free field measurements. The generation of seeding particles by either condensation or atomization was explained along

with the inherent problems associated with particle sizes and acoustic oscillations.

The application of LDA to the free field situation was discussed. The free field calibration facility currently in use at NPL was described. The surfaces of the chamber are lined with sound absorbing material to prevent reflections and create a free field environment. The frequency range of the calibration procedure and the generation of a mono-frequency sound field is suited to the use of frequency domain analysis or photon correlation techniques. The introduction of high levels of seeding into the chamber is impractical as is the use of smoke particles and oil droplets. A photon correlation LDA system minimises the amount of seeding required. Although, the technique requires further development for free field measurements. The proposed arrangement of the LDA system with the free field chamber was outlined. Problems arising from the limitations of both digital correlation and frequency domain analysis were discussed. Finally, if the acousto-optic effect can no longer be considered negligible, signal processing difficulties will arise.

Chapter 9

Summary and conclusions

9.1 Achievement of aims

The initial research aims set out in section 1.3 have all been achieved. In this chapter each aim is restated and the extent to which the aim has been fulfilled is assessed.

9.1.1 Investigation of techniques for processing continuous Doppler signals

The first aim was to investigate techniques for processing continuous Doppler signals.

Two different methods were looked at, both of which required initial digital sampling of the bandpass filtered photodetector signal, i.e. the Doppler signal. The first

method involved the Fourier transform of the sampled signal to generate the frequency spectrum. The second method involved applying a Hilbert transform demodulation routine to the sampled signal.

A sinusoidal mono-frequency acoustic field generates a Doppler signal of the form of a frequency modulated wave with carrier frequency equal to the frequency shift and modulation frequency equal to the acoustic frequency. The frequency positions and amplitudes of the spectral peaks in the frequency spectrum are used to calculate the acoustic particle velocity amplitude, and the mean flow velocity. Demodulation of the Doppler signal in the time domain, using the Hilbert transform method, yields the instantaneous frequency which is proportional to the instantaneous acoustic particle velocity.

9.1.2 Investigation of techniques for processing discrete pulse Doppler signals

The second aim was to investigate techniques for processing discrete pulse Doppler signals generated by photon correlation LDA.

The photomultiplier signal is correlated with itself to produce the autocorrelation function. This operation is performed using a digital correlator which counts the number of pulses occurring in a set number of consecutive discrete time intervals. The complete description of the time-dependent ACF for a sinusoidal mono-frequency acoustic

field takes into account the Gaussian envelope on the fringe pattern and involves the interaction of cosine term with a zero order Bessel function. The positions of the peaks and minima of the ACF are used to determine acoustic particle velocity amplitude and mean flow velocity.

The introduction of a frequency shift to one of the illuminating beams in the LDA system masks the contribution to the ACF arising from the acoustic oscillation, making it difficult to extract velocity information. The Fourier transform of ACF generates the power spectral density of the Doppler signal. However, this is of limited use as the form of the Fourier transform is not easily deduced for the complex ACF.

9.1.3 Development of the photon correlation apparatus

The third aim was to develop the photon correlation apparatus for the measurement of acoustic particle velocity.

Unlike the continuous detection LDA system, which has been used in previous studies [40] [44], the photon correlation system required initial development of the detector optics and electronic processing system before acoustical measurements could be made. The detector optics for the photomultiplier consisted of lens unit, with variable focal length and aperture size, to focus the light onto a pin hole and a second lens located directly behind the pin hole to expand the light onto the cathode. The signal processing to produce the autocorrelation function of the photomultiplier signal

is performed using a new generation of digital correlator and controlling software. A computer program was written to extract velocity information from the ACF using a least squares fitting procedure to find the optimum values of particle velocity amplitude and mean flow velocity, i.e. the values which minimise the sum of the squared relative error between the theoretical expression and the experimental data.

9.1.4 LDA measurements in sound fields

The fourth aim was to verify that both the continuous signal and the photon correlation LDA systems correctly measure acoustic particle velocity amplitude by performing LDA measurements in a mono-frequency standing wave and comparing with pressure measurements made with a microphone.

The theoretical relationship between acoustic particle velocity and acoustic pressure in a standing wave was established by considering the interaction of transmitted and reflected plane waves in a terminated tube. To derive pressure from particle velocity requires the characteristic acoustic impedance of the air inside the tube. This can be calculated from measurements of the air temperature, the relative humidity, and the atmospheric pressure.

The viscous drag force was used to theoretically assess the extent to which seeding particles follow the acoustic oscillation. It was found that smoke particles, produced by burning incense sticks, faithfully follow the fluid velocity for frequencies less than

or equal to 6 kHz. The haze or fog particles, produced by the evaporation and condensation of a water based-liquid, may theoretically lag an acoustic oscillation with frequency of 2 kHz by up to 30 ° due to the large range of particle diameters.

LDA measurements were carried out in a mono-frequency standing wave set up in a glass tube driven by a loudspeaker. Pressure amplitude derived from LDA measurements of velocity amplitude was compared with probe microphone measurements of pressure amplitude. Using the continuous detection LDA system and the frequency domain analysis technique, the particle velocity amplitude was measured with an accuracy of ± 0.1 dB for velocities corresponding to SPLs in the range of 88 dB to 94 dB and frequencies in the range of 660 Hz to 2 kHz. In comparison, using the Hilbert transform technique the particle velocity amplitude was measured with an accuracy of ± 0.75 dB over the same SPL and frequency ranges. With digital correlation, the particle velocity amplitude was measured with an accuracy of ± 0.25 dB for velocities corresponding to SPLs in the range of 106 dB to 108 dB and frequencies in the range of 660 Hz to 2 kHz.

9.1.5 Assessment of the uncertainty in the LDA measurements

The fifth aim was to assess the uncertainty associated with the LDA measurements.

The uncertainty in the LDA measurement was evaluated by considering the individual components required to determine velocity and pressure amplitude. The fringe

spacing is central to the calculation of velocity and depends on the wavelength of the laser light and the angle between the two illuminating beams. The associated uncertainty in the fringe spacing was estimated for the transmitter optics of both LDA systems by considering the error in the beam angle. The acoustic frequency is required to calculate velocity and the associated uncertainty can be determined from the standard deviation of its measurement. With the frequency domain analysis and Hilbert transform techniques, several measurements are averaged and this introduces a contribution to the uncertainty in the velocity. Combining the individual components using a standard method gives the overall uncertainty in the LDA velocity measurement.

The characteristic acoustic impedance is required to derive acoustic pressure from particle velocity. The uncertainties in both the calculation of air density and speed of sound contribute to the uncertainty in the pressure amplitude derived from the LDA velocity measurement. These values are combined with the total uncertainty in the velocity to give an overall uncertainty in the pressure. For measurements performed with both LDA systems, this overall uncertainty was found to be less than or equal to 0.1 dB.

9.1.6 Development of a microphone calibration technique

The sixth aim was to develop a microphone calibration technique based on LDA measurements of acoustic particle velocity amplitude and to determine the sensitivity of a microphone using both laser Doppler systems.

The frequency response of the probe microphone was measured relative to a reference microphone. Using the frequency response information, the sensitivity of the reference microphone is determined from a measurement of particle velocity amplitude and a measurement of the probe microphone output voltage. The LDA derived sensitivity is compared to the sensitivity measured by reciprocity calibration. With the continuous detection LDA system and frequency domain analysis, the measured microphone sensitivity was within 0.1 dB of the calibrated value for velocities corresponding to an SPL of approximately 94 dB and frequencies in the range of 660 Hz to 2 kHz. The total uncertainty in the measurement is less than or equal to 0.1 dB. With the photon correlation system the measured sensitivity was within 0.2 dB of the calibrated value for velocities corresponding to an SPL of approximately 107 dB and frequencies in the range of 660 Hz to 2 kHz. The total uncertainty in the measurement is 0.08 dB.

9.1.7 Assessment of applying LDA to free field measurements

The seventh and final aim was to assess the feasibility of applying LDA to the measurement of acoustic particle velocity in a free field with the subsequent aim of developing a free field microphone calibration technique.

Initial measurements have been carried out in a free field using the photon correlation system. Particle velocity amplitude was measured in front of a loudspeaker and found to follow the expected behaviour. Although the results are not very accurate,

they do demonstrate the potential for further development of the digital correlation technique in such an acoustic environment.

The design and arrangement of a free field LDA calibration facility was discussed. The use of a photon correlation system allows seeding levels to be kept to a minimum. Calibration measurements are carried out with mono-frequency sound signals and digital correlation has been shown to be an effective signal processing technique for such acoustic fields. The arrangement of the LDA apparatus, i.e. the transmitter and detector optics, in conjunction with a free field chamber was proposed.

9.2 Further work

There are several ways in which the work of this thesis could be extended.

Further development of the photon correlation LDA system is necessary to improve the accuracy of the measurements. Realigning or modifying the transmitter optics could remove beam intensity mismatches which produce the damping observed in the measured ACF of the photomultiplier signal. This would improve the existing signal processing technique as it may be possible to completely account for the measured ACF using the theoretical expression derived in Appendix B. An investigation into extending the dynamic range of the technique is required and this would initially involve studying the effects of decreasing the fringe spacing by increasing the beam intersection angle or reducing the wavelength of the laser light.

The free field photon correlation experiment, described in section 7.7, can be improved upon by using foam wedges and a sound absorbing surface to reduce reflections and prevent standing waves in the laboratory. Alternatively, the experiment could be conducted in an anechoic chamber. Having acquired measurements from an improved free field environment, consideration can be given to the extraction of velocity information from the measured ACF by simulating the time-dependent part of the ACF for a periodic flow plus a frequency shift. The application of LDA to microphone calibration requires the measurement of lower particle velocity amplitudes and higher acoustic frequencies than have been studied here. Using the free field experiment, the effects of increasing the acoustic frequency and decreasing the fringe spacing can be investigated. The limitations of digital correlation, in terms of the sample time and the number of available channels, can also be established.

With the existing photon correlation system, the photomultiplier signal is analysed over several acoustic periods to calculate the time-averaged ACF and determine particle velocity amplitude. An alternative method, called periodic sampling, involves the use of a gating technique to sample the photomultiplier signal, with a series of square pulses, at specific phase positions in the acoustic cycle [86]. The photomultiplier signal is analyzed for the duration of the pulse to determine the particle velocity at the phase position [15]. The existing experiment could be modified by using the loudspeaker driving signal to trigger the generation of pulse at predetermined delays. Measuring the particle velocity at the phase position corresponding to the maximum value may yield an improved result compared to determining the velocity amplitude

from the time-averaged ACF.

In this study, free field measurements with the continuous detection system have not been performed. It would be relatively straightforward to carry out this experiment as the detector and transmitter optics could swapped with those of the photon correlation system. The fog generator can be used to seed the air in the vicinity of the probe volume. Considerably more seeding is necessary than with photon correlation but the minimum amount required for continuous detection could be established. Repeating the measurements in front of loudspeaker and comparing with the photon correlation results will determine if continuous detection offers any advantages in the free field application.

Appendix A

Derivation of the photodetector fringe current

A.1 Photocurrent generated by the two beams

The photocurrent generated by the scattered light from the two illuminating beams incident on a particle is calculated by Durrani and Greated [33], such that

$$i_F = \eta \left(\frac{1}{2} M C_{SC}\right)^2 (|E_1(x_1, y_1, z_1)|^2 + |E_2(x_2, y_2, z_2)|^2 + 2Re[E_1(x_1, y_1, z_1) E_2^*(x_2, y_2, z_2)]) \quad \text{(A.1)}$$

where M is the magnification factor of the detector optics, C_{SC} is the scattering cross section of the particle, η is the sensitivity of the detector, * denotes complex conjugate.

The field incident on the particle due to beam 1 propagating in the direction (x_1, y_1, z_1) is

$$E(x_1, y_1, z_1) = E_0 \exp\left(-\frac{x_1^2 + z_1^2}{2r_0^2} + jky_1\right) \tag{A.2}$$

and the field incident on the particle due to beam 2 propagating in the direction (x_2, y_2, z_2) is

$$E(x_2, y_2, z_2) = E_0 \exp\left(-\frac{x_2^2 + z_2^2}{2r_0^2} + jky_2\right). \tag{A.3}$$

The wavelength of the incident radiation, $\lambda = 2\pi/k$. The waist radius of the beams at focus, r_0, is measured from the centre to the point where the intensity is $1/e$ of the peak intensity.

With the particle located at $\mathrm{x} = (x, y, z)$, the equations

$$\begin{aligned} x_1 &= x\cos\theta - y\sin\theta \\ y_1 &= y\cos\theta + x\sin\theta \\ x_2 &= x\cos\theta + y\sin\theta \\ y_2 &= y\cos\theta - x\sin\theta \\ z_1 &= z_2 = z \end{aligned} \tag{A.4}$$

allow the transformation of the coordinates of any point between the three orientations.

The terms in equation A.1 may be evaluated to give

$$\begin{aligned} |E_1|^2 &= E_0^2 \exp\left(-\frac{x_1^2+z_1^2}{r_0^2}\right) \\ &= E_0^2 \exp\left(-\frac{x^2\cos^2\theta - y^2\sin^2\theta + z^2}{r_0^2}\right) \exp\left(\frac{xy\sin 2\theta}{r_0^2}\right) \end{aligned} \quad \text{(A.5)}$$

$$\begin{aligned} |E_2|^2 &= E_0^2 \exp\left(-\frac{x_2^2+z_2^2}{r_0^2}\right) \\ &= E_0^2 \exp\left(-\frac{x^2\cos^2\theta + y^2\sin^2\theta + z^2}{r_0^2}\right) \exp\left(-\frac{xy\sin 2\theta}{r_0^2}\right) \end{aligned} \quad \text{(A.6)}$$

$$\begin{aligned} Re[E_1 E_2^*] &= E_0^2 \exp\left(-\frac{x_1^2+z_1^2}{2r_0^2} + jky_1\right) \exp\left(-\frac{x_2^2+z_2^2}{2r_0^2} - jky_2\right) \\ &= E_0^2 \exp\left(-\frac{x_1^2+z_1^2+x_2^2+z_2^2}{2r_0^2}\right) \cos k(y_1 - y_2) \\ &= E_0^2 \exp\left(-\frac{x^2\cos^2\theta + z^2 + y^2\sin^2\theta}{r_0^2}\right) \cos k(2x\sin\theta)\,. \end{aligned} \quad \text{(A.7)}$$

Substituting equations A.5, A.6, and A.7 back into equation A.1 gives

$$\begin{aligned} i_F(\mathbf{x}) = \eta &\left(\frac{1}{2}MC_{SC}\right)^2 E_0^2 \\ &\left[\exp\left(-\frac{x^2\cos^2\theta + y^2\sin^2\theta + z^2}{r_0^2}\right) \exp\left(\frac{xy\sin 2\theta}{r_0^2}\right)\right. \\ &+ \exp\left(-\frac{x^2\cos^2\theta + y^2\sin^2\theta + z^2}{r_0^2}\right) \exp\left(-\frac{xy\sin 2\theta}{r_0^2}\right) \\ &\left.+2\exp\left(-\frac{x^2\cos^2\theta + z^2 + y^2\sin^2\theta}{r_0^2}\right) \cos k(2x\sin\theta)\right]\,. \end{aligned} \quad \text{(A.8)}$$

Simplifying equation A.8 using the definition for a hyperbolic function in [87], gives

$$\begin{aligned} i_F(\mathbf{x}) &= \eta\left(\frac{1}{2}MC_{SC}\right)^2 E_0^2 \\ &\left[\exp\left(-\frac{x^2\cos^2\theta + y^2\sin^2\theta + z^2}{r_0^2}\right) 2\cosh\left(\frac{xy}{r_0^2}\sin 2\theta\right)\right. \\ &\left.+2\exp\left(-\frac{x^2\cos^2\theta + y^2\sin^2\theta + z^2}{r_0^2}\right)\cos k(2x\sin\theta)\right] . \end{aligned} \quad \text{(A.9)}$$

This waist radius, r_0, is $1/\sqrt{2}$ times the radius at $1/e^2$ of the peak intensity. This may be expressed as

$$r_0 = \frac{d_{e^{-2}}}{2\sqrt{2}} \quad \text{(A.10)}$$

where $d_{e^{-2}}$ is the focused beam diameter and is measured between points where the intensity is $1/e^2$ of the peak intensity at the centre. Substituting equation A.10 and $k = 2\pi/\lambda$, the photodetector fringe current may be expressed as

$$\begin{aligned} i_F(\mathbf{x}) &= 2\eta\left(\frac{1}{2}MC_{SC}\right)^2 I_0 \exp\left(-\frac{8(x^2\cos^2\theta + y^2\sin^2\theta + z^2)}{d_{e^{-2}}^2}\right) \\ &\times\left[\cosh\left(\frac{8xy}{d_{e^{-2}}^2}\sin 2\theta\right) + \cos\left(\frac{4\pi}{\lambda}x\sin\theta\right)\right] \end{aligned} \quad \text{(A.11)}$$

where I_0 is the intensity of the two beams at the focal point, E_0^2.

Appendix B

Derivation of the time-dependent autocorrelation function

B.1 Mean flow superimposed onto alternating velocity

Following the derivation of Hann and Greated in [17] , the time-independent pedestal term is ignored and the time-dependent part of the ACF may be expressed as

$$R(\tau) = \frac{\kappa^2 C_1 g_0}{2} \frac{\sqrt{\pi}}{4\beta} \int_{u_0\tau - u'_m}^{u_0\tau + u'_m} \frac{\exp(-4\beta^2 x^2)(1 + \cos Dx)}{\pi\sqrt{u'^2_m - (x - u_0\tau)^2}} dx \,. \tag{B.1}$$

Using the substituting $x = u_0\tau + u'_m \sin\alpha$, the integral in equation B.1 becomes

$$\int_{-\pi/2}^{\pi/2} \frac{1}{\pi} \exp\Big(-4\beta^2(u_0\tau + u'_m \sin\alpha)^2\Big)\Big(1 + \cos(Du_0\tau + Du'_m \sin\alpha)\Big) d\alpha \,. \tag{B.2}$$

Equation B.2 can be expanded to give

$$\frac{1}{\pi}\exp(-4\beta^2 u_0^2\tau^2)\int_{-\pi/2}^{\pi/2}\exp(-8\beta^2 u_0\tau u'_m\sin\alpha)\exp(-4\beta^2 u'^2_m\sin^2\alpha)$$
$$\times\Big(1+\cos(Du_0\tau)\cos(Du'_m\sin\alpha)-\sin(Du_0\tau)\sin(Du'_m\sin\alpha)\Big)d\alpha\ . \tag{B.3}$$

Substituting $p = 8\beta^2 u_0\tau u'_m$ and $q = 2\beta^2 u'^2_m$, equation B.1 may be expressed as

$$R(\tau) = \frac{\kappa^2 C_1 g_0}{2}\frac{\sqrt{\pi}}{4\beta}\exp(-4\beta^2 u_0^2\tau^2)(F_1+F_2+F_3) \tag{B.4}$$

where

$$F_1 = \frac{1}{\pi}\int_{-\pi/2}^{\pi/2}\exp(-p\sin\alpha)\exp(-2q\sin^2\alpha)d\alpha \tag{B.5}$$

$$F_2 = \frac{1}{\pi}\cos(Du_0\tau)$$
$$\times\int_{-\pi/2}^{\pi/2}\exp(-p\sin\alpha)\exp(-2q\sin^2\alpha)\cos(Du'_m\sin\alpha)d\alpha \tag{B.6}$$

$$F_3 = -\frac{1}{\pi}\sin(Du_0\tau)$$
$$\times\int_{-\pi/2}^{\pi/2}\exp(-p\sin\alpha)\exp(-2q\sin^2\alpha)\sin(Du'_m\sin\alpha)d\alpha\ . \tag{B.7}$$

The integrals F_1, F_2, and F_3 must be evaluated and combined to generate the ACF.

Applying the double angle formula [87], equation B.5 can be written as

$$F_1 = \frac{1}{\pi}\exp(-q)\int_{-\pi/2}^{\pi/2}\exp(-p\sin\alpha)\exp(q\cos 2\alpha)d\alpha\ . \tag{B.8}$$

Using the generating function of the modified Bessel function in [55] and the definitions of the hyperbolic functions in [87], equation B.8 may be expressed as

$$\begin{aligned} F_1 &= \frac{1}{\pi}\exp(-q)\int_{-\pi/2}^{\pi/2}[\cosh(p\sin\alpha)-\sinh(p\sin\alpha)] \\ &\quad\times\left(I_0(q)+2\sum_{n=1}^{\infty}I_n(q)\cos 2n\alpha\right)d\alpha \end{aligned} \tag{B.9}$$

The sinh term is an odd function and disappears. Equation B.9 can be simplified using [54]

$$\int_0^{\pi/2}\cosh(p\sin\alpha)cos(2n\alpha)d\alpha = (-1)^n\frac{\pi}{2}I_{2n}(p) \tag{B.10}$$

to give

$$F_1 = \exp(-q)\left(I_0(p)I_0(q)+2\sum_{n=1}^{\infty}(-1)^n I_n(q)I_{2n}(p)\right)\ . \tag{B.11}$$

Applying the double angle formula and using the Bessel function expansion for a cosine with a sinusoidal argument in [54] allows equation B.6 to be expressed as

$$\begin{aligned} F_2 &= \frac{1}{\pi}\exp(-q)\cos(Du_0\tau)\int_{-\pi/2}^{\pi/2}\exp(-p\sin\alpha)\exp(q\cos 2\alpha)d\alpha \\ &\quad\times\left(J_0(Du'_m)+2\sum_{k=1}^{\infty}J_{2k}(Du'_m)\cos(2k\alpha)\right)d\alpha \\ &= \cos(Du_0\tau)\Big(J_0(Du'_m)F_1+2\sum_{k=1}^{\infty}J_{2k}(Du'_m)F_4\Big) \end{aligned} \tag{B.12}$$

where

$$F_4 = \frac{1}{\pi}\exp(-q)\int_{-\pi/2}^{\pi/2}\exp(-p\sin\alpha)\exp(q\cos 2\alpha)\cos(2k\alpha)d\alpha\ . \qquad \text{(B.13)}$$

The first exponential in equation B.13 is expanded in terms of cosh and sinh and the second exponential in terms of the modified Bessel function. As the integral containing the sinh term is zero when evaluated between the limits, equation B.13 is

$$\begin{aligned} F_4 &= \frac{2}{\pi}\exp(-q)\int_0^{\pi/2}\cosh(p\sin\alpha)\cos(2k\alpha)I_0(q)d\alpha \\ &\quad +4\sum_{m=1}^{\infty}I_m(q)\int_0^{\pi/2}\cosh(p\sin\alpha)\cos(2k\alpha)\cos(2m\alpha)d\alpha\ . \end{aligned} \qquad \text{(B.14)}$$

By combining the two cosines [87], the second term in equation B.14 becomes

$$2\sum_{m=1}^{\infty}I_m(q)\int_0^{\pi/2}\cosh(p\sin\alpha)\Big(\cos(2[m-k])+\cos(2[m+k])\Big)d\alpha\ . \qquad \text{(B.15)}$$

Using equation B.10 and equation B.15, equation B.14 is expressed as

$$\begin{aligned} F_4 &= \exp(-q)\Bigg(I_0(q)(-1)^k I_{2k}(p) \\ &\quad +\sum_{m=1}^{\infty}I_m(q)\Big[(-1)^{m-k}I_{2(m-k)}(p)+(-1)^{m+k}I_{2(m+k)}(p)\Big]\Bigg)\ . \end{aligned} \qquad \text{(B.16)}$$

Equation B.7 is evaluated by expanding the first exponential in terms of cosh and sinh and using the double angle formula on the second exponential to expand it into a

series containing modified Bessel functions [54],

$$F_3 = -\frac{1}{\pi}\exp(-q)\sin(Du_0\tau)\int_{-\pi/2}^{\pi/2}\Big(I_0(q)+2\sum_{r=1}^{\infty}I_r(q)\cos(2r\alpha)\Big) \times \sinh(p\sin\alpha)\sin(Du'_m\sin\alpha)d\alpha\ . \tag{B.17}$$

The terms containing cosh are odd overall and have been ignored. Those with sinh cannot be ignored. The last sin term can be expanded [54], such that

$$\sin(Du'_m\sin\alpha) = 2\sum_{s=0}^{\infty}J_{2s+1}(Du'_m)\sin[(2s+1)\alpha] \tag{B.18}$$

to give

$$F_3 = -\frac{2}{\pi}\exp(-q)\sin(Du_0\tau)\sum_{s=0}^{\infty}J_{2s+1}(Du'_m) \times\int_{-\pi/2}^{\pi/2}\Big(I_0(q)+2\sum_{r=1}^{\infty}I_r(q)\cos(2r\alpha)\Big)\sinh(p\sin\alpha)\sin[(2s+1)\alpha]d\alpha\ . \tag{B.19}$$

Using

$$\int_{-\pi/2}^{\pi/2}\sinh(p\sin\alpha)\sin[(2s+1)\alpha]d\alpha = \pi(-1)^s I_{2s+1}(p) \tag{B.20}$$

from [54], equation B.19 may be written as

$$F_3 = -2\exp(-q)\sin(Du_0\tau)\sum_{s=0}^{\infty}J_{2s+1}(Du'_m)\Bigg((-1)^s I_0(q)I_{2s+1}(p) + \sum_{r=1}^{\infty}I_r(q)[(-1)^{s+r}I_{2s+2r+1}(p)+(-1)^{r-s-1}I_{2r-2s-1}(p)]\Bigg)\ . \tag{B.21}$$

From equations B.11, B.12, B.16, and B.21 and noting that from [17]

$$\sum_{k=1}^{\infty} J_{2k}(Du'_m)(-1)^k I_{2k}(8\beta^2 u_0 \tau u'_m) = J_0\left(u'_m\sqrt{D^2-\beta^2u_0^2\tau^2}\right) - J_0(Du'_m) \quad \text{(B.22)}$$

and

$$\sum_{s=0}^{\infty} J_{2k}(Du'_m)(-1)^s I_{2s+1}(8\beta^2 u_0 \tau u'_m) = 0 \quad \text{(B.23)}$$

the full expression for the time-dependent part of the autocorrelation function is given by

$$\begin{aligned}
R(\tau) \;=\; & \frac{\kappa^2 C_1 g_0}{2}\frac{\sqrt{\pi}}{4\beta}\exp(-4\beta^2u_0^2\tau^2)\exp(-2\beta^2u_m'^2) \\
& \Bigg\{\Big(1+\cos(Du_0\tau)J_0(Du'_m)\Big) \\
& \times\left[I_0(8\beta^2u_0\tau u'_m)I_0(2\beta^2u_m'^2) + 2\sum_{n=1}^{\infty}(-1)^n I_n(2\beta^2u_m'^2)I_{2n}(8\beta^2u_0\tau u'_m)\right] \\
& +I_0(2\beta^2u_m'^2)\cos(Du_0\tau)\left(J_0\Big(u'_m\sqrt{D^2-\beta^4u_0^2\tau^2}\Big) - J_0(Du'_m)\right) \\
& +2\cos(Du_0\tau)\sum_{k=1}^{\infty}J_{2k}(Du'_m)\sum_{m=1}^{\infty}I_m(2\beta^2u_m'^2)(-1)^{m-k}I_{2(m-k)}(8\beta^2u_0\tau u'_m) \\
& +2\cos(Du_0\tau)\sum_{k=1}^{\infty}J_{2k}(Du'_m)\sum_{m=1}^{\infty}I_m(2\beta^2u_m'^2)(-1)^{m+k}I_{2(m+k)}(8\beta^2u_0\tau u'_m) \\
& -2\sin(Du_0\tau)\sum_{s=0}^{\infty}J_{2s+1}(Du'_m)\sum_{r=1}^{\infty}J_r((2\beta^2u_m'^2)(-1)^{s+r}I_{2s+2r+1}(8\beta^2u_0\tau u'_m) \\
& -2\sin(Du_0\tau)\sum_{s=0}^{\infty}J_{2s+1}(Du'_m)\sum_{r=1}^{\infty}J_r((2\beta^2u_m'^2)(-1)^{r-s-1}I_{2r-2s-1}(8\beta^2u_0\tau u'_m)\Bigg\}.
\end{aligned} \quad \text{(B.24)}$$

Appendix C

Evaluation of the measurement uncertainty

C.1 Introduction

The evaluation of uncertainty is an integral part of any measurement procedure. The method adopted in the present study, and at the National Physical Laboratory (NPL), follows a recommended process for combining the different types of uncertainty to produce an overall value [78]. In the first stage of the process, the individual components of the uncertainty are classified as one of two types; type A or type B. Then the magnitude of each component is estimated by considering the standard deviation resulting from the characteristics of the probability density distributions. Finally, the individual components are combined into the overall uncertainty figure.

C.2 Type A uncertainty

An example of a type A evaluation of standard uncertainty is the calculation of the standard deviation for the mean of a series of independent observations. The observations will not all be exactly the same because they are influenced by independent random variables. The mean value gives an estimate of the true value and this estimate improves as the number of observations is increased. In the limit as the number of observations tends to infinity, the mean value gives the true value. The infinite set of observations is called the population. In reality there will be a finite limit to the number of observations required to give a mean value close enough to the true value for any differences to be negligible. In most situations the population values have a Gaussian or Normal distribution [53]. Scaling the y axis so that the total area under the curve is unity gives the probability density function displayed in figure C.1. The probability of observing a value in a particular range, e.g. a to b, is given by the area under the distribution curve

The spread of the population is a measure of the type A component of the uncertainty and can be evaluated from the standard deviation. An estimate of the population standard deviation is determined from a sample of n values of x with mean value $\bar{x}$ using the expression from [87] for the variance

$$\sigma_A^2 = \frac{1}{n-1}\sum_{i=1}^{n}(x_i - \bar{x})^2 \,. \tag{C.1}$$

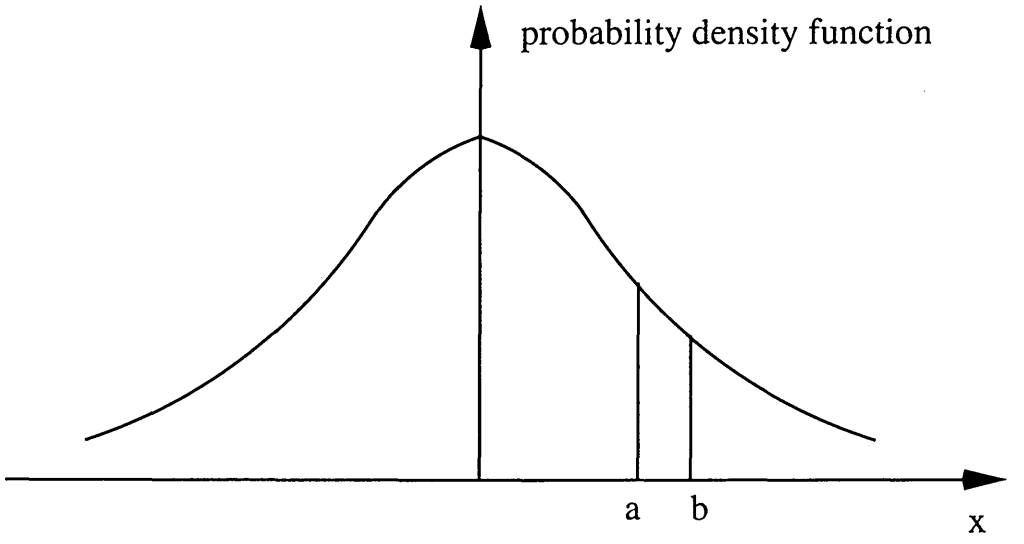

Figure C.1: Gaussian distribution of the probability density.

The standard uncertainty in the sample mean is calculated in [78], such that

$$u_A = \frac{\sigma_A}{\sqrt{n}} . \tag{C.2}$$

Increasing the number of observations reduces the uncertainty. However, as n increases, significantly more samples must be obtained in order to reduce u_A by a sizeable amount.

C.3 Type B uncertainty

Type B uncertainties typically arise from corrections required to change a measurement to the true value [88]. These corrections are not known exactly but during the measurement process their value remains constant. It is the uncertainty in the correction that contributes to the uncertainty in the measurement. There will usually be several type

B components of uncertainty to consider. A detailed knowledge of the measurement process enables the identification and evaluation of the individual components.

The uncertainty due to an individual type B component is evaluated by considering the probability distribution and standard deviation associated with the particular parameter. For example, if the limits of a type B uncertainty are $\pm a$ there is an equal probability of a measured value being anywhere between these limits. This gives a probability distribution which is rectangular in shape and a standard deviation of [78]

$$\sigma = \frac{a}{\sqrt{3}} . \tag{C.3}$$

Other types of distribution result in different relationships between the standard deviation and the limits of the range. It may not be possible to deduce the true form of the probability density function. In such circumstances the rectangular distribution is used as this gives a conservative estimate for the uncertainty.

After the type B components have been identified and assessed to give the associated standard deviations, they are combined into a single value. The individual standard deviations are expressed as percentages of their respective values and combined as a root sum square to give

$$u_B = \sqrt{\sigma_1^2 + \sigma_2^2 + \ldots} \tag{C.4}$$

C.4 Overall uncertainty

The combined standard uncertainty is

$$u = \sqrt{u_A^2 + u_B^2} \tag{C.5}$$

where u_A is the total type A component and u_B is the total type B component.

The Central Limits Theorem states that when a number of arbitrary distributions are combined the resulting distribution will be approximately Gaussian [53]. This is illustrated in figure C.2. For the region bounded by $\bar{x} \pm u$, the probability of the actual value lying in this range is given by the area under the curve between the limits, $\pm u$, and is approximately 68% [88].

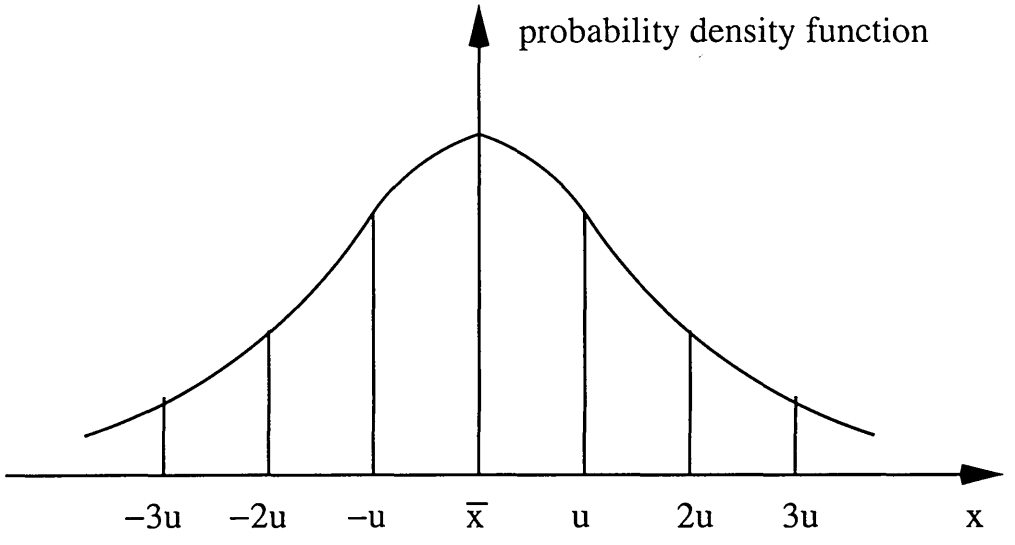

Figure C.2: Combined probability distribution. Adapted from figure 5 of [88].

The range, $\bar{x} \pm u$, is called the confidence interval as it quantifies the confidence that

can be placed in a measurement. The combined standard uncertainty can be multiplied by a coverage factor, k, to give the expanded uncertainty, $U = ku$. This increases the confidence interval and the probability that the actual value lies within the range. For example, $k = 2$ increases the probability to approximately 95 % and $k = 3$ increases the probability to approximately 99 %. Only the approximate confidence level can be stated due to the assumption that the combined distribution is Gaussian.

Correction to equation B.24

Equations B.22 and B.23 in Appendix B have been found to be invalid [89] and so equation B.24 on page 277 is incorrect.

From equations B.11, B.12, B.16, and B.21 the full expression for the time-dependent part of the autocorrelation function is now given by

$$
\begin{aligned}
R(\tau) \;=\; & \frac{\kappa^2 C_1 g_0}{2}\frac{\sqrt{\pi}}{4\beta}\exp(-4\beta^2 u_0^2\tau^2)\exp(-2\beta^2 u_m'^2) \\
& \Bigg\{\Big(1+\cos(Du_0\tau)J_0(Du_m')\Big) \\
& \times\Big[I_0(8\beta^2 u_0\tau u_m')I_0(2\beta^2 u_m'^2)+2\sum_{n=1}^{\infty}(-1)^n I_n(2\beta^2 u_m'^2)I_{2n}(8\beta^2 u_0\tau u_m')\Big] \\
& +2\cos(Du_0\tau)\sum_{k=1}^{\infty}J_{2k}(Du_m')(-1)^k I_{2k}(8\beta^2 u_0\tau u_m')I_0(2\beta^2 u_m'^2) \\
& +2\cos(Du_0\tau)\sum_{k=1}^{\infty}J_{2k}(Du_m')\sum_{m=1}^{\infty}I_m(2\beta^2 u_m'^2)(-1)^{m-k}I_{2(m-k)}(8\beta^2 u_0\tau u_m') \\
& +2\cos(Du_0\tau)\sum_{k=1}^{\infty}J_{2k}(Du_m')\sum_{m=1}^{\infty}I_m(2\beta^2 u_m'^2)(-1)^{m+k}I_{2(m+k)}(8\beta^2 u_0\tau u_m') \\
& -2\sin(Du_0\tau)\sum_{s=0}^{\infty}J_{2s+1}(Du_m')I_0(2\beta^2 u_m'^2)I_{2s+1}(8\beta^2 u_0\tau u_m') \\
& -2\sin(Du_0\tau)\sum_{s=0}^{\infty}J_{2s+1}(Du_m')\sum_{r=1}^{\infty}I_r(2\beta^2 u_m'^2)(-1)^{r+s}I_{2r+2s+1}(8\beta^2 u_0\tau u_m') \\
& -2\sin(Du_0\tau)\sum_{s=0}^{\infty}J_{2s+1}(Du_m')\sum_{r=1}^{\infty}I_r(2\beta^2 u_m'^2)(-1)^{r-s-1}I_{2r-2s-1}(8\beta^2 u_0\tau u_m')\Bigg\}.
\end{aligned}
\tag{B.24}
$$

By considering a typical magnitude for β and noting the behaviour of $e^{-q}I_n(q)$, the

expression for the normalised ACF simplifies to

$$\tilde{R}(\tau) \simeq \frac{1}{2}\exp(-4\beta^2 u_0^2\tau^2)\left\{1+\cos(Du_0\tau)J_0\left(Du'_m\right)\right\}$$

which is equal to equation 4.34 as $D^2 >> 4\beta^2 u_0^2\tau^2$.

Bibliography

[1] S Ballantine. Technique of microphone calibration. *Journal of the Acoustical society of America*, 3:319–360, 1932.

[2] International Electrotechnical Commission. IEC 61094-2:1992, Measurement microphones, part2 : Primary method for the pressure calibration of laboratory standard microphones by the reciprocity method.

[3] K. J. Taylor. Absolute calibration of microphones by a laser-Doppler technique. *Journal of the Acoustical Society of America*, 70(4):939–945, 1981.

[4] H. Yeh and H. Z. Cummins. Localized fluid flow measurements with an He-Ne laser spectrometer. *Applied Physics Letters*, 4:176–178, 1964.

[5] M. J. Rudd. A new theoretical model for the laser Doppler meter. *Journal of Scientific Instruments*, 2(2):55–58, 1969.

[6] T. S. Durrani and C. A. Greated. *Laser systems in flow measurements.* Plenum Press, 1977.

[7] F. Durst, A. Melling, and J. H. Whitelaw. *Principles and practice of laser Doppler anemometry*. Academic Press, 1976.

[8] C. A. Greated and T. S. Durrani. Signal analysis for laser velocimeter measurements. *Journal of Applied Physics E: Scientific Instruments*, 4(1):24–26, 1971.

[9] K. J. Taylor. Absolute measurement of acoustic particle velocity. *Journal of the Acoustical Society of America*, 59(3):691–694, 1976.

[10] M. R. Davis and K. J. Hews-Taylor. Laser-Doppler measurement of complex acoustic impedance. *Journal of Sound and Vibration*, 107(3):451–470, 1986.

[11] F. J. Vignola, Y. H. Berthelot, and J. Jarzynski. Laser detection of sound. *Journal of the Acoustical Society of America*, 90(3):1275–1286, 1991.

[12] V. A. Grechikhin and B. S. Rinkevichius. Digital Hilbert transform for processing laser Doppler vibrometry signals. In *Proceedings of 2nd International Conference on Vibration Measurement by Laser Techniques*, Ancona, Italy, 1996.

[13] T. Loizeau and Y. Gervais. Measurement of the acoustic velocity by laser Doppler anemometry. *Acustica*, 83:945–954, 1997.

[14] S. H. Jack. Laser Doppler anemometry in sound fields. Master's thesis, University of Edinburgh, 1997.

[15] J. P. Sharpe and C. A. Greated. The measurement of periodic acoustic fields using photon correlation spectroscopy. *Journal of Applied Physics D: Applied Physics*, 20(4):418–423, 1987.

[16] J. P. Sharpe, C. A. Greated, and D. M. Campbell. The measurement of complex acoustic impedance using photon correlation spectroscopy. *Acustica*, 66:286–289, 1988.

[17] D. Hann and C. A. Greated. Acoustic measurements in flows using photon correlation spectroscopy. *Measurement Science and Technology*, 5(2):157–164, 1994.

[18] C. A. Greated. Measurement of acoustic velocity fields. *Strain*, pages 21–24, 1986.

[19] E. C. Wente. A condenser transmitter as a uniformly sensitive instrument for the absolute measurement of sound intensity. *Physical Review*, 10(1):39–63, 1917.

[20] H. D. Arnold and I. B. Crandall. The thermophone as a precsion source of sound. *Physical Review*, 10(1):22–38, 1917.

[21] R. K. Cook. Absolute pressure calibration of microphones. *Journal of the Acoustical Society of America*, 12:415–420, 1941.

[22] W. R. Maclean. Absolute measurement of sound without a primary standard. *Journal of the Acoustical Society of America*, 12:140–146, 1940.

[23] International Electrotechnical Commission. IEC 61094-1:1992, Measurement microphones, part1 : Specification for laboratory standard microphones.

[24] Brüel & Kjær. *Microphone handbook*, 1996.

[25] G. S. K. Wong and T. F. W. Embleton. *AIP handbook of condenser microphones: Theory, calibration, and measurements.* AIP Press.

[26] D. R. Jarvis. *Realization of the standard of sound pressure through the calibration of half-inch laboratory condenser microphones.* PhD thesis, Kings College (University of London), 1989.

[27] R. G. Barham. *Free-field reciprocity calibration of laboratory standard microphones.* PhD thesis, University of Southampton, 1995.

[28] T. S. Durrani and C. A. Greated. *Laser systems in flow measurements*, chapter 5. Plenum Press, 1977.

[29] H-E de Bree, Leussink, P. J., T. Korthorst, and M. Elwenspoek. The two sensor Microflown: a novel device measuring acoustical flows. *Sensors and Actuators A*, 54:552–557, 1996.

[30] G. K. Behler and M. Vörlander. Optical measuring and calibration techniques for microphones. In *Proceedings of Forum Acusticum*, Berlin, Germany, 1999.

[31] F. J. M. van der Eerden, H. E. de Bree, and H. Tijdeman. Experiments with a new acoustic particle velocity sensor in an impedance tube. *Sensors and Actuators A*, 69:126–133, 1998.

[32] G. K. Behler and M. Vörlander. Method and application of an optical measuring and calibration technique for microphones. In *Proceedings of 17th International Congress on Acoustics*, Rome, Italy, 2001.

[33] T. S. Durrani and C. A. Greated. *Laser systems in flow measurements*, chapter 2. Plenum Press, 1977.

[34] R. J. Goldstein, editor. *Fluid mechanics measurements*. Hemisphere Publishing Corporation, 1983.

[35] C. L. Dancey and J. Hetmanski. Beam waist misalignment error estimates in laser Doppler anemometry. *Journal of Propulsion and Power*, 11(5):1078–1080, 1995.

[36] P. C. Miles. Geometry in the fringe field formed in the intersection of two gaussian beams. *Applied Optics*, 35(30):5887–5895, 1996.

[37] F. Durst and W. H. Stevenson. Properties of focused laser beams and the influence on optical anemometry signals. In *Minnesota Symposium on Laser Anemometry Proceedings*, pages 371–388, 1976.

[38] W. K. George and N. S. Berman. Doppler ambiguity in laser Doppler velocimeters. *Applied Physics Letters*, 23(5):222–223, 1973.

[39] F. G. Stremler. *Introduction to communication systems*. Addison-Wesley, 1990.

[40] J. S. Cullen. *A study of brass instrument acoustics using an artificial lip reed mechanism, laser Doppler anemometry and other techniques*. PhD thesis, University of Edinburgh, 2000.

[41] T. S. Durrani and C. A. Greated. *Laser systems in flow measurements*, chapter 3. Plenum Press, 1977.

[42] M. R. Spiegel and J. Liu. *Mathematical handbook of formula and tables.* McGraw-Hill, 1999.

[43] E. B. Wylie and V. L. Streeter. *Fluid transients.* McGraw-Hill, 1978.

[44] J. S. Cullen, C. A. Greated, and D. M. Campbell. LDA measurement of sound: amplitude modulation of laser Doppler signals. *Measurement Science and Technology*, 10(9):812–823, 1999.

[45] W. H. Press, S. A. Teukolsky, W. T. Vetterling, and B. P. Flannery. *Numerical recipes in C: The art of scientific computing.* Cambridge University Press, 1992.

[46] D. Hann and C. A. Greated. The measurement of sound fields using laser Doppler anemometry. *Acustica*, 85:401–411, 1999.

[47] T. S. Durrani and C. A. Greated. *Laser systems in flow measurements*, chapter 1. Plenum Press, 1977.

[48] S. H. Jack, D. B. Hann, and C. A. Greated. Influence of the acousto-optic effect on laser Doppler anemometry signals. *Review of Scientific Instruments*, 69(12):4074–4081, 1998.

[49] S. H. Jack, D. B. Hann, and C. A. Greated. The influence of a standing wave on laser Doppler signals. *Measurement Science Technology*, 10(12):1279–1285, 1999.

[50] T. M. Smith and A. Korpel. Measurement of light-sound interaction efficiencies in solids. *IEEE Journal of Quantum Electronics*, 1:283–284, 1965.

[51] T. S. Durrani and C. A. Greated. *Laser systems in flow measurements*, chapter 4. Plenum Press, 1977.

[52] J. P. Sharpe and C. A. Greated. A stochastic model for photon correlation measurements in sound fields. *Journal of Applied Physics D: Applied Physics*, 22(10):1429–1433, 1989.

[53] A. Papoulis. *Probability, random variables, and stochastic processes.* New York:McGraw-Hill, 1991.

[54] N. W. McLachlan. *Bessel functions for engineers.* London: Oxford University Press, 1934.

[55] C. J. Tranter. *Bessel functions with some physical aplications.* London: English Universities Press, 1968.

[56] G. N. Watson. *A treatise on the theory of Bessel functions.* Cambridge University Press, 1952.

[57] Brüel & Kjær. *Half inch condenser microphones: Instructions and applications*, 1966.

[58] Brüel & Kjær. *Product data: condenser microphone cartridges.*

[59] D. E. Hall. *Basic acoustics.* Krieger, 1993.

[60] L. E. Kinsler, A. R. Frey, A. B. Coppens, and J. V. Sanders. *Fundamentals of acoustics.* John Wiley and Sons, Inc., 1982.

[61] R. S. Davis. Equation for the determination of the density of moist air. *Metrologia*, 29:67–70, 1992.

[62] P. Giacomo. Equation for the determination of the density of moist air. *Metrologia*, 18:33–40, 1982.

[63] R. G. Barham. Personal correspondence, 2000.

[64] O. Cramer. The variation of the specific heat ratio and the speed of sound in air with temperature, pressure, humidity and CO_2 concentration. *Journal of the Acoustical Society of America*, 93(5):2510–2516, 1993.

[65] Spectra-Physcs. *Spectra-Physcs Helium Neon laser manual*, 1985.

[66] DANTEC. *Laser Doppler anemometry*, 1983.

[67] Uniphase. *Uniphase model 1300 series Helium Neon laser systems*, 1994.

[68] Malvern Instruments. *Malvern Adjustable Beam Splitter and Polarisation Unit Type RF 307*, 1980.

[69] Brookhaven. *Instruction nanual for BI-9000AT digital correlator*, 1998.

[70] F. J. Vignola, Y. H. Berthelot, S. Jones, and J. Jarzynski. Equation of motion of microparticles in suspension in an insonified medium. *Journal of the Acoustical Society of America*, 92(3):332–334, 1992.

[71] A. Melling. Tracer particles and seeding for particle image velocimetry. *Measurement Science and Technology*, 8(12):1406–1416, 1997.

[72] Y. S. Cheng, W. E. Bechtold, C. DC. Yu, and I. F. Hung. Incense smoke: Characterization and dynamics in indoor environments. *Aerosol Science and Technology*, 23:271–281, 1995.

[73] K. P. Hinz, R. Kaufmann, and B. Spengler. Laser induced mass analysis of single particles in the airborne state. *Analytical Chemistry*, 66(13):2071–2076, 1994.

[74] JEM Smoke Machine Company Ltd. *Hydrosonic 2000 instruction manual*, 2000.

[75] J. C. Valière, P. Herzog, V. Valeau, and G. Tournois. Acoustic velocity measurements in air by means of laser Doppler velocimetry: dynamic and frequency range limitations and signal processing improvements. *Journal of Sound and Vibration*, 229:607–626, 2000.

[76] F. Bowman. *Introduction to Bessel functions*. Longmans, Green and co. ltd., 1938.

[77] D. Matovic and C. Tropea. Spectral peak interpolation with application to LDA signal processing. *Measurement Science and Technology*, 2(11):1100–1106, 1991.

[78] B. N. Taylor and C. E. Kuyatt. Guidlines for evaluating and expressing the uncertainty of NIST measurement results, 1994. NIST technical note 1297.

[79] M. Pentz and M. Shott. *Handling experimental data*. Open University Press, 1994.

[80] R. G. Barham. Personal correspondence, 2000.

[81] S. Poggi. *Contribution to the development of a system for measuring the acoustic particle velocity by Laser Doppler Velocimetry: evaluation of results, applications.* PhD thesis, de l'Universit du Maine,Le Mans, France, 2000.

[82] Malvern Instruments. *K9023 Phase Modulator handbook*, 1980.

[83] L. L. Beranek. *Acoustic measurements.* John Wiley and sons, 1959.

[84] P. Herzog, J. C. Valiere, and S. Dufosse. Laser Doppler velocimetry in acoustics: principles and signal processing. In *Proceedings of 15th International Congress on Acoustics*, Trondheim, Norway, pages 91–94, 1995.

[85] M. E. Delany and E. N. Bazley. The high frequency performance of wedge-lined free field rooms. *Journal of Sound and Vibration*, 55(2):195–214, 1977.

[86] I. Grant and C. A. Greated. Periodic sampling in laser anemometry. *Journal of Applied Physics E: Scientific Instruments*, 13(5):571–574, 1980.

[87] G. James, D. Burley, D. Clements, P. Dyke, J. Searl, and J. Wright. *Modern engineering mathematics.* Addison-Wesley, 1993.

[88] R. G. Barham. Calibration principles. National Physical Laboratory.

[89] T. Schlicke. Personal correspondence, 2002.

Publications

Conference paper

T. J. MacGillivray, R. Barham, D. M. Campbell, and C. A. Greated. The calibration of microphones using laser Doppler anemometry. In the *Proceedings of 17th International Congress on Acoustics*, Rome, Italy, September 2001.

Journal papers

T. J. MacGillivray, R. Barham, D. M. Campbell, and C. A. Greated. The development of a microphone calibration technique using laser Doppler anemometry. *Acustica*, 88(1):135-141, 2002.

T. J. MacGillivray, R. Barham, D. M. Campbell, and C. A. Greated. The development of a microphone calibration technique using photon correlation spectroscopy. Submitted for publication in *Acustica*.

ACUSTICA · acta acustica
Vol. 88 (2002) 135 – 141
© S. Hirzel Verlag · EAA

The development of a microphone calibration technique using Laser Doppler Anemometry.

T MacGillivray*, D Campbell, C Greated
Fluid Dynamics and Acoustics Group, Department of Physics and Astronomy, The University of Edinburgh, James Clerk Maxwell Building, Kings Buildings, Edinburgh EH9 3JZ

R Barham
Acoustics Standards, Centre for Mechanical and Acoustical Metrology, National Physical Laboratory, Queens Road, Teddington, Middlesex TW11 0LW

Summary
The details of a working system for the calibration of microphones based on the direct measurement of acoustic particle velocity using Laser Doppler Anemometry (LDA) are presented and discussed. The calibration is carried out using a standing wave generated inside a glass tube attached to a loudspeaker. The probe microphone used to monitor pressure amplitude is fitted in the end of the tube. The pressure amplitude at the end is calculated from velocity measurements using the LDA system and the characteristic acoustic impedance of the air inside the tube. The frequency response of the probe is characterized separately. A measurement microphone system supplied by the National Physical Laboratory (NPL) has been calibrated using this apparatus. The sensitivity of the microphone is determined to within ±0.1 dB of the sensitivity obtained by reciprocity calibration for frequencies between 600 Hz and 2 kHz.

PACS no. 43.38.Kb, 43.58.Vb, 43.60.Qv

1. Introduction

The provision of primary measurement standards for physical quantities is the remit of national metrology laboratories around the world. In the early days of modern acoustical measurement, the primary standard was based on the so-called Rayleigh disk. Acoustic particle velocity was determined from the degree of rotation of a small light weight disk suspended in the acoustic field by a fine thread along its diameter. In the 1960s reciprocity calibration of microphones provided the potential for lower uncertainty and was adopted by the International Electrotechnical Commission (IEC) as the preferred method of realizing the primary standard and this arrangement persists today [1]. Essentially the calibration of the microphone requires the sensitivity, that is the output voltage for a given sound pressure, to be determined. Since its adoption the reciprocity method has been refined to the point where further efforts to develop it are producing ever diminishing returns.

During this time, advances in optical technologies, and particularly lasers, has resulted in a number of practical LDA applications being developed. There is therefore potential to apply these to the measurement of acoustic particle velocity and return to measurement standards derived from this. The aim of the research is to develop and assess a method for microphone calibration based on measurements made with a laser Doppler system.

Received 25 April 2001,
accepted 10 2001.

* Electronic mail: tm@ph.ed.ac.uk

2. LDA for sound measurement

The reciprocity method of calibration is indirect in that no evaluation of the acting sound pressure is required. In contrast, optical methods can provide a direct approach where the sound pressure is determined from the measurement of acoustic particle velocity using a laser Doppler system. Taylor developed such a system, based on a traveling wave tube, thus enabling the sound pressure at a point in a tube where a microphone is positioned to be calculated from the velocity measurement [2]. By measuring the output voltage of the microphone, its sensitivity is found.

Taylor's apparatus suffered from poor signal-to-noise ratio and the analysis ignored ambiguity noise and assumed the Doppler signal had a constant amplitude. Although an uncertainty of 0.03 dB was claimed, this required a large sample of measurements to be taken resulting in prolonged measurement time that was impractical for routine implementation. Consequently the method was regarded as a means of validating reciprocity rather than providing a viable alternative to it.

Taylor's experimental set up can now be improved upon but before these improvements are discussed, it is necessary to review the basic theory for LDA measurements. In the dual beam LDA configuration, interference fringes are formed at the intersection of two laser beams. As particles move across the ellipsoidal fringe volume they scatter light into a photodetector which is frequency shifted by an amount proportional to the velocity of motion of the particles.

A frequency shift is introduced to one of the beams. The fringe pattern moves through the fringe volume at a speed corresponding to the beat frequency between the beams [3]. The resulting Doppler signal can be analysed

ACUSTICA · acta acustica
Vol. 88 (2002)

to give particle velocity. The instantaneous frequency, i.e. the Doppler frequency, of the signal is of the form [4]

$$F_D = F_s + \frac{U}{\Lambda} + \frac{d\phi}{dt} \tag{1}$$

where F_s is the frequency shift introduced to one of the beams, U is the velocity, Λ is the spacing between fringes, and the $d\phi/dt$ term is called ambiguity noise. Λ depends on the acute angle of intersection of the beams 2θ and on the wavelength of the laser light λ, $\Lambda = \lambda/2\sin\theta$. The ambiguity noise arises because the Doppler signal is composed of the superposition of multiple signals generated by individual particles. The individual signals have a random phase ϕ related to the initial position of the generating particle. The Doppler frequency varies randomly about $F_s + U/\Lambda$ due to the ambiguity noise.

An sinusoidal acoustic field of single frequency f_m generates a Doppler signal of the form of a frequency modulated wave with carrier frequency F_s, modulation frequency f_m, and peak frequency deviation ΔF_m [5]. The peak frequency deviation is given by

$$\Delta F_m = \frac{2\pi f_m x_m}{\Lambda} \tag{2}$$

where x_m is the acoustic particle displacement amplitude. The acoustic particle velocity amplitude $u_m = 2\pi f_m x_m$ and so equation (2) can be written as

$$\Delta F_m = \frac{u_m}{\Lambda}. \tag{3}$$

The peak frequency deviation is directly proportional to the acoustic particle velocity amplitude.

The frequency spectrum of the frequency modulated signal consists of a spectral component centered on the frequency shift and side lobes spaced at discrete multiples of the acoustic frequency. The amplitudes of the peaks are proportional to successive orders of the Bessel function of the first kind with argument $\Delta F/f_m$. Using equation (3), the ratio of amplitudes between the nth peak from the centre and the centre peak will be

$$J_n\left(\frac{u_m}{\Lambda f_m}\right) / J_0\left(\frac{u_m}{\Lambda f_m}\right). \tag{4}$$

The Bessel function of zero order and argument α is defined by the infinite power series [6]

$$J_0(\alpha) = 1 - \frac{\alpha^2}{2^2} + \frac{\alpha^4}{2^2.4^2} - \frac{\alpha^6}{2^2.4^2.6^2} + \ldots \tag{5}$$

Similarly, the Bessel function of order one and argument α is defined by

$$J_1(\alpha) = \frac{\alpha}{2} - \frac{\alpha^3}{2^2.4} + \frac{\alpha^5}{2^2.4^2.6} - \ldots \tag{6}$$

For small α, equation (4) reduces to

$$\frac{J_1(\alpha)}{J_0(\alpha)} \simeq \frac{4\alpha}{(8-\alpha^2)}. \tag{7}$$

Substituting $\alpha = \Delta F/f_m$ allows equation (7) to be resolved to give u_m.

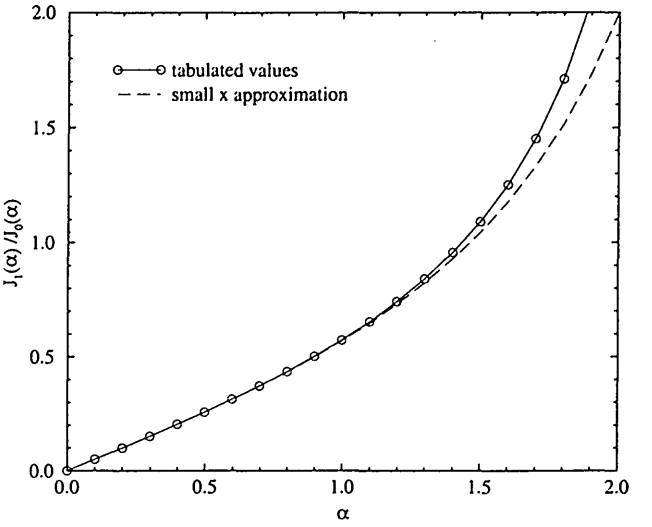

Figure 1. Variation of the ratio of $J_1(\alpha)$ to $J_0(\alpha)$ with argument α.

Extensive tables of values for $J_0(\alpha)$ and $J_1(\alpha)$ have been calculated [7]. The graph in figure 1 shows how the ratio of $J_1(\alpha)$ to $J_0(\alpha)$ changes with argument in the range $0 \leq \alpha < 2$. The points on the solid line correspond to values of the ratio evaluated using tables of Bessel functions. The dashed line corresponds to the small argument approximation in equation (7) and is valid for $\alpha < 1.3$. The particle velocity amplitude can be determined using the ratio of $J_1(\alpha)$ to $/J_0(\alpha)$ to predict α from the graph.

3. Experimental apparatus

Figure 2 shows the LDA system used to capture the Doppler signals produced by acoustic particle motion. DANTEC 55x series transmitter optics and a 20 mW He-Ne laser ($\lambda = 633$ nm) produce the fringe pattern. The beams intersect at an acute angle of $2\theta = 22.1°$ resulting in a fringe spacing of $\Lambda = 3.29\mu$m. DANTEC 55x series photomultiplier and optics detect the scattered light. A Bragg cell incorporated into the transmitter optics produces a 40 MHz optical frequency shift. A DANTEC 55N12 frequency shifter electronically downshifts the photomultiplier signal to an equivalent frequency shift of $F_s = 100$ kHz. The signal is bandpass filtered at 2–200 kHz to remove the pedestal value and to prevent aliasing. An IOtech Wavebook 512 connected to a PC makes a 32768 point sample at 0.5 MHz of both the photomultiplier signal and the probe microphone output.

A loudspeaker generated an acoustic field inside a sealed glass tube. The tube has an internal diameter of 32.80 mm and a length of 748 mm and was terminated with a rigid end through which probe microphone could be inserted. The combined tube-loudspeaker system was driven at the natural resonant frequencies to produce

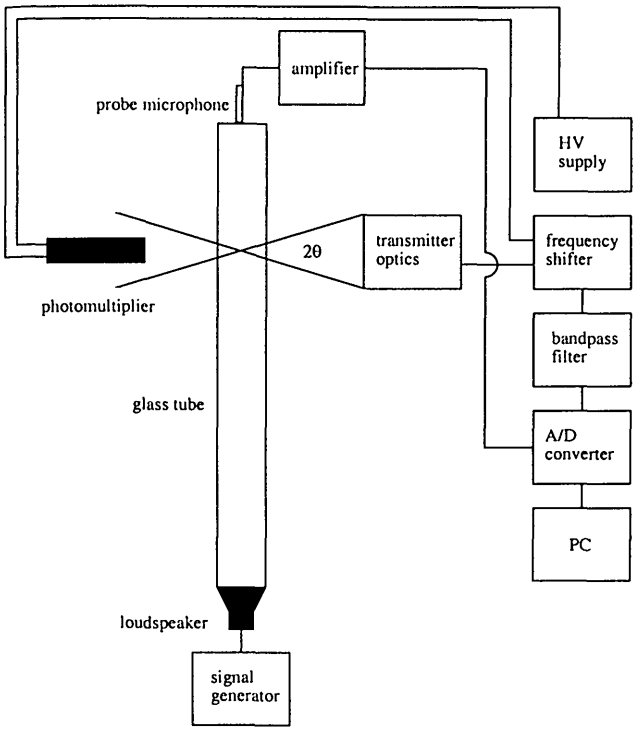

Figure 2. Diagram of the LDA apparatus and standing wave tube.

standing waves. All LDA measurements were carried out at the position of the first or second velocity antinode from the rigid end.

To compare LDA velocity measurements with the probe microphone pressure measurements it is necessary to determine the characteristic impedance of air, ρc. The density of air and the speed of sound in air are calculated independently, as functions of the environmental conditions [8, 9, 10]. The atmospheric pressure and the relative humidity were measured using an electronic barometer. The air temperature inside the tube was measured by removing the probe microphone and inserting a probe thermometer.

The measurements of acoustic pressure amplitude were made using a probe microphone attachment for a half-inch microphone cartridge. The probe tube has a length of 230 mm and a diameter of 3.9 mm and was fixed to a Brüel and Kjær type 4133 microphone. The probe distorts the frequency response. The effects of the probe tube were characterized relative to the response of a reference microphone allowing voltage amplitude to be transformed into pressure amplitude measured in Pascals. The reference microphone was a Brüel and Kjær type 4192. The probe was also characterized relative to the half inch microphone system supplied by NPL.

Incense smoke was used to seed the air inside the tube by removing the probe microphone and inserting a burning incense stick for a period of approximately 5 seconds. The particles have typical diameters of 0.5 μm which is less than the fringe spacing [11]. The particles follow the oscillations of the air sufficiently for acoustic frequencies of less than 10 kHz [5].

4. Frequency analysis

An example of the Doppler signals captured with the apparatus is shown in figure 3. The Fast Fourier transform (FFT) of the signal generates the frequency spectrum and is illustrated in figure 4. The signal is more complex than the frequency modulated form envisaged. The amplitude of the signal varies randomly due to the random nature of the seeding particle distribution and varies periodically at the acoustic frequency. Although for time domain analysis techniques this can cause problems due to dropout [12], it has negligible effects on the frequency spectrum.

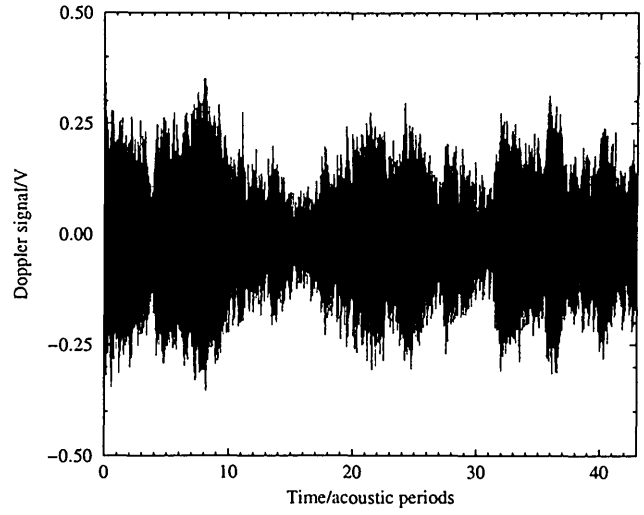

Figure 3. A measured Doppler signal generated by an acoustic field with frequency, $f_m = 660$ Hz.

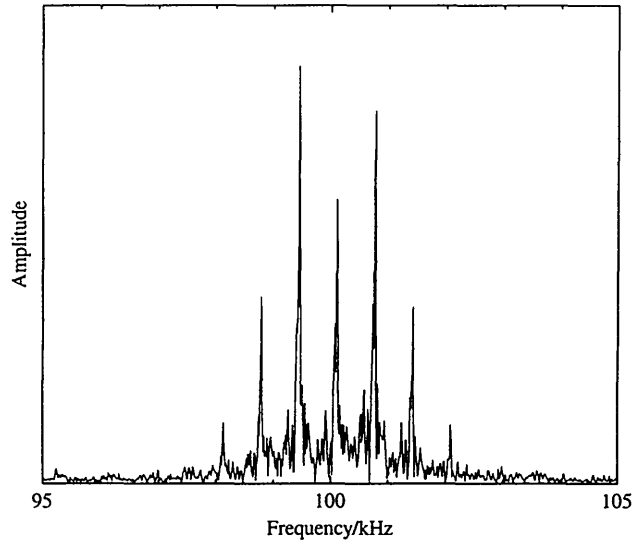

Figure 4. A section of the frequency spectrum about the shift frequency, $F_s = 100$ kHz.

The Doppler signal is sampled and windowed before the frequency spectrum is calculated. Each spectral peak

ACUSTICA · acta acustica
Vol. 88 (2002)

has a finite width determined by the windowing operation and the spectral width of the ambiguity noise. In our case the combined spectral width of the peaks is very narrow compared to the bandwidth of the frequency spectrum and is assumed negligible. The amplitude of a spectral peak is indicated by its height. Using the amplitudes of the first two side peaks and the centre peak, the Bessel function argument and the particle velocity amplitude are deduced. An interpolation routine based on a variable width cosine squared estimator provides an accurate means of determining the height of a spectral peak [13].

The mean value of particle velocity amplitude is obtained by sampling a set of 20 Doppler signals generated by a particular pressure amplitude and frequency of standing wave. Two values of the Bessel function argument are deduced from each frequency spectrum and used to calculate velocity amplitude. The mean value and standard deviation are determined for the set of signals.

5. Uncertainty analysis

The uncertainty in the measurement of the mean value of acoustic particle velocity amplitude is evaluated by considering the individual components of the calculation.

The fringe spacing is required to calculate velocity amplitude and depends on the wavelength of the laser light and the angle between the two beams. The beam angle is obtained from

$$\sin\theta = \frac{d}{\sqrt{d^2 + f^2}} \tag{8}$$

where $2d$ is the distance between the parallel beams and f is the focal length of the focusing lens. The error in equation (8) will provide the major contribution to the uncertainty in Λ. This is expressed as

$$\frac{\sigma_\Lambda}{\Lambda} = \frac{\sigma_{\sin\theta}}{\sin\theta} \tag{9}$$

where σ_Λ and $\sigma_{\sin\theta}$ are the standard deviations in Λ and $\sin\theta$, respectively. For the transmitter optics of the experimental apparatus, $2d = 60$ mm and $f = 310$ mm giving a fringe spacing of $\Lambda = 3.29\mu$m. The associated uncertainty is estimated to be ± 0.01 μm.

The acoustic frequency is required to calculate velocity amplitude and is obtained from the display of the signal generator used to drive the loudspeaker. This has a resolution of $\sigma_f = \pm 1$ Hz giving an uncertainty of $u_f = \sigma_f/\sqrt{3}$ [14].

Averaging n measurements gives an uncertainty in the mean value of velocity amplitude of $u_A = \sigma_A/\sqrt{n}$ where σ_A is the standard deviation [14]. The individual components of uncertainty are expressed as percentages of their respective values and combined as

$$U = \sqrt{\sigma_\Lambda^2 + u_f^2 + u_A^2}\,. \tag{10}$$

Equation (10) gives the total uncertainty in the mean value of velocity amplitude.

The uncertainties in the calculations of air density, speed of sound and the mean value of velocity amplitude contribute to the uncertainty in pressure amplitude derived from LDA measurements. The uncertainties in ρ and c are estimated to be 0.025% and 0.05%, respectively. These values are combined with the uncertainty given in equation (10) to give the total uncertainty in LDA derived pressure amplitude.

For each Doppler signal sampled, the probe microphone voltage signal is recorded and transformed into pressure amplitude. The uncertainty in the mean value of pressure amplitude derived from the probe microphone is calculated from the standard deviation.

As well as the measurement errors described above there are also several other considerations. The probe tube forms part of the rigid termination of the standing wave tube. As the probe diameter is very small compared to the tube diameter it is assumed that the effect on the impedance when it forms part of the termination is negligible.

There is a small mean flow velocity in the tube when the standing waves are generated. The size of the velocity is estimated by examining the positions of the side lobes either side of the central peak on the frequency spectrum. The mean flow velocity contributes to the broadening of the spectral peaks in the frequency spectrum. In our case this broadening effect is smaller than the broadening effect due to the windowing operation and size the mean flow velocity is smaller than the acoustic particle velocity amplitudes.

As a sound wave propagates through a medium it generates areas of expansion and compression. This strain field moves with the acoustic wave through the medium creating temporal and spatial variations in the refractive index of the medium. The fringe pattern may oscillate in space due to the refractive index variations in the beams. This is called the acousto-optic effect [15]. However, as the beam distances involved are very small, the acoustic frequencies are relatively low, and the measurements are conducted in air the acousto-optic effect is assumed negligible.

6. Results and discussion

Measurements were performed with $f_m = 660$ Hz. The pressure amplitude at the end of the tube was monitored using the probe microphone characterized relative to the response of the type 4192 microphone. The level of pressure amplitude was varied and sets of Doppler signals were recorded. The average ratio of the first side peak amplitude to the central side peak amplitude was calculated for each of the measurement sets. The results are displayed in figure 5. The solid line corresponds to the expected behaviour of the ratio using the values in figure 1 (with $\rho = 1.2$ kgm^{-3} and $c = 343.5$ ms^{-1}). The dashed line corresponds to the behaviour of the ratio using the small argument approximation in equation (7).

Decreasing the pressure amplitude results in a decrease of the ratio. The side peaks gradually die away until they

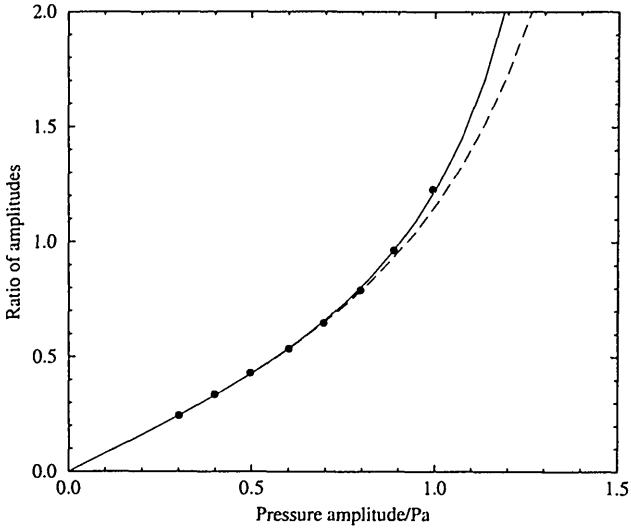

Figure 5. Variation of the ratio of amplitudes with pressure amplitude for an acoustic field with frequency, $f_m = 660$ Hz.

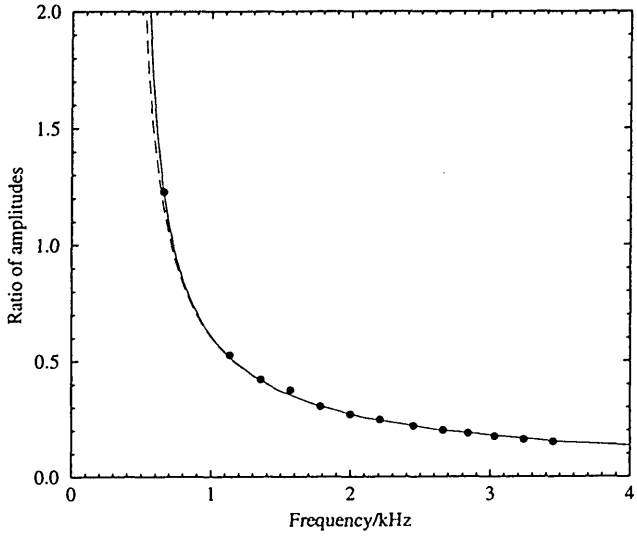

Figure 6. Variation of the ratio of amplitudes with frequency for a pressure amplitude $\simeq 1$ Pa measured at the end of the tube.

are indistinguishable from the noise level present in the frequency spectrum leaving only the central peak. At this point the particle displacement amplitude is small compared to the fringe spacing and the central peak results from the fringes moving across the near stationary particles. The lowest measurable velocity amplitude is determined by the smallest side peak amplitude that can be determined above the noise level. For the results shown in figure 5, the lower limit was approximately 1 mms^{-1}. The measured values agree with the expected ratio. For a pressure amplitude greater than 0.8 Pa ($\alpha > 1.3$), the small argument approximation no longer holds resulting in an underestimation of the ratio compared with the measured values.

A constant level of pressure amplitude was maintained at the end of the tube while measurements were performed for acoustic frequencies in the range 660 Hz to 4 kHz. The average ratio of amplitudes was calculated for each set of Doppler signals recorded and the results displayed in figure 6. The solid line corresponds to the expected behaviour of the ratio using the values in figure 1 (with $\rho = 1.2$ kgm^{-3} and $c = 343.5$ ms^{-1}). The dashed line corresponds to the behaviour of the ratio using the small argument approximation in equation (7).

The ratio decreases with increasing acoustic frequency. The side peaks gradually die away until they are indistinguishable from the noise level and leaving only the central peak in the frequency spectrum. For a constant level of pressure amplitude, as the frequency increases the particle displacement decreases. The displacement will eventually be small compared to the fringe spacing. The scattered light results from the moving fringes, producing only the central peak in the spectrum. The measured values are consistent with the expected behaviour. The small argument approximation is valid for $\alpha < 1.3$ which corresponds to $f_m > 800$ Hz. For frequencies below this value, the ratio is underestimated by equation (7).

Figure 7 shows the measurements of particle velocity amplitude from a set of 20 Doppler signals recorded with $f_m = 660$ Hz. The mean value of the RMS pressure amplitude derived from the probe microphone was found to be 0.995 ± 0.001 Pa for the period over which the Doppler signals were recorded. A single LDA measurement may differ from the probe microphone measurement by as much as 0.4 dB. The mean value of particle velocity amplitude, calculated from 20 Doppler signals, is $\bar{u}_m = 3.436 \pm 0.012$ mms^{-1} giving a RMS pressure amplitude of 0.992 ± 0.005 Pa at the end of the tube. The discrepancy between the LDA measurement and the probe microphone measurement is -0.03 ± 0.04 dB. The LDA and probe microphone derived pressure amplitudes agree to within the calculated uncertainties when 20 measurements are averaged.

The discrepancy between the pressure amplitude derived from LDA measurements and the pressure amplitude derived from probe microphone measurements was determined for $f_m = 660$ Hz and velocity amplitudes in the range 1 mms^{-1} to 3.5 mms^{-1}. The results are displayed in figure 8 and show that the LDA and probe microphone measurements agree to within the calculated uncertainties. For a pressure amplitude of 0.5 Pa and greater, the discrepancy is within ± 0.1 dB. For pressure amplitudes between 0.3 and 0.5 Pa, the discrepancy is within ± 0.15 dB. Below 0.3 Pa the side peaks become indistinguishable from the noise level present in the spectrum and no value for particle velocity amplitude can be evaluated. The uncertainty in the discrepancy is evaluated from the uncertainties in the LDA and probe microphone measurements of pressure amplitude. The size of this uncertainty increases with decreasing pressure amplitude. The uncertainty in the particle velocity amplitude is typically ± 0.02 mms^{-1}. As the velocity amplitude decreases the percentage contribution to the uncertainties in the pressure amplitude and the discrepancy value increases.

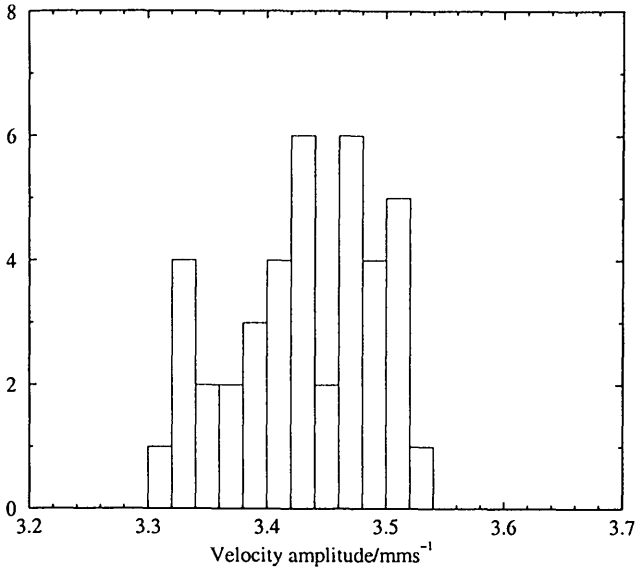

Figure 7. Distribution of particle velocities for a set of measurements subjected to an acoustic field with frequency, $f_m = 660$ Hz.

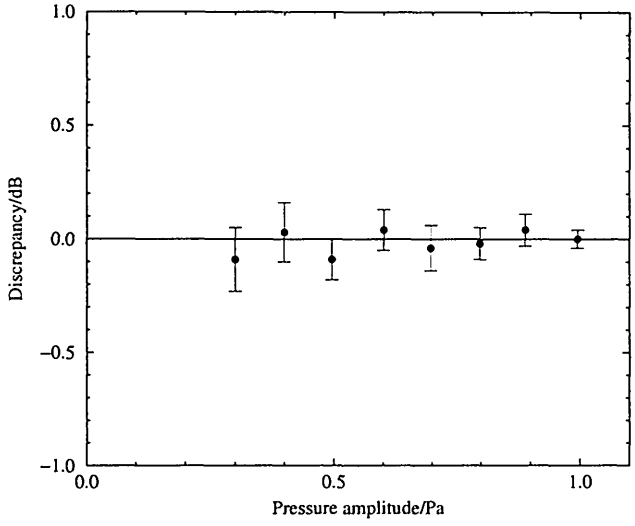

Figure 8. Discrepancy between pressure amplitude derived from LDA measurements and pressure amplitude derived from probe microphone measurements for $f_m = 660$ Hz.

A constant level of pressure amplitude was maintained at the end of the tube. The discrepancy between LDA measurements of pressure amplitude and probe microphone measurements of pressure amplitude was determined for various acoustic frequencies. The results are shown in figure 9. The RMS pressure amplitude at the end of the tube was measured with the probe microphone to be approximately 1.0 Pa. The LDA and probe microphone measurements agree to within the calculated uncertainties. For f_m in the range 660 Hz to 4 kHz, the discrepancy is within ± 0.1 dB. The size of the uncertainty in the discrepancy increases with acoustic frequency. The particle velocity amplitude decreases with increasing frequency and constant pressure amplitude. The size of the uncertainty in

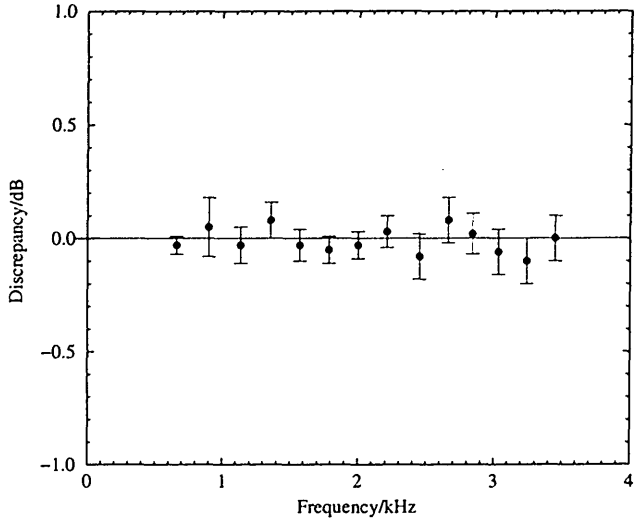

Figure 9. Discrepancy between pressure amplitude derived from LDA measurements and pressure amplitude derived from probe microphone measurements against f_m.

the velocity amplitude results in an increased percentage contribution to the uncertainty in pressure amplitude and the discrepancy value.

The probe microphone was characterized relative to the NPL microphone system. This allowed the sensitivity of the NPL system to be derived from LDA measurements of the pressure amplitude at the end of the tube and the probe microphone voltage. The results for several acoustic frequencies are shown in figure 10. The particle velocity amplitudes were between 3.4 mms^{-1} and 4.0 mms^{-1}. The horizontal line corresponds to the calibrated sensitivity level, obtained by reciprocity, of -38.00 ± 0.03 dB re. 1 VPa^{-1}. The measured sensitivities agree with the calibrated value to within $\pm$ 0.1 dB for acoustic frequencies in the range 660 Hz to 2 kHz.

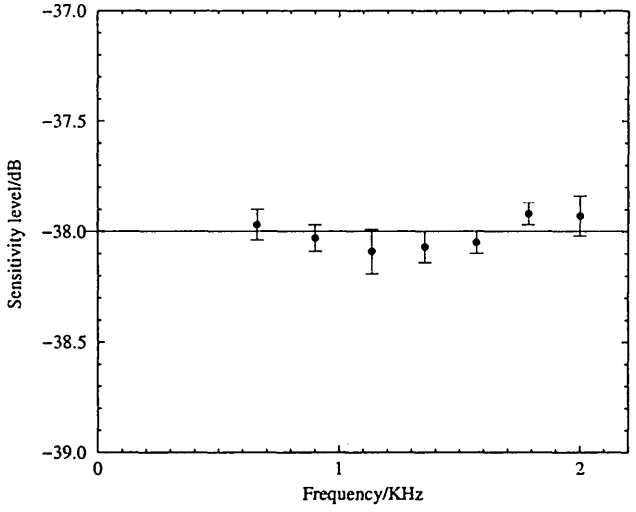

Figure 10. Sensitivity level derived from LDA velocity measurements and probe microphone voltage measurements.

7. Conclusions

Acoustic particle velocity amplitude is obtained from a ratio quantity that relates acoustic displacements to the wavelength of laser light. Laser Doppler anemometry has been used to measure acoustic particle velocity amplitude and acoustic pressure amplitude in a standing wave. The peaks in the frequency spectra generated from the captured Doppler signals follow the behaviour defined by the equations relating particle velocity amplitude and Bessel functions. The pressure amplitude derived from LDA measurements and the pressure amplitude derived from probe microphone measurements agree to within ± 0.1 dB for acoustic frequencies in the range 660 Hz to 4 kHz and particle velocity amplitudes in the range 1 mms^{-1} to 3.5 mms^{-1}. The sensitivity of a microphone system was measured to within ± 0.1 dB of the calibrated level.

These results have been obtained following the first phase of development of the system. Further work will be conducted to improve the agreement with traditional calibration methods. In the future it is planned that similar measurements be performed in a free-field room, enabling an absolute free-field calibration of a microphone to be performed.

Acknowledgement

This work has been supported by the National Physical Laboratory.

References

[1] International Electrotechnical Commission. *IEC* 61094-2: 1992, Measurement microphones - Part2 : Primary method for the pressure calibration of laboratory standard microphones by the reciprocity method.

[2] K. J. Taylor: Absolute calibration of microphones by a laser-Doppler technique. Journal of the Acoustical Society of America **70** (1981) 939–945.

[3] F. Durst, A. Melling, J. H. Whitelaw: Principles and practice of laser-doppler anemometry. Academic Press, 1976.

[4] R. J. Goldstein: Fluid mechanics measurements. Hemisphere Publishing Corporation, London, 1983.

[5] K. J. Taylor: Absolute measurement of acoustic particle velocity. Journal of the Acoustical Society of America **59** (1976) 691–694.

[6] F. Bowman: Introduction to Bessel functions. Longmans, Green and co. ltd., 1938.

[7] G. N. Watson: A treatise on the theory of bessel functions. Cambridge University Press, 1952.

[8] P. Giacomo: Equation for the determination of the density of moist air. Metrologia **18** (1982) 33–40.

[9] R. S. Davis: Equation for the determination of the density of moist air. Metrologia **29** (1992) 67–70.

[10] O. Cramer: The variation of the specific heat ratio and the speed of sound in air with temperature, pressure, humidity and CO_2 concentration. Journal of the Acoustical Society of America **93** (1993) 2510–2516.

[11] Y. S. Cheng, W. E. Bechtold, C. C. Yu, I. F. Hung: Incense smoke: Characterization and dynamics in indoor environments. Aerosol Science and Technology **23** (1995) 271–281.

[12] J. S. Cullen, C. A. Greated, D. M. Campbell: LDA measurement of sound: amplitude modulation of laser Doppler signals. Measurement Science and Technology **10** (1999) 812–823.

[13] D. Matovic, C. Tropea: Spectral peak interpolation with application to LDA signal processing. Measurement Science and Technology **2** (1991) 1100–1106.

[14] B. N. Taylor, C. E. Kuyatt: Guidelines for evaluating and expressing the uncertainty of NIST measurement results. NIST technical note 1297 (1994) 1–20.

[15] S. H. Jack, D. B. Hann, C. A. Greated: Influence of the acousto-optic effect on laser Doppler anemometry signals. Review of Scientific Instruments **69** (1998) 4074–4081.

The development of a microphone calibration technique using photon correlation spectroscopy.

T MacGillivray*
Wellcome Trust Clinical Research Facility (Edinburgh), The University of Edinburgh, Western General Hospital, Edinburgh EH4 2XU, UK

D Campbell, C Greated
Fluid Dynamics and Acoustics Group, Department of Physics and Astronomy, The University of Edinburgh, James Clerk Maxwell Building, Kings Buildings, Edinburgh EH9 3JZ, UK

R Barham
Acoustics Standards, Centre for Mechanical and Acoustical Metrology, National Physical Laboratory, Queens Road, Teddington, Middlesex TW11 0LW, UK

Summary
Laser Doppler Anemometry (LDA) measurements of acoustic particle velocity, utilizing the photon correlation method of signal processing, provide the basis for a working microphone calibration system. The calibration is performed using a standing wave generated inside a glass tube attached to a loudspeaker. From the photon correlation LDA velocity measurement and a knowledge of the characteristic acoustic impedance of the air inside the tube, the pressure amplitude at the end is calculated. The frequency response of a probe microphone fitted in the end of the tube is characterized separately, relative to a measurement microphone system supplied by the National Physical Laboratory (NPL). The LDA apparatus has been used to calibrate the measurement microphone system. For frequencies between 600 Hz and 2 kHz, the sensitivity of the microphone is determined to within ±0.2 dB of the sensitivity obtained by reciprocity calibration. While this is not state-of-the-art in terms of microphone calibration, it marks the first stage of an on-going project to establish the next generation of primary standards for sound pressure. Further work will be conducted with the emphasis on free-field measurements.

PACS no. 43.58.Vb, 43.60.Qv, 43.38.Kb

1. Introduction

Reciprocity calibration of microphones was adopted by the International Electrotechnical Commission (IEC) in the 1960s as the preferred method of realizing the primary standard for sound pressure and this arrangement persists today [1]. The calibration of a microphone requires the measurement of sensitivity. The reciprocity method is indirect in that no evaluation of the acting sound pressure is required. It yields in a primary standard that is dependent upon the response of transducers. Some therefore have cause to argue that this cannot be regarded as a primary standard. In contrast, optical methods provide a direct approach where the sound pressure is determined from the measurement of acoustic particle velocity. Taylor developed a LDA calibration system based on a travelling wave tube [2]. Improvements to Taylor's apparatus have previously been described by the authors [3]. The method involves analysis of the continuous Doppler signal in the frequency domain to determine acoustic particle velocity, and hence sound pressure.

Photon correlation spectroscopy is an alternative method of processing the signal from the photodetector in the LDA system. It has been used successfully to measure the absolute acoustic particle velocity in sound fields [4, 5]. With recent advances in digital correlation technologies, there is potential to apply the photon correlation technique to the measurement of microphone sensitivity and develop a calibration method.

Received 13 February 2002,
accepted .

* Electronic mail: T.J.MacGillivray@ed.ac.uk

2. Photon correlation for sound measurement

In the dual beam LDA mode, interference fringes are formed at the intersection of two laser beams. Light scattered onto the surface of a photomultiplier tube by particles transversing the ellipsoidal fringe volume is frequency shifted by an amount proportional to the velocity of motion. The detector current is proportional to the light intensity integrated over the detector surface [6]. If the scattered light intensity is low enough, the photomultiplier signal can be interpreted as a series of discrete pulses, each pulse corresponding to the emission of a single electron from the cathode material.

The correlation between the photomultiplier signal, $V(t)$, and a delayed version of the signal, $V(t-\tau)$, gives the autocorrelation function (ACF). In the ACF, the positions of the peaks and the turning points are determined by the mean flow velocity and the acoustic particle velocity [7]. By deducing the form of the signal for a particle as a function of position within the fringe volume, the shape of ACF can be established and the acoustic velocity may be calculated.

ACUSTICA · acta acustica
Vol. (2002)

The total detector output signal is the sum of contributions arising from individual particles in the fringe volume and is given by [6]

$$V(t) \simeq \kappa \sum_p \mathcal{K}_p W(\beta\xi_p(t))\Big(1 + \cos D\xi_p(t)\Big) \quad (1)$$

where

$$D = \frac{4\pi \sin\theta}{\lambda} \quad (2)$$

and the summation extends over all the particles in the flow. κ is a constant that depends on the optical geometry and the sensitivity and load resistance of the detector, $\mathcal{K}_p$ characterises the particle scattering cross section, $\xi_p(t)$ is the pth particle displacement at time t, λ is the wavelength of the laser light, and 2θ is the acute angle between the two illuminating beams. $W(\beta\xi_p(t))$ is the spatial weighting function, i.e. the weighting function defined in terms of particle position rather than time variables, and represents the envelope on the fringes due to the Gaussian cross section of the laser beams. It is expressed as

$$W(\beta\xi_p(t)) = we^{(-8\xi_p^2(t)\beta^2)} \quad (3)$$

where

$$w = I_0 \exp\left(-\frac{8(z^2 + y^2\sin^2\theta)}{d_{e^{-2}}^2}\right) \quad (4)$$

and

$$\beta = \frac{\cos\theta}{d_{e^{-2}}} . \quad (5)$$

The focused laser beam waist diameter, $d_{e^{-2}}$, is measured between points where the intensity is $1/e^2$ of the peak intensity at the centre.

To determine the ACF for the signal $V(t)$, the initial position of the pth particle (i.e. at $t = 0$) is defined as ξ_p and the position at a time τ later along the flow axis is

$$\zeta_p = \xi_p + \int_0^\tau U_p(t)dt = \xi_p + \eta_p(\tau) . \quad (6)$$

The x axis is at right angles to the fringes, the y axis is parallel to the fringes, and the z axis is perpendicular to both of the other two axes. Consider particle motion involving a mean flow in the x direction superimposed onto an acoustic oscillation, also in the x direction. The instantaneous velocity of the particle is

$$U_p(t) = u_0 + u_m \sin(2\pi f_m t + \phi_m) \quad (7)$$

where u_0 is the mean flow velocity, u_m is the acoustic particle velocity amplitude, f_m is the acoustic frequency, and ϕ is a random phase.

Following the derivation of Durrani and Greated in [6], it is assumed that ζ and ξ are independent random variables as the position of a particle depends only on the initial position and the instantaneous velocity. The ACF of the photomultiplier voltage signal is given by

$$\begin{aligned} R(\tau) &= E[V(t)V(t+\tau)] \\ &= \left(\kappa C_0 g_0 \int_{-\infty}^{\infty} W(\beta x)(1 + \cos Dx)dx\right)^2 \\ &\quad + \frac{\kappa^2 C_1 g_0}{2} \\ &\quad \times \int_{-\infty}^{\infty} p_\eta(x;\tau) R_W(\beta x)(1 + \cos Dx)dx \end{aligned} \quad (8)$$

where

$$R_W(\beta x) = \frac{\sqrt{\pi}}{4\beta} \exp(-4\beta^2 x^2) \quad (9)$$

is the autocorrelation of the spatial weighting function. $E[\ ]$ is the expectation operator, $C_0 = E[K_p]$, $C_1 = E[K_p^2]$, g_0 is the average number of particles per unit length of the measuring volume, and $p_\eta(x;\tau)$ is the probability density of the variable $\eta(t)$.

The first term in equation (8) is the square of the mean value of the Doppler signal. It can be ignored as it is time-independent if the scattering particle concentration is constant. It contains no velocity information and only contributes a constant or pedestal value to the ACF [8].

The derivation of the autocorrelation function requires the probability density function $p_\eta(x;\tau)$ of the variable $\eta_p(\tau)$ to be determined. From equations (6) and (7)

$$\begin{aligned} \eta_p(\tau) &= u_0\tau + u_m \int_0^\tau \sin(2\pi f_m t + \phi_m)dt \\ &= u_0\tau + \frac{u_m}{\pi f_m} \\ &\quad \times \Big[\sin(\pi f_m \tau)\sin(\pi f_m \tau + \phi_m)\Big] . \end{aligned} \quad (10)$$

Using the relationship for a function of random variables in [9], gives

$$\begin{aligned} p_\eta(x;\tau) &= \frac{1}{\pi\sqrt{u_m'^2 - (x - u_0\tau)^2}} \\ &\quad -x + u_0\tau \le u_m' \le x - u_0\tau \end{aligned} \quad (11)$$

where

$$u_m' = \frac{u_m}{\pi f_m}\Big[\sin(\pi f_m \tau)\Big] . \quad (12)$$

The time-independent pedestal term is ignored and equation (8) becomes

$$\begin{aligned} R(\tau) &= \frac{\kappa^2 C_1 g_0}{2}\frac{\sqrt{\pi}}{4\beta} \\ &\quad \times \int_{u_0\tau - u_m'}^{u_0\tau + u_m'} \exp(-4\beta^2 x^2)(1 + \cos Dx) \\ &\quad \times \frac{dx}{\pi\sqrt{u_m'^2 - (x - u_0\tau)^2}} . \end{aligned} \quad (13)$$

Following the derivation of Hann and Greated in [10] and simplifying using a typical magnitude for β and noting the behaviour of $e^{-q}I_n(q)$ for small q [11], the normalised ACF is

$$R(\tau) \simeq \frac{1}{2}\exp(-4\beta^2 u_0^2\tau^2) \left\{1 + \cos(Du_0\tau)J_0\left(Du'_m\right)\right\}. \quad (14)$$

For a mean flow superimposed onto an acoustic oscillation, the ACF decays to zero which reflects the eventual transition of the particles across the probe volume. In equation (14), interaction of the $J_0(\,)$ term with sinusoidal argument and the cosine term produces beats in the ACF. From a knowledge of the zeros and peaks of the zero order Bessel function, the acoustic particle velocity and the superimposed mean flow velocity may be determined.

3. Experimental apparatus

The photon correlation LDA system is illustrated in figure 1. The beam from a 20 mW He-Ne laser ($\lambda = 633$ nm) is split into two parallel beams which are focused by a 100 mm focal length lens to form a fringe volume at an acute angle of $2\theta = 11.42°$. The resulting fringe separation is $\Lambda = 2\pi/D = 3.18\mu$m. A Brookhaven BI-DS1 photomultiplier and optics, mounted at an angle of 15° to the horizontal beam plane, detects the scattered light. A BI-9000AT Digital Correlator PCI board correlated the photomultiplier signal with itself to produced the ACF.

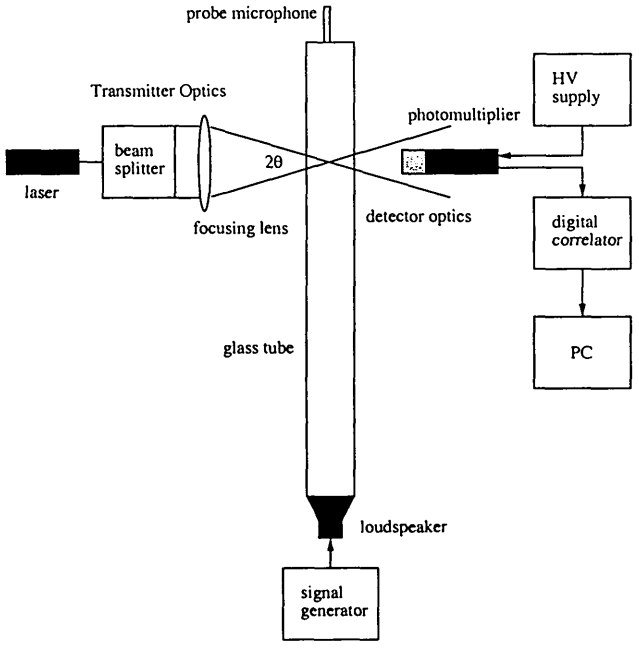

Figure 1. Diagram of the LDA apparatus and standing wave tube.

An acoustic field was produced inside a glass tube sealed to a loudspeaker. The tube, of internal diameter 32.80 mm and length 748 mm, was rigidly terminated with a piece of perspex. This contained a small hole into which the probe microphone was fitted. The combined tube-loudspeaker system was driven at its natural resonant frequencies to generate standing waves. All LDA measurements were carried out at the position of the first or second velocity antinode from the rigid end.

The probe microphone was used to monitor the pressure amplitude at the termination and consisted of a probe attachment for a half-inch microphone cartridge. The probe tube has a length of 230 mm and a diameter of 3.9 mm and was fixed to a Brüel and Kjær type 4133 microphone. However, the probe tube distorts the frequency response of the microphone. The effects of the probe tube were characterized relative to the response of a reference microphone allowing probe microphone voltage amplitude to be transformed into pressure amplitude measured in Pascals. The reference microphone was a Brüel and Kjær type 4192. The probe was also characterized relative to the half inch microphone system supplied by NPL.

In order to compare LDA velocity measurements with the probe microphone pressure measurements, the characteristic impedance of air, ρc, is required. The density of air and the speed of sound in air are calculated independently as functions of the atmospheric pressure, air temperature, and relative humidity [12, 13, 14]. The atmospheric pressure and the relative humidity were measured using an electronic barometer while the air temperature inside the tube was measured by removing the probe microphone and inserting a probe thermometer.

The air inside the tube was seeded with incense smoke by removing the probe and inserting a burning incense stick for a period of approximately 2 seconds. Incense smoke particles have typical diameters of 0.5 μm [15], which is less than the fringe spacing, and will follow the oscillations of the air sufficiently for acoustic frequencies of less than 10 kHz [16]. The amount of seeding required is considerably less than the amount required for the frequency analysis method described in [3].

4. Signal analysis

To calculate the ACF of the photomultiplier signal, the digital correlator counts the number of pulses occurring in consecutive time intervals or channels. The time interval is denoted by $\Delta\tau$ and the number of channels in the correlator by n. The measured ACF, computed by the digital correlator, is a discrete function of $n\Delta\tau$ instead of a continuous function of the delay time, τ.

With $u_0 = 0$, the theoretical ACF will repeat for $\pi f_m\tau = \pi$ as $J_0(\,)$ is an even function. The first minimum of the zero order Bessel function occurs at 3.832 [17]. Using equation (14) this gives

$$u_m = \frac{3.832\Lambda f_m}{2\sin(\pi f_m\tau_m)} \quad (15)$$

where τ_m is the delay time to the first minimum of the ACF. To see the first minimum, τ_m must occur before the

ACUSTICA · acta acustica
Vol. (2002)

first half period of the sinusoidal argument of the Bessel function. From equation (15)

$$\frac{u_m}{f_m} > \frac{3.832\Lambda}{2} . \tag{16}$$

The limit to the acoustic particle velocity amplitude that can be measured is proportional to the fringe spacing, Λ. The fringe spacing may be decreased by increasing the beam intersection angle or decreasing the wavelength of the laser light.

Figure 2 illustrates the autocorrelation functions of the photomultiplier signal generated by a standing wave with acoustic frequency $f_m = 660$ Hz and RMS pressure amplitude at the end of the tube in the range of 1.0 Pa to 10 Pa. A sample time of $\Delta\tau = 5\mu$s with $n = 200$ channels was used. As the pressure amplitude at the rigid end increases, the delay time to the first minimum of the ACF decreases. From equation (15), this indicates an increase in the acoustic particle velocity amplitude with an increase in the pressure amplitude. The ACF decays with $n\Delta\tau$ which may indicate the presence of a small mean flow velocity as well as a slight mismatch in beam intensities or a small misalignment of the optics.

Figure 3 illustrates the autocorrelation functions of the photomultiplier signal generated by a standing wave with a constant level of pressure amplitude at the end of the tube and with acoustic frequencies between 660 Hz and 2 kHz. The delay time to the first minimum of each ACF is the same, indicating that the particle velocity amplitude remains constant. $R(n\Delta\tau)$ decays with $n\Delta\tau$ which may be due to the presence of a small mean flow velocity as well as the other possible sources of damping.

An example of a measured ACF obtained using the apparatus is shown in figure 4. Also shown are ACFs calculated using equation (14) with $|u_0| = 0$ mms^{-1}, 0.5 mms^{-1}, and 1.0 mms^{-1}. It can be seen that the measured ACF follows the form predicted by the equation, i.e. the interaction of the cosine term with the zero order Bessel function. However, the shape of the measured ACF cannot be completely accounted for by equation (14) as the theoretical expression never completely fits all the points.

Acoustic particle velocity amplitude and mean flow velocity amplitude are obtained by fitting the expression in equation (14) to the measured ACF using a least squares fit routine which finds the values of u_m and u_0 that minimise the sum of the squared relative error. The squared relative error is defined as the difference between the square of the RHS of equation (14) and the square of the measured ACF, all divided by the square of the measured ACF.

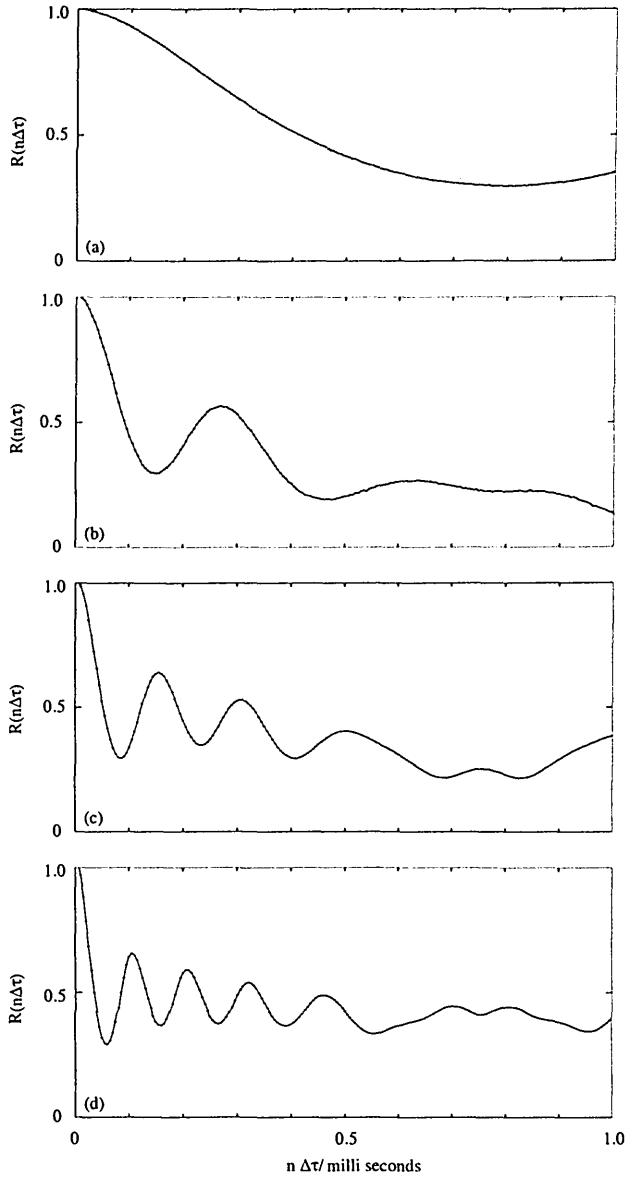

Figure 2. Measured ACF for the photomultiplier signal generated by a standing wave with $f_m = 660$ Hz and (a) with a RMS pressure amplitude measured at rigid end of 1.0 Pa, (b) 4.0 Pa, (c) 7.0 Pa, and (d) 10.0 Pa.

5. Uncertainty analysis

The uncertainty in the measurement of the acoustic particle velocity amplitude is evaluated by considering the individual components of the calculation in equation (15).

The fringe spacing depends on the wavelength of the laser light and the acute angle between the two illuminating beams. Provided the initial beams are parallel, the beam angle is obtained from

$$\sin\theta = \frac{d}{\sqrt{d^2 + f^2}} \tag{17}$$

where $2d$ is the distance between the parallel beams and f is the focal length of the focusing lens. The error in equation (17) provides the major contribution to the uncertainty in the fringe spacing, Λ. If σ_Λ and $\sigma_{\sin\theta}$ denote the standard deviations in Λ and $\sin\theta$ respectively, this may be expressed as [18]

$$\frac{\sigma_\Lambda}{\Lambda} = \frac{\sigma_{\sin\theta}}{\sin\theta} . \tag{18}$$

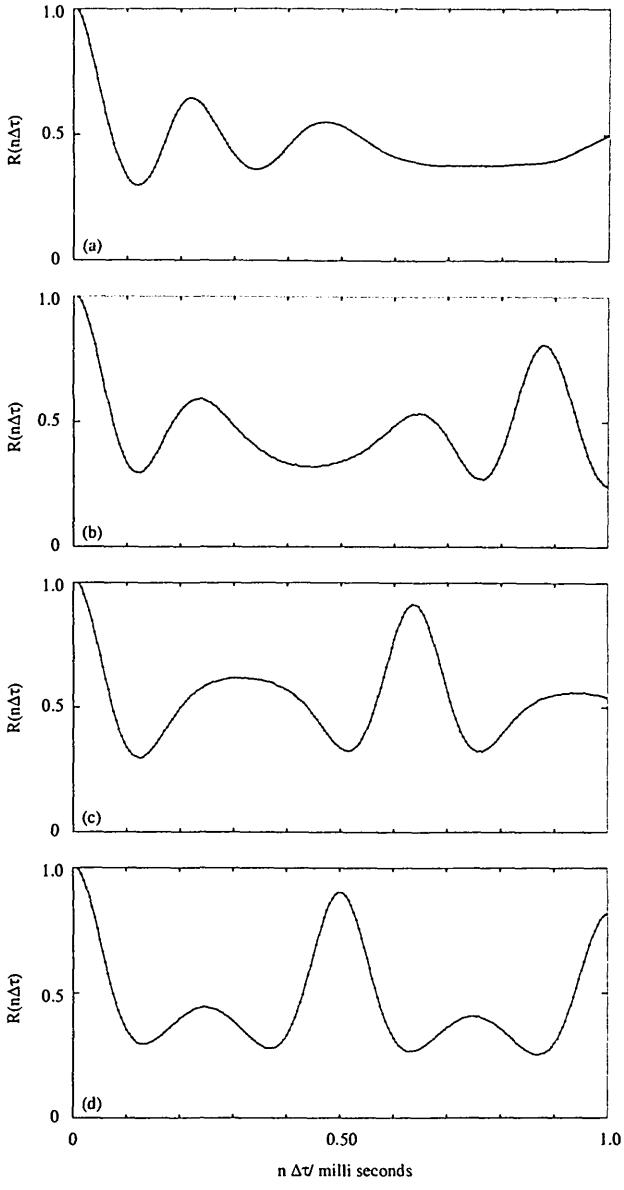

Figure 3. Measured ACF for the photomultiplier signal generated by a standing wave with a RMS pressure amplitude measured at rigid end of 5.0 Pa and (a) with frequency f_m = 660 Hz, (b) 1135 Hz, (c) 1570 Hz, and (d) 2000 Hz.

For the transmitter optics of the LDA apparatus shown in figure 1, $2d$ = 20 mm and f = 100 mm giving a fringe spacing and associated uncertainty of $\Lambda = 3.18 \pm 0.02\,\mu$m.

The acoustic frequency is obtained from the sinusoidal voltage signal used to do drive the loudspeaker to the nearest ± 1 Hz, which gives an uncertainty of $u_f = 1/\sqrt{3}$ Hz [19]. The optimum value of u_m is found with an accuracy of $\sigma_u = 0.01$ mms^{-1}.

Provided the individual components of uncertainty are statistically independent, they may be expressed as percentages of their respective values and combined as

$$U = \sqrt{\sigma_\Lambda^2 + u_f^2 + \sigma_u^2}\,. \qquad (19)$$

to give the total uncertainty in the particle velocity amplitude.

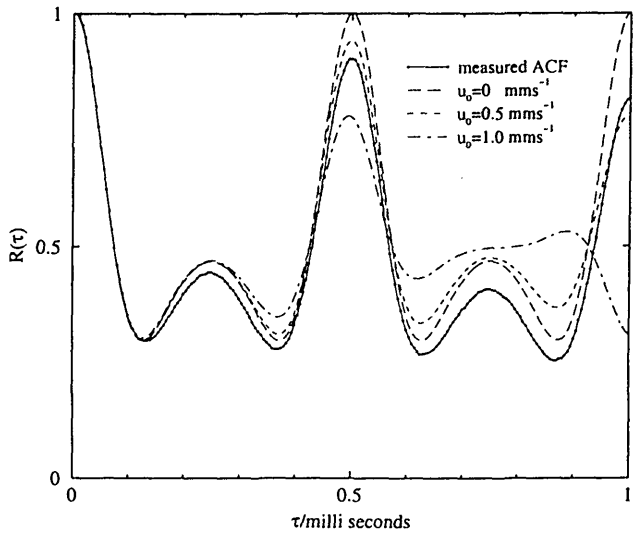

Figure 4. Measured ACF for the photomultiplier signal generated by an acoustic field with frequency, f_m = 2 kHz. Also shown is the theoretical form of the ACF with $|u_0|$ = 0 mms^{-1}, 0.5 mms^{-1}, and 1.0 mms^{-1}.

Contributions to the total uncertainty in the pressure amplitude derived from photon correlation LDA measurements arise from the uncertainties in the calculations of air density, speed of sound, and particle velocity amplitude. The uncertainties in ρ and c are estimated to be 0.025% and 0.05%, respectively. These values are combined with the uncertainty in equation (19) to give the total uncertainty in LDA derived pressure amplitude.

There are other considerations in addition to the measurement errors described above. These include the termination of the glass tube, the acousto-optic effect, laser beam intensity mismatches, and optical misalignments.

The probe tube forms part of the rigid termination of the standing wave tube. As the probe diameter is very small compared to the tube diameter it is assumed that the effect on the impedance when it forms part of the termination is negligible.

As a sound wave propagates through a medium it generates areas of expansion and compression. This strain field moves with the acoustic wave through the medium creating temporal and spatial variations in the refractive index of the medium. The fringe pattern may oscillate in space due to the refractive index variations in the beams. This is called the acousto-optic effect [20]. However, the acousto-optic effect can safely be ignored as the beam distances involved are very small, the acoustic frequencies are relatively low, and the measurements are conducted in air.

In deriving the theoretical form of the ACF of the photomultiplier signal it was assumed that the two illuminating beam intensities are equal and that the optical systems are properly aligned. However, any mismatch in the beam intensities and small misalignments of the transmitter and detector optics will contribute to the shape of the measured ACF. These factors introduce uncertainties which are not accounted for in the calculation of the total uncertainty in

velocity amplitude, and hence LDA derived pressure amplitude.

6. Results and discussion

The measurements displayed in figure 5 were performed for an acoustic field with frequency, $f_m = 660$ Hz. The RMS pressure amplitude, measured at the rigid end of the tube, was varied between 4.0 Pa and 5.0 Pa. The sample time was set at $\Delta\tau = 2\mu$s giving $n = 80$ channels in the digital correlator. The gradient of the best fit straight line to the measured points corresponds to a characteristic impedance of 412 Pasm^{-1} while the characteristic impedance calculated from the environmental conditions was found to be 409 Pasm^{-1}. The uncertainty in the pressure amplitude derived from the probe microphone is ± 0.03 Pa

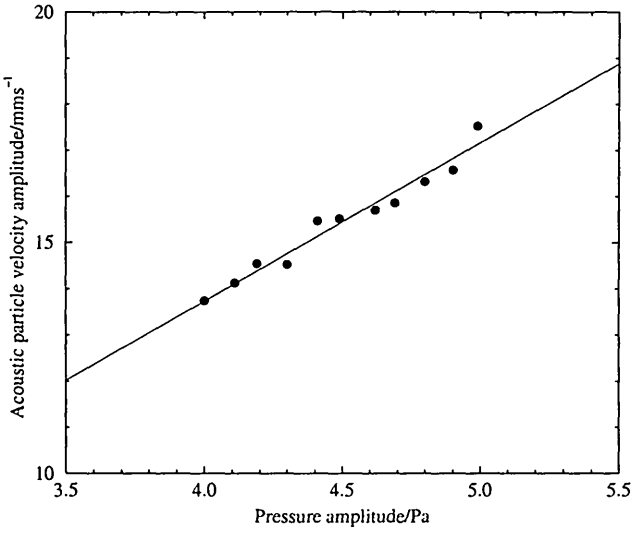

Figure 5. Photon correlation measurements of acoustic particle velocity amplitude for acoustic field with frequency, $f_m = 660$ Hz.

The measurements displayed in figure 6 were performed with $f_m = 2$ kHz and with a RMS pressure amplitude varied between 4.0 Pa and 5.5 Pa. The sample time was set at $\Delta\tau = 2\mu$s giving $n = 80$ channels in the digital correlator. The gradient of the best fit straight line to the measured points corresponds to a characteristic impedance of 407 Pasm^{-1} while the characteristic impedance calculated from the environmental conditions was found to be 409 Pasm^{-1}. The uncertainty in the pressure amplitude derived from the probe microphone is again ± 0.03 Pa.

Figure 7 shows the discrepancy between the pressure amplitude derived from the photon correlation LDA measurements in figure 5 and the pressure amplitude derived from the probe microphone. The measured particle velocity amplitudes were in the range of 13.7 mms^{-1} to 17.6 mms^{-1}. It can be seen from the graph that the discrepancies are within ± 0.2 dB for RMS pressure amplitudes

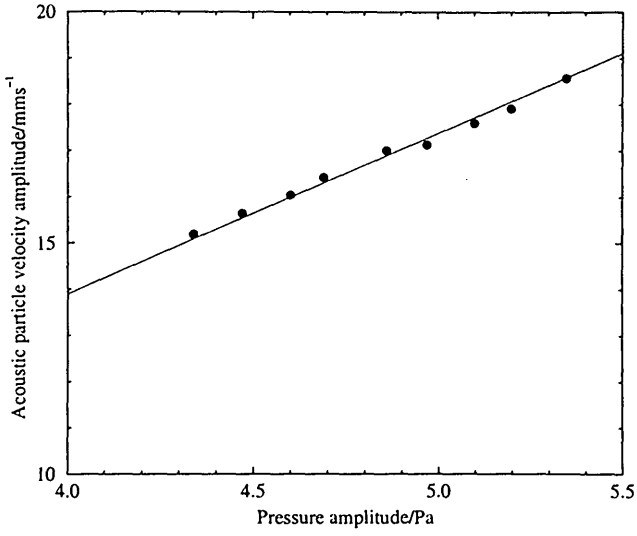

Figure 6. Photon correlation measurements of acoustic particle velocity amplitude for acoustic field with frequency, $f_m = 2$ kHz.

in the range of 4.0 Pa to 5.0 Pa. Below 4.0 Pa, the delay time to the minimum of the measured ACF approaches the maximum delay time, $n\Delta\tau$, and the least squares fitting procedure cannot be used. The uncertainty in the discrepancy is less than 0.1 dB for the range of pressure amplitudes considered. The size of the uncertainty in the discrepancy increases with decreasing pressure amplitude. This is because the uncertainty in the velocity amplitude obtained by the least squares fitting procedure is ± 0.01 mms^{-1}. As particle velocity decreases this results in a larger percentage contribution to the total uncertainty in pressure amplitude.

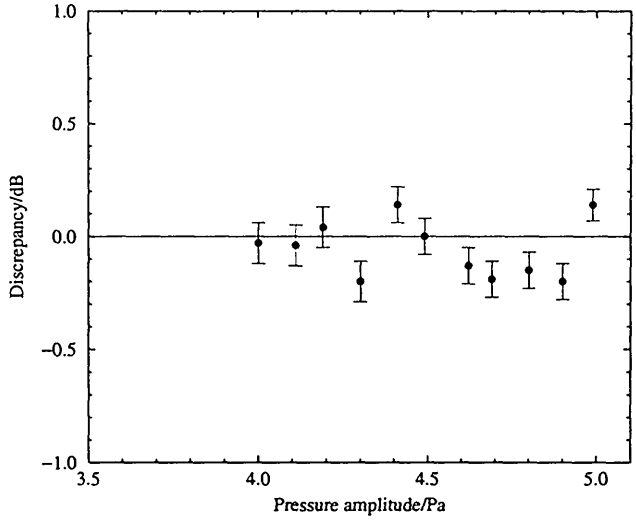

Figure 7. Discrepancy between pressure amplitude derived from LDA photon correlation measurement and probe microphone measurement for acoustic field with $f_m = 660$ Hz.

The discrepancy between the pressure amplitude derived from LDA measurements in figure 6 and the pres-

sure amplitude derived from the probe microphone measurements is displayed in figure 8. The measured particle velocity amplitudes were in the range of 14.7 mms^{-1} to 18.6 mms^{-1}. It can be seen from the graph that the discrepancies are within ±0.11 dB for RMS pressure amplitudes in the range of 4.3 Pa to 5.4 Pa. The discrepancy between LDA and probe microphone measurements improves with increasing acoustic frequency. This is because at higher acoustic frequencies the interaction of the cosine term with the zero order Bessel function in equation (14) is more pronounced. A more accurate measurement of u_m is obtained compared to lower acoustic frequencies where the first minimum of the Bessel function is masked by the cosine term.

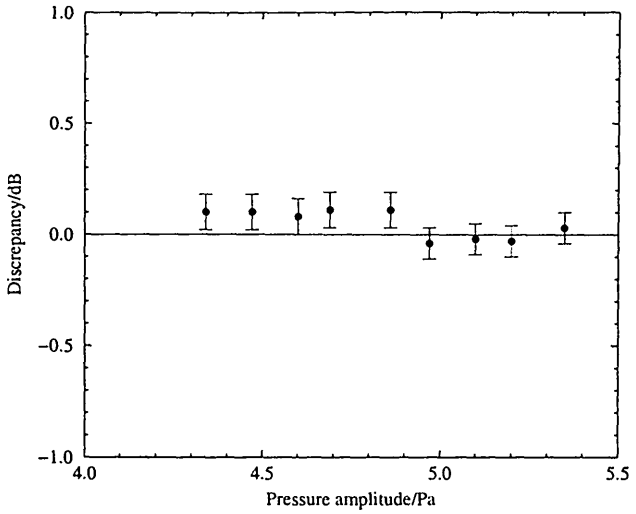

Figure 8. Discrepancy between pressure amplitude derived from LDA photon correlation measurement and probe microphone measurement for acoustic field with $f_m = 2$ kHz.

The uncertainty in the calculated discrepancy when $f_m = 2$ kHz is approximately ±0.08 dB for a RMS pressure amplitude greater than 4.4 Pa. This uncertainty increases with decreasing pressure amplitude because the uncertainty in the measured velocity amplitude remains at ±0.01 mms^{-1}, resulting in a larger percentage contribution to the total uncertainty as the particle velocity decreases. Below a RMS pressure amplitude of 4.4. Pa and with $f_m = 2$ kHz, the delay time to the minimum of the measured ACF approaches the maximum delay time and no value of velocity amplitude can be obtained.

Characterizing the probe microphone relative to the NPL microphone system allowed the sensitivity of the system to be derived from LDA measurements of the pressure amplitude at the end of the tube and the probe microphone voltage. The results for several acoustic frequencies in the range of 660 Hz to 2 kHz are displayed in figure 9. The horizontal line corresponds to the calibrated level, obtained by reciprocity, of −38.00 ± 0.03 dB. The acoustic particle velocity amplitudes were measured to be between 17.5 mms^{-1} and 19.0 mms^{-1}. It can be seen that the measured sensitivities agree with the calibrated value to within ± 0.2 dB for the frequency range considered. The uncertainty in the LDA derived sensitivity was evaluated to be ±0.08 dB. For the results conducted at $f_m = 660$ Hz, 1355 Hz, 1785 Hz, and 2000 Hz the measured sensitivity levels lie above the horizontal line and out with the calculated uncertainties. This indicates that the technique is slightly underestimating the particle velocity amplitude. However, the measurements are still consistent with the calibrated level which has an associated uncertainty of ±0.03 dB.

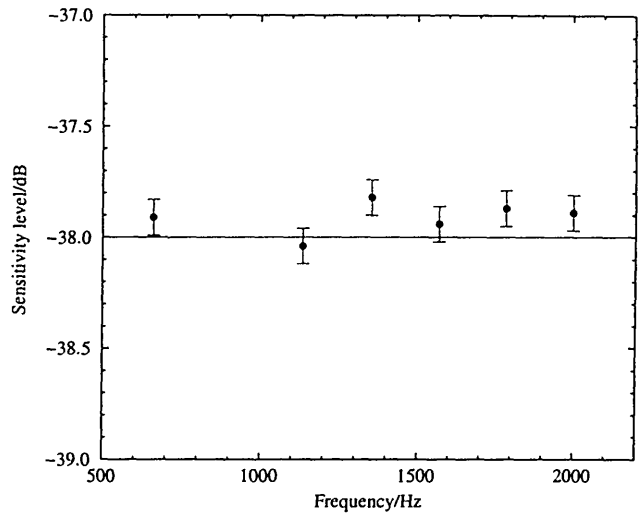

Figure 9. Sensitivity level derived from photon correlation LDA measurements and probe microphone voltage readings.

The LDA calibration measurements presented here do not yield standardized sensitivity as the acoustic field inside the glass tube is neither a true pressure-field nor a true free-field. However, the results do suggest that there is potential for the further development of the calibration technique for use in such environments.

7. Conclusions

Photon correlation LDA has been used to measure acoustic particle velocity and acoustic pressure in a standing wave. Acoustic particle velocity amplitude is obtained from analysis of the autocorrelation function of the photomultiplier signal. The measured autocorrelation function follows the behaviour predicted by the theoretical expression, derived by considering the form of the detector signal for particles moving in the fringe volume. The pressure amplitude derived from LDA velocity measurements and the pressure amplitude derived from probe microphone measurements agree to within ±0.2 dB for acoustic frequencies in the range of 660 Hz to 2 kHz and particle velocity amplitudes in the range of 13 mms^{-1} to 19 mms^{-1}. The sensitivity of a measurement microphone system was measured to within ±0.2 dB of the calibrated level.

Further work will be conducted to improve the agreement with traditional calibration methods. It is planned

that similar measurements be performed in a free-field chamber, enabling an absolute free-field calibration of a microphone to be performed.

Acknowledgement

The authors gratefully acknowledge the National Measurement System Policy Unit of the UK Department of Trade and Industry for supporting this project.

References

[1] International Electrotechnical Commission. *IEC* 61094-2: 1992, Measurement microphones - Part2 : Primary method for the pressure calibration of laboratory standard microphones by the reciprocity method.
[2] K. J. Taylor: Absolute calibration of microphones by a laser-Doppler technique. Journal of the Acoustical Society of America **70** (1981) 939–945.
[3] T. MacGillivray, D. M. Campbell, C. Greated, R. Barham: The development of a microphone calibration technique using Laser Doppler Anemometry. Acustica **88** (2002) 135–141.
[4] C. A. Greated: Measurement of acoustic velocity fields. Strain (1986) 21–24.
[5] J. P. Sharpe, C. A. Greated: The measurement of periodic acoustic fields using photon correlation spectroscopy. Journal of Applied Physics D: Applied Physics **20** (1987) 418–423.
[6] T. S. Durrani, C. A. Greated: Laser systems in flow measurements. Plenum Press, 1977.
[7] F. Durst, A. Melling, J. H. Whitelaw: Principles and practice of laser-doppler anemometry. Academic Press, 1976.
[8] J. P. Sharpe, C. A. Greated: A stochastic model for photon correlation measurements in sound fields. Journal of Applied Physics D: Applied Physics **22** (1989) 1429–1433.
[9] A. Papoulis: Probability, random variables, and stochastic processes. New York:McGraw-Hill, 1991.
[10] D. Hann, C. A. Greated: Acoustic measurements in flows using photon correlation spectroscopy. Measuring Science and Technology **5** (1994) 157–164.
[11] C. J. Tranter: Bessel functions with some physical aplications. London: English Universities Press, 1968.
[12] P. Giacomo: Equation for the determination of the density of moist air. Metrologia **18** (1982) 33–40.
[13] R. S. Davis: Equation for the determination of the density of moist air. Metrologia **29** (1992) 67–70.
[14] O. Cramer: The variation of the specific heat ratio and the speed of sound in air with temperature, pressure, humidity and CO_2 concentration. Journal of the Acoustical Society of America **93** (1993) 2510–2516.
[15] Y. S. Cheng, W. E. Bechtold, C. C. Yu, I. F. Hung: Incense smoke: Characterization and dynamics in indoor environments. Aerosol Science and Technology **23** (1995) 271–281.
[16] K. J. Taylor: Absolute measurement of acoustic particle velocity. Journal of the Acoustical Society of America **59** (1976) 691–694.
[17] G. N. Watson: A treatise on the theory of bessel functions. Cambridge University Press, 1952.
[18] M. Pentz, M. Shott: Handling experimental data. Open University Press, 1994.
[19] B. N. Taylor, C. E. Kuyatt: Guidelines for evaluating and expressing the uncertainty of NIST measurement results. NIST technical note 1297 (1994) 1–20.
[20] S. H. Jack, D. B. Hann, C. A. Greated: Influence of the acousto-optic effect on laser Doppler anemometry signals. Review of Scientific Instruments **69** (1998) 4074–4081.